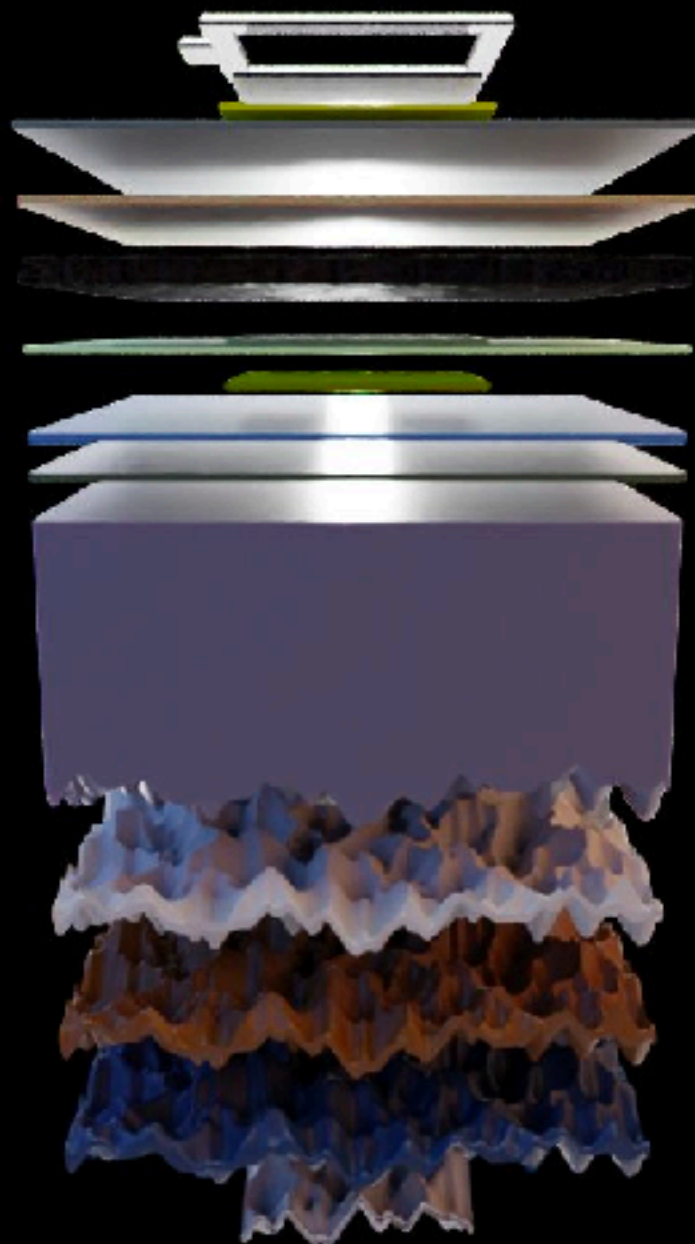


# Optimizations of high-efficiency silicon heterojunction solar cells for tandem applications



Delft University of Technology

Giulia Paggiaro

 TU Delft



# Optimizations of high-efficiency silicon heterojunction solar cells for tandem applications

by

Giulia Paggiaro

to obtain the degree of Master of Science  
at the Delft University of Technology.

Student number: 5132819  
Project duration: December 1, 2020 – September 17, 2021  
Supervisors: Prof. dr. Olindo Isabella  
Dr. Amarante Bottger  
Ir. Yifeng Zhao  
Dr. Luana Mazzarella

*Cover image adapted from:* <https://www.printedelectronicsworld.com/articles/22706/perovskite-silicon-tandem-solar-cells-on-threshold-of-30-efficiency>

## **Graduate**

Giulia Paggiaro

MSc Materials Science and Engineering (MSE)

Specialization in Materials for sustainable development

Faculty of Mechanical, Maritime and Materials (3mE), TU Delft

paggiaro.giulia@gmail.com

## **MSc Thesis Committee**

Prof. dr. Olindo Isabella - PVMD, Department of Electrical Sustainable Energy, TU Delft

Dr. Amarante Bottger - Department of Materials Science and Engineering, TU Delft

Ir. Yifeng Zhao - PVMD, Department of Electrical Sustainable Energy, TU Delft

Dr. Luana Mazzarella - PVMD, Department of Electrical Sustainable Energy, TU Delft

Prof. dr. Adriana Creatore - Plasma and Materials Processing group, Department of Applied Physics, TU Eindhoven

Dr. Vera Popovich - Department of Materials Science and Engineering, TU Delft

## **Delft University of Technology**

Department of Electrical Sustainable Energy - Photovoltaic Materials and Devices (PVMD)

# Preface

*"Solar power is going to be absolutely essential to meeting growing energy demands while staving off climate change." — Ramez Naam*

The impact of the ever-pressing climate change effect can be seen everywhere. Without urgent action, we may be heading towards a catastrophic temperature rise. The temperature rise predictions far exceed the goals set by the 2015 Paris Agreement which called for efforts to keep global warming under 2 degrees Celsius with respect to the pre-industrial level. This sense of urgency is a driving force for me to contribute to this matter in my thesis research, using my specialization in materials engineering. I hope this Master thesis research about the optimization of silicon heterojunction solar cells for tandem applications can ultimately provide scientific value for the advancement of photovoltaic technology. With this, I hope that this research can enable solar technology to become more competitive with conventional and non-renewable electricity sources and therefore can have a positive impact on climate change at a global level.

I would like to express my gratitude towards my supervisors for their support, guidance, and constant encouragement. I would also like to thank my family, my friends, and my roommates who always give me unconditional love and support, making the process of this Master's thesis more enjoyable.

Giulia Paggiaro  
Delft, September 2021



# Abstract

Silicon heterojunction (SHJ) solar cells have exhibited efficiencies well above 25%. To further boost the efficiencies of c-Si-based solar cells, high-bandgap perovskite cells are stacked on top achieving a record efficiency of 29.52%. However, as most of the high-quality perovskite films are solution-processed, the front surface of the bottom device should be flat. Therefore, in this work SHJ bottom c-Si cells featuring front-side-flat and rear-side-textured morphology, which delivers high  $V_{OC}$  together with excellent near-infrared response, have been optimized as bottom cells for tandem configurations.

Firstly, RF-PECVD deposition conditions of a (i)a-Si:H monolayer for symmetric  $\langle 100 \rangle$  flat c-Si surfaces were optimized. The optimized (i)a-Si:H monolayer (10-nm-thick) was obtained using pure  $\text{SiH}_4$ , which results in rather moderate passivation performances ( $\tau_{\text{eff}} = 1.2$  ms,  $i\text{-}V_{OC} = 701$  mV).

To improve further the passivation quality of monolayer (i)a-Si:H on flat  $\langle 100 \rangle$  surface, other passivation approaches aiming at incorporating more H without promoting detrimental epitaxial growth have been investigated. With a bilayer deposition approach, which features firstly a less H-containing (i)a-Si:H to prevent epitaxial growth and then a second H-rich (i)a-Si:H layer, the passivation properties were slightly enhanced to  $\tau_{\text{eff}}=1.4$  ms and a  $i\text{-}V_{OC}=704$  mV. Subsequently, by combining the bilayer approach with a post HPT,  $\tau_{\text{eff}}$  of 2.0 ms and an  $i\text{-}V_{OC}$  of 714 mV were achieved. Finally, by combining the bilayer approach with an intermediate HPT, the optimal passivation sample was deposited, with  $\tau_{\text{eff}}$  of 2.4 ms and an  $i\text{-}V_{OC}$  of 720 mV on the flat  $\langle 100 \rangle$  surface.

To gain a better understanding of the correlation between passivation qualities and the microstructure properties of (i)a-Si:H on flat  $\langle 100 \rangle$  surface, the layers have been characterized mainly via Fourier-transform infrared spectroscopy (FTIR). From the analysis, it can be concluded that the passivation layer that contains sufficient H and a higher fraction of monohydrides is beneficial for achieving a better passivation quality.

For the two-terminal tandem solar cells, bottom cells with (*n*)-contact on top are preferred due to the optical advantage of the perovskite top cells with the p-i-n configuration. Therefore, a first tandem cell with (*n*)a-Si:H has been fabricated in collaboration with TU Eindhoven resulting in 22.2% efficiency. Starting from this first fabricated tandem cell, its main optical limitations have been identified by performing advanced optical simulations using GenPro4, and the main strategies to overcome these optical drawbacks have been defined. By optimizing the front anti-reflection layers ( $\text{MgF}_2$  and ITO) thicknesses (at 100 nm and 20 nm, respectively), and reducing  $\text{C}_{60}$  thickness from 20 to 10 nm, front reflections, and parasitic absorption can be minimized. Thus a gain of implied photocurrent density of  $1.8 \text{ mA/cm}^2$  for the tandem cell was obtained. Further, by implementing (*n*)nc-SiOx:H doped layer in the SHJ bottom cell, instead of standard (*n*)a-Si:H layer the reflection between the top and bottom cell is also reduced, and enhanced light incorporation into the bottom cell is obtained. By adopting all the above-mentioned optimizations and also adjusting the perovskite layer from 473 nm to 530 nm, a total improvement of  $2.7 \text{ mA/cm}^2$  in implied photocurrent density with respect to the initial 22.2% tandem cell can be achieved.

After having identified different optically optimized SHJ bottom cells for tandem applications, both rear junction and front junction single-side-textured SHJ solar cells were fabricated. Firstly, the passivation quality of (i)a-Si:H/(*n*)-layer and (i)a-Si:H/(*p*)-layer on different (i)a-Si:H were investigated. Then RJ solar cells with three different (*n*)-type layers [(*n*)nc-SiOx:H;(*n*)nc-Si:H;(i)a-Si:H] have been fabricated with optimal thicknesses individuated from the tandem optical simulations. Furthermore, a tunnel recombination junction SHJ solar cell with a layer stack of (*n*)nc-Si:H/(*p*)nc-SiOx:H/(*p*)nc-Si:H has been fabricated and measured as well. In conclusion, various doped contacts (both *n*- and *p*-type) were successfully implemented into SHJ solar cells, which delivered  $V_{OC}$ s range from 700 to 714 mV and FFs range from 77.8% to 80.9%. Therefore, different well-functioning SHJ solar cells have been developed and are ready to be implemented as bottom cells for high-efficiency tandem devices.



# Contents

Abstract	v
List of Figures	ix
List of Tables	xiii
1 Introduction	1
1.1 Perovskite/silicon tandem solar cells: a promising technology	1
1.2 Perovskite/silicon tandem solar cells: architectures	3
1.3 The choice of a single-side-textured SHJ bottom cells	4
1.4 Challenges for a single-side-textured SHJ bottom cell	4
1.5 Master Thesis research outline	5
1.6 Research proposal	5
2 Fundamentals	7
2.1 Hydrogenated amorphous silicon	7
2.1.1 Microstructure of (i)a-Si:H	7
2.1.2 Growth mechanisms of (i)a-Si:H	8
2.1.3 Effect of c-Si surface orientation on (i)a-Si:H growth	10
2.1.4 Passivation mechanisms of (i)a-Si:H	11
2.2 Hydrogenated nanocrystalline silicon	12
2.2.1 Atomic structure	12
2.2.2 Growth mechanism	13
3 Instrumentation for SHJ solar cells fabrication and characterization	15
3.1 The fabrication process of SHJ solar cells	15
3.1.1 Wafer texturing	16
3.1.2 Wafer cleaning	16
3.1.3 RF-PECVD	17
3.1.4 Radio-frequency Magnetron Sputtering	18
3.1.5 Screen printing	19
3.2 Characterization tools for the (i)a-Si:H layer	20
3.2.1 Spectroscopic Ellipsometry	20
3.2.2 Photoconductance Lifetime Tester	21
3.2.3 FTIR	23
3.2.4 J-V measurement	25
3.2.5 SunsVoc measurement	25
3.2.6 EQE	26
3.2.7 UV-Vis-NIR spectroscopy	27
4 Optimization of hydrogenated intrinsic amorphous silicon	29
4.1 Experimental methodology for the optimization of (i)a-Si:H	29
4.1.1 Pre-deposition treatments	29
4.1.2 Deposition	29
4.1.3 Analysis and characterizations	30
4.2 Optimization strategy	31
4.2.1 Monolayer passivation optimizations	31
4.2.2 Monolayer with post HPT	44
4.2.3 Bilayer passivation	44
4.2.4 Bilayer passivation with post deposition treatments	47
4.3 Summary	51

5	Optical simulations	53
5.1	The initial tandem cell structure	53
5.2	The simulations software	54
5.3	Identification of major limitations of the first fabricated tandem cell and the resulting optical simulations	54
5.3.1	Optimization of front ITO and MgF <sub>2</sub> thicknesses	55
5.3.2	Optimization of the C <sub>60</sub> thickness	56
5.3.3	Optimization of the n-type layer of the SHJ bottom cell	57
5.3.4	Optimization of the perovskite thickness.	61
5.4	Summary of the guidelines to improve the tandem cell performance	63
6	Single-side-textured SHJ solar cells	65
6.1	Fabrication process	66
6.1.1	Pre-deposition treatments	66
6.1.2	Depositions	66
6.1.3	Analysis and characterizations	66
6.2	RJ SHJ solar cells	68
6.2.1	RJ SHJ solar cells with (n)nc-SiO <sub>x</sub> :H	68
6.2.2	RJ SHJ solar cells with different types of (n)-type layers	74
6.3	FJ SHJ solar cells	78
6.4	TRJ SHJ solar cells.	82
6.5	Summary	84
7	Conclusions	85
7.1	Optimization of hydrogenated intrinsic amorphous silicon passivating layer	85
7.2	Optimization of single-side-textured SHJ solar cells for tandem applications	85
8	Outlooks	87
8.1	Layer optimization for the single-side-textured SHJ bottom cell	87
8.2	Optimization of the perovskite/c-Si tandem cell layer stack.	87
9	Acknowledgments	89
A	Appendix	91
A.1	Thesis Approach	91
A.1.1	Methodology for experimental results collection and elaboration	91
A.1.2	Work Package Definition	92
A.2	Monolayer with post HPT	93
	Bibliography	95

# List of Figures

1.1	Different perovskite/silicon tandem cell architectures: a) four-terminal(4T) mechanically stacked; b) two-terminal (2T) monolithic cell; c) four-terminal optical spectral splitting; d) four-terminal reflective tandem. . . . .	2
1.2	Spectral irradiance absorbance of silicon (Si) and perovskite (P). . . . .	3
1.3	Perovskite/silicon solar cells architectures: p-i-n perovskite/Rear Emitter SHJ (a); n-i-p perovskite/Front Emitter (b) . . . . .	3
2.1	Schematic 2D representation of the microstructure of amorphous silicon with four typical defects: (1) monovacancies; (2) divacancies; (3) nanosized voids with monohydrides and (4) dihydrides . . . . .	8
2.2	Schematics of the interaction between SiH <sub>3</sub> and the growing surface. . . . .	9
2.3	Different c-Si surfaces: <111> orientation (a); <100> unreconstructed surface; <100>- 2x1 reconstructed surface. . . . .	10
2.4	Schematic of the mechanism of surface passivation of c-Si surface. . . . .	11
2.5	The various phases of thin-film silicon with a highly crystalline phase on the left and amorphous silicon on the right. . . . .	12
2.6	Schematic cross-sectional sketch of the nanocrystalline silicon layer growth on (i)a-Si:H coated substrate. On the right, the F <sub>C</sub> evolution of the nanocrystalline phase is depicted as function of the film thickness for the different stages: incubation, nucleation, nanogrowth and stationary growth. . . . .	13
3.1	Diagram of PECVD deposition system . . . . .	17
3.2	The schematic top-view of AMIGO PECVD (Elettrorava, S.p.A) in PVMD group with six deposition chambers. All chambers are connected to pumps to make high vacuum transfer and deposition. . . . .	17
3.3	Diagram of a typical magnetron sputtering system. . . . .	19
3.4	Diagram of a typical screen printing process. Top figure: the screen printing process; Bottom figure: at the end of the process. . . . .	19
3.5	Diagram of the SE measurement setup. . . . .	20
3.6	The typical elaboration sequences for physical properties characterization through SE measurements. . . . .	21
3.7	Schematic representation of a photoconductance lifetime tester. . . . .	21
3.8	Plot of minority carries lifetime as a function of their concentration, for different recombination mechanisms. . . . .	22
3.9	Schematic representation of FTIR interferometer. . . . .	23
3.10	An example of measured J-V curve with the definition of fill factor and efficiency. . . . .	25
3.11	Schematic illustration of the different components of an UV-Vis-NIR spectrophotometer. . . . .	27
3.12	Schematic representation of the optical design of a UV-Vis-NIR spectrometer with a 150 mm integrating sphere with a detail on the positions where the test sample has to be placed to measure either the transmittance or reflectance. . . . .	27
4.1	Schematic representation of symmetric passivation of flat <100> c-Si surfaces . . . . .	30
4.2	$\tau_{\text{eff}}$ , $i\text{-}V_{\text{OC}}$ and layer thickness of symmetrical passivation samples as a function of substrate temperature. . . . .	33
4.3	Microstructure factor ( $R^*$ ) and hydrogen content [ $C_{\text{H}}(\text{total}) = C_{\text{H}}(\text{WM}) + C_{\text{H}}(\text{SM})$ ] as a function of substrate temperature, obtained by FTIR analysis elaboration. . . . .	33
4.4	FTIR spectra and fitting of WM,LSM, HSM for samples deposited at different substrate temperatures. . . . .	34

4.5	$\tau_{\text{eff}}$ , $i$ - $V_{\text{OC}}$ and layer thickness of symmetric passivation samples as a function of chamber pressure. . . . .	36
4.6	Microstructure factor ( $R^*$ ) and hydrogen content [ $C_{\text{H}}$ (total) = $C_{\text{H}}$ (WM) + $C_{\text{H}}$ (SM)] as a function of chamber pressure, obtained by FTIR analysis elaboration. . . . .	36
4.7	FTIR spectra and fitting of WM,LSM, HSM for samples deposited at different pressures. . . . .	37
4.8	Effective lifetime, implied open-circuit voltage and layer thickness of symmetric passivation samples as a function of hydrogen dilution ratio. . . . .	39
4.9	Microstructure factor ( $R^*$ ) and hydrogen content [ $C_{\text{H}}$ (total) = $C_{\text{H}}$ (WM) + $C_{\text{H}}$ (SM)] as a function of DR, obtained by FTIR analysis elaboration. . . . .	39
4.10	FTIR spectra and fitting of WM,LSM, HSM for samples deposited at different DR. . . . .	40
4.11	Effective lifetime, implied open-circuit voltage and layer thickness of symmetric passivation samples as a function of the deposition power density. . . . .	42
4.12	Microstructure factor ( $R^*$ ) and hydrogen content [ $C_{\text{H}}$ (total) = $C_{\text{H}}$ (WM) + $C_{\text{H}}$ (SM)] as a function of power density, obtained by FTIR analysis elaboration. . . . .	42
4.13	FTIR spectra and fitting of WM,LSM, HSM for samples deposited at different power density. . . . .	43
4.14	Bilayer passivation . . . . .	44
4.15	Effective lifetime, implied open-circuit voltage and layer thickness of symmetric passivation samples as a function of bilayer thickness ratios. . . . .	45
4.16	Microstructure factor ( $R^*$ ) and hydrogen content [ $C_{\text{H}}$ (total) = $C_{\text{H}}$ (WM) + $C_{\text{H}}$ (SM)] for the monolayer and bilayer (i)a-Si:H. . . . .	46
4.17	FTIR spectra and fitting of WM,LSM, HSM for the monolayer and bilayer (i)a-Si:H. . . . .	46
4.18	Bilayer passivation with a) post HPT; b) intermediate HPT . . . . .	47
4.19	Effective lifetime, implied open-circuit voltage and layer thickness of symmetric passivation samples as a function of post HPT treatment time. . . . .	48
4.20	Effective lifetime, implied open-circuit voltage and layer thickness of symmetric passivation samples as a function of intermediate HPT treatment time. . . . .	49
4.21	Microstructure factor ( $R^*$ ) and hydrogen content [ $C_{\text{H}}$ (total) = $C_{\text{H}}$ (WM) + $C_{\text{H}}$ (SM)] for monolayer (i)a-Si:H, bilayer and bilayer with intermediate HPT. . . . .	50
4.22	FTIR spectra and fitting of WM,LSM, HSM for monolayer (i)a-Si:H, bilayer and bilayer with intermediate HPT. . . . .	50
5.1	A 22.2% efficiency perovskite/c-Si tandem cell developed by TU Delft and TU Eindhoven . . . . .	53
5.2	GenPro4 simulations of the the 22.2% efficiency perovskite/c-Si tandem cell developed by TU Delft and TU Eindhoven . . . . .	54
5.3	GenPro4 simulations of the matched tandem cell implied photocurrent for ITO and $\text{MgF}_2$ thicknesses varying from 0 to 180 nm. . . . .	55
5.4	GenPro4 simulations of the tandem cell with optimized $\text{MgF}_2$ (100 nm) and ITO (20 nm). . . . .	56
5.5	GenPro4 simulations of the tandem cell with optimized $\text{MgF}_2$ (100 nm), ITO (20 nm) and $\text{C}_{60}$ (10 nm) . . . . .	57
5.6	GenPro4 simulated implied photocurrent of the tandem cell, c-Si and perovskite subcells as a function of the ( $n$ )a-Si:H thickness . . . . .	58
5.7	GenPro4 simulated implied photocurrent of the tandem cell, c-Si and perovskite subcells as a function of the ( $n$ )nc-Si:H thickness . . . . .	59
5.8	GenPro4 simulations of the tandem cell with optimized $\text{MgF}_2$ (100 nm), ITO (20 nm), $\text{C}_{60}$ (10 nm) and ( $n$ )nc-SiOx:H (110 nm) . . . . .	60
5.9	GenPro4 simulated implied photocurrent of the tandem cell, c-Si and perovskite subcells as a function of the ( $n$ )nc-SiOx:H thickness . . . . .	60
5.10	GenPro4 simulations of the tandem cell with optimized $\text{MgF}_2$ (100 nm), ITO (20 nm), $\text{C}_{60}$ (10 nm), ( $n$ )nc-SiOx:H (110 nm) and perovskite (530 nm). . . . .	61
5.11	GenPro4 simulated implied photocurrent of the tandem cell, c-Si and perovskite subcells as a function of the perovskite thickness [for the cell with 110 nm ( $n$ )nc-SiOx:H . . . . .	62
5.12	GenPro4 simulated implied photocurrent of the tandem cell, c-Si and perovskite subcells as a function of the perovskite thickness [for the cell with 5 nm ( $n$ )a-Si:H . . . . .	62
6.1	The schematic architecture of single side-textured silicon heterojunction (SHJ) solar cell: a) rear emitter (RE) SHJ; b) front emitter (FE) SHJ. . . . .	65

6.2	The front side of the fabricated SHJ solar cell. . . . .	67
6.3	An example of EQE and 1-R plot. The black area (EQE) indicates the amount of charge carriers photogenerated in the absorber layer and successfully collected at the contacts; the grey area (1-R) indicates the optical and electrical losses in the cell; the white area instead indicates light reflections. . . . .	67
6.4	Schematic representation of symmetric deposition of ( <i>n</i> )nc-SiOx:H layer stack on various (i)a-Si:H layer coated flat <100> c-Si surfaces. a) monolayer (i)a-Si:H; b) bilayer (i)a-Si:H; c) bilayer (i)a-Si:H with post HPT treatment; d) bilayer (i)a-Si:H with intermediate HPT treatment. . . . .	69
6.5	$\tau_{\text{eff}}$ and $i\text{-}V_{\text{OC}}$ for each set of combination of (i)a-Si:H/( <i>n</i> )nc-SiOx:H stack on flat <100> coated c-Si surfaces. Set 1) monolayer (i)a-Si:H; Set 2) bilayer (i)a-Si:H; Set 3) bilayer (i)a-Si:H with post HPT treatment; Set 4) bilayer (i)a-Si:H with intermediate HPT treatment. . . . .	70
6.6	Schematic representation the fabricated single-side-textured RJ SHJ solar cell with ( <i>n</i> )nc-SiOx:H.	70
6.7	The J-V parameters of single-side-textured RJ SHJ cell with different ( <i>n</i> )nc-SiOx:H thicknesses. . . . .	71
6.8	The simulated implied photocurrent density, reflection losses and parasitic absorptions of RJ SHJ with different ( <i>n</i> )nc-SiOx:H thicknesses ( GenPro4) . . . . .	72
6.9	The experimentally measured EQE ans 1-R curves of single-side-textured RJ SHJ cells with different ( <i>n</i> )nc-SiOx:H thicknesses. . . . .	73
6.10	The simulated implied photocurrent density, reflection losses and parasitic absorption of RJ SHJ with different ( <i>n</i> )nc-SiOx:H thicknesses (GenPro4). . . . .	73
6.11	Schematic representation the fabricated single-side-textured RJ SHJ solar cell with a) 60 nm ( <i>n</i> )nc-SiOx:H; b) 20 nm ( <i>n</i> )nc-Si:H; c) 5 nm ( <i>n</i> )a-Si:H . . . . .	74
6.12	The J-V parameters of single-side-textured RJ SHJ cell with different ( <i>n</i> )-type layers. . . . .	74
6.13	The experimentally measured EQE ans 1-R curves of single-side-textured RJ SHJ cells with different ( <i>n</i> )-type layers. . . . .	76
6.14	The simulated single-side-textured RJ SHJ cells with different ( <i>n</i> )-type layers with GenPro4 software. . . . .	76
6.15	The simulated implied photocurrent density, reflection losses and parasitic absorptions of RJ SHJ with different ( <i>n</i> )-type layers (GenPro4) . . . . .	77
6.16	Schematic representation of symmetric deposition of ( <i>p</i> )-type layer stack on various (i)a-Si:H layer coated flat <100> c-Si surfaces. a) monolayer (i)a-Si:H; b) bilayer (i)a-Si:H; c) bilayer (i)a-Si:H with post HPT treatment; d) bilayer (i)a-Si:H with intermediate HPT treatment. . . . .	79
6.17	$\tau_{\text{eff}}$ and $i\text{-}V_{\text{OC}}$ for each set of combination of (i)a-Si:H/( <i>p</i> )-bilayer stack on flat <100> coated c-Si surfaces. Set 1) monolayer (i)a-Si:H; Set 2) bilayer (i)a-Si:H; Set 3) bilayer (i)a-Si:H with post HPT treatment; Set 4) bilayer (i)a-Si:H with intermediate HPT treatment . . . . .	79
6.18	Schematic representation of the fabricated single-side-textured FJ SHJ solar cell. . . . .	80
6.19	The J-V curve of single-side-textured FJ SHJ cell, with details about the values of main measured parameters of the cell. . . . .	81
6.20	Single-side-textured FJ SHJ cell: a) the measured EQE and reflectance b) the simulated absorptance with GenPro4 software . . . . .	81
6.21	Schematics of monolithic tandem structures with a) an interlayer of tunneling junction; b) TCO. Also some representative cells are reported from the literature. Cell a) uses an tunneling interlayer made of a stack of (n+)nc-Si:H/(p+)nc-Si to connect a fully textured Si bottom subcell and a p-i-n perovskite top subcell, resulting in a tandem efficiency of 25.2%. Cell b) uses a ITO recombination layer, to connect a single-side-textured c-Si bottom cell and a p-i-n perovskite top cell, leading to a tandem efficiency of 25.4%. . . . .	82
6.22	Schematic representation the fabricated single-side-textured SHJ solar cell with a TRJ made of a layer stack of ( <i>n</i> )nc-Si:H/( <i>p</i> )nc-SiOx:H/( <i>p</i> )nc-Si:H. . . . .	83
6.23	The J-V curve of single-side-textured TRJ SHJ cell . . . . .	83
6.24	Single-side-textured TRJ SHJ cell: a) the measured EQE and reflectance b) the simulated absorptance with GenPro4 software. . . . .	84
A.1	$\tau_{\text{eff}}$ , $i\text{-}V_{\text{OC}}$ of symmetric passivation samples deposited with monolayer (i)a-Si:H + post HPT treatment (variuos test were performed for the HPT). . . . .	93



# List of Tables

3.1	Corresponding relations between specified absorptions peaks and vibration modes. . . . .	24
4.1	The variation ranges of the main parameters of RF-PECVD . . . . .	31
4.2	Process parameters for deposition during investigation of substrate temperature effect . . . . .	32
4.3	Process parameters for deposition during the investigation of the chamber pressure effect . . . . .	35
4.4	Process parameters for deposition during investigation of hydrogen dilution ratio effect . . . . .	38
4.5	Process parameters for deposition during investigation of RF power . . . . .	41
4.6	Deposition parameters of optimized hydrogenated intrinsic amorphous silicon layer . . . . .	43
4.7	Deposition parameters of $i_1$ and $i_2$ hydrogenated intrinsic amorphous silicon layer for bilayer passivation . . . . .	45
4.8	Deposition parameters of $i_1$ and $i_2$ hydrogenated intrinsic amorphous silicon layers and post HPT for passivation of the c-Si surface . . . . .	47
4.9	Deposition parameters of $i_1$ and $i_2$ hydrogenated intrinsic amorphous silicon layers and intermediate HPT for passivation of the c-Si surface . . . . .	48
6.1	Deposition parameters the ( $n$ )nc-SiO <sub>x</sub> :H deposited on top of different (i)a-Si:H layers . . . . .	69
6.2	$iFF$ , $FF$ , $pFF$ and $R_{S_{SunS}Voc}$ of single-side-textured RJ SHJ cell with different ( $n$ )nc-SiO <sub>x</sub> :H thicknesses. . . . .	71
6.3	$iFF$ , $FF$ , $pFF$ and $R_{S_{SunS}Voc}$ of single-side-textured RJ SHJ cell with different ( $n$ )-type contacts. . . . .	75
6.4	Deposition parameters the ( $p$ )-bilayer [4 nm ( $p$ )nc-SiO <sub>x</sub> :H + 16 nm ( $p$ )nc-Si:H] deposited on top of different (i)a-Si:H layers . . . . .	78
6.5	The results of the manufactured single-side-textured SHJ solar cells with the best performance. . . . .	84



# 1

## Introduction

### 1.1. Perovskite/silicon tandem solar cells: a promising technology

With the sun providing the Earth with more than 10,000 times the energy humans currently consume [1] solar energy has the potentiality to be a promising alternative to conventional primary energy sources [2, 3]. The most important solar energy harvesting process is photovoltaic (PV) technology, which directly converts solar energy into electricity [3]. Nowadays it is essential to reduce the cost of photovoltaic energy generation in order to increase its competitiveness with conventional electricity sources [4, 5]. One way to enable the cost-reduction of PV technologies is by increasing their energy conversion efficiencies. Indeed higher efficiencies require a smaller area to install the same PV power and thus non-modular costs, which have a quite relevant importance effect on the cost of the PV system, can be reduced [3]. In order to increase the efficiency of PV devices, a research-driven improvement of the current technology is needed.

Among all the PV technologies, crystalline silicon (c-Si) solar cells are dominant in the photovoltaic sector with a market penetration of 95% [6]. With a record power conversion efficiency (PCE) of 26.7%, c-Si solar cells are approaching their theoretical efficiency limit of 29.4% [4, 7, 8]. It is crucial to improve the harvesting of the solar spectrum to boost their efficiency over this limit. In order to do so, multijunction solar cells, which combine multiple absorbers with different bandgaps, can be utilized. Coupling cells with different bandgaps allows the absorption of sunlight in different spectral bands, specifically in the long- and short-wavelength regions. Each wavelength region can be efficiently converted to electric power and a high output solar cell can be obtained [9].

The simplest multijunction solar cell also referred to as a tandem solar cell, is fabricated by stacking together two solar cells, one with a high bandgap and one with a narrow bandgap. Such a cell is defined as a two-junction tandem solar cell. As the light will enter the device from the top, the highest bandgap cell acts as the top cell while the lowest bandgap cell acts as a bottom cell. The top and the bottom cells usually absorb short- and long-wavelength spectra respectively [3].

There are two main types of basic tandem cell architectures, as shown in Fig.1.1: the mechanically stacked four-terminal (4T) and monolithic two-terminal (2T) tandem devices [10].

In the 4T device in Fig. 1.1 (a), two solar cells with different bandgaps are processed independently and then are mechanically stacked. The 4T device structure can also be achieved with other strategies, such as spectral splitting [11] or reflective tandems [12] which are schematically represented in 1.1 (c) and (d). The major advantage of the 4T configuration is that the output power is extracted separately from each subcell, as they are electrically independent [13]. This allows independent optimization of each subcell implying no device processing and structural restrictions. However, a 4T device has the disadvantage of requiring more functional materials and layers than a 2T device (transparent conductive oxides (TCOs), metal contacts, etc.), which increases their costs and can enhance optical and electrical losses. It also requires more non-modular components, such as two junction boxes and more wiring. For these reasons, 4T tandem solar cells are usually costly and this limits their extensive applications. On the contrary, monolithic 2T tandem devices are usually preferred and are currently the main subjects of scientific researches [14].

In a 2T (monolithic) device, illustrated in Fig. 1.1 (b), the top cell is deposited onto the bottom cell. As the top cell is processed directly on the bottom cell, the top cell processing has to meet some processing restriction requirements, such as temperature limits, to not degrade the bottom cell. Additionally, the bottom

cell has to be a suitable substrate for the top cell deposition. This is especially challenging for cells with textured surfaces. As said before the monolithic 2T is usually the preferred configuration although it has more processing restrictions than a 4T device. It allows the minimum use of functional layers and therefore can grant the fabrication of a low-cost device with low optical and electrical losses [15]. Moreover, it favors a cheaper and easier integration in a PV system, requiring only one junction box, whereas the 4T device would need two. For the reasons mentioned above, the monolithic 2T devices have the highest potential to reduce the levelized cost of electricity and they are a promising technology for PV applications [14].

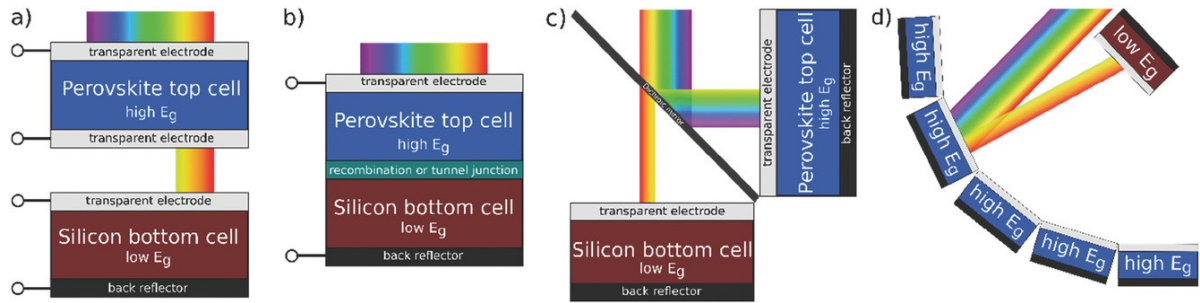


Figure 1.1: Different perovskite/silicon tandem cell architectures: a) four-terminal(4T) mechanically stacked; b) two-terminal (2T) monolithic cell; c) four-terminal optical spectral splitting; d) four-terminal reflective tandem [15]

In a monolithic tandem device, the top and the bottom cell are connected in series. The voltage of the two-junction solar cell is enhanced since it corresponds to the sum of the voltage of the top and bottom cells. The current density ( $J_{SC}$ ) of the tandem solar cell instead is limited by the subcell with the lower  $J_{SC}$ . Therefore it is required that both subcells deliver the same, or at least similar, photocurrent for achieving a high-efficiency device. This requirement is referred to as “current matching” [3].

To get current matching and obtaining a high conversion efficiency, appropriate top and the bottom cell should be selected. The most suitable top and bottom cells can be found by estimating the optimal theoretical bandgaps of each subcell, as it has been done in different studies [16, 17]. Crystalline silicon with a bandgap of 1.12 eV [3] has been proven to be an optimal bottom cell for tandem applications [16]. Among different c-Si solar cells, silicon heterojunction (SHJ) solar cells, that have reached high PCE with stunning open-circuit voltage (VOC) above 730 mV [18–21], are the most attractive for being integrated in a tandem structure. Considering a c-Si bottom cell, the optimum bandgap value for the top cell material has been calculated to be around 1.65 to 1.7 eV [16, 17].

The research of a top cell with a bandgap close to the optimal range has led to the identification of metal halide perovskites (MHPs) as promising top cell candidates. Among the numerous intriguing material properties of MHPs [22] the tunable bandgap of 1.5-1.8 eV through fine-tuning of the elemental composition counts among the most useful, since in principle it allows to achieve current matching through bandgap’s optimizations [17].

Therefore recently monolithic perovskite/ silicon tandem structures [15, 19, 20, 23–25] have gained the attention of the scientific community. Perovskite allows to enhance absorption of the low wavelength range portion of the solar spectrum as schematically shown by the absorption spectrum in Fig. 1.2, and the spectra utilization is enhanced. Perovskite/SHJ tandem cells are promising because their optical characteristics allow current matching but also because they enable a cost-effective power generation (allowed both by the low cost 2T configuration and by the low-cost material of the silicon and perovskite subcells) [15]. Their theoretical efficiency has been estimated to be 45.1% [26]. Oxford PV has recently reported a new record efficiency of 29.52 % [27] which is nearly 3% higher than the record efficiency for silicon single-junction cells. This, again, indicates that the monolithic perovskite/SHJ tandem cells have great potential to contribute to the advancement of solar cell technologies. In general, the increasing efficiency of perovskite/c-Si tandem cells is mostly due to the optimization of both the perovskite top cell and SHJ bottom cell. This MSc thesis research project focuses on the optimization of the SHJ bottom cell for monolithic perovskite/SHJ tandem solar cells applications.

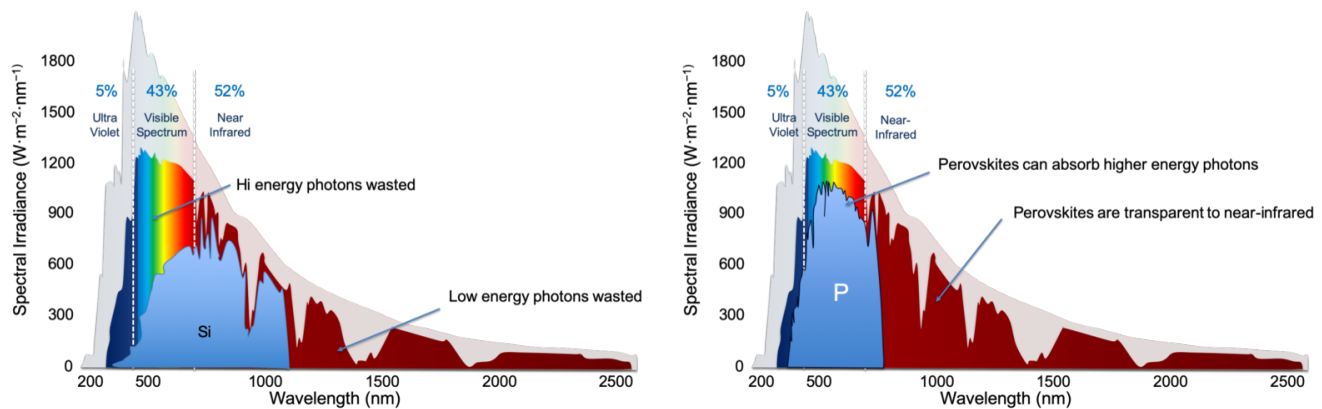


Figure 1.2: Spectral irradiance absorbance of silicon (Si) and perovskite (P). Figure adapted from [28].

## 1.2. Perovskite/silicon tandem solar cells: architectures

The general structure of a perovskite/silicon tandem cell is discussed in this chapter. Note that in the Fig. used in this chapter (Fig. 1.3) the bottom SHJ is depicted as a single-side-textured cell, which is the selected structure for this research, as extensively explained in section 1.3. However, also a fully textured SHJ can be used and the general layer stacking of the solar cell does not change.

Two possible architectures of the solar cells can be adopted as depicted in Fig. 1.3. The SHJ bottom cells can be designed with a rear junction (RJ) or a front junction (FJ) configuration. In a RJ SHJ solar cell, a stack made of an intrinsic hydrogenated amorphous silicon ((i)a-Si:H) and a (*n*)-type surface field layer is deposited on the flat front side (sunny side) of the cell, and a stack of (i)a-Si:H and (*p*)-type emitter layer is deposited on the textured rear side. In a FJ SHJ solar cell instead, the architecture is flipped: the (*p*)-type emitter is deposited on the front flat sunny side and the (*n*)-type surface field layer on the textured rear side. The perovskite top cell can also be designed with two different structures: 'regular' which consists of a *n*-doped-intrinsic-*p*-doped (*n-i-p*) stacking; or 'inverted' which instead is characterized by a *p*-doped-intrinsic-*n*-doped (*p-i-n*) layers' stacking. For the formation of a tandem cell, a *p-i-n* perovskite is deposited onto a RJ SHJ bottom cell [Fig. 1.3 (a)] while a *n-i-p* perovskite onto a FJ SHJ bottom cell [Fig. 1.3 (b)] [14].

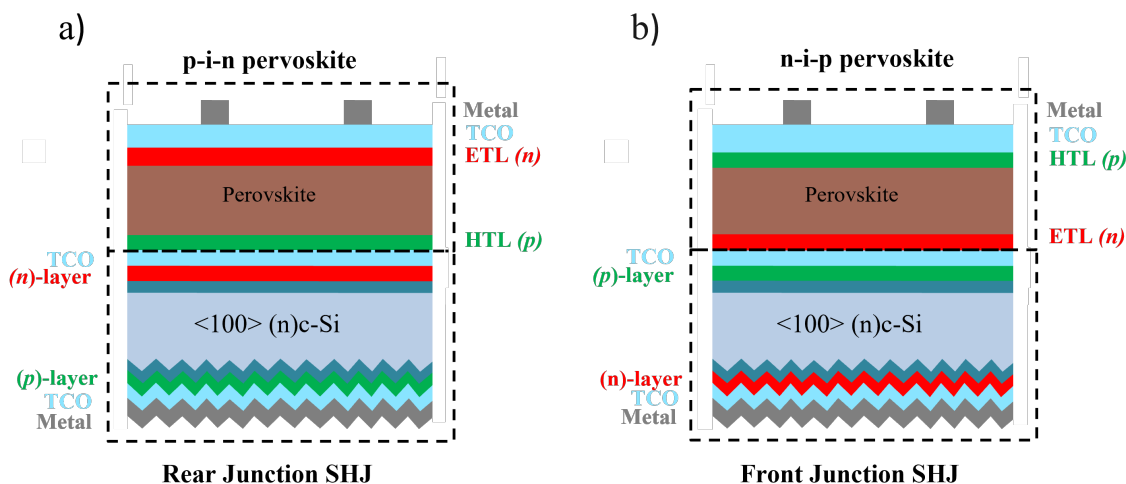


Figure 1.3: Perovskite/silicon solar cells architectures: *p-i-n* perovskite/Rear Emitter SHJ (a); *n-i-p* perovskite/Front Emitter (b)

Recently, the application of *p-i-n* perovskite top-cells prevailed over the *n-i-p* architecture [21]. Moreover, a study by Altazin et al. compared *n-i-p* and *p-i-n* perovskite cells for monolithic perovskite/silicon application and found that *p-i-n* solar cell architecture is the most promising in terms of maximum achievable photocurrent for both flat and textured silicon bottom cells [29]. Furthermore, the cells with the highest efficiency have been produced by using *p-i-n* perovskite/ RJ SHJ architectures [19, 20, 23–25]. For the

mentioned reasons, this research will mainly focus on RJ SHJ bottom cells for p-i-n perovskite/RE SHJ tandems. However also a FJ SHJ solar cell has been investigated to test its performance and compare it to RJ SHJ solar cells. Indeed, this could open interesting research paths, as few n-i-p perovskite/FE SHJ tandem cells with quite modest efficiencies have been reported in the literature [14, 30].

### 1.3. The choice of a single-side-textured SHJ bottom cells

The monolithic integration of a perovskite top cell on a silicon bottom cell is challenging due to the structural and processing restrictions, for both the top cell and the bottom cell.

The perovskite top cell has to meet different processing requirements, imposed by the temperature sensitivity of the SHJ bottom cell. In particular, the process temperature of the top cell has to be relatively low (<250 °C) [14]. This limitation is mainly due to the thermal stability of the intrinsic passivation layers of SHJ cells [31]. One suitable option for this problem is the deposition of a perovskite top cell at low temperatures.

The SHJ bottom cell, which is the main focus of this research, has to meet two main challenges: it has to guarantee minimum optical and electrical losses and it has to be a suitable substrate for efficient deposition of a perovskite top cell. In order to minimize optical losses and achieve a high optical absorption in SHJ solar cells, normally randomly textured surfaces, obtained through a chemical etching process, are used [32]. The pyramidal structure of the surface provides an effective light coupling and light trapping and enhances the near-infrared (NIR) response of the cell [33]. For this reason, few studies have focused on the deposition of perovskite on a textured pyramidal SHJ substrate (e.g. with thermal evaporation method [19]) but these structures generally result in expensive processing and are still in the development stage mainly due to the not so common physical and chemical vapour phase deposition methods of perovskite cells if compared to spin coating [19]. Although a textured SHJ is effective in enhancing light absorption, it is not suitable for allowing a wet chemical deposition of perovskite solar cells. Indeed a smooth substrate is required to deposit the perovskite solar cell with wet chemical deposition methods, such as spin coating [23, 34, 35] that has been proven to lead to the fabrication of the cheapest, most efficient, and most stable perovskite solar cells [36].

Thus, an important technical decision has to be made to optimize perovskite/SHJ tandem cells: effort should be focused on optimizing cheap and effective methods for depositing perovskite on textured SHJ substrates, which allows optimal optical absorption; or on optimizing single-side-textured SHJ solar cells, with a front flat side which allows the deposition of the cheapest and best-performing perovskite solar cells.

In this research, the chosen approach is to optimize a single-side-textured SHJ solar cells, which seem to be the most promising and cheap way to produce tandem cells. With this design, several groups have reported high tandem efficiencies [20, 23, 34]. The flat front side allows maintaining the advantage of the economical and efficient wet chemical perovskite processing while the textured rear side enhances the near-infrared response of the cell [24].

### 1.4. Challenges for a single-side-textured SHJ bottom cell

The choice of a single-side-textured SHJ solar cell as a bottom cell for the tandem cell introduces some challenges which need to be addressed if the realization of high-efficiency perovskite/c-Si tandem devices is aimed. Two main challenges can be identified.

The first challenge is related to the deposition of the (i)a-Si:H layer on a flat c-Si substrate with <100> surface orientation. It is widely accepted that the introduction of (i)-a-Si:H between the crystalline silicon (c-Si) substrate and the doped layers is crucial for obtaining a high open-circuit voltage and thus high-efficiency SHJ solar cells, mainly due to excellent surface passivation (as explained extensively in section 2.1.4) [37, 38]. Up to now most of the scientific studies have focused on optimizing the deposition of (i)a-Si:H on textured <111> oriented c-Si surfaces. Thus the optimization of the deposition conditions of (i)a-Si:H on flat <100> surfaces has to be investigated to guarantee optimal passivation and highly-efficient single-side-textured SHJ solar cells.

Aside from the (i)-a-Si:H layer, the second main challenge is related to the optimization of the whole SHJ architecture for tandem applications. In particular, it is critical to optimize the doped contact stacks to provide better band bending between c-Si/i-a-Si:H, minimized current losses (e.g minimized reflection and parasitic absorption), and decreased contact resistivity at the TCO/doped layers interface. These features enable higher efficiency devices [39].

## 1.5. Master Thesis research outline

The main challenges of single-side-textured SHJ solar cells have been identified in section 1.4. According to these challenges, a full Master's thesis research proposal is presented in this chapter (chapter 1).

In chapter 2 the main fundamental knowledge about the material properties of passivation layers and doped layers are introduced. Besides, the growth and passivation mechanism of these layers are explained. In chapter 3 the main tool and experimental techniques that are used to manufacture and characterize the SHJ solar cells and the layer's properties are discussed. After that, the main findings of this research are presented in three chapters:

- In chapter 4 the optimization of the (i)a-Si:H deposition on a flat surface in terms of passivation quality, uniformity, and reproducibility are discussed.
- After having optimized the intrinsic layer, a first single-side-textured SHJ solar cell has been used to fabricate a first tandem cell in collaboration between TU Delft (c-Si bottom cell) and TU Eindhoven (perovskite top cell). In chapter 5 the main optical limitations of the cell have been identified by performing advanced optical simulations and some strategies to overcome these drawbacks are defined. Thus new optimized configurations of both the top perovskite and bottom SHJ cell have been identified.
- In chapter 6 the optimized single-side-textured SHJ bottom cells for tandem applications are successfully fabricated, measured, and analyzed.

Lastly, the main results are summarized, the conclusions are drawn and the outlooks are given for further research on this topic.

## 1.6. Research proposal

Following the introduction, the main challenges and areas of concern for single-side-textured SHJ for perovskite/c-Si tandem devices were identified in section 1.4. Based on these points, a research proposal is presented in this chapter. The research objective and research questions are also defined. For more details, the approach taken in the Master thesis research is explained in section A.1 in the Appendix, by presenting the methodology and the thesis workflow.

### Research Objective and Research Questions

The research objective of the research is defined as follows:

*The objective of this research is to optimize single-side-textured silicon heterojunction solar cells for tandem silicon/perovskite applications.*

Based on the identification of the main challenges of perovskite/c-Si tandem solar cells, two main research questions of this research are defined below as the most relevant for contributing in providing scientific value in this field. In order to support answering the research questions in a detailed manner, sub-questions (SQ) are also defined.

1. How to optimize deposition parameters of (i)a-Si:H in terms of good passivation quality, uniformity, and reproducibility?
  - **SQ-1A:** How do deposition parameters affect the passivation quality of the (i)a-Si:H layer?
  - **SQ-1B:** How do different deposition approaches or post-deposition treatments affect the quality of the (i)a-Si:H layer?
2. How to optimize the single-side-textured silicon heterojunction solar cell for tandem application?
  - **SQ-2A:** How can the device be optimized for tandem-oriented applications? What is the optimized layer stack for the bottom SHJ cell and perovskite top cells for tandem applications?
  - **SQ-2B:** What is the electrical and optical performance of the optimized single-junction single-side-textured SHJ bottom solar cell?
  - **SQ-2C:** How do different (*n*)-doped layers affect the quality of the RJ single-side-textured SHJ device? What is the optimized combination of i/n layer stack for achieving optimized SHJ solar cells performance?

- **SQ-2D:** What is the optical and electrical performance of single-junction FJ SHJ solar cells? What is the optimized combination of i/p layer stack for achieving optimized SHJ solar cells performance?

Note that to meet the second research objective, a collaboration between TU Delft and TU Eindhoven (top perovskite cell) is held to fabricate and test monolithic 2T perovskite/SHJ solar cells. Moreover, during this research, a careful assessment and prioritization of the research questions have been performed: research question 1 has been identified as the first important question to be addressed since it is crucial for obtaining a high-efficiency device. Due to time limitations and also depending on the availability of experimental tools, some other interesting investigations are left out from this research but they are included in the outlooks for further research on this topic.

# 2

## Fundamentals

In this chapter, a literature research about the material properties of the intrinsic and doped layers of silicon heterojunction (SHJ) solar cells is reported. In particular, the properties of two main materials are investigated: hydrogenated amorphous silicon (a-Si:H) and hydrogenated nanocrystalline silicon (nc-Si:H).

### 2.1. Hydrogenated amorphous silicon

SHJ solar cells are optimal bottom cells for tandem applications due to the well-passivated c-Si wafer surface, which leads to a high open-circuit voltage ( $V_{OC}$ ) and high efficiencies. In particular, the typical  $V_{OC}$  of SHJ can exceed 750 mV [37, 40] and is significantly higher than the  $V_{OC}$  of homojunction cells that reaches a maximum of 700 mV [14].

One of the key points for achieving a SHJ cell with a high  $V_{OC}$  and a good device performance is the implementation of an intrinsic hydrogenated amorphous layer ((i) a-Si:H) between the c-Si substrate and the doped layers. The incorporation of this layer provides excellent chemical passivation of the c-Si surface, which is key for obtaining performant SHJ solar cells [37, 38, 41, 42]. The a-Si:H can also be doped to be used as a doped layer in SHJ solar cells [43].

In this chapter, the main characteristics of (i)a-Si:H layer, in terms of its microstructure, growth mechanism, and passivation mechanisms are presented.

#### 2.1.1. Microstructure of (i)a-Si:H

The microstructure of (i)a-Si:H layer is characterized by an amorphous, disordered lattice, as illustrated in Fig. 2.1. The Si atoms are arranged in tetrahedral coordination on short-range order ( $<1\text{nm}$ ) and lack long-range order, which makes the microstructure amorphous [44]. The lack of long-range order is caused by different lattice distortion factors, such as bond angle and bond length variations between nearest neighbors [45]. Moreover, since the lattice is amorphous and highly distorted, not all silicon atoms are bonded with neighboring atoms, thus dangling bonds and defects are present. The dangling bonds in the amorphous network are usually grouped in monovacancy, divacancy, trivacancy, 2 monovacancies, 6-ring void, platelet, and even nanosized voids [46].

The term hydrogenated indicates the presence of hydrogen in the amorphous network. Hydrogen acts as a defect passivator and passivates some of the dangling bonds in the lattice. The typical value of hydrogen content in a-Si:H varies between 5% and 15%. This allows obtaining a defect density of the order of  $10^{16}\text{cm}^{-3}$ , which makes a-Si:H suitable for PV applications. Non-hydrogenated amorphous Si would not be suitable for PV applications, due to extremely high defect density ( $10^{19}\text{cm}^{-3}$ ) that leads to a high charge carrier recombination [3].

The microstructure of the a-Si:H, its hydrogen content, and its chemical species composition are affected by deposition conditions. Generally, Fourier Transform Infrared Spectroscopy (FTIR) is used to determine the microstructural composition of a-Si:H amorphous layers, as discussed in detail in chapter 3. According to the results reported by Meddeb et al. [47] if monohydrides (MHs or Si-H:  $2000\text{cm}^{-1}$  [48]) (corresponding to low stretching mode, as described in section 3.2.3) are the majority species in the amorphous layer a more compact and less defective structure is formed. Instead, if the dihydrides (DHs or Si-H<sub>2</sub>:  $2090\text{cm}^{-1}$  [48]) (corresponding to high stretching mode, as described in section 3.2.3) are the main components a highly

defective and microvoids containing layer is formed. This can be explained through the effect of different radicals on the growth mechanism of the layer (section 2.1.2). The percentage of monohydrides or multi-hydrogen hydride can be identified with the microstructure factor ( $R^*$ ), which corresponds to the ratio of the FTIR intensities at  $2090\text{ cm}^{-1}$  modes over the sum of the intensity of  $2000\text{ cm}^{-1}$  and  $2090\text{ cm}^{-1}$  modes (see chapter 3). Lower  $R^*$  is correlated with a lower fraction of microvoids and better passivation qualities.

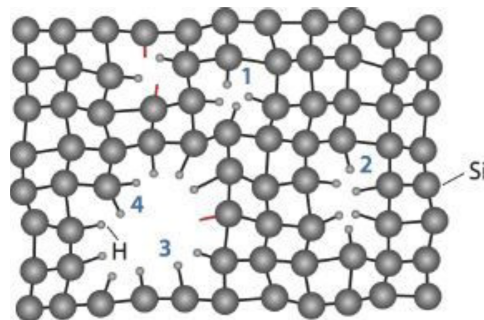


Figure 2.1: Schematic 2D representation of the microstructure of amorphous silicon with four typical defects: (1) monovacancies; (2) divacancies; (3) nanosized voids with monohydrides and (4) dihydrides [49]

### 2.1.2. Growth mechanisms of (i)a-Si:H

The most common method used to deposit the intrinsic a-Si:H layer is plasma-enhanced chemical vapor deposition (PECVD) [32, 50] (the working principle of PECVD is explained in section 3.1.3).

In the last decades, numerous studies have investigated the a-Si:H growth mechanism from  $\text{SiH}_4$  plasma, which is the most used gas for (i)a-Si:H deposition [32]. In this section, the most important growth model is described. The growth of a-Si:H layers, from a  $\text{SiH}_4$  plasma can be viewed as a three-step process:

1. Generation of radicals. Electrons in the plasma collide with  $\text{SiH}_4$  molecules and produce neutral radicals ( $\text{SiH}_3$ ,  $\text{SiH}_2$ ,  $\text{SiH}$ ,  $\text{Si}$ ,  $\text{H}$ ). Other species can be produced, as described in more detail by Van et al. [32]. For simplifications, it can be assumed that, among the produced species,  $\text{SiH}_3$  radicals are dominant in low pressure and low power plasma conditions [51, 52]
2. Transport and diffusion of those radicals to the growing film surface
3. Reaction of radicals at the film surface to form hydrogen-terminated a-Si:H film

In short, once the radicals have been generated, they diffuse to the growing surface and react with it to form stable  $\text{SiH}_4$  molecules and Si-Si bonds [45].

The reaction of the radicals with the substrate (step 3) can be further explained as theorized by Perrin et al. [52] and Matsuda et al. [51], which assume  $\text{SiH}_3$  to be the dominant radical in the plasma leading to low defect density a-Si:H [51–53]. A schematic of the main interactions of the  $\text{SiH}_3$  radical with the substrate is illustrated in Fig.2.2.

The  $\text{SiH}_3$  diffuse towards an hydrogen-terminated surface. Due to low deposition temperature ( $<200^\circ\text{C}$ ) and thus moderate thermal energy, the  $\text{SiH}_3$  radicals weakly adsorb (physisorb) on a Si-H surface state. After being physisorbed it diffuses along the surface by hopping from one surface site to another. During surface diffusion, the  $\text{SiH}_3$  radical can:

- Abstract a surface H atom and thus create a surface dangling bond and gaseous  $\text{SiH}_4$
- Chemisorb on a surface dangling bond, which has been created through the extraction of an H atom from the surface, contributing to the film growth. Note that the film growth happens with a two-step reaction; first a by creating a dangling bond on the surface which allows another radical to deposit on the site [51]. Therefore two  $\text{SiH}_3$  radicals are necessary for the growth of the film.
- React with another physisorbed  $\text{SiH}_3$ , forming gaseous  $\text{Si}_2\text{H}_6$
- Desorb from the physisorbed state (desorption depends on energetic considerations and probability of sticking to the surface site)

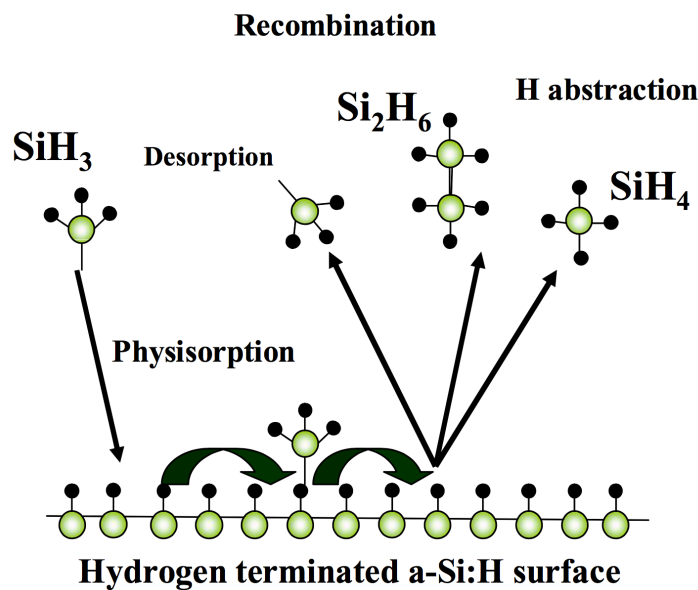


Figure 2.2: Schematics of the interaction between SiH<sub>3</sub> and the growing surface [32]

This model can explain the relatively low and temperature-dependent surface roughness of a-Si:H due to the occurrence of diffusion of the radical along the surface [53]. This model is the most used for describing the a-Si:H growth mechanism. However, it involves some assumptions and simplifications, such as the assumption that SiH<sub>3</sub> radical is the dominant radical. This assumption is valid at peculiar growth conditions, specifically low pressure and low RF power (low pressures (<10 Pa) and low RF power (<10 mW/cm<sup>2</sup>)) [32, 54]. Different deposition conditions would require the necessity to consider other radicals as relevant for the film growth process. Moreover, the growth surface is idealized as flat and H-terminated. In reality, the presence of surface roughness and dangling and strained bonds should be considered. Further models that include the possibility of a SiH<sub>3</sub> radical to insert directly into a strained Si-Si bond have also been developed by von Keudell et al. [55].

### The effect of different radicals on the growth mechanism of (i)a-Si:H

The main assumption of the above-described model is that SiH<sub>3</sub> is the dominant radical for film growth. In reality, different radicals species contribute to the film growth (for detailed explanation on [32, 56]), and depending on their chemical properties, flux, and energy they affect the growth mechanism and the quality of the deposited material [56]. In this section, the effect of SiH<sub>3</sub> and SiH<sub>2</sub> on the film quality is explained. The main difference between their interaction with the surface depends on their sticking probability and their surface mobility on the substrate.

As stated before SiH<sub>3</sub> radicals are the main precursors required for high-quality film [51, 52]. This is because they are low reactive and very mobile, with a low sticking coefficient and thus they diffuse along the surface and fill surface valleys and non-uniformities. As a consequence, a film with conformal step coverage, smooth surface, and low microvoids density can be deposited [57, 58].

On the contrary SiH<sub>2</sub> radicals have been proven to contribute to the formation of highly defective layers [47]. This can be explained by the fact that they have a high sticking coefficient and tend to attach wherever they impact, almost without diffusing along the surface. Due to a poor surface diffusion and a high sticking coefficient, SiH<sub>2</sub> follows a ballistic-like deposition a leads to the formation of films with a not uniform surface coverage and columnar structure [56–59]. This ballistic-like deposition causes the formation of voids [57]. Moreover, another effect accompanied by high SiH<sub>2</sub> amount is the increased generation rate of polysilane (gas particle formation), Si<sub>2</sub>H<sub>6</sub>, according to equation 2.1 below. The resultant Si<sub>2</sub>H<sub>6</sub> species can be an obstacle to film deposition and thus lead to a poor interface [60].



In summary,  $\text{SiH}_3$  is known to have much larger surface mobility than  $\text{SiH}_2$  and hence tends to produce a-Si:H film of better quality. A plasma analysis during the deposition process can therefore be very useful for allowing the identification of a  $\text{SiH}_3$  rich plasma that leads to the deposition of a high-quality film.

The influence of  $\text{SiH}_2$  on the formation of a highly defective and microvoid-rich microstructure can explain the use of FTIR analysis for the determination of the (i)a-Si:H quality. In particular, this can be explained by the fact that if dihydrides are the dominant species the film is highly defective and contains microvoids, while if monohydrides are the main components of the film the amorphous layer is more compact and less defective structure [47].

### 2.1.3. Effect of c-Si surface orientation on (i)a-Si:H growth

The crystallographic orientation of the c-Si surface can play a role in determining the growth mechanism of the (i)a-Si:H passivating layer.

Textured c-Si substrates are usually fabricated through etching Si<100> substrates, which lead to the exposure of Si<111> faceted pyramids [32]. Since textured surfaces are the most common for SHJ for their optical advantages (as explained in the introduction chapter, the deposition of (i)a-Si:H on Si<111> surfaces is quite common in the scientific literature. The choice of a single-side-textured SHJ introduces the challenge of understanding how the growth mechanism of the (i)a-Si:H layer on a <100> surface differs from <111> textured surface. A better understanding will allow improving the quality of the flat (i)a-Si:H/c-Si interface and thus the device performance, and to optimize the deposition of (i)a-Si:H on <100> c-Si surfaces.

Different studies have compared the deposition of (i)a-Si:H layer on <100> and <111> c-Si surfaces. It has been found that the two surface orientations have a different predisposition to epitaxial growth. Under equivalent conditions, film growth on a <100>-oriented Si surfaces is much more likely to result in crystalline epitaxial growth [61–64]. Indeed epitaxial growth is influenced by the length of the adatoms diffusion in the film growth surface which depends also on surface orientation [62]. Si<111> surfaces are characterized by one dangling bond per surface atom, which sticks out perpendicularly (Fig. 2.3 (a) ). The Si<100> surface instead is characterized by two broken bonds per atom, tilted with respect to another (Fig. 2.3(b)) [65]. Thus, for <100> planes each silicon atom in the growing plane has to form two bonds with the atoms in the previous one. In other words, it is constrained to be incorporated in that crystalline lattice position. On the contrary, in the case of a <111> c-Si surface, the incorporation of silicon atom entails the formation of only one bond with the atoms in the growing surface, and this can make epitaxial growth less probable [63]. Usually for <111> high temperatures are needed for epitaxial growth to occur [66]. Moreover, <100> surface can easily reconstruct, in a Si(100)-(2x1) dimers configuration, illustrated in figure 2.3 (c), which is known to play an essential role in epitaxial growth [67]

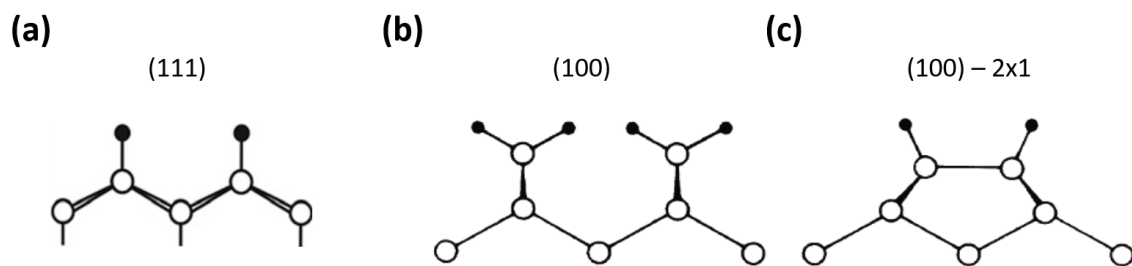


Figure 2.3: Different c-Si surfaces: <111> orientation (a); <100> unreconstructed surface; <100>- 2x1 reconstructed surface [65]

It is critically important to avoid epitaxial growth at the (i)a-Si:H/c-Si interface to obtain high-efficiency SHJ solar cells [64]. Thus, deposition conditions on (i)a-Si:H on <100> c-Si surface, which is more prone to epitaxial growth have to be adjusted with respect to the deposition conditions of <111> c-Si surface. For example, Demareux et al. found that in <100> epitaxial growth happens even at lower hydrogen dilution ratio [62].

### 2.1.4. Passivation mechanisms of (i)a-Si:H

The reduction of charge recombination is mandatory to produce a device with high performance. Indeed recombination prevents charge carriers to be collected and thus will lower the open-circuit voltage of the solar cell device [3, 68].

The presence of unsaturated dangling bonds at the c-Si surface leads to a large density of trap and recombination sites. To reduce charge recombination c-Si surface must be well passivated. In this section, after introducing different passivation methods, the passivation mechanism of (i)a-Si:H is explained.

Generally, two main methods are used for passivating the c-Si surface. They reduce charge recombination in two different ways: i) by minimizing the dangling bond density (chemical passivation) ii) by reducing the density of one carrier type near the surface, through field effect (field-effect passivation is usually done by depositing conductive materials, such as SiO<sub>2</sub> and SiN<sub>x</sub> on the surface)[69]. Chemical passivation is the most used passivation method for SHJ. Moreover, it has the advantage that can be obtained at relatively low processing temperatures, and therefore it has broad applications [70]. In this research the chemical passivation of c-Si surface via the deposition of (i)a-Si:H is performed.

Chemical passivation of the c-Si surface of SHJ is done by depositing (i)a-Si:H on top of the c-Si layer [37, 38], which leads to a reduction of the c-Si surface defect density due to the passivation of dangling bonds due to the formation of bonds between dangling bonds and Si or H atoms, as shown in Fig. 2.4. In other words, a high level of hydrogenation of the a-Si:H/c-Si interface is desired. In this way, the performance of the cell can be increased and the interface properties are enhanced [40, 71].

The passivation quality is usually described in terms of the effective lifetime of the charge carriers ( $\tau_{\text{eff}}$ ) and implied open-circuit voltage ( $iV_{\text{OC}}$ ) which can be measured with the characterization methods explained in chapter 3 thanks to the excellent bulk quality of c-Si Wafer.

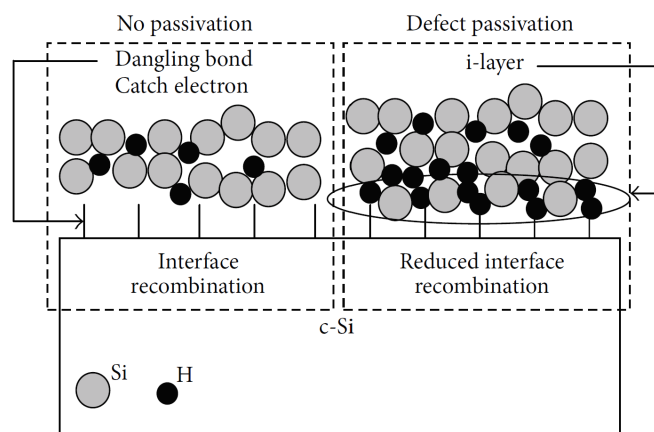


Figure 2.4: Schematic of the mechanism of surface passivation of c-Si surface [60]

### The importance of the deposition of a good quality (i)a-Si:H layer for optimal passivation

The optimization of the (i)a-Si:H layer is a trade-off between its bulk series resistance and lifetime. The series resistance is related to the defect inside the a-Si:H network and the lifetime is related to the passivation of a-Si:H/c-Si interface. When both aspects are optimized, a high-quality SHJ solar cell can be fabricated [72].

It is therefore crucial that the deposited (i)a-Si:H layer meets certain quality conditions to ensure the fabrication of a high-performance solar cell. The first quality condition of the (i)a-Si:H layer is the presence of an abrupt surface at the interface with c-Si. No crystalline epitaxial growth of the film has to happen as it is known to provide bad passivation qualities [64]. Moreover, the deposited layer has to be homogeneous, low defective, and with a low fraction of microvoids. Indeed, inhomogeneity, a high defect density in the bulk (i)a-Si:H and microvoids can introduce new recombination sites. Thus, the growth of the (i)a-Si:H layer has to be optimized by tuning deposition conditions in order to obtain the desired film quality.

To summarize, (i)a-Si:H is fundamental to chemically passivate the c-Si surface, but the choice of the deposition conditions of the passivating layer is critical to avoid epitaxial growth, guarantee sufficient passivation at the c-Si/a-Si:H surface, and deposit a low defective (i)a-Si:H film.

### The influence of the (i)a-Si:H thickness on passivation properties

For obtaining good surface passivation and avoid the introduction of additional defects and recombination center the thickness of the deposited (i)a-Si:H layer has to be around an optimal value. In particular, intrinsic a-Si:H films with a thickness of about 4–20 nm are used for chemically passivating the c-Si surface of SHJ solar cells [50]. The optimal (i)a-Si:H has to be thick enough to provide sufficient surface passivation and homogeneity if deposited, but thin enough to avoid significant recombination in (i)a-Si:H bulk.

The minimum thickness of the (i)a-Si:H layer has been reported to be around 4 nm. Delgiannis et al. found that a layer thickness <4nm leads to a significant decrease in passivation quality (measured in terms of  $\tau_{\text{eff}}$ ). This may be due to the inhomogeneity of the deposited layer and the insufficient surface passivation [73].

Once met the minimum thickness requirements, the intrinsic layer should not be too thick in order to maximize  $J_{\text{SC}}$  and FF of the solar cells [32]. Thus, as stated before, apart from the (i)a-Si:H/c-Si interface, recombination centers can also be present in the bulk (i)a-Si:H. For thicker passivation layers the bulk (i) a-Si:H defect density becomes relevant and limits the effective charge lifetime and the performance of the cell. Instead, when the thin layer is applied, the importance of the a-Si:H/c-Si interface over the bulk quality of a-Si:H [74] is higher. Moreover, thin layer helps to limit parasitic absorption.

In summary, the optimal thickness of the (i)a-Si:H layer integrated in SHJ solar cells is in the range of 4-20 nm [75, 76]. It is also important to note that in this range (in particular for layer smaller than 10 nm) a relevant decrease in  $\tau_{\text{eff}}$  with thickness is observed [75]. Therefore, it is important, when comparing the passivation quality of different layers, to compare layers with a comparable thickness to get comparable passivation.

## 2.2. Hydrogenated nanocrystalline silicon

Hydrogenated nanocrystalline silicon (nc-Si:H) can be deposited by PECVD as well and it is used to deposit doped contact in SHJ solar cells [77, 78]. In the following sections, the atomic structure and the growth mechanism of nc-Si:H are discussed.

### 2.2.1. Atomic structure

The microstructure of nc-Si:H is characterized by small nanocrystals embedded in an amorphous matrix (a-Si:H) that are a few tens of nanometers big. [3]. In the film, H atoms are preferentially located in the a-Si:H network, where they contribute to the passivation of dangling bonds, or at the crystal grain boundaries due to the low solubility of H into the crystalline phase [79].

The material can show a wide range of structure evolution from fully amorphous to highly crystalline depending on the deposition parameters [80, 81], as shown in Fig. 2.5. On the left side of the figure, a fully crystalline phase is shown, which contains cracks and pores. Instead, on the right side of the picture, a fully amorphous matrix is shown. When moving from the right to the left side the fraction of crystalline grains increases [3].

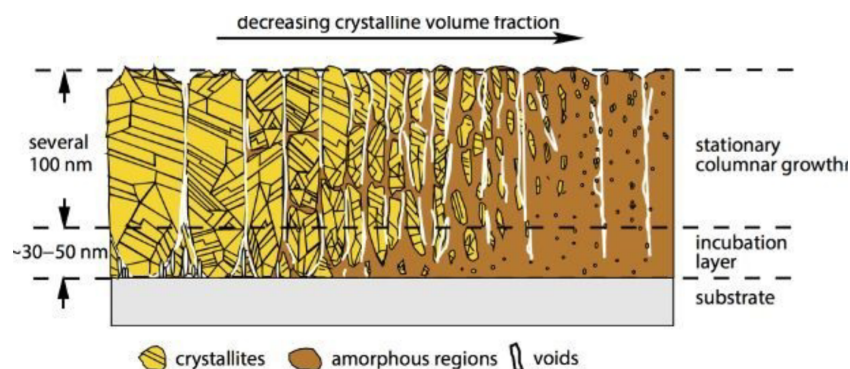


Figure 2.5: The various phases of thin-film silicon with a highly crystalline phase on the left and amorphous silicon on the right [3]

Note that The nc-Si:H can be alloyed with oxygen atoms to form nc-SiOx:H. The characteristic microstructure of nc-SiOx:H is analogous to the one of nc-Si:H but in this case nanocrystals are embedded in a highly transparent, oxygen-rich amorphous silicon oxide (a-SiOx:H) matrix as indicated by TEM investigations [82].

### 2.2.2. Growth mechanism

With respect to a-Si:H, a higher hydrogen flow is used to entail hydrogen-induced crystallization [83] and it plays an important role in the growth of high-quality nc-Si:H films.

A simplified sketch of the growth of the nc-Si:H film is shown in Fig. 2.6. This model of growth is theorized by a four stages approach by Cabarrocas et al. [84] which has been also supported by in situ ellipsometry studies [85]. During the initial stages of growth, an incubation (amorphous) layer is formed with a thickness that is usually in the order of few nanometers [86] and highly depends on the substrate [87]. The incubation layer is believed to control the transition from the amorphous to the nanocrystalline regime affecting the evolution and, consequently, the properties of the entire nc-Si:H film. Different treatments have been reported in the literature to guarantee prompt nanocrystal nucleation and reduce the thickness of the incubation layer, such as seed layer or CO<sub>2</sub> plasma treatment [87, 88]. Afterward, the nanocrystalline phase increases progressively until the growth becomes stationary. The crystal growth happens usually in a cone-shaped manner and this makes the crystalline fraction variable along the film thickness [89].

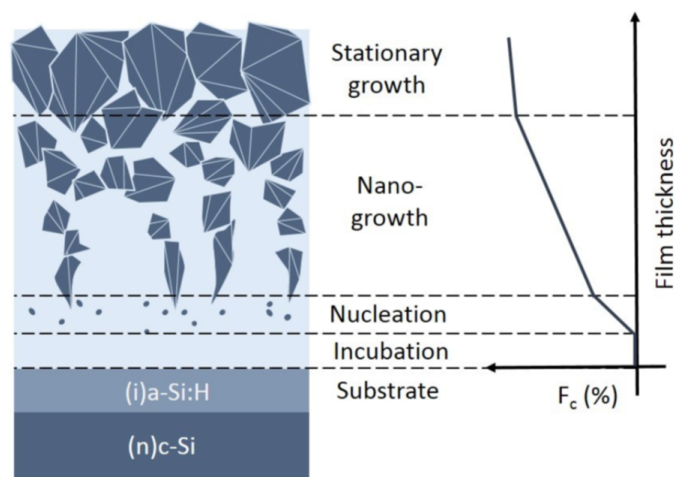


Figure 2.6: Schematic cross-sectional sketch of the nanocrystalline silicon layer growth on (i)a-Si:H coated substrate. On the right, the  $F_C$  evolution of the nanocrystalline phase is depicted as function of the film thickness for the different stages: incubation, nucleation, nanogrowth and stationary growth [90].

In order to explain H-induced crystallization, the chemical annealing mechanism has been proposed, where H aids crystallization by annihilating the strained Si-Si bonds in the a-Si:H film [91]. This mechanism at the atomic-scale level has been further investigated with molecular-dynamics simulations and infrared spectroscopy by Sriraman et al., which have proven that H-induced crystallization is caused by the insertion of H atoms into strained Si-Si bonds through the formation of Si-H-Si bonds configurations. As the H atoms diffuse through the a-Si:H matrix, they either break or perturb strained Si-Si bonds result in the transformation of the film's structure from amorphous to nanocrystalline [83].



# 3

## Instrumentation for SHJ solar cells fabrication and characterization

In this chapter, the tools and techniques that are used to fabricate and characterize the SHJ solar cells are introduced. Firstly, the main steps of the fabrication process are described and each procedure is explained in detail in sections. After that, the main characterization techniques are also explained.

### 3.1. The fabrication process of SHJ solar cells

The fabrication of solar cells starts from a FZ n-type <100> oriented c-Si wafer, with resistivity of ( $3\pm 2 \Omega\text{cm}$ ) and thickness ( $280\pm 20 \mu\text{m}$ ). To fabricate single-side textured wafers a texturing process is done on one side of the c-Si wafer. In order to do that, a 200nm-thick  $\text{SiN}_x$  layer is deposited on one side of the substrate to protect one flat side from the texturing process in the TMAH solution. As a result, the non-masked side is textured by immersing the wafer in a TMAH solution, and a pyramidal textured side is obtained.

In the specific, the fabrication process of single-side textured FBC-SHJ solar cells involves different steps. The main steps are listed below:

- Deposition of  $\text{SiN}_x$  on one side of the wafer
- Texturing of one side of the wafer, by 5% TMAH treatment. The texturing process is explained in detail in this chapter in section 3.1.1.
- Removal of  $\text{SiN}_x$ , by immersion in BHF.
- Cleaning of the sample with the wet-chemical cleaning procedure. This procedure is explained in details in this chapter in section 3.1.2.
- Deposition of (i)a-Si:H/doped layer stack on the front flat side and (i)a-Si:H/doped layer stack on the rear textured side in RF-PECVD Amigo.
- Deposition of a transparent conductive oxide, ITO, on both front and rear sides by using sputtering in Zorro.
- Screen printing on both front and rear sides.

A detailed explanation of the working principle of RE-PECVD, sputtering, and screen printing are also reported in this chapter in sections 3.1.3, 3.1.4, and 3.1.5 respectively.

### 3.1.1. Wafer texturing

The texturing process of the single side of the silicon wafer is done with an anisotropic etching method. In this research, the process consists in dipping the wafers in a hot ( $75 \pm 2^\circ\text{C}$ ) alkaline etching solution 5% tetramethylammonium hydroxide (TMAH,  $(\text{CH}_3)_4\text{NOH}$ ) for 15 minutes, which is realized by mixing 1L 25% TMAH (SIGMA-ALDRICH), 120 mL ALKA-TEX.8 (ISRA) and 4L deionized water (DI water). ALKA-TEX.8 is used for reducing the texture time and extending the lifetime of the etching bath. The etching solution acts on one side of the wafer only, since the other side is coated with a 200 nm thick  $\text{SiN}_x$  layer.

After the etching treatment of a single-side flat  $\langle 100 \rangle$  surface, a  $\langle 111 \rangle$  oriented textured random upright-pyramid surface is obtained. This happens because the  $\langle 100 \rangle$  c-Si orientation is etched faster than the  $\langle 111 \rangle$  orientation. As a consequence, a  $\langle 111 \rangle$  oriented textured random upright-pyramid surface is obtained, with a pyramid size of about several microns ( $0.5 \mu\text{m}$  to  $2.1 \mu\text{m}$ ), as reported by [92]. The pyramidal textured surface has some optical advantages. It allows the light incident on the pyramidal surface to be partially transmitted into the inner structure and partially reflected towards other pyramids' surfaces. In this way, the light ray can be coupled into the wafer again and the scattered light can travel a longer optical path in the wafer. This leads to fewer reflection losses and enhanced absorption [3].

### 3.1.2. Wafer cleaning

In order to produce a high-performance solar cell, the c-Si wafer has to be free of contaminants and with a low defect density. Contaminants and defects are present both on planar and textured c-Si surfaces. Textured surfaced however are more prone to contamination than planar surfaces. Indeed, after texturing, the defect density increases due to a larger surface area, and contamination becomes more probable.

In order to minimize wafer's contamination, a wafer cleaning procedure is done. The main purposes of the cleaning procedure are:

- To remove the impurities or any other contaminants (such as organics and metals) left from the texturing process
- To smooth surface irregularities, defined as nano-roughness, induced by the texturing process. The nano-roughness, which is an extended layer with several Å of length, contributes to increasing the defect densities by forming stretched and dangling bonds.
- To partially passivate the dangling bonds at c-Si surface and remove oxides from the surface.

The combination of all the cleaning steps is often referred to as nitric acid oxidation cycle (NAOC). The full cycle consists of wet-chemical oxidation followed by hydrofluoric (HF) dip. The detailed steps are described below:

- The single-side textured wafers are firstly immersed into the concentrated  $\text{HNO}_3$  (99%) at room temperature for 10 minutes to remove organic contaminants.
- They are rinsed with de-ionized (DI) water for 5 minutes.
- They are immersed into the 69.5%  $\text{HNO}_3$  at a temperature of  $110 \pm 5^\circ\text{C}$  for 10 minutes to clean metal contaminants.
- Again, they are rinsed with DI water for 5 minutes.
- Lastly, a hydrofluoric (HF) dip with Marangoni (0.55% HF) is conducted. During this process, the dangling bonds of the c-Si surface are partially passivated and the oxide layers on the surface are removed. The chosen HF dip duration is 5 minutes. A too-short HF treatment is not desired since it may be ineffective in removing all the oxidants. A too-long process has to be avoided too since it can increase surface roughness [93].

In total, the complete NAOC cycle is repeated one time for double-side flat wafers. Instead for single-side textured wafers, it is repeated three times (as suggested from [73]). After the NAOC cleaning cycle is concluded the clean wafer is loaded immediately into the vacuum chamber of the RF-PECVD machine. Note that, to avoid re-oxidation, the time interval between the last step of the cleaning cycle and the vacuum chamber loading should be as short as possible. In general, this time interval is kept within 5 minutes.

### 3.1.3. RF-PECVD

For the deposition of both passivation and doped layers, the radio frequency (RF) plasma-enhanced chemical vapor deposition (PECVD) called AMIGO (Elettrorava, S.p.A) at TU Delft is used.

A typical RE-PECVD chamber is illustrated in Fig. 3.1. Besides, a schematic top-view of AMIGO PECVD chamber is also shown in Fig. 3.2, and it consists of individual deposition chambers to prevent cross-contamination.

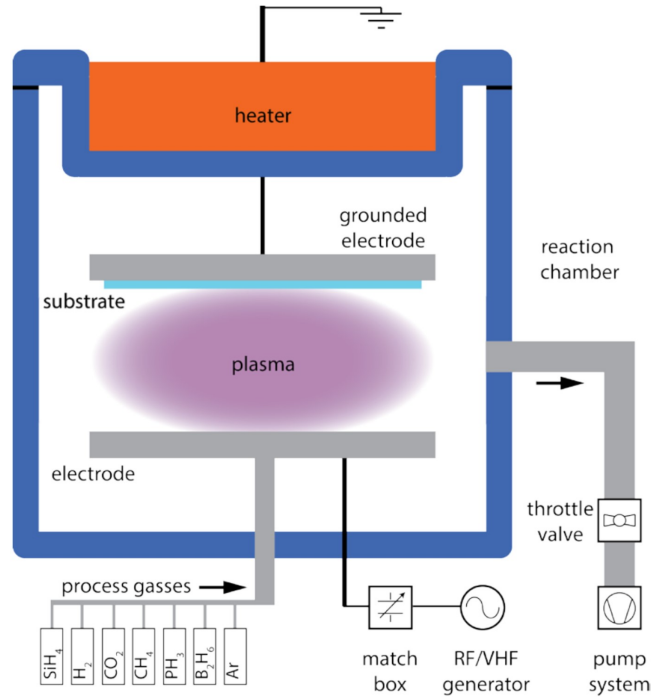
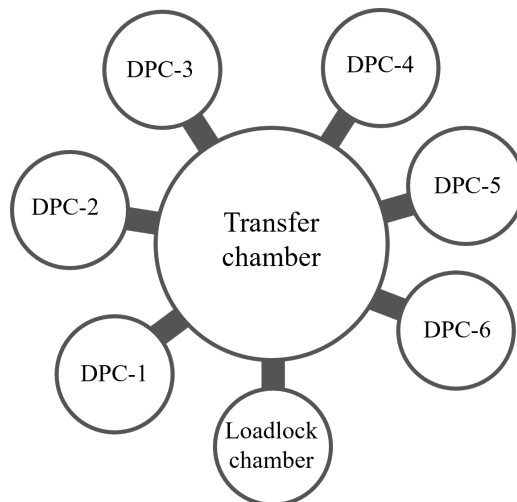


Figure 3.1: Diagram of PECVD deposition system . Adapted from [94]



### Amigo RF-PECVD (Elettrorava, S.p.A)

Figure 3.2: The schematic top-view of AMIGO PECVD (Elettrorava, S.p.A) in PVMD group with six deposition chambers. All chambers are connected to pumps to make high vacuum transfer and deposition.

The process begins with loading the sample, that has gone through some pre-deposition treatments, in the PECVD loadlock chamber (LLC). Here an ultrahigh vacuum is created (UHV). After that, the sample is transferred to specific reaction chambers (DPC), which are also in UHV conditions, according to the deposition purposes. Then gas precursors are injected into the chamber. Depending on the material that has to be deposited, a wide range of gas precursors can be used. For the deposition of (i)a-Si:H mainly silane ( $\text{SiH}_4$ ) and hydrogen ( $\text{H}_2$ ) are used. Instead, for the deposition of the doped layers, dopant gases are added to the chamber as well, such as diborane ( $\text{B}_2\text{H}_6$ ) and phosphine ( $\text{PH}_3$ ). Moreover, methane ( $\text{CH}_4$ ) and carbon dioxide ( $\text{CO}_2$ ) can be also used to introduce carbon and oxygen in the deposited layers respectively. Once the atoms and molecules of the gas precursor have been injected into the UHV reaction chamber, they are ionized and converted into plasma through an energy source. The energy source in RF-PECVD is an oscillating electric field between two conductive electrodes, that is regulated through an RF signal of 13.56 MHz [3]. As a consequence, electrons are accelerated by the electric field, they collide with the gas molecules generating radicals, ions, neutral atoms, molecules, and electrons. Since the collision happens in the gas phase the surface temperature remains relatively low during the deposition. The generated particles will interact with the substrate and contribute to the layer's growth. Specifically, only neutral or positively charged particles can interact with the surface, while others are confined in the plasma due to the formation of a plasma sheath as extensively described by Van et al. [32]. For the manufacture of single-side textured SHJ solar cells in this thesis project, the DPC<sub>3</sub> chamber of RF-PECVD AMIGO is used for i-layer deposition, DPC<sub>2</sub> for n-type layers, DPC<sub>1</sub> for p-type layers.

Besides the simplicity of the process, the main advantages of RF-PECVD are:

- The fact that it allows deposition of thin films at low operating temperatures, below 200°C [3]. Low temperatures are allowed because PECVD does not involve the use of thermal energy sources as other CVD methods. Instead, highly energetic radicals and molecules are formed in the plasma through an electric field energy source.
- The wide range of gas precursor that can be used, which allow the deposition of a wide range of thin films. Moreover, doping or optimization can be easily done by simply adding a gas mixture into the gas flow or adjusting deposition conditions.
- The ease of producing high-quality thin films. The produced films are of high quality, they show appropriate adhesion to the substrate, desirable surface coverage, and uniformity [3].

The quality of the deposited layer can be controlled by varying the deposition parameters (i.e the pressure and temperature in the reaction chamber, the gas flow rates of the different process gases, the power coupled into the plasma by the radio frequency (RF) generator) [38, 41, 57, 95]. All those parameters together can be systematically optimized for excellent properties of obtained layers.

#### 3.1.4. Radio-frequency Magnetron Sputtering

Radio-frequency (RF) magnetron sputtering belongs to the class of physical vapor deposition (PVD) methods. It is normally used to deposit the TCO layers and metal contacts in solar cells. A typical chamber of an RF-magnetron sputter is shown in Fig. 3.3. During RF magnetron sputtering, highly energetic inert gas particles, such as Argon (Ar), bombard a target (cathode) when RF power is applied. As a consequence, atoms and discharged electrons are sputtered from the target. The sputtered atoms diffuse towards a substrate or vacuum chamber (anode) and they deposit on the substrate after a random walk. Instead, discharged electrons collide with Ar atoms in the chamber to create extra ions and free electrons, to sustain the plasma environment.

In this research, ZORRO sputtering tool (Polyteknik) is used to sputter the transparent coating oxide, in the specific indium tin oxide (ITO). For ITO deposition, the target consists of a layer with a composition 90 wt.%  $\text{In}_2\text{O}_3$  and 10 wt. %  $\text{SnO}_2$ .

The ITO deposition can damage the passivation, as reported in ref. [96]. Therefore, a two-step deposition is applied. It consists of a low-power pre-deposition followed by the main deposition at high power. In this way, damages can be contained and deposition of ITO with optimal contact and optical properties can be obtained.

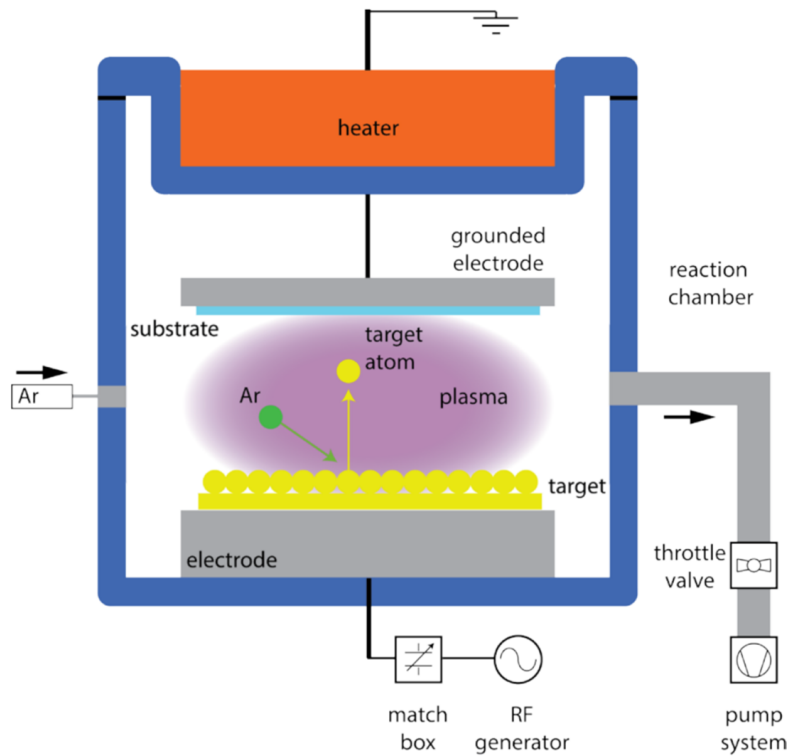


Figure 3.3: Diagram of a typical magnetron sputtering system. Adapted from [94]

### 3.1.5. Screen printing

After a cell precursor is formed, the last step is to deposit the metal contacts, which are the limiting factor to the performances of the fabricated solar cells [39]. Diverse metallization technologies can be used: metal evaporation, screen printing, or electroplating. In this research, screen printing has been adopted.

A schematic illustration of the screen printing is shown in Fig. 3.4. During screen printing, a liquid viscous metallic paste is swept by a squeegee on the surface of a screen, which consists of an interwoven thin-wire mesh with designed openings for grid patterning. The paste then goes through the opening of the screen and is printed on the substrate (cell precursors). After screen printing, the SHJ solar cell is treated in air at 170°C for 30 min, to allow the formation of the metal contacts.

In this thesis project, a low-temperature silver (Ag) polymer-based paste, from DuPont™, is used. With this paste, contact formation can happen at low temperatures. A more detailed explanation of screen printing can be found in ref. [97].

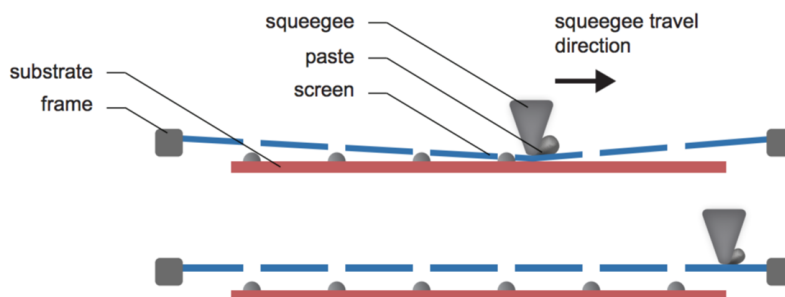


Figure 3.4: Diagram of a typical screen printing process. Top figure: the screen printing process; Bottom figure: at the end of the process. Adapted from [97].

## 3.2. Characterization tools for the (i)a-Si:H layer

In order to understand the quality of the deposited thin-film layers and the performance of the fabricated solar cells, several characterization techniques have been used and they are explained in the following sections.

### 3.2.1. Spectroscopic Ellipsometry

Spectroscopic Ellipsometry (SE) is an optical characterization technique that measures the change of light polarization upon reflection or transmission after the light interaction with the sample. The collected data can be elaborated and fitted with an optical model which is used to calculate the layer thickness, optical constants, and other physical parameters [98].

A general schematic representation of the SE setup is illustrated in figure 3.5. The setup includes a light source, a polarizer, a polarization analyzer, and a detector. The sample is placed on the stage. The unpolarized light from the light source will go through the polarizer in order to obtain a linearly polarized light source. The light is reflected from the sample, it becomes elliptically polarized, and it is analyzed through the polarization analyzer.

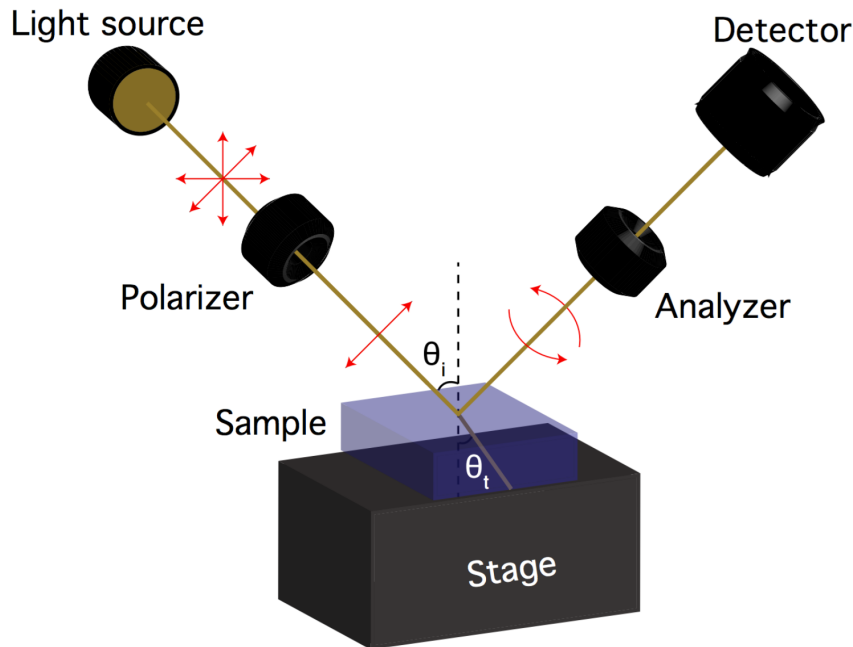


Figure 3.5: Diagram of the SE measurement setup. Adapted from [73]

The SE measurement process is illustrated in figure 3.6. Two important properties are measured: the amplitude ratio ( $\psi$ ) and the phase difference ( $\Delta$ ) between p- and s- polarized light waves. Elaborating and fitting the collected data with optical models allows obtaining values of optical constants and layer thickness. Those values can be further elaborated to obtain other physical parameters. For a-Si:H layers, the Cody-Lorentz model is mainly used [99].

In this thesis project, a SE by J.A. Woollam Co., M-2000DI is used. It is mainly used for thickness measurements allowing to check deposition rate and layers uniformity. The main advantage of this technique is that it allows a precise thickness measurement if the correct fitting model is used. Indeed the general accuracy for thickness measurements is around  $0.1 \text{ \AA}$  [98]. Moreover, it does not involve contact with the sample, and it is a non-destructive measurement technique. It however has one main limitation: the roughness of the measured samples should be as low as possible, and thus textured wafers cannot be measured directly by SE. Since this optimization is focused on the front flat surface of the SHJ solar cell, this limitation does not affect the aim of this research.

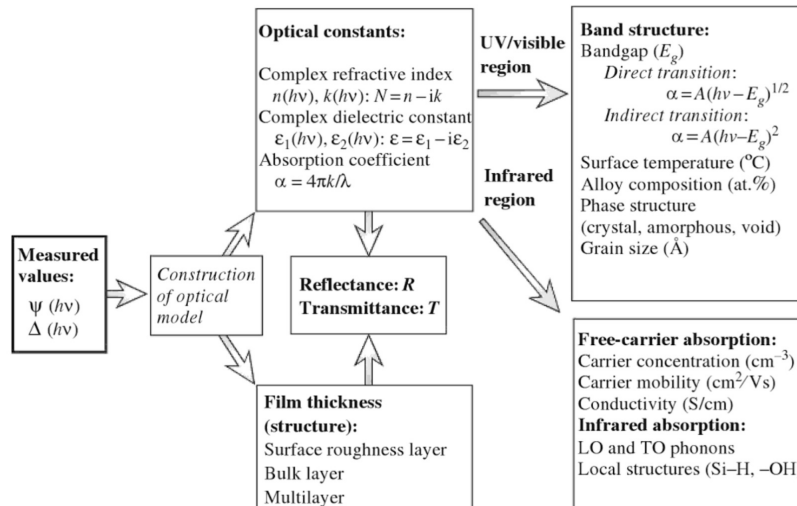


Figure 3.6: The typical elaboration sequences for physical properties characterization through SE measurements. Adapted from [98]

### 3.2.2. Photoconductance Lifetime Tester

In this research, a Sinton WCT-120 photoconductance lifetime tester has been used. The photoconductance lifetime tester is used to characterize the passivation quality of the solar cell layers and solar cell precursors in terms of effective charge carrier lifetime ( $\tau_{\text{eff}}$ ), implied open-circuit voltage ( $iV_{\text{OC}}$ ), and reverse-biased saturation current ( $J_0$ ).

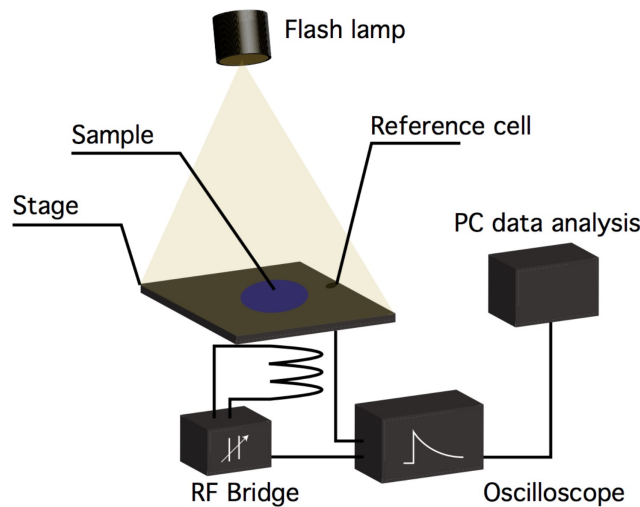


Figure 3.7: Schematic representation of a photoconductance lifetime tester. Adapted from [73]

A schematic representation of a general setup is shown in Fig. 3.7. In general, the test sample is placed on a stage at uniform and constant temperature and on top of the stage, there is a light intensity detector (a photodiode). A coil, located near the wafer and below the stage, is coupled in an inductive way to the RF Bridge.

A flash lamp, placed above the samples, illuminates the sample with light flashes, for short time periods which can be set in the measurement settings. The light flash induces changes of the photoconductance of the sample. In particular, excess charge carriers will be generated, and thus the conductance will increase. Meanwhile, the changes in conductivity are measured by the coil and then are elaborated through optical models to obtain the  $\tau_{\text{eff}}$ ,  $iV_{\text{OC}}$ , and  $J_0$  [100].

For an n-type semiconductor, the photoconductivity ( $\sigma_L$ ) (which is defined as the change in conductivity due to optical excitation) is related to the excess minority carriers (holes) density by the equation 3.1:

$$\theta_L = q\Delta p(\mu_n + \mu_p) \quad (3.1)$$

where  $q$  is the electron charge,  $\Delta p$  is the excess carrier density,  $\mu_n$  and  $\mu_p$  are mobility for electrons and holes, respectively. Therefore,  $\Delta p$  can be calculated from the photoconductivity, as showed in the equation above.

The measurement can be conducted with two different modalities: the quasi-steady-state-photoconductance (QSSPC) mode and the transient photoconductance decay (Transient PCD) mode. The two modes can be set by adjusting the decay time constant of the flash lamp. A long time constant leads to QSSPC while a short time constant leads to transient PCD mode. For samples with minority charge carrier lifetime of  $\tau_{\text{eff}} < 200 \mu\text{s}$ , the QSSPC mode is recommended while if  $\tau_{\text{eff}} > 200 \mu\text{s}$ , PCD is used. Based on the continuity equation,  $\tau_{\text{eff}}$  can be expressed as indicated in the equation below:

$$\tau_{\text{eff}} = \frac{\Delta p}{G(t) - \frac{\partial \Delta p}{\partial t}} \quad (3.2)$$

where  $G(t)$  is the generation rate and it is calculated from the photodiode. As stated above, for QSSPC mode, it is assumed that the light is varying very slowly so that  $\delta \Delta p / \delta t$  is neglected because  $G(t) \gg \delta \Delta p / \delta t$ . Instead, for transient measurements, the pulse of light is used only to excite the carriers and is off during the actual measurement so that  $G(t)$  can be approximated to zero.

In the analysis results,  $\tau_{\text{eff}}$  is shown as a function of the minority carrier density (MCD). Typically,  $\tau_{\text{eff}}$  value is taken at a minority carrier density of  $10^{15} \text{ cm}^{-3}$  because it is the most relevant value for evaluating surface recombination, as confirmed by Zhang et al. [93]. In particular, at this minority carrier density and lower ones ( $\text{MCD} < 10^{15} \text{ cm}^{-3}$ ), the Shockley-Read Hall (SRH) recombination is dominant and more hints on the defectivity can be obtained. Instead at higher level ( $\text{MCD} > 10^{15} \text{ cm}^{-3}$ ), Auger and radiative recombination are more relevant [101]. This can be also observed from Fig. 3.8 below. Moreover, a minority carrier density of  $10^{15}$  is similar to the injection level under one-sun conditions.

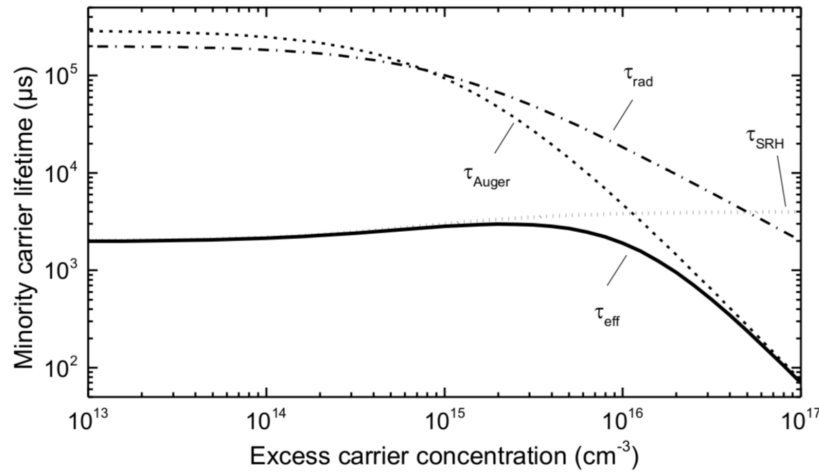


Figure 3.8: Plot of minority carries lifetime as a function of their concentration, for different recombination mechanisms. Adapted from [102]

The  $iV_{\text{OC}}$  is calculated based on minority carrier density from the equation reported below:

$$iV_{\text{OC}} = \frac{K_B T}{q} \ln \left( \frac{\Delta p (N_D + \Delta p)}{n_i^2} \right) \quad (3.3)$$

where  $N_D$  is the concentrations of donors. In this master thesis project, lifetime measurement is extensively used to assess the passivation qualities of the intrinsic (i)a-Si:H passivating layers. It is also used to trace process-induced damages during the SHJ fabrication, such as ITO sputtering;

### 3.2.3. FTIR

In this thesis, a Fourier transform infrared spectroscopy (FTIR) instrument by Thermo Scientific Nicolet 5700 has been used. FTIR is a characterization technique used for evaluating the quantitative chemical composition of the deposited layers. Specifically, for (i)a-Si:H the quantitative composition of hydrogen bonding configurations ( $\text{Si-H}_x$ ) and hydrogen content in the network can be obtained. This reflects the quality of the film microstructure and its passivation quality, as discussed in detail in chapter 2.

The FTIR technique is based on the analysis of the infrared absorption, reflection, or transmission spectra of the measured sample. The material molecular composition can be obtained from the spectra since each molecule has a different infrared response.

The measuring process is described in the following lines. Infrared light, emitted from a beam source, passes through an aperture, which is used to control the incident light fraction. The light beam which is incident on the sample has different wavenumbers that vary in the mid-infrared range (wavenumber from  $400$  to  $4000\text{ cm}^{-1}$ ). This can be realized by using an interferometer, schematically represented in Fig. 3.9. By controlling the mirror position in the interferometer, specific wavelengths can be blocked or transmitted, thanks to the interference principle. An interferogram signal is created, which is detected by a detector and elaborated by a computer with a Fourier transformation.

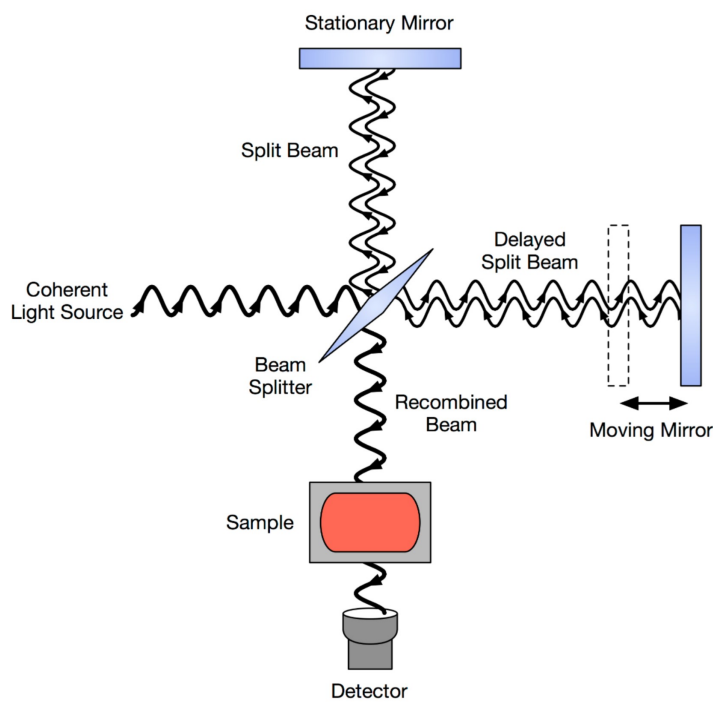


Figure 3.9: Schematic representation of FTIR interferometer. Adapted from [103]

To measure only the thin film spectra, the bare wafer is measured first, then the wafer coated with the layer is measured. In this way, the background spectra of the wafer can be subtracted and the obtained spectrum can be regarded as the one of the thin-film layers. An absorption vs wavelength is measured, then the wavelength is usually transformed in wavenumber ( $\text{cm}^{-1}$ ), according to the equation below. Thus the final graph plots absorption vs wavenumber.

$$\text{Wavenumber } [\text{cm}^{-1}] = \frac{10^7 \frac{\text{nm}}{\text{cm}}}{\text{Wavelength } [\text{nm}]} \quad (3.4)$$

The typical spectrum shapes is characterized by single or multiple absorption peaks at specified wavenumbers. The wavenumbers corresponding to the peaks indicate the presence of peculiar bonding configurations in the sample and correspond to the vibration frequency of these molecular bonds. The width of the peak is an indication of the number of molecules. In the case of a-si:H, the spectrum is characterized by different absorption peaks, among which the most important are Si-H wagging mode (WM) and two stretching modes

(SMs). The WM corresponds to the absorption peak at  $640 \text{ cm}^{-1}$ . The two SMs are divided in low stretching mode (LSM) corresponding to wavenumber range of  $1980$  to  $2030 \text{ cm}^{-1}$  and high stretching mode (HSM) corresponding to  $2060$  to  $2160 \text{ cm}^{-1}$ , although slightly different values can be reported in the literature [104]. LSM corresponds to monohydrides; HSM corresponds to both dihydrides and clustered monohydride which form internal voids [105]. The absorption peak position and the corresponding bonding configurations or vibration modes are summarized in Tab. 3.1 below.

Table 3.1: Corresponding relations between specified absorptions peaks and vibration modes.

Wavenumber [cm-1]	Vibration mode	Reference
640	WM SiH	[106]
2000	SM SiH	[48]
2090	SM SiH <sub>2</sub>	[48]

In this thesis FTIR characterization is performed on (i)a-Si:H coated sample, to correlate the passivation quality to the microstructure of the passivating layers. The FTIR spectra are fitted to obtain two important quantities: the hydrogen content in the film ( $C_H$ ) and the microstructure factor ( $R^*$ ) [107]. The fitting procedure is explained in detail in the following lines.

The fitting procedure starts with a baseline correction of the absorption-wavenumber spectra obtained for the measurement. Then, the spectra are elaborated in the following way to calculate  $C_H$  and  $R^*$ , as described below.

As described by Beer-Lambert law:

$$I = I_0 \exp(-\alpha t) \quad (3.5)$$

where  $I$  and  $I_0$  are the transmitted and total incident intensity,  $t$  is the sample thickness. Moreover, the transmittance ( $T$ ) is defined as the ratio  $I/I_0$ . By using the definition of  $T$  equation can be re-elaborated in terms of the transmittance. The absorption coefficient can thus be expressed as:

$$\alpha = -\frac{\ln(T)}{t} \quad (3.6)$$

The integrated absorption ( $I$ ), over the different wavenumbers, can be derived from the absorption coefficient:

$$I = \int \left( \frac{\alpha}{w} \right) dw \quad (3.7)$$

where  $w$  is the wavenumber [ $\text{cm}^{-1}$ ]. By using this definition of  $I$ , the integrated absorption of WM ( $I_{WM}$ ), LSM ( $I_{LSM}$ ) and HSM ( $I_{HSM}$ ) can be calculated, by fitting the  $\alpha/w$  graph with a Gaussian function and calculating the area under the peak. From the obtained integrated absorption,  $R^*$  and  $C_H$  can be derived. The ( $R^*$ ) is calculated as follows [107]:

$$R^* = \frac{I_{HSM}}{I_{LSM} + I_{HSM}} = \frac{I_{2090}}{I_{2000} + I_{2090}} \quad (3.8)$$

where  $I_{2090}$  and  $I_{2000}$  are integrated absorption of Gaussian peaks at  $2090 \text{ cm}^{-1}$  and  $2000 \text{ cm}^{-1}$ . A low  $R^*$  is related to a less defective structure (for more details read chapter 2). Instead, the  $C_H$  is calculated as follows:

$$C_{H\text{-tot}} = \frac{N_{H\text{-tot}}}{N_{Si}} \times 100\% \quad (3.9)$$

where  $N_{Si}$  is the density of Si atoms ( $5 \times 10^{22} \text{ cm}^{-3}$  [107]) and  $N_{H\text{-tot}}$  instead is the density of hydrogen atoms and is computed from the FTIR analysis.  $N_{H\text{-tot}}$  is obtained as follows:

$$N_{H\text{-tot}} = N_{H\text{-WM}} + N_{H\text{-LSM}} + N_{H\text{-HSM}} = I_{WM} \cdot A_{H\text{-WM}} + I_{LSM} \cdot A_{H\text{-LSM}} + I_{HSM} \cdot A_{H\text{-HSM}} \quad (3.10)$$

where  $A_{H\text{-WM}} = (2.1 \pm 0.2) \times 10^{19} \text{ cm}^{-2}$ ,  $A_{H\text{-LSM}} = (9.0 \pm 1) \times 10^{19} \text{ cm}^{-2}$  and  $A_{H\text{-HSM}} = (2.2 \pm 0.2) \times 10^{20} \text{ cm}^{-2}$  [107].

As stated before in section 2.1.4, ultra-thin (i) a-Si:H layers with a thickness of the order of 4-20 nm should be employed. The low a-Si:H thickness could lead to experimental difficulties, as many characterization techniques rely on a certain amount of material to yield a detectable signal. This is especially true for FTIR measurements. Thus, thicker (i)a-Si:H layers should be deposited if FTIR characterization is aimed. In this research 30 nm thick intrinsic layers are deposited on flat <100> n-type c-Si Czochralski wafers with a thickness of  $525 \pm 20 \mu\text{m}$  and resistivity of  $15 \pm 5 \Omega\text{cm}$  for FTIR characterization.

### 3.2.4. J-V measurement

In this research, a J-V measurement of the fabricated solar cells is performed with a AAA class Wacom WXS-90S-L2 solar simulator. The test is done under standard test conditions (STC), defined as irradiance of  $1000 \text{ W/m}^2$ , AM 1.5 spectrum, and solar cell temperature of  $25^\circ\text{C}$ . The AM 1.5 spectrum is simulated by a halogen lamp and a Xenon lamp. Before measuring the devices, two reference solar cells are used for calibration.

The current-voltage characteristic (J-V curve) (Fig. 3.10) is extracted from the measurement. Besides, the most important parameters for solar-cell characterization are obtained from the J-V curve such as  $V_{OC}$ ,  $J_{SC}$ , FF, and  $\eta$  as schematically shown in Fig. 3.10. Moreover, the slope on the  $J_{SC}$  side represents the shunt resistance ( $R_{SH}$ ) of the device, while the slope at the  $V_{OC}$  side indicates the series resistance ( $R_S$ ) and therefore the curve can be used to get hints on the resistances. Both resistances can influence the FF. In this project, the  $R_{SH}$  is generally high enough to make almost no shunt happens inside the cell, while most of the time limited FFs are due to high  $R_S$  of the devices.

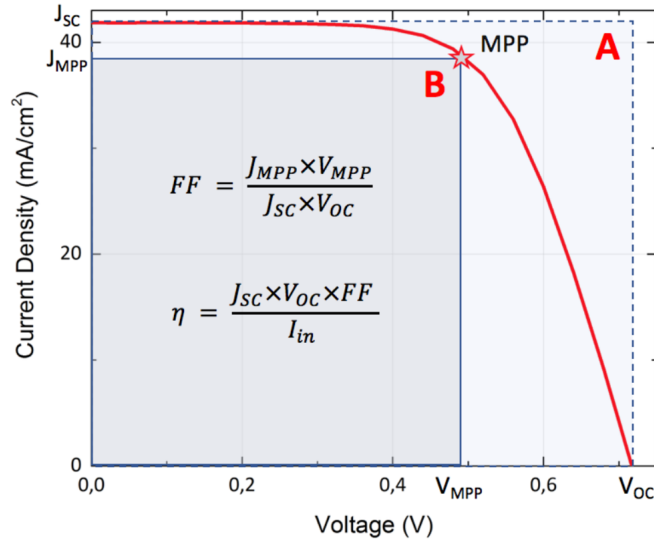


Figure 3.10: An example of measured J-V curve with the definition of fill factor and efficiency [102]

### 3.2.5. SunsVoc measurement

In this thesis, the SunsVoc-150 (Sinton) illumination-voltage tester is used for SunsVoc measurement of the SHJ solar cells after metallization.

The SunsVoc uses the  $J_{SC}$  measured from Wacom as an input for the measurement. A flash lamp with a slow decay is used to provide a pseudo I-V curve since only the voltage is measured. The obtained I-V curve is not influenced by the series resistance. The measured SunsVoc gives a hint of the upper limit of  $V_{oc}$  that can be measured from Wacom. From the measurement also the pseudo fill factor (pFF) can be obtained, which is normally compared with the FF obtained from the J-V measurement to get a clue about the FF losses induced by  $R_S$ . Indeed, the  $R_S$  losses can be calculated as follows [108]:

$$R_{S, \text{SunsVoc}} = (pFF - FF) \frac{V_{oc} J_{sc}}{J_{mpp}^2} \quad (3.11)$$

### 3.2.6. EQE

In this thesis, external quantum efficiency (EQE) measurements are performed on the fabricated solar cells. The EQE is defined as the fraction of electron-hole pairs photogenerated in the absorber layer (and successfully collected at the contacts) over the total photons incident on the solar cell. Specifically, it is defined as follow:

$$EQE(\lambda) = \frac{I_{ph}(\lambda)}{q\Psi_{ph,\lambda}} \quad (3.12)$$

where  $I_{ph}(\lambda)$  is the photogenerated current and  $\Psi_{ph,\lambda}$  is the spectral photon flow incident on the solar cell. Given that EQE is expressed as the fraction of photons leading to effective generation and collection of charge carriers, its value goes from 0 to 1, and it gives an indication of optical and electrical losses within the solar cell.

In this thesis, a home-built EQE measurement system (also defined as spectral response setup) is used. It consists of a light source (a halogen (Ha) gas discharge lamp), a calibrated photodiode (or solar cell), and a current meter. The light source can produce a very broad spectrum of wavelengths, which then is filtered by monochromators to obtain very narrow wavelength bands of photon energies (monochromatic light rays). This is important since EQE is wavelength dependent and thus the cell must be illuminated and measured with monochromatic light. Furthermore, it is important to mention that the light source must be as stable as possible during the whole measurement to assume that the photon  $\Psi_x$  in the reference photodiode and the solar cell under investigation is the same.

Since  $\Psi_{ph,\lambda}$  is not directly measurable, a calibrated photodiode with known EQE is utilized for determining the  $\Psi_{ph,\lambda}$  based on the following equation:

$$\Psi_{ph,\lambda} = \frac{I_{ph}^{ref}(\lambda)}{qEQE^{ref}(\lambda)} \quad (3.13)$$

where  $EQE^{ref}(\lambda)$  is known from the reference diode,  $I_{ph}^{ref}(\lambda)$  is easily measurable. From this equation  $\Psi_{ph,\lambda}$  can be determined in order to have an input for the EQE measurement of the actual sample. After calibration, the EQE measurement is performed on the sample and  $EQE(\lambda)$  of the sample is obtained. From this measurement, the  $J_{SC-EQE}$  can be determined in the following way:

$$J_{SC} = -q \int_{\lambda_1}^{\lambda_2} EQE(\lambda) \phi_{ph,\lambda}^{AM1.5} d\lambda \quad (3.14)$$

where  $\phi_{ph,\lambda}^{AM1.5}$  is the spectral flux and can be calculated with:

$$\phi_{ph,\lambda}^{AM1.5} = \frac{P_{ph,\lambda}^{AM1.5}}{hc} \quad (3.15)$$

where  $h$  is the Planck constant,  $c$  is the speed of light in vacuum, and  $P_{ph,\lambda}^{AM1.5}$  is the power density.

In this research, the EQE measurement done for the fabricated SHJ solar cells is performed in the wavelength between 300 nm to 1200 nm. This is because the spectral power density of wavelength below 300 nm of AM 1.5 is almost negligible, and 1200 nm is the limited wavelength of light absorption due to the bandgap of the c-Si absorber. Since the EQE measurement also includes the reflectance losses, the total reflectance of the cell ( $R$ ) is also measured (by UV-Vis-NIR spectroscopy (see section 3.2.7)) to obtain the Internal Quantum Efficiency (IQE). The IQE is defined as the probability that a photogenerated carrier is absorbed. Or, in other words, IQE is the ratio of charge carriers that are successfully collected at the contacts to photons that are absorbed by the cell's absorber:

$$IQE(\lambda) = \frac{EQE(\lambda)}{1 - R(\lambda)} \quad (3.16)$$

where  $R(\lambda)$  is the reflectance at a wavelength  $\lambda$ , and thus so  $1 - R(\lambda)$  corresponds to the effective absorbance if the rear side of the solar cell is opaque (and thus no transmissions happen).

### 3.2.7. UV-Vis-NIR spectroscopy

Ultraviolet-Visible-Near-Infrared spectroscopy (UV-Vis-NIR) is a characterization technique used to analyze the optical properties of materials in the ultraviolet, visible, and near-infra-red region of the spectrum. In general absorptions, transmissions, and reflections of samples can be investigated. In this thesis, a LAMBDA 1050+ UV-Vis-NIR spectrophotometer (PerkinElmer) is used to determine the reflectance ( $R$ ) of the fabricated solar cells, which is then used to get an idea of the IQE (see section 3.2.6) and thus of the photogenerated photons which are successfully collected from the metal contacts and the photons that instead are lost through reflections or other optical and electrical losses. A schematic illustration of the UV-Vis-NIR spectrometer is shown in Fig. 3.11.

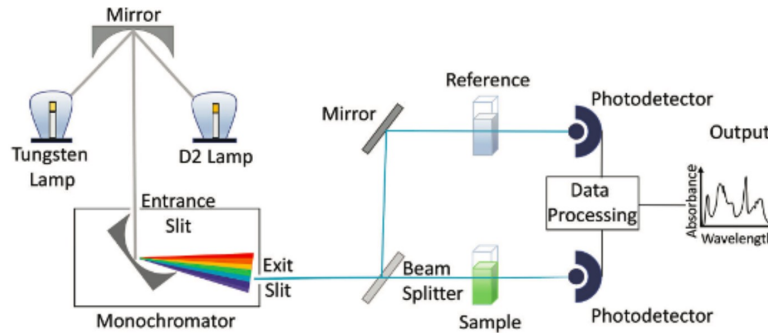


Figure 3.11: Schematic illustration of the different components of an UV-Vis-NIR spectrophotometer [109]

During a UV-Vis-NIR measurement, the sample is illuminated with light of different wavelengths. Usually two different light sources are employed: a tungsten lamp (emitting wavelengths in the visible-NIR range) and a deuterium (D2) lamp (generating UV light). Then, the light is filtered by a monochromator which selects the wavelengths and illuminates the sample with monochromatic light. The output light rays are split so that they strike both a reference sample and the sample to be measured. The sample under examination is placed in different positions in the spectrometer according to the optical property to be measured. The absorbance spectrum is obtained by locating the sample inside an integrating sphere, namely a cavity whose inner walls are made of a highly reflective material, e.g. barium sulfate ( $\text{BaSO}_4$ ). This cavity allows the contribution of the total scattering and reflection components to be taken into account, thus providing a more accurate measurement. The transmittance and reflectance spectra are measured by placing the sample on the front side and the rear side of the integrating sphere, respectively (Fig. 3.12). The signal is then collected by photodetectors and is analyzed to give the desired spectra (absorbance, reflectance, transmittance) as output [109]. In this report, reflectance ( $R$ ) is measured for each given wavelength of light and by scanning through all the wavelengths from 300 nm to 1200 nm.

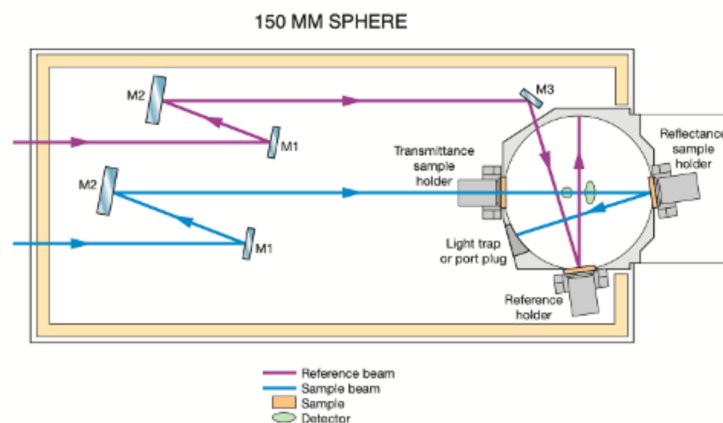


Figure 3.12: Schematic representation of the optical design of a UV-Vis-NIR spectrometer with a 150 mm integrating sphere with a detail on the positions where the test sample has to be placed to measure either the transmittance or reflectance [110]



# 4

## Optimization of hydrogenated intrinsic amorphous silicon

As introduced in chapter 2, the implementation of an intrinsic hydrogenated amorphous layer ((i)-a-Si:H) between the c-Si substrate and the doped layers is crucial to achieving SHJ with a high  $V_{OC}$ . In particular, the typical  $V_{OC}$  of SHJ can exceed 750 mV [37, 40] and is significantly higher than the  $V_{OC}$  of homojunction cells that reaches a maximum of 700 mV [14]. The intrinsic layer provides excellent chemical passivation of the c-Si surface, which allows obtaining good-performance SHJ solar cells [37, 38, 41, 42]. Due to the key importance of the (i)a-Si:H layer, it is mandatory to optimize its passivation qualities to produce high-efficiency solar cells.

In this chapter, the optimizations of the (i)a-Si:H passivation layer on flat <100> c-Si surfaces are discussed. The optimizations are aimed at depositing a layer with optimized passivation qualities, uniformity, and reproducibility. The approach was mainly to find the optimal deposition parameters and conditions that led to the best layer qualities. Moreover, an extensive characterization has been conducted to find the correlation between the optimal deposition conditions and the layer properties.

The experimental methodology is firstly discussed. After that, the optimization approaches and results are presented.

### 4.1. Experimental methodology for the optimization of (i)a-Si:H

In this section, the experimental methodology used for the intrinsic layer optimization is explained in detail. The pre-deposition treatments, deposition, and the main analysis and characterizations of the deposited layer are discussed.

#### 4.1.1. Pre-deposition treatments

The silicon wafers used for the passivation optimization are Topsil n-type double-side polished FZ <100> c-Si with a range of resistivity ( $3\pm 2 \Omega\text{cm}$ ) and thickness ( $280\pm 20 \mu\text{m}$ ). Contamination-free and low surface defect density c-Si substrate are required for an optimal passivation performance. Thus, a wet-chemical wafer cleaning procedure is performed as a pre-deposition treatment. The detailed process is explained in chapter 3. Since double-side-flat c-Si wafers are used for the (i)a-Si:H optimization, the cleaning cycle is repeated for just one time, as stated in chapter 3.

#### 4.1.2. Deposition

The deposition process happens in the RF-PECVD just after the pre-deposition treatments are concluded and the wafer is stored in the vacuum chamber or the RF-PECVD machine. The working principle of RF-PECVD is discussed in detail in chapter 3. The RF-PECVD used in this research is the so-called AMIGO PECVD (Elettorava, S.p.A.) in Else Kooi Lab (EKL) at Delft University of Technology. The deposition process is automated. The input parameters are given in the form of an excel file, where all the single process steps are inputted. For the optimization of the intrinsic layer, symmetric (i)a-Si:H layer deposition is done on double-side flat <100> c-Si wafers, as schematically illustrated in Fig. 4.1.

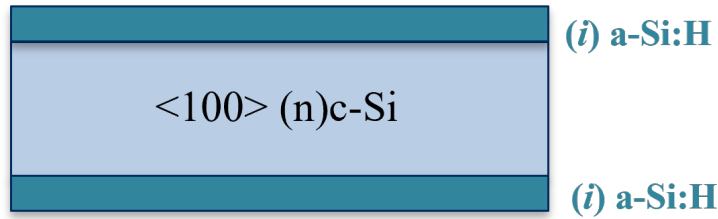


Figure 4.1: Schematic representation of symmetric passivation of flat  $\langle 100 \rangle$  c-Si surfaces

#### 4.1.3. Analysis and characterizations

After the intrinsic layer has been deposited, the layer is analyzed with different characterization techniques. These characterization techniques are performed on each sample just after the layer deposition. A detailed explanation of the working principle of each technique mentioned below is explained in chapter 3.

- Photoconductance lifetime tester: for the measurement of the passivation qualities of the (i)a-Si:H film, mainly in terms of  $\tau_{\text{eff}}$ ,  $i\text{-}V_{\text{OC}}$ .
- Spectroscopic ellipsometry: for thickness measurements of the (i)a-Si:H layer. Thicknesses measurements are performed at different points of the samples to check the uniformity of deposition. In particular, measurements are taken from four different points on both sides of the wafers, with a total of eight measurements per sample. Thicknesses measurements are also required to check the comparability of the passivation qualities of different samples. Indeed, as explained in detail in chapter 2, the passivation quality is dependent on the (i)a-Si:H layer thickness [75].
- Fourier transform infrared spectroscopy (FTIR): for evaluating the microstructure quantitative composition of the deposited films. This analysis is used to correlate the microstructure properties of the film to its passivation qualities. According to the results reported by Meddeb et al. [47] if monohydrides (MHs or Si-H:  $2000\text{ cm}^{-1}$  [48]) (corresponding to low stretching mode, as described in section 3.2.3) are the majority species in the amorphous layer a more compact and less defective structure is formed. In contrast, if the dihydrides (DHs or Si-H<sub>2</sub>:  $2090\text{ cm}^{-1}$  [48]) (corresponding to high stretching mode, as described in section 3.2.3) are the main components a highly defective and microvoids containing layer is formed. This can be explained through the effect of different radicals on the growth model (section 2.1.2). The percentage of monohydrides or multi-hydrogen hydride can be identified with the microstructure factor ( $R^*$ ), which corresponds to the ratio of the FTIR intensities at  $2090\text{ cm}^{-1}$  modes over the sum of the intensity of  $2000\text{ cm}^{-1}$  and  $2090\text{ cm}^{-1}$  modes. Lower  $R^*$  is correlated with a lower fraction of microvoids, and thus a best passivation quality. The hydrogen content in the layer can be calculated from the FTIR analysis as well, from the sum of the hydrogen content associated with the wagging mode (at  $640\text{ cm}^{-1}$  [48]) and the stretching modes (at  $2000$  and  $2090\text{ cm}^{-1}$  [48]). A detailed description of the fitting procedure of FTIR data to calculate microstructure factor ( $R^*$ ) and the hydrogen content ( $C_{\text{H}}$ ) is reported in chapter 3. Note that for FTIR characterizations, intrinsic 30 nm thick layers were deposited on flat  $\langle 100 \rangle$  n-type c-Si Czochralski wafers with a thickness of  $525 \pm 20\ \mu\text{m}$  and resistivity of  $15 \pm 5\ \Omega\text{cm}$ .

## 4.2. Optimization strategy

In this research, different optimization strategies have been investigated. Firstly, the PECVD deposition conditions of (i)a-Si:H monolayer for symmetric passivation of flat <100> c-Si surfaces were optimized. After that, to improve further the passivation quality of the monolayer (i)a-Si:H layer, other passivation approaches were analyzed. Specifically, hydrogen plasma treatment (HPT) [95, 111], bilayer deposition [112], and the combination of bilayer deposition with different HPT treatments [47, 95] have been tested. In this section, all these are analyzed and discussed in detail.

### 4.2.1. Monolayer passivation optimizations

At first, the symmetric deposition of an (i)a-Si:H monolayer on top of <100> n-type c-Si surfaces was optimized. The single (i)a-Si:H layers are deposited through RF-PECVD under a wide range of PECVD deposition parameters. The microstructure and thus properties of (i)a-Si:H are strongly influenced by the deposition parameters and conditions [61, 71, 72]. The deposition parameters should be tuned in order to i) deposit an (i)a-Si:H layer which provides good c-Si surface passivation; ii) prevent the initiation of the localized epitaxial growth at the a-Si:H/c-Si interface; iii) reduce the defects and microvoids in (i)a-Si:H bulk films and guarantee sufficient hydrogen content for dangling bonds passivations. Indeed in general device-grade a-Si:H layer aims at both an excellent surface passivation of a-Si:H/c-Si interface and a good quality bulk (i)a-Si:H (i.e. the material with the lowest defect and microvoid density and sufficient hydrogen content). When both aspects are optimized, a high-quality cell can be obtained [72].

Four main parameters were varied: substrate temperature, the pressure of the reaction chamber, RF power, and hydrogen dilution ratio (DR) The hydrogen dilution ratio (DR) is defined as the ratio of  $H_2$  and  $SiH_4$  flow rates during PECVD deposition, as reported in equation 4.2. It is an indication of the amount of  $H_2$  that is used for depositing the (i)a-Si:H film.

$$DR = \frac{\text{Flow rate } (H_2)}{\text{Flow rate } (SiH_4)} \quad (4.1)$$

The main parameters with the corresponding variation are listed in Tab. 4.1. The effects of each parameter were studied while keeping the other parameters constants. Therefore, four main deposition series were obtained.

For each deposition series, the (i)a-Si:H film properties are compared and some typical parameters are plotted, namely the  $\tau_{\text{eff}}$ ,  $i-V_{\text{OC}}$   $R^*$  and  $C_H$ . These quantities are obtained from the characterization techniques mentioned in the experimental methodology section (section 4.1). Additionally, the thickness of each layer is plotted. The thickness value reported in the graphs is the average value of the eight measured points and the error bar represents the standard deviation. As stated before, the thickness of each sample is aimed to be kept the same, for a reliable comparison of the passivation qualities, which are thickness-dependent [75]. All samples are aimed to be symmetrically passivated by a 10 nm (i)a-Si:H layer.

Table 4.1: The variation ranges of the main parameters of RF-PECVD

Parameter	Variation	Unit
Substrate Temperature	140-200	°C
Pressure	0.3 - 1.2	mbar
Power density	18 - 26.4	mW/cm <sup>2</sup>
Hydrogen dilution ratio	0 - 3	-

It is important to have a clear overview on the effect of each parameter on the properties of the film. For this reason, before the analysis of the experimental results of this thesis work, a brief literature review on the effect of each deposition parameter on the deposited (i)a-Si:H is firstly reported in the following sections. Note that, as understood by the literature, the optimal conditions are strongly process and equipment-dependent. Thus it is difficult to quantify the range of value for each parameter a priori from the literature since different studies report quite different values of the process conditions. Therefore the ranges are not reported in the literature review sections. In this research, the deposition conditions are optimized for the Amigo RF-PECVD deposition machine at PVMD group at TU Delft. The variation range of each parameter reported in the experimental sections was based on some previous researches [102] and then experimentally defined.

### Substrate temperature - literature review

The temperature of the substrate ( $T_s$ ) is one of the main deposition parameters which affect the properties of a-Si:H. According to different studies, it has been found that the optimal  $T_s$  for optimal passivation properties correspond to the transition temperature from amorphous to crystalline state (which correspond to the occurrence of epitaxial growth) [38].

In particular, too low surface temperatures are not desired as they lead to poor passivation qualities [38, 113, 114]. This is because at low substrate temperatures, a high fraction of Si-H<sub>2</sub> is present in the a-si:H network. Thus the film microstructure has a large amount of microvoids (as explained in section 2.1.2) [38, 113, 114], which lead to poor passivation qualities. Moreover, the thermal diffusion of the high mobility SiH<sub>3</sub> radicals is lowered and the film quality degrades since the radical have a worst diffusion on the film and thus uniformity is compromised and the formation of microvoids is favored (see chapter2 for more details on the growth mechanism of a-Si:H).

A too high surface temperature can be also deleterious for the quality of the passivating layer, as demonstrated by different studies [45, 113, 115]. Wang et al. have demonstrated that when the temperature is increased above a certain point, the hydrogen content in the a-Si:H is too low to saturate the dangling bonds and hydrogen effusion (out-diffusion) occurs. This results in an increased defect density in the (i)a-Si:H bulk [45] and reduces the amount of H reaching the c-Si/(i)a-Si:H interface, thus less dangling bonds are passivated. In addition, a high substrate temperature can cause the rupture of Si-H bonds and consequently initiate detrimental epitaxial growth [113]. In general, epitaxial growth has been found to happen rather easily when the substrate temperature is high and RF power is low [115]. Thus, if the temperature is increased, a high power, i.e enhanced ion bombardment is necessary to form a good quality film [115].

In conclusion, an optimal value of  $T_s$  should be found, neither too low nor too high. The optimal  $T_s$  value should be high enough to promote the diffusion of the radicals along the substrate, to guarantee the deposition of a uniform layer with a low SiH<sub>2</sub> fraction and defect density.  $T_s$  should also not be too high to guarantee a high enough hydrogen content in the network and to avoid epitaxial growth [38, 113].

### Substrate temperature - experimental results

The effect of  $T_s$  on the layer passivation qualities has been investigated. The detailed deposition parameters for the substrate temperature deposition series are reported in Tab. 4.2.

Table 4.2: Process parameters for deposition during investigation of substrate temperature effect

Layer	$T_s$ [°C]	Pressure [mbar]	Power density [mW/cm <sup>2</sup> ]	Dilution ratio [-]	Flow rate [sccm]	Frequency [MHz]
(i)a-Si:H	140-200	0.7	20.8	0	40	13.56

In Fig. 4.2 the  $\tau_{\text{eff}}$ ,  $i\text{-}V_{\text{OC}}$  and layer thickness are plotted as a function of the substrate temperature. As can be seen from the figure, the thickness of the samples is comparable and is around 10 nm. Moreover, the growth of (i)a-Si:H films is quite homogeneous for all the samples, as indicated by the small error bar in the thickness measurements. However, it can be noticed that as the substrate temperature increases (above 180°C), the non-homogeneity becomes larger.

In terms of passivation qualities, it can be noticed that too low and too high temperatures are not optimal. The best passivation qualities are obtained for a  $T_s=160^\circ\text{C}$ .

The different passivation qualities as a function of the temperature can be explained with the  $R^*$  and  $C_H$  values obtained from the FTIR characterization analysis, as reported in Fig. 4.3. The FTIR spectra are also reported in Fig. 4.4. It can be observed that the layers deposited at  $T_s=160^\circ\text{C}$  are the less defective, as indicated by the lowest microstructure factor  $R^*$  of about 0.13. Also the sample deposited at  $T_s=200^\circ\text{C}$  has a low microstructure factor  $R^*$  but this is probably due to the very low amount of H in the film, which is not sufficient to passivate dangling bonds and leads to the degradation of the film's passivation qualities. Indeed it can be observed that as the temperature increases the hydrogen content decreases both for WM and SM, due to the effusion (out diffusion) of hydrogen from the layer. This suggests that the layer with the best passivation qualities has a hydrogen content that is sufficient to guarantee the passivation of dangling bonds while a keeping a low defectivity (low  $R^*$ ). The above-mentioned qualities, i.e and lower defectivity (lower  $R^*$ ) and enough H content in the network, explain why the films deposited at  $T_s=160^\circ\text{C}$  have better passivation qualities than the films deposited at other surface temperatures. At low surfaces temperatures the hydrogen

content is quite high but also the  $R^*$  which indicates higher defectivity. This is probably attributed to the fact that at low surface temperatures, the diffusions of the radicals deposited on the surface is low and thus microvoids formations is enhanced [38, 57, 113, 114]. At high surface temperature instead hydrogen effusion (out-diffusion) occurs and the hydrogen content in the a-Si:H is too low to saturate the dangling bonds, which can also result in an increased defect density in the (i)a-Si:H bulk [45].

In conclusion,  $T_s=160^\circ\text{C}$  is the optimized substrate temperature and is chosen for later optimizations.

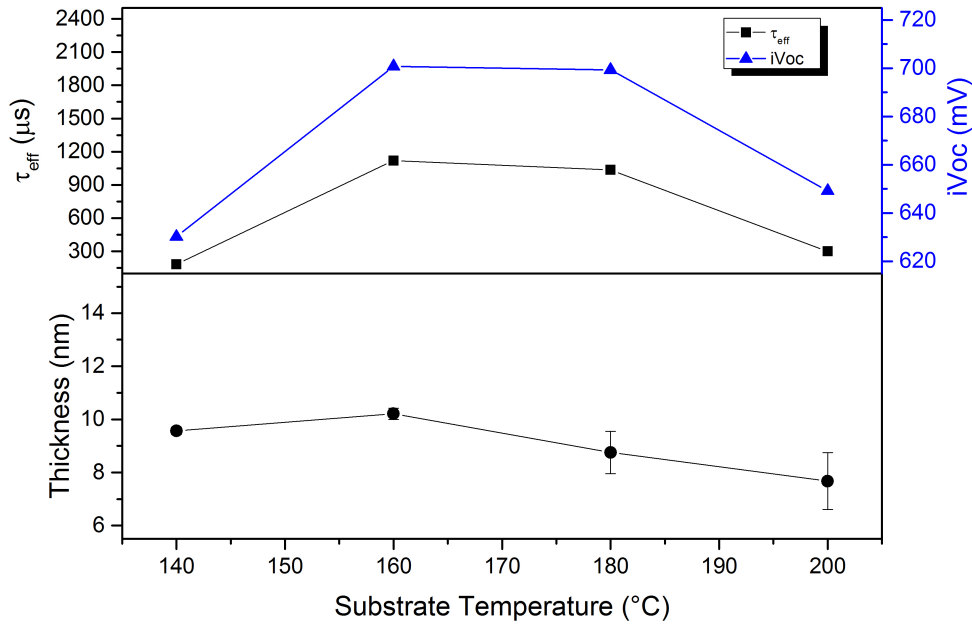


Figure 4.2:  $\tau_{\text{eff}}$ ,  $i\text{-}V_{\text{OC}}$  and layer thickness of symmetrical passivation samples as a function of substrate temperature.

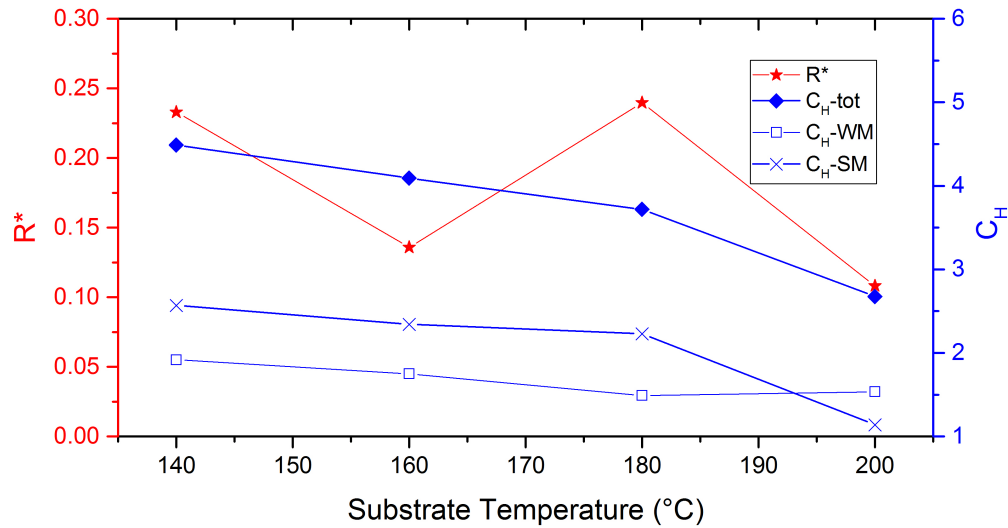


Figure 4.3: Microstructure factor ( $R^*$ ) and hydrogen content [ $C_{\text{H}}(\text{total}) = C_{\text{H}}(\text{WM}) + C_{\text{H}}(\text{SM})$ ] as a function of substrate temperature, obtained by FTIR analysis elaboration.

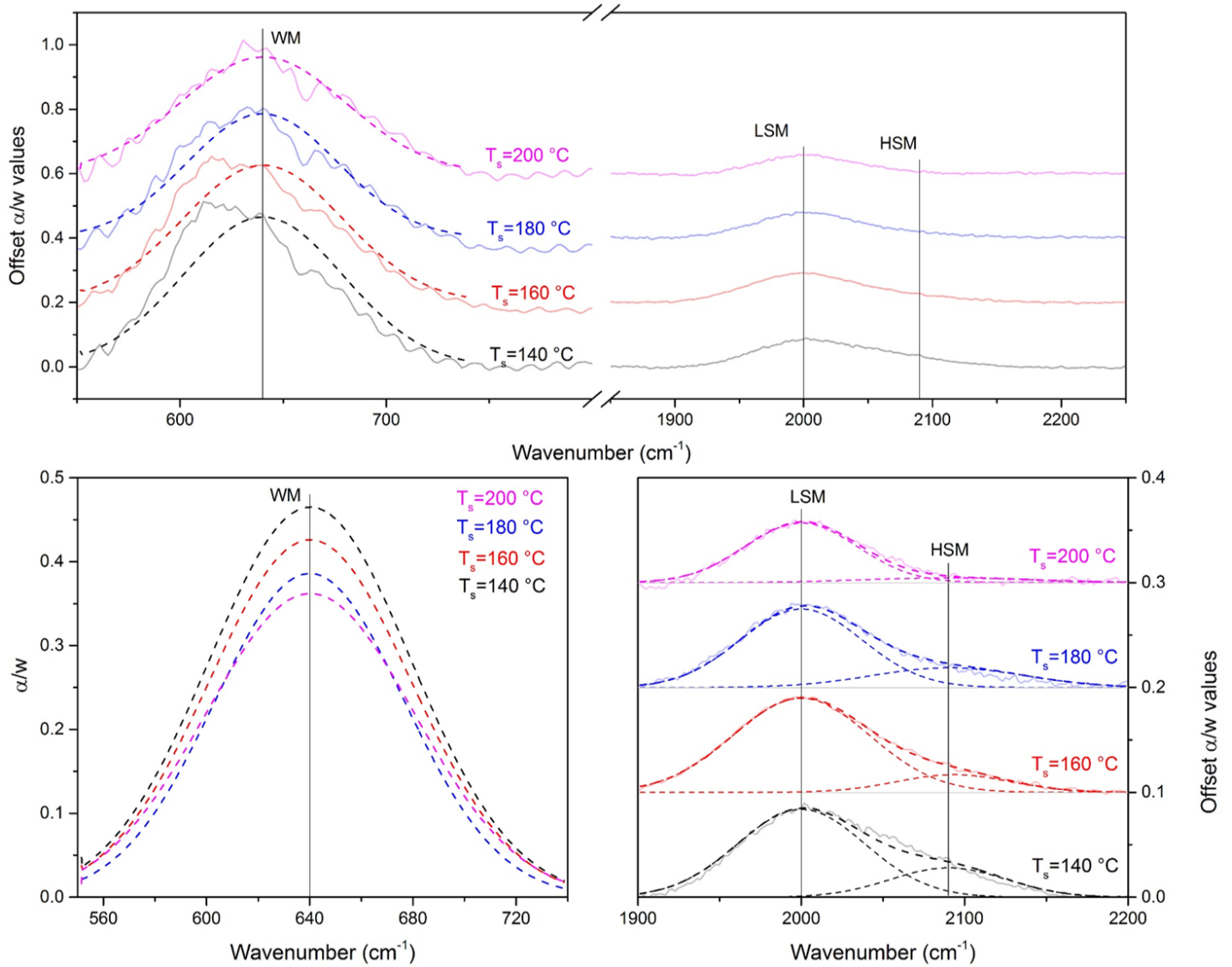


Figure 4.4: FTIR spectra and fitting of WM, LSM, HSM for samples deposited at different substrate temperatures.

### Pressure - literature review

Pressure is another important deposition parameter. An appropriate choice of pressure should aim at i) guaranteeing acceptable uniformity of the deposited layers ii) enabling the deposition of a film with good passivation quality.

Generally, too low pressures are not desired. Indeed they can induce film non-uniformities [57]. Moreover, when the pressure is too low the ion bombardment effect is relevant since there is less probability of radical interaction with other gas particles [116]. Indeed in too low pressure environments radicals bombard the substrate and stick to crystal sites, providing substrate damages, inducing microvoids and defects formations, and also favoring crystalline growth [117].

If the pressure is high enough, above a certain value, the passivation qualities are improved. A high pressure is beneficial for different reasons. Firstly, it could lead to a higher hydrogen incorporation into the a-Si:H network which allows better passivation of dangling bonds and defects sites [38]. Secondly, it reduces the average ion bombardment on the substrate. Indeed, the probability of ion collisions in the plasma is increased and the mean free path of radicals before collision is reduced [117]. Moreover, high pressures favor the role of high-mobility radicals  $\text{SiH}_3$  in the films growth of relative species (such as  $\text{SiH}_2$  and H) due higher number of ionization events, that allow the formation of a higher quality film [117]. Finally, at high pressure the epitaxial growth is prevented [62, 115]. This can be due to higher deposition rates, which have the effect of reducing the mean free path of the adatom on the film growth surface, suppressing the probability of epitaxial crystalline film growth, as found by Demaurex [62] and Fujiwara and Kondo [71].

However, the same reduced diffusion or radicals due to an increased deposition rate, while decreasing the probability of epitaxial growth can increase the amount of clustered microvoids formation [57] (see chapter 3 for more details on the growth mechanism). However, too high pressures can lead to a too high hydrogen content into the amorphous network, and consequently this could also favor dihydrides or clustered monohydrides formation. Thus a too high pressure could also be deleterious to the film properties leading to the formation of a void-rich material.

In conclusion, an optimal value of pressure has to be found, as a trade-off of the aforementioned factors. It is also important to keep in mind that usually pressure is adjusted according to RF power conditions, to obtain an optimal power/pressure ratio.

### Pressure - experimental results

The effect of the pressure of the deposition chamber on the layer passivation qualities has been investigated. The detailed deposition parameters for the pressure deposition series are reported in Tab. 4.3. Note that the temperature has been chosen on the basis of the preceding optimization.

Table 4.3: Process parameters for deposition during the investigation of the chamber pressure effect

Layer	$T_s$ [°C]	Pressure [mbar]	Power density [mW/cm <sup>2</sup> ]	Dilution ratio [-]	Flow rate [sccm]	Frequency [MHz]
(i)a-Si:H	160	0.3-1.2	20.8	0	40	13.56

In Fig.4.5 the  $\tau_{\text{eff}}$ ,  $i-V_{\text{OC}}$  and the layer thickness are plotted as a function of the pressure. As can be seen from the figure, the thickness of the samples is comparable and is around 10 nm. However, for too low pressures of 0.3 and 0.5 mbar the (i)a-Si:H layer is significantly non-homogeneous. This is in line with what was found in previous studies [57]. Therefore, these layers are not good candidates in terms of uniformity.

The optimal passivation qualities are obtained for  $p=0.7$  mbar while for higher pressures the passivation quality drops.

These trends can be explained through the  $R^*$  and  $C_H$  values obtained from the FTIR characterizations, reported in Fig. 4.6. The FTIR spectra are also reported in Fig. 4.7. The sample deposited with pressure  $p=0.7$  mbar is less defective, as indicated by the lowest  $R^*$ . For pressures higher than 0.7 mbar, and thus the film defectivity ( $R^*$ ) increases. This may be due to a too high deposition rate that reduces radicals diffusion on the surface and, although this prevents epitaxial growth, it favors the formation of microvoids [57]. In terms of hydrogen content, the sample at  $p=0.7$  mbar has probably enough hydrogen in the structure to guarantee the passivation of enough dangling bonds, which explains its good passivation qualities. Note that for the samples deposited at  $p=0.3$  mbar the hydrogen content estimated from the FTIR spectra seems to be very high. However, this is mainly due to the difficulty of fitting FTIR data, since the film thickness was highly

inhomogeneous and thickness is one of the main parameters affecting FTIR fitting analysis (see chapter 3). Therefore we consider the FTIR results for that sample not accurate. At this low pressure a high  $R^*$  would indeed be expected, due to increased radicals bombardments, that stick to crystal sites providing substrate damages, inducing defects formations, and also favoring crystalline growth [117].

To conclude, the sample deposited at  $p=0.7$  mbar is characterized by the best microstructure and thus has the best passivation qualities. Therefore, pressure  $p=0.7$  mbar is chosen for later optimizations.

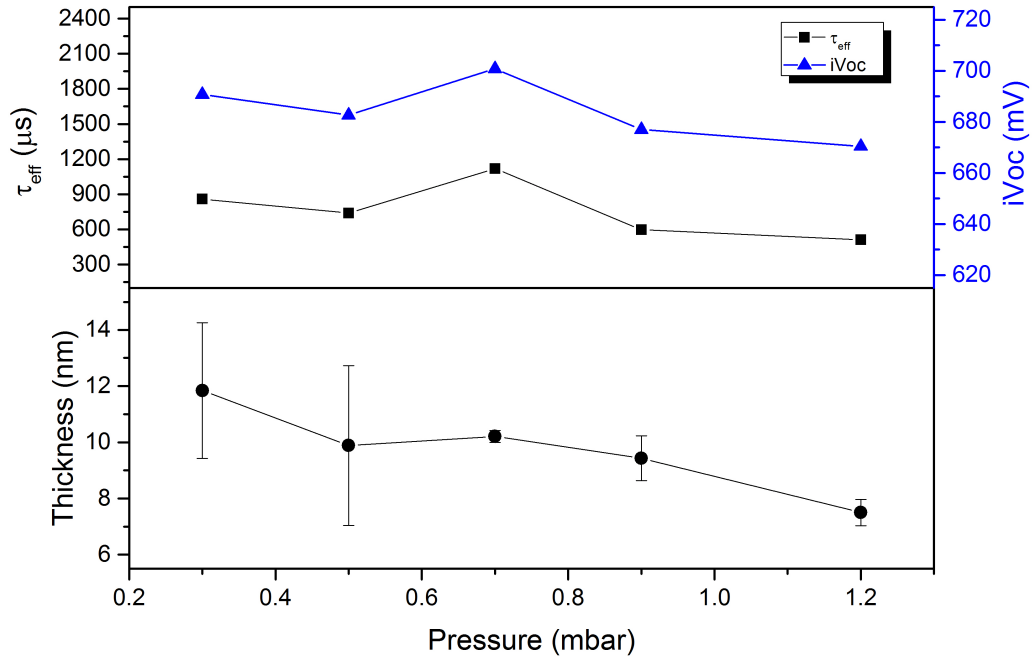


Figure 4.5:  $\tau_{\text{eff}}$ ,  $iV_{\text{OC}}$  and layer thickness of symmetric passivation samples as a function of chamber pressure.

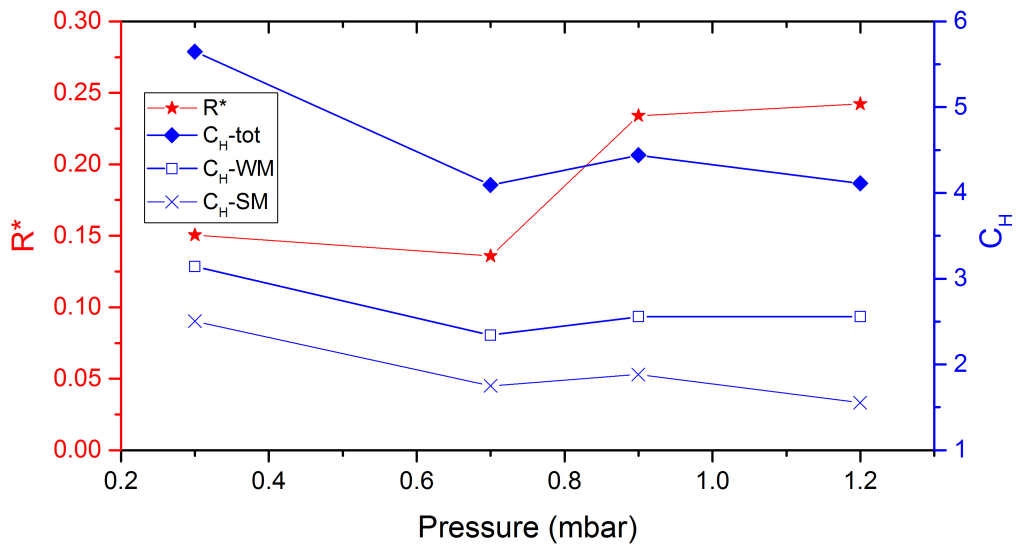


Figure 4.6: Microstructure factor ( $R^*$ ) and hydrogen content [ $C_{\text{H}}$  (total) =  $C_{\text{H}}$  (WM) +  $C_{\text{H}}$  (SM)] as a function of chamber pressure, obtained by FTIR analysis elaboration.

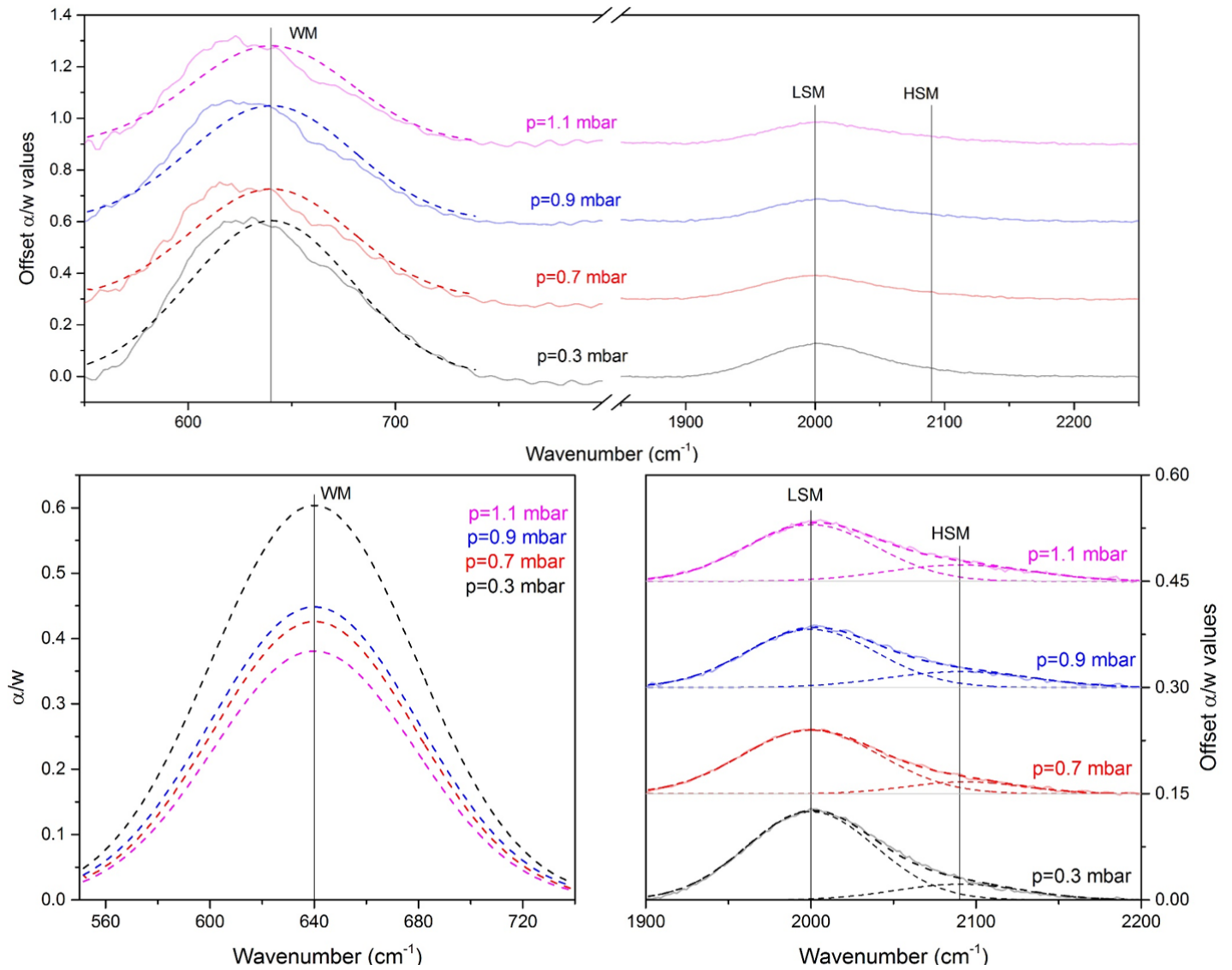


Figure 4.7: FTIR spectra and fitting of WM, LSM, HSM for samples deposited at different pressures.

### Hydrogen dilution ratio - literature review

The (i)a-Si:H layers are deposited by PECVD with SiH<sub>4</sub> precursors, diluted with H<sub>2</sub>. The hydrogen dilution ratio (DR) is defined as the ratio of H<sub>2</sub> and SiH<sub>4</sub> flow rates, as reported in equation 4.2. It is an indication of the amount of H<sub>2</sub> that is used for depositing the (i)a-Si:H film.

$$DR = \frac{\text{Flow rate (H}_2\text{)}}{\text{Flow rate (SiH}_4\text{)}} \quad (4.2)$$

Different scientific researches focused on studying the effect of hydrogen dilution ratio on the passivation quality of (i)a-Si:H. In particular, a common observation is that a low or moderate DR is beneficial for the film's passivation qualities. However, by further increasing the DR beyond a certain value the passivation quality of the film deteriorates [38, 47, 118, 119].

A too high DR has been found to degrade the film quality and initiate epitaxial growth at the a-Si/c-Si interface [72, 119]. Some studies attribute the transition from amorphous to crystalline at high DR to a hydrogen-induced etching phenomena at the growth surface. This can result in rearrangement of the network that leads to epitaxial growth. Moreover, the hydrogen etching effect may lead to surface damages and poor film qualities [47, 120].

It is interesting to note that the case of zero hydrogen dilution ratio is debatable in the literature. Some studies claimed that at zero DR there is not enough hydrogen to passivate the dangling bond inside the (i)a-Si:H and at the c-Si surface. Thus the film is highly defective and the performance of the cell is reduced [60, 72]. In line with these findings, other researchers have reported that the H<sub>2</sub>-undiluted intrinsic layer may have high microvoid density, due to excessive incorporation of Si-H<sub>2</sub> dihydride. On the contrary, other studies have proven excellent passivation with no hydrogen dilution, especially for deposition of (i)a-Si:H on a flat surface [121]. Therefore, the dilution ratio should be carefully optimized in order to guarantee enough hydrogen content and to improve the microstructure quality of the deposited films.

In summary, zero or a low hydrogen dilution ratio [121] (usually up to DR=1 [38]) should lead to optimized film properties. A too high value of DR can instead deteriorate the film qualities.

### Hydrogen dilution ratio - experimental results

In this section, the effect of DR on the passivation qualities of (i)a-Si:H is investigated. The detailed deposition parameters for the DR deposition series are reported in Tab. 4.4. Note that T<sub>s</sub> and pressure are chosen on the base of the previous optimization series.

Table 4.4: Process parameters for deposition during investigation of hydrogen dilution ratio effect

Layer	T <sub>s</sub> [°C]	Pressure [mbar]	Power density [mW/cm <sup>2</sup> ]	Dilution ratio [-]	Flow rate [sccm]	Frequency [MHz]
(i)a-Si:H	160	0.7	20.8	0-3	40	13.56

In Fig.4.8 the  $\tau_{\text{eff}}$ ,  $i\text{-}V_{\text{OC}}$  and layer thickness are plotted as a function of the DR. As can be seen from Fig.4.8, when DR>1, the layer barely grows. This is in accordance to what was previously found in the PVMD group [102, 122]. This may be due to inappropriate deposition conditions, for example in terms of power and pressure, for those dilution ratios. Therefore, the points for DR>1 are shown with an empty white symbol. Instead, for DR<1 the layers are deposited with quite comparable thickness, of about 10 nm. For these samples the layer growth is also quite uniform, as can be seen from the small error bar in the thickness measurements. However, it can be noticed that for DR=1 the non-homogeneity becomes larger. In terms of passivation qualities, they are quite comparable for all the samples even if they are the highest for DR=0 to DR=1 (Fig. 4.8).

The R\* and C<sub>H</sub> calculated from the FTIR characterization analysis are reported Fig.4.9. The FTIR spectra and the fitting of them are also reported in Fig. 4.10. It was found that the layers deposited at DR=0 and DR=1 are the less defective, as indicated by the lowest R\*. For DR=0.5 and 0.75 the R\* is slightly higher which may be due to a soft hydrogen etching effect that could lead to rearrangement in the network and promote the formation of clustered SiH<sub>2</sub> [47, 120]. The fact that the layer deposited at DR=1 has a lower R\* may be due to experimental errors and difficulty in achieving a reproducible parameter. Indeed, as stated above, the layer deposited with DR=1 is not homogeneous and not reproducible in terms of passivation qualities when different layers were processed with the same processing parameters, which can be due to difficult to control the chamber environment and plasma conditions, as found by previous researches [123]. For these

reproducibility issues and from the difficulty to obtain constant good passivation qualities, intrinsic layers with small DR deposited on top of <100>c-Si surfaces are not a good candidate for being a high-quality passivation layer. Based on the aforementioned analysis DR=0 is chosen for later optimizations and has good passivation properties.

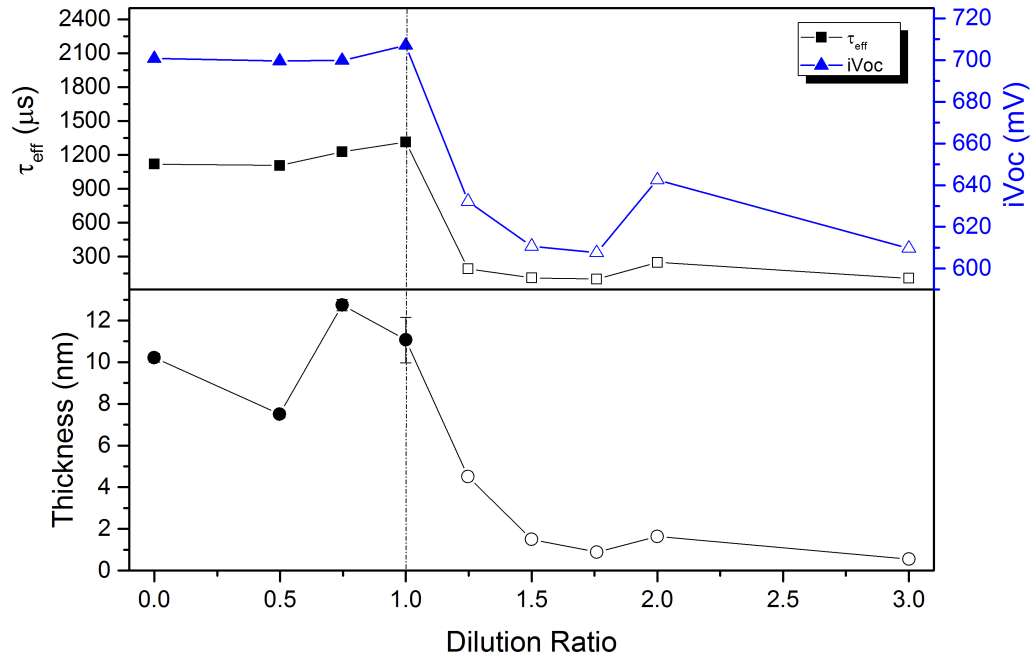


Figure 4.8: Effective lifetime, implied open-circuit voltage and layer thickness of symmetric passivation samples as a function of hydrogen dilution ratio.

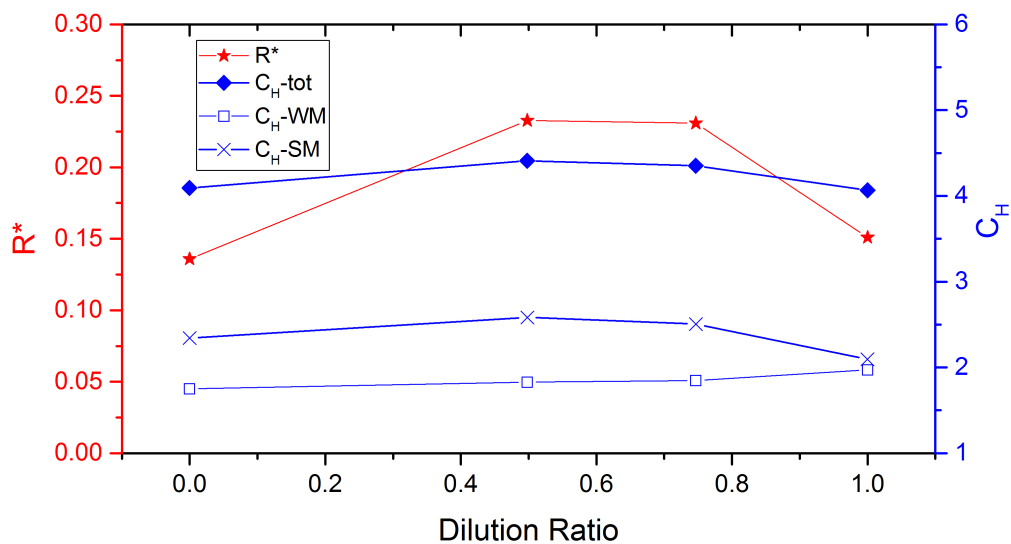


Figure 4.9: Microstructure factor ( $R^*$ ) and hydrogen content [ $C_H$  (total) =  $C_H$  (WM) +  $C_H$  (SM)] as a function of DR, obtained by FTIR analysis elaboration.

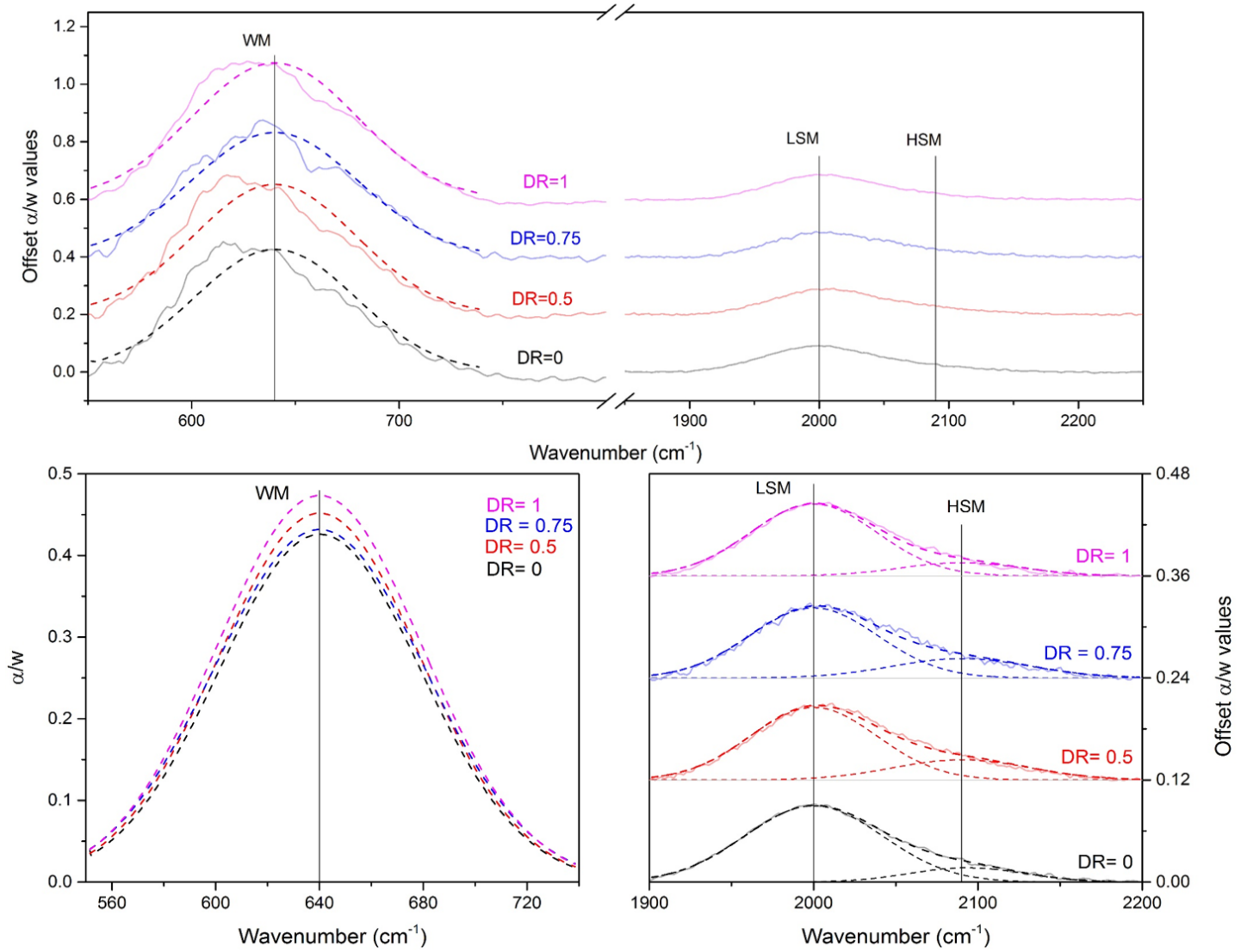


Figure 4.10: FTIR spectra and fitting of WM, LSM, HSM for samples deposited at different DR.

### RF Power - literature review

RF power also influences the passivation qualities of (i)a-Si:H film. Moreover, it influences the dissociation of the silane gas molecules and thus it affects the deposition rate of thin films. As a general observation, the deposition rate increases with the deposition power.

A too low RF power density seems to be disadvantageous. It has been found that at very low RF power epitaxial growth occurs at any surface temperature. This may be because there is a decrease in ion bombardment and thus less energy for the diffusion of radicals [115] ( $< 11 \text{ mW/cm}^2$  for  $130 \text{ }^\circ\text{C}$  and  $< 32 \text{ mW/cm}^2$  for  $180 \text{ }^\circ\text{C}$ ).

A too high RF power has also a detrimental effect on passivation quality, even if epitaxial growth is suppressed and the film results amorphous. This can be due to enhanced damage of the c-Si substrate due to a significant ion bombardment [115]. Moreover, a film deposited at high power, and thus at a high deposition rate, has a high microvoid content with poor passivation qualities [57]. This can be due to a higher fraction of  $\text{SiH}_2$  contributing to the film growth. Gallagher et al. have proved that as power and gas flow increase (generally conditions for high deposition rates), the probability for  $\text{SiH}_2$  radicals to reach the surface is enhanced [58].

In short, a trade-off between a too low and too high RF value has to be considered. RF power is optimized to avoid epitaxial growth, guarantee a low ion bombardment and a low  $\text{SiH}_2$  content [115].

### RF Power - experimental results

In this section, the effect of the deposition power density ( $P_{\text{density}}$ ) is investigated. The detailed deposition parameters for the deposition pressure series are reported in Tab. 4.5. Note that the other parameters are chosen on the basis of the previous optimization.

Table 4.5: Process parameters for deposition during investigation of RF power

Layer	$T_s$ [ $^\circ\text{C}$ ]	Pressure [mbar]	Power density [ $\text{mW/cm}^2$ ]	Dilution ratio [-]	Flow rate [sccm]	Frequency [MHz]
(i)a-Si:H	160	0.7	18.0-26.4	0	40	13.56

In Fig.4.11 the  $\tau_{\text{eff}}$ ,  $i\text{-}V_{\text{OC}}$  and layer thickness are plotted as a function of the deposition power. As can be seen from the figure, it was quite difficult to keep the average thickness of the samples around 10 nm, due to the difficult determination of deposition rates. In terms of deposition homogeneity instead the growth of (i)a-Si:H films is quite homogeneous for all the samples, as can be seen from the very small error bar in the thickness measurements.

For low power density ( $P_{\text{density}}=18 \text{ mW/cm}^2$ ) the passivation quality is quite poor. Moreover, when the power increases beyond  $20.8 \text{ mW/cm}^2$  the passivation quality drops, even if the thickness is increased (which should be associated to better passivation). The best passivation qualities are obtained for a deposition power density  $P_{\text{density}}=20.8 \text{ mW/cm}^2$ .

The trend of the passivation qualities as a function of the power density can be explained with the  $R^*$  values obtained from the FTIR characterization analysis, reported in Fig. 4.12. The  $C_H$  content in all the layers is instead quite comparable. The FTIR spectra with the fitting are also reported in Fig. 4.13. For low power density ( $P_{\text{density}}=18 \text{ mW/cm}^2$ ) the passivation quality is quite poor. This may be due to a higher  $R^*$  and thus higher defectivity attributed to a decreased ion bombardment effect and thus less energy for the diffusion of radicals [115]. However, another reason for that could be that the deposited layer is quite thinner than others due to a difficult experimental determination of deposition rates. The layers deposited with power  $P_{\text{density}}=20.8 \text{ mW/cm}^2$  are the less defective, as indicated by the lowest  $R^*$ . This indicates a less defective film and it relates to better passivation qualities. Lastly, it can be observed that as the power density increases the  $R^*$  increases as well. This may be attributed to an enhanced damage of the c-Si substrate with increasing RF power density due to a significant ion bombardment [115]. Another reason could be a higher deposition rate which promotes radicals to stick to crystal sites without diffusing much on the surface, promoting the formation of microvoids [57].

For the above-mentioned reasons, the sample deposited at  $P_{\text{density}}=20.8 \text{ mW/cm}^2$  is characterized by the best microstructure and thus has the best passivation qualities.

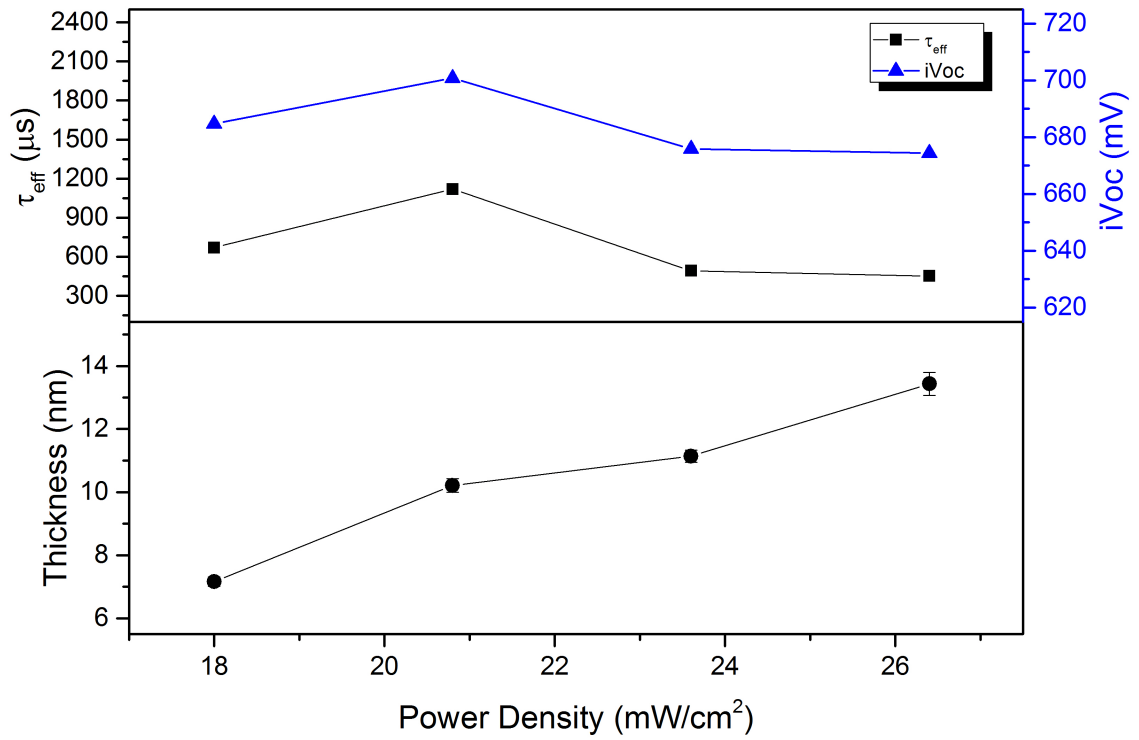


Figure 4.11: Effective lifetime, implied open-circuit voltage and layer thickness of symmetric passivation samples as a function of the deposition power density.

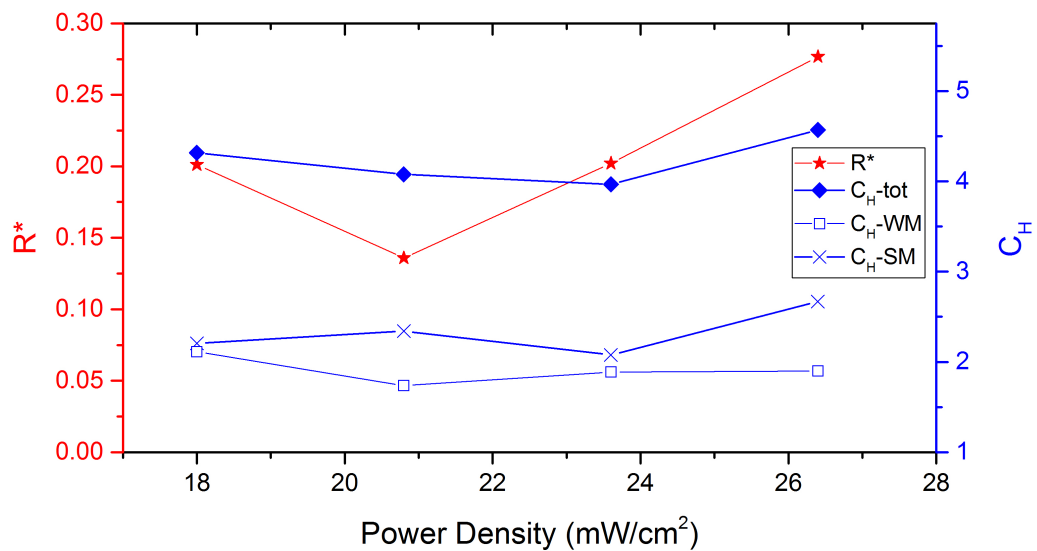


Figure 4.12: Microstructure factor ( $R^*$ ) and hydrogen content [ $C_{\text{H}}$  (total) =  $C_{\text{H}}$  (WM) +  $C_{\text{H}}$  (SM)] as a function of power density, obtained by FTIR analysis elaboration.

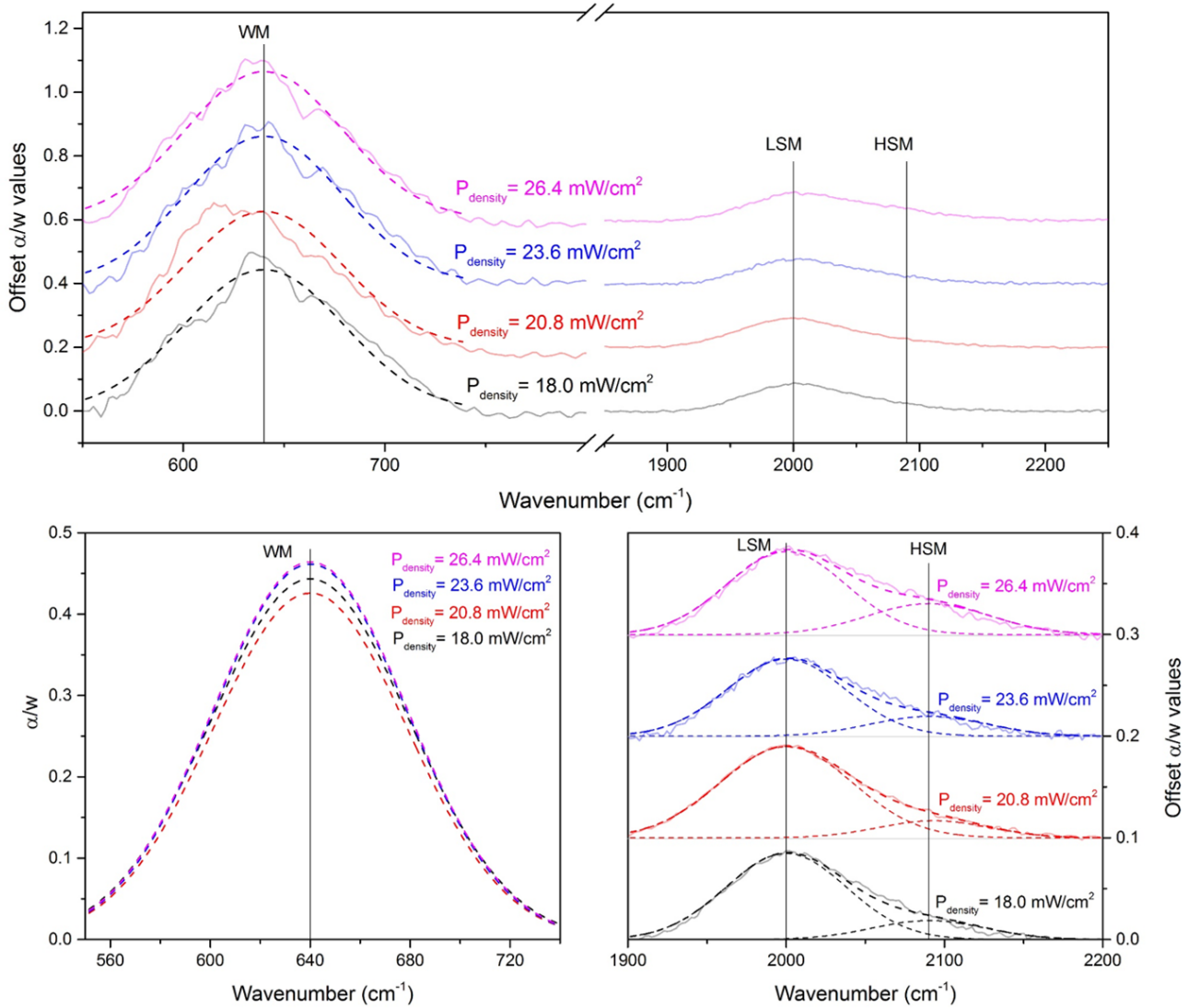


Figure 4.13: FTIR spectra and fitting of WM, LSM, HSM for samples deposited at different power density.

### Monolayer passivation optimization - conclusions

Based on the optimization of four different deposition parameters, the optimized deposition conditions for the monolayer (i)a-Si:H are reported in Tab. 4.6. The layer is optimized in terms of passivation quality, uniformity and reproducibility. With a 10 nm (i)a-Si:H layer, an effective lifetime  $\tau_{\text{eff}}=1.1$  ms and an  $i\text{-}V_{\text{OC}}=701$  mV can be obtained.

To understand better the relations between passivation qualities and the microstructure properties (i)a-Si:H on flat <100> surface, the layers have been characterized via Fourier-transform infrared spectroscopy (FTIR) and spectroscopic ellipsometry (SE). In conclusion, the monolayer that contains a sufficient H, a higher fraction of monohydrides and fewer defects (low  $R^*$ ) is beneficial for achieving a better passivation quality.

Table 4.6: Deposition parameters of optimized hydrogenated intrinsic amorphous silicon layer

Layer	$T_s$ [°C]	Pressure [mbar]	Power density [mW/cm <sup>2</sup> ]	Dilution ratio [-]	Flow rate [sccm]	Frequency [MHz]
(i)a-Si:H	160	0.7	20.8	0	40	13.56

### 4.2.2. Monolayer with post HPT

It has been shown that the presence of hydrogen is crucial for achieving good passivation [124] as indicated by the  $i$ - $V_{OC}$  of SHJ cells precursors [71]. In order to incorporate hydrogen in the structure, hydrogen plasma treatments after the intrinsic layer deposition have been proposed in the scientific literature [95]. This approach has proven to enhance the charge carrier lifetime due to the diffusion of hydrogen atoms to the a-Si:H(i)/c-Si-interface. Therefore the chemical passivation improves due to dangling bond saturation. Furthermore, this passivation strategy is especially advantageous for the passivation of  $\langle 100 \rangle$  c-Si surfaces which are prone to epitaxial growth, since it avoids the introduction of defect-creating strain into the amorphous network [95].

Thus, after having optimized the monolayer (i)a-Si:H deposition, the application of a post HPT treatment has been investigated. However, the optimization of the conditions of the HPT treatment on the monolayer resulted to be difficult and not replicable. The passivation quality of the samples deteriorated in all the cases. The results of the passivation qualities are reported in the Appendix (section A.2). This is probably due to the difficulty of experimentally optimize the treatment in the AMIGO PECVD deposition tool. Therefore, other approaches have been investigated and they are discussed in the following sections.

### 4.2.3. Bilayer passivation

So far as seen from our optimized single (i)a-Si:H layer, the best passivation quality achieved is still moderate as compared to those reported in the literature [95, 125]. Since HPT treatment after monolayer deposition couldn't be experimentally optimized, the bilayer passivation approach has been investigated.

The bilayer passivation is a two-step deposition strategy. It consists of depositing a first layer of intrinsic amorphous silicon ( $i_1$ ) followed by a second layer ( $i_2$ ), as schematically shown in Fig. 4.14. Compared to the single (i)a-Si:H passivating layer, the bilayer can form a more abrupt interface with less local crystallization and strains and improve the passivation qualities [112, 126].

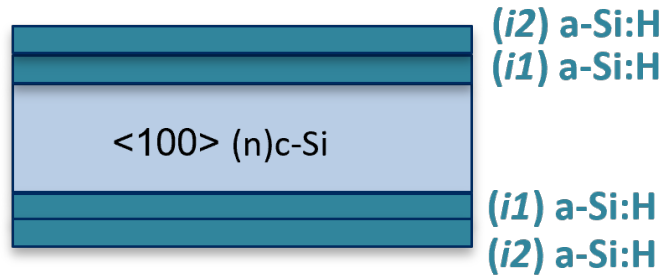


Figure 4.14: Bilayer passivation

In this study, the deposition conditions of each layer have been optimized in order to achieve the best passivation qualities. The detailed optimized deposition conditions of  $i_1$  and  $i_2$  layers are summarized in Tab. 4.7.

- $i_1$ : it is deposited with the previously optimized monolayer deposition conditions, so with a pure silane plasma
- $i_2$ : it is deposited with a higher hydrogen dilution ratio, and adjusted pressure.

These conditions resulted to be advantageous for passivation qualities, as proven by a previous research by Zhang et al. [127].

### Bilayer thickness optimization

Once optimized the deposition conditions, the optimal thicknesses for  $i_1$  and  $i_2$  are investigated. In particular, the total thickness of the bilayer structure is aimed to be kept at 10 nm and different  $i_1$  and  $i_2$  thickness ratios have been tested.

The passivation quality of the layer as a function of  $i_1$  and  $i_2$  thickness ratios is shown in Fig. 4.15. Note that the thickness of  $i_1$  is shown in the top horizontal line and the  $i_2$  thickness on the bottom horizontal line. The sum of those two values is expected to be around 10 nm.

Table 4.7: Deposition parameters of  $i_1$  and  $i_2$  hydrogenated intrinsic amorphous silicon layer for bilayer passivation

Layer	$T_s$ [°C]	Pressure [mbar]	Power density [mW/cm <sup>2</sup> ]	Dilution ratio [-]	Flow rate [sccm]	Frequency [MHz]
(i1)a-Si:H	160	0.7	20.8	0	40	13.56
(i2)a-Si:H	160	1.4	20.8	3	40	13.56

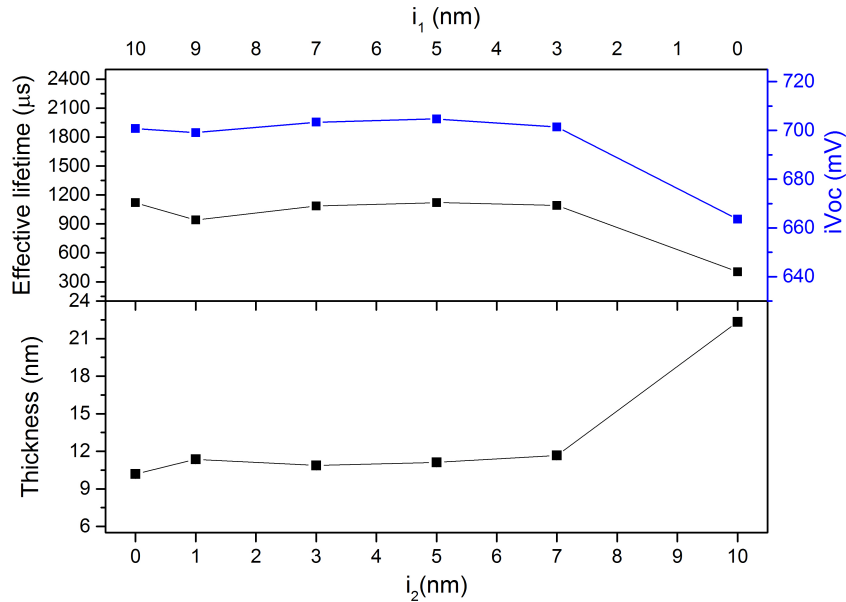


Figure 4.15: Effective lifetime, implied open-circuit voltage and layer thickness of symmetric passivation samples as a function of bilayer thickness ratios.

For the sample with single  $i_2$  layer it can be observed that the deposited layer is quite thick. This happens because, since it was found from some preliminary tests that  $i_2$  layer was barely growing on  $\langle 100 \rangle$  flat surfaces, the deposition time was drastically increased to obtain some deposition. However, despite the deposited layer is very thick, the passivation is poor. Therefore, a  $i_2$  layer only passivation is not performing well. This is in line to what was already found in the monolayer optimization: a too high DR ratio is not desired as it has been found to degrade the film quality and initiate epitaxial growth at the a-Si/c-Si interface [72, 119].

In terms of passivation performance, it is quite similar for each sample except for  $i_2$  layer only. The highest passivation qualities are obtained for the (5nm)  $i_1$  + (5nm)  $i_2$  bilayer structure with a  $\tau_{eff}=1.4$  ms and a  $iV_{OC}=705$  mV. Compared to the single  $i_1$ , all the bilayer structures can improve the effective lifetime. Therefore this highlights the advantages of the bilayer structure if compared to the monolayer structure.

The better performance of the bilayer structure than the monolayer (i)a-Si:H can be explained through the  $R^*$  and  $C_H$  values obtained from the FTIR characterization analysis, reported in Fig. 4.16. The FTIR spectra with the fitting are also reported in Fig. 4.17. The bilayer structure has the advantage of incorporating a first  $i_1$  layer which effectively inhibits plasma damage and epitaxial growth, ensuring a sharp a-Si/c-Si interface, and a second  $i_2$  layer that ensures sufficient hydrogen diffusion to a-Si/c-Si which further saturates residual dangling bonds [126]. This is proven by a FTIR analysis (Fig. 4.16) which shows that bilayer has a higher H content than the monolayer (i)a-Si:H, which may indeed improve dangling bonds passivation and therefore the film's passivation qualities. The microstructure factor  $R^*$  seems to be higher for the bilayer, which indicates a slightly higher defectivity. However, this probably doesn't degrade much the passivation quality since it's probably a less relevant than having an improved surface dangling bonds passivation. The advantages of enhanced dangling bonds passivation while keeping a low defective layer on top of the c-Si surface (the  $i_1$  layer) make the bilayer structure better than the monolayer in terms of passivation qualities.

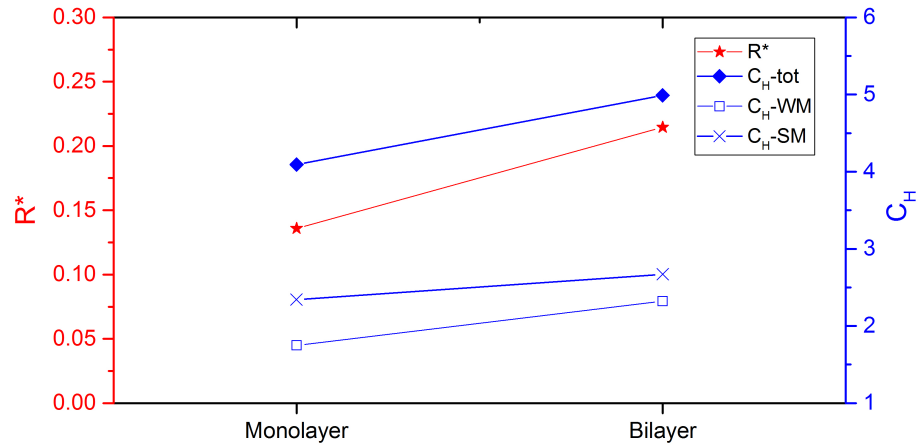


Figure 4.16: Microstructure factor ( $R^*$ ) and hydrogen content [ $C_H$  (total) =  $C_H$  (WM) +  $C_H$  (SM)] for the monolayer and bilayer (i)a-Si:H.

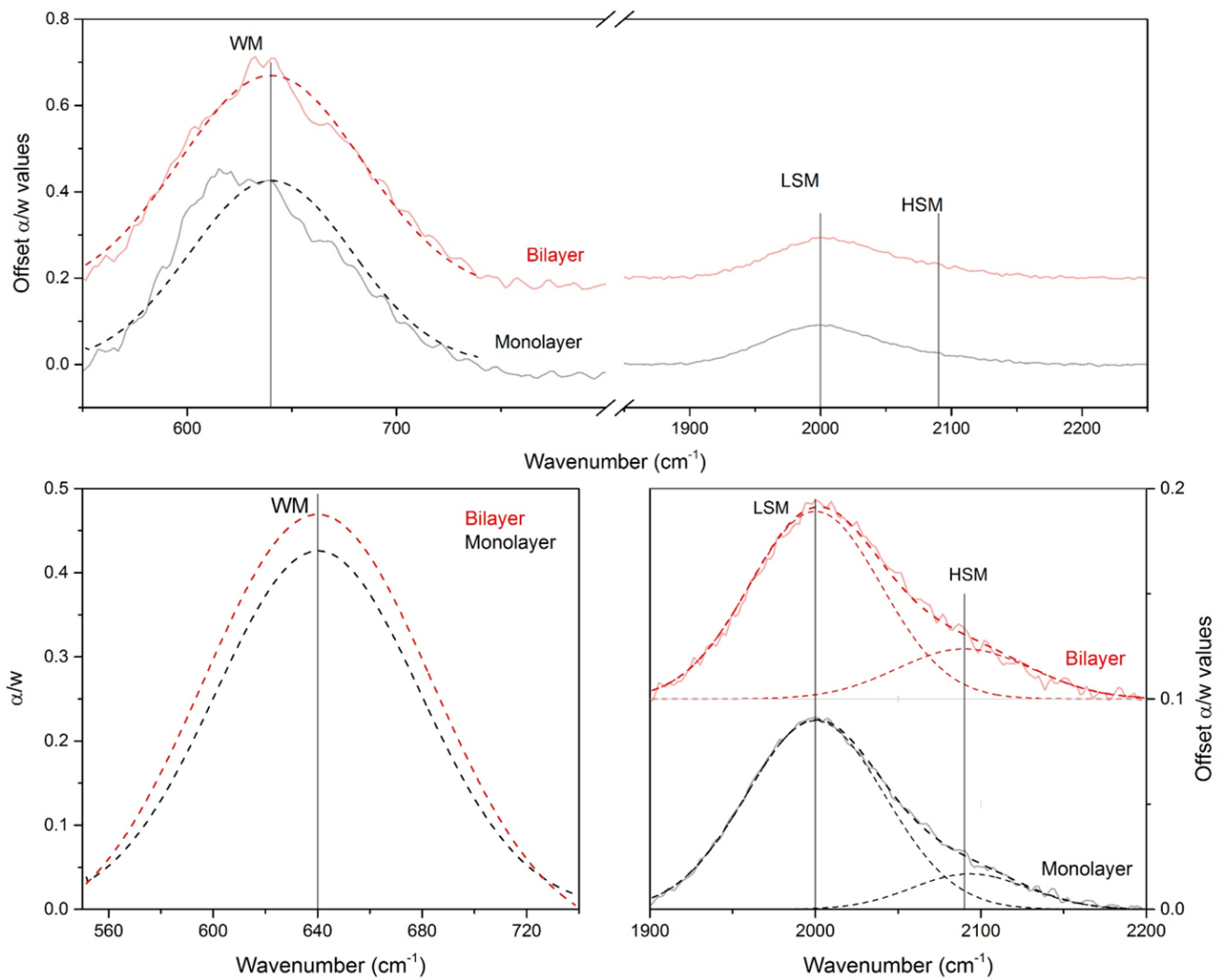


Figure 4.17: FTIR spectra and fitting of WM, LSM, HSM for the monolayer and bilayer (i)a-Si:H.

#### 4.2.4. Bilayer passivation with post deposition treatments

In order to incorporate more hydrogen in the structure, hydrogen plasma treatments during [121] and post-deposition [47, 95] have been proposed. In both cases, hydrogen incorporation led to a significant improvement in the passivation quality due to the diffusion of hydrogen atoms to the a-Si:H(i)/c-Si-interface. Moreover, this approach is especially used for the passivation of <100> c-Si surfaces which are prone to epitaxial growth, to enhance passivation quality without introducing defect-creating strain into the amorphous network [95].

In this research, the combination of bilayer structure with different HPT treatments is investigated. In particular, two main processes are analyzed:

- Bilayer with post HPT: a hydrogen plasma treatment is applied just after the complete bilayer deposition. A schematic representation of the process is shown in Fig. 4.18 a).
- Bilayer with intermediate HPT: a hydrogen plasma treatment is applied after the first  $i_1$  layer and before the second  $i_2$  layer deposition. A schematic representation of the process is shown in Fig. 4.18 b).

In the following sections, the results of the two deposition approaches are discussed in detail.

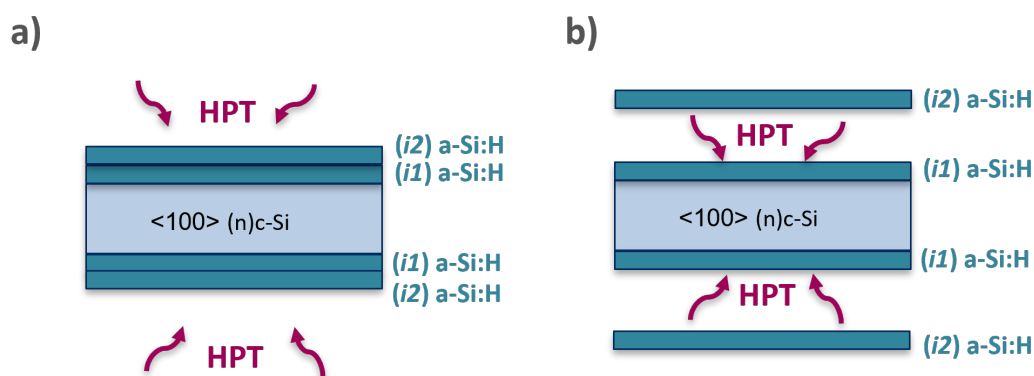


Figure 4.18: Bilayer passivation with a) post HPT; b) intermediate HPT

#### Bilayer with post HPT treatment

The effect of a post HPT treatment after the bilayer deposition has been investigated. After some initial testing, a power density of 41.6 mW/cm<sup>2</sup> was selected as optimal for HPT treatment. After that, the effect of the duration of the post HPT has been investigated and optimized. The main deposition conditions of the bilayer and the HPT treatment are reported in Tab. 4.8.

Table 4.8: Deposition parameters of  $i_1$  and  $i_2$  hydrogenated intrinsic amorphous silicon layers and post HPT for passivation of the c-Si surface

Layer	$T_s$ [°C]	Pressure [mbar]	Power density [mW/cm <sup>2</sup> ]	Dilution ratio [-]	Flow rate [sccm]	Frequency [MHz]	Duration [sec]
(i1)a-Si:H	160	0.7	20.8	0	40	13.56	-
(i2)a-Si:H	160	1.4	20.8	3	40	13.56	-
HPT (post)	160	2.2	41.6	-	200	13.56	0-60

The effect of post HPT treatment time on the passivation quality is showed below in Fig. 4.19. The HPT time has been varied between 0 and 60 seconds. The optimal post HPT time was found to be 50 seconds. Note that the HPT time seems to have not a significant effect on improving the passivation qualities for durations <50 sec. This may be related to a too short treatment which correlates to a low amount of hydrogen diffusing towards the layer and the surface to passivate dangling bonds. The optimal time is 50 seconds of post HPT

treatment and the main reasons for increasing passivation properties with a well-adjusted HPT was found to be due to diffusion of hydrogen atoms to the a-Si:H(i)/c-Si-interface and improved chemical passivation due to dangling bond saturation [95]. For longer HPT duration (>50 sec) the passivation quality starts to drop again. This is probably related to excessive hydrogen incorporation, which can induce the formation of a too high amount of defects and clustered microvoids and damages at the c-Si/a-Si:H interface [47, 120]. It can also be noted that when HPT time increases, the thickness of the intrinsic layers slightly decreases which can be attributed to a hydrogen etching effect.

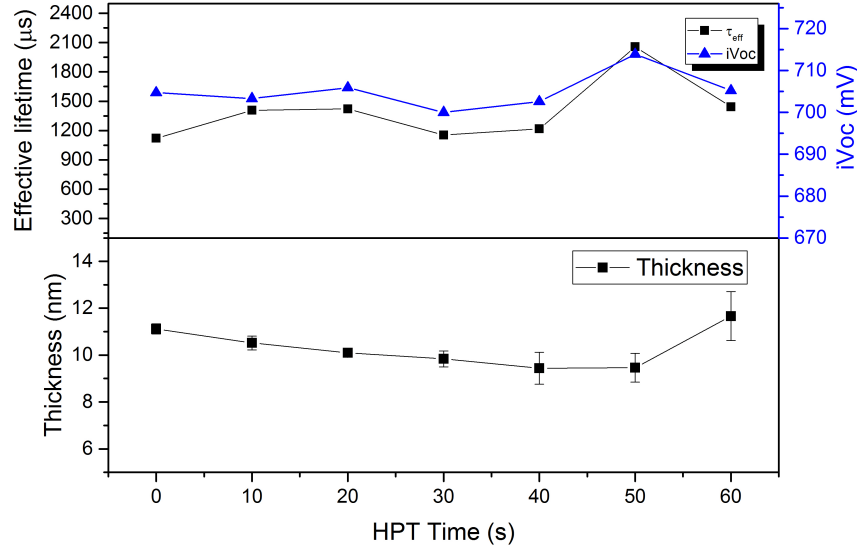


Figure 4.19: Effective lifetime, implied open-circuit voltage and layer thickness of symmetric passivation samples as a function of post HPT treatment time.

To conclude, a post HPT treatment with an optimized duration of 50 seconds enhances the passivation properties. By combining the bilayer approach with a post HPT, the best sample showed a  $\tau_{\text{eff}}$  of 2.0 ms and an  $i-V_{OC}$  of 714 mV for a total thickness of 10-nm (i)a-Si:H on the flat <100> surface. This can be related to higher incorporation of H that improves the saturation of dangling bonds at c-Si/(i)a-Si:H interface, while without promoting detrimental epitaxial growth.

### Bilayer with intermediate HPT treatment

The effect of HPT treatment after the  $i_1$  layer and before the deposition of  $i_2$  layer is analyzed. Again, after some initial testing, a power density of  $41.6 \text{ mW/cm}^2$  was selected as optimal for HPT treatment. Then the effect of the duration of the intermediate HPT has been investigated and optimized. The main deposition conditions and HPT parameters are reported in Tab. 4.9.

Table 4.9: Deposition parameters of  $i_1$  and  $i_2$  hydrogenated intrinsic amorphous silicon layers and intermediate HPT for passivation of the c-Si surface

Layer	$T_s$ [°C]	Pressure [mbar]	Power density [mW/cm <sup>2</sup> ]	Dilution ratio [-]	Flow rate [sccm]	Frequency [MHz]	Duration [sec]
(i1)a-Si:H	160	0.7	20.8	0	40	13.56	-
HPT (intermediate)	160	2.2	41.6	-	200	13.56	0-40
(i2)a-Si:H	160	1.4	20.8	3	40	13.56	-

The HPT time has been varied between 0 sec and 40 sec. The effect of duration of the intermediate HPT treatment on the passivation quality is shown in Fig. 4.20. The average thickness of the deposited samples

is quite comparable. It is interesting to note that in this case, the hydrogen etching effect seems to be very minor. It is assumed that this is because the HPT duration is quite short to induce a significant etching effect.

In all cases, the intermediate HPT treatment enhances the passivation quality of the sample if compared to the bilayer passivation. However, an optimal HPT treatment time can be observed. If the HPT treatment duration is too short (<20 sec), the passivation quality does not increase significantly. This may be due to a quite low amount of hydrogen diffusing towards the layer and the c-Si/(i)a-Si:H interface to passivate the dangling bonds. On the other hand, when HPT treatment is too long (>20 sec) a decrease in passivation quality is observed. This may be due to excessive hydrogen incorporation in the film which can enhance the film defectivity.

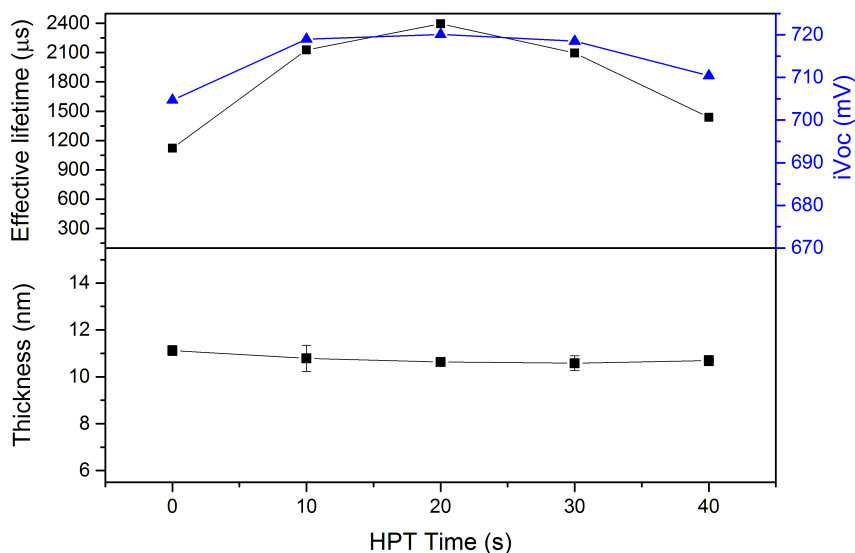


Figure 4.20: Effective lifetime, implied open-circuit voltage and layer thickness of symmetric passivation samples as a function of intermediate HPT treatment time.

In conclusion, an intermediate HPT treatment with an optimized duration of 20 seconds is beneficial for improving the passivation quality of the film. By combining the bilayer approach with an intermediate HPT, the best sample showed a  $\tau_{\text{eff}}$  of 2.4 ms and an  $i-V_{OC}$  of 720 mV for a total thickness of 10-nm (i)a-Si:H on the flat <100> surface.

The improved performance of the bilayer structure with and intermediate HPT can be explained through the  $R^*$  and  $C_H$  values obtained from the FTIR characterization analysis, reported in Fig. 4.21. The FTIR spectra with the fitting are also reported in Fig. 4.22. As can be seen from Fig. 4.21, the intermediate HPT enhances the hydrogen incorporation in the passivation layers, similarly to what was found by Mews et al. [95]. As a consequence, the chemical passivation improves due to a higher dangling bonds saturation [95]. In particular, the intermediate HPT is applied to the first  $i_1$  undiluted layer only, thus the diffusion of H to the a-Si:H(i)/c-Si-interface is facilitated. Indeed, if compared to a post HPT treatment, the intermediate HPT makes the diffusion of H to the c-Si surface easier, since H has to diffuse through a thinner layer. Moreover, choosing an intermediate HPT can also avoid excessive H incorporation in the second layer  $i_2$  which is already deposited with a high hydrogen dilution.

An increase in  $R^*$  is also observed for the layer deposited with HPT treatment. It is pretty commonly reported in the literature that HPT affects film compactness and H bonding reconfigure in favor of multi-vacancy bonding configurations. However this reconfiguration doesn't degrade the passivation qualities since the post-deposition incorporation of hydrogen seems not to be related to an increase of strain in the layer, being the source of metastable defects creation [95].

A similar H diffusion phenomenon happens for the bilayer structure. In this case, during the deposition of the  $i_2$  layer some H diffuses through the underlying  $i_1$  layer improving the dangling bonds passivation [126]. However, with a HPT treatment the amount of H that diffuses through the surface is enhanced and this can be a reason why even better passivation is achieved.

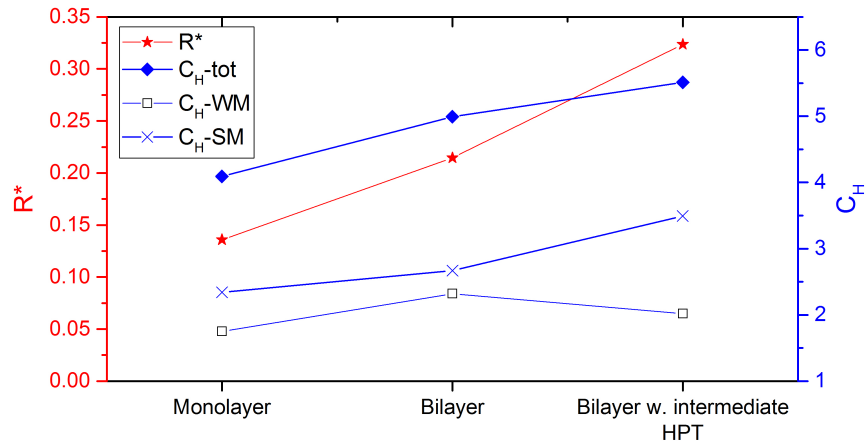


Figure 4.21: Microstructure factor ( $R^*$ ) and hydrogen content [ $C_H$  (total) =  $C_H$  (WM) +  $C_H$  (SM)] for monolayer (i)a-Si:H, bilayer and bilayer with intermediate HPT.

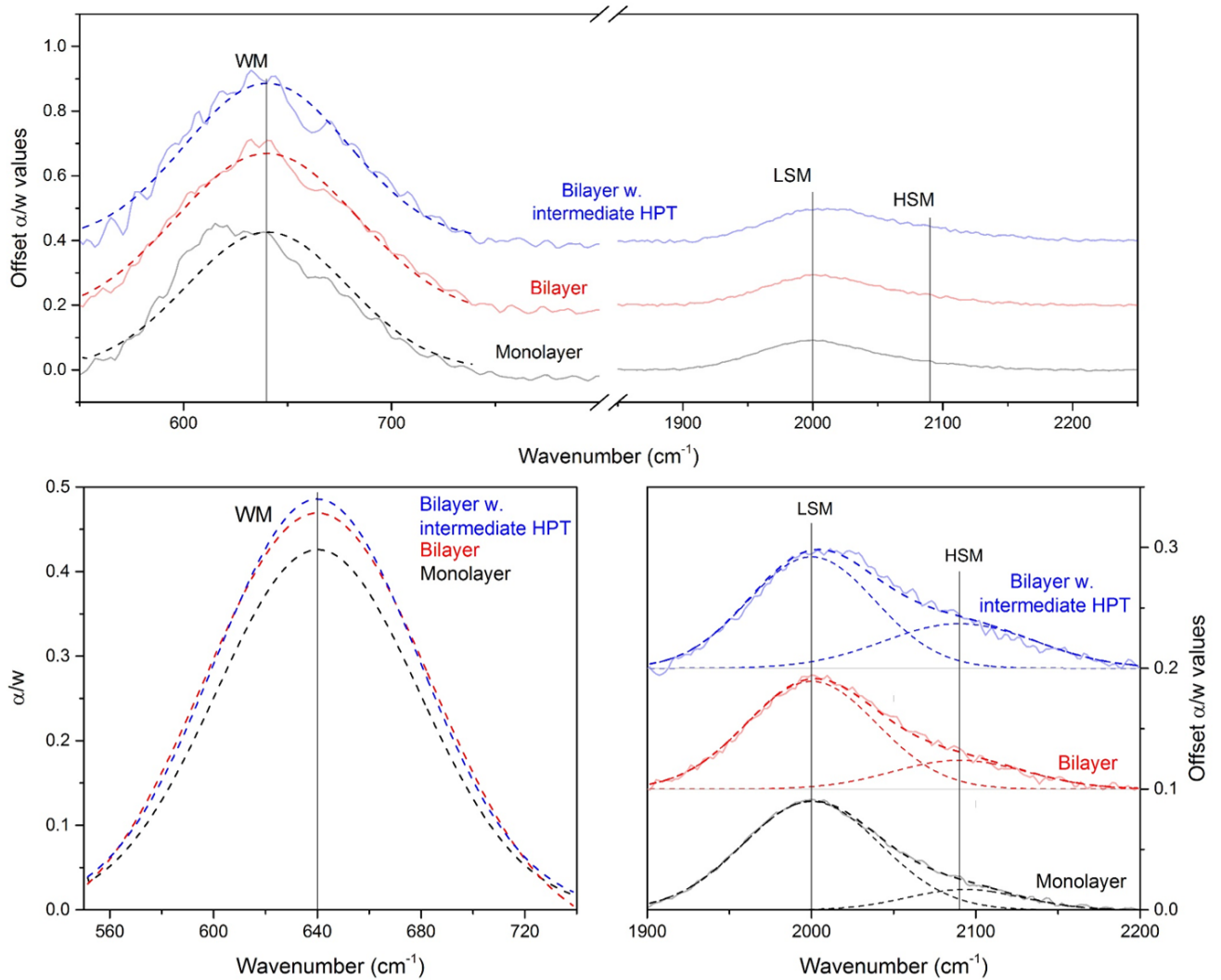


Figure 4.22: FTIR spectra and fitting of WM, LSM, HSM for monolayer (i)a-Si:H, bilayer and bilayer with intermediate HPT.

### 4.3. Summary

In summary, the first thesis objective was to optimize the passivation layer on the <100> c-Si front flat surface. Firstly, RF-PECVD deposition conditions of a (i)a-Si:H monolayer for symmetric flat c-Si surfaces were optimized. The optimized (i)a-Si:H monolayer (10-nm-thick) was obtained using pure SiH<sub>4</sub> resulting in quite mediocre performances ( $\tau_{\text{eff}} = 1.2$  ms,  $i\text{-}V_{\text{OC}} = 701$  mV).

To improve further the passivation quality of monolayer (i)a-Si:H on flat <100> surface, other passivation approaches aiming at incorporating more H without promoting detrimental epitaxial growth have been investigated. With a bilayer approach, which features firstly a less H-containing (i)a-Si:H to prevent epitaxial growth and then a second H-rich (i)a-Si:H layer, the passivation properties were slightly enhanced to  $\tau_{\text{eff}}=1.4$  ms and a  $i\text{-}V_{\text{OC}}=704$  mV. Subsequently, by combining the bilayer approach with a post HPT,  $\tau_{\text{eff}}$  of 2.0 ms and an  $i\text{-}V_{\text{OC}}$  of 714 mV were achieved. Finally, by combining the bilayer approach with an intermediate HPT, the optimal passivation sample was deposited, with  $\tau_{\text{eff}}$  of 2.4 ms and an  $i\text{-}V_{\text{OC}}$  of 720 mV on the flat <100> surface.

To gain a better understanding of the correlation between passivation qualities and the microstructure properties of (i)a-Si:H on flat <100> surface, the layers have been characterized mainly via Fourier-transform infrared spectroscopy (FTIR). In conclusion, the passivation layer that contains sufficient H, a higher fraction of monohydrides is beneficial for achieving a better passivation quality.



# 5

## Optical simulations

In this paragraph, some optical simulations of the tandem cell are presented. Firstly, the detailed layer stack of the first tandem cell fabricated by TU Delft and TU Eindhoven is presented. Based on the first design of the tandem structure the main optical limitations are identified. Starting from this, multiple optical simulations are performed in order to find some possible guidelines to improve cell performance. The main optimization suggestions are in terms of layer thicknesses or layer materials (refractive index). They are summarized in the last section of this paragraph.

### 5.1. The initial tandem cell structure

The architecture of the first perovskite/c-Si tandem cell and the detailed layer stack is indicated in Fig. 5.1. The thicknesses of each layer are also specified.

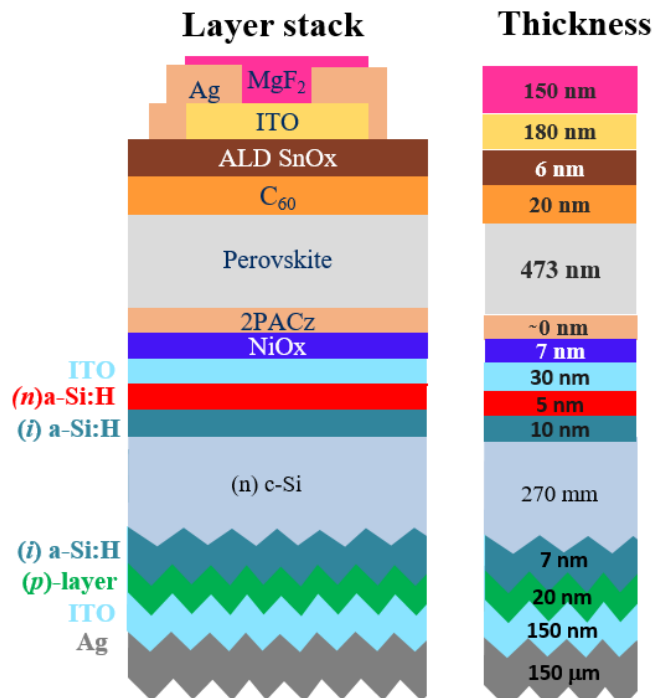


Figure 5.1: A 22.2% efficiency perovskite/c-Si tandem cell developed by TU Delft and TU Eindhoven

## 5.2. The simulations software

Optical simulations were carried out using GenPro4 developed by the PVMD group at TU Delft [128]. The layer thicknesses reported in Fig. 5.1 were used and the refractive indexes and extinction coefficients of each layer were taken from experimental measurements carried out with spectral ellipsometry.

The GenPro4 software is a MATLAB-based optical model that combines wave and ray optics. The solar cell is represented as a multilayered structure. The fraction of incident light absorbed in each layer, taking into account scattering and trapping of light at the interfaces, is calculated. From these values, the implied photocurrent is calculated. It is important to note that this program is a purely optical model. The electrical characteristics of the solar cell are not taken into account. More details about the working principles and equations used in GenPro4 can be found in ref. [128].

## 5.3. Identification of major limitations of the first fabricated tandem cell and the resulting optical simulations

The first step that was taken was to simulate the fabricated 22.2% efficiency tandem cell with GenPro4 software. The results of the simulation are shown in Fig. 5.2 which shows the absorptance of each layer as a function of wavelength. The desired absorptions in the perovskite and c-Si absorbers are indicated by a light grey and dark grey area respectively, and correspond to the implied photocurrent density ( $\text{mA}/\text{cm}^2$ ) of top and bottom cell respectively. Besides the desired light absorption in the tandem cell, there are some significant parasitic absorption losses. The parasitic absorptions are quantified in the brackets for each layer and are also shown in the graph. For example, the yellow and orange areas represent the absorption losses in the ITO and the  $\text{C}_{60}$ , respectively. Moreover, the white area represents the reflectance losses, which are also quantified in brackets in the legend.

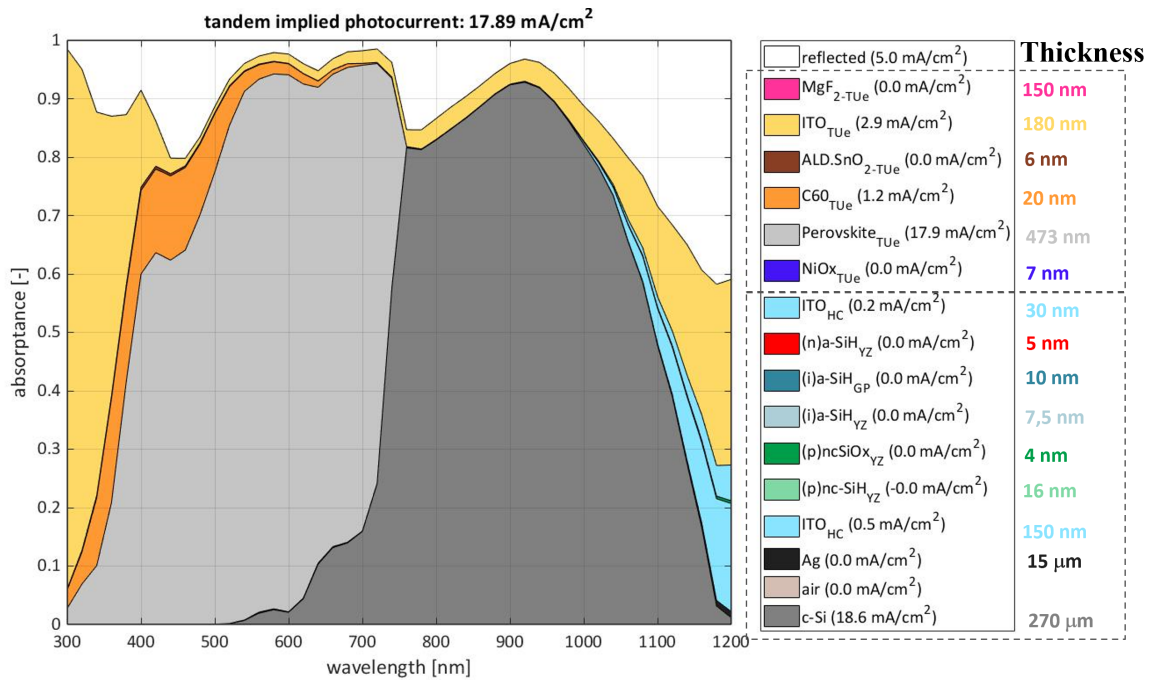


Figure 5.2: GenPro4 [128] simulations of the the 22.2% efficiency perovskite/c-Si tandem cell developed by TU Delft and TU Eindhoven

In this way, the major optical limitations of the cell were identified. As can be seen from Fig. 5.2, the cell has five main optically weak points:

- A high front reflection, indicated by high reflectance losses ( $5 \text{ mA/cm}^2$ ), especially a high white area dip in the short wavelength region
- A high parasitic absorption of the front ITO ( $2.9 \text{ mA/cm}^2$ )
- A high parasitic absorption of the  $\text{C}_{60}$  layer ( $1.2 \text{ mA/cm}^2$ )
- A high reflection at the interface of the top cell and bottom cell indicated by a high white area dip in wavelength range of around 700-900 nm
- An implied photocurrent of the tandem cell which is limited by the perovskite top cell

In order to find feasible and efficient strategies to tackle these limitations, different simulations have been conducted. They are discussed in detail in the following paragraphs.

### 5.3.1. Optimization of front ITO and $\text{MgF}_2$ thicknesses

Firstly, numerous simulations with varying the front  $\text{MgF}_2$  and ITO layers (also called double-layer anti-reflection coatings, DLARC) have been performed. The thicknesses of both ITO and  $\text{MgF}_2$  are varied between 0 and 180 nm while the thickness of the other layers is kept the same as the 22.2% efficiency cell. The goal is to determine the best thickness combination of the anti-reflection layers that results in both minimized front reflection and minimized ITO parasitic absorption.

The results of these simulations are shown in the contour plot in Fig. 5.3 where the matched implied photocurrent of the tandem cell is plotted as a function of the thickness. As can be seen from Fig. 5.3, the implied photocurrent density is maximized for a specific range of  $\text{MgF}_2$  and ITO thicknesses. In particular, the maximum value of tandem implied photocurrent density is  $19.7 \text{ mA/cm}^2$  reached with the combination of a 20 nm ITO and a 100 nm  $\text{MgF}_2$ . However, it is good to state that an ITO of 20 nm is probably too thin to fulfill the electrical requirements of the tandem cell, as its sheet resistance will increase with a thinner layer [129]. Therefore it is useful to determine how thick can the ITO be deposited without compromising the obtaining of a high implied photocurrent of the tandem cell. As can be seen from the red area in Fig. 5.3, ITO can be up to 60 nm thick (if combined with a  $\text{MgF}_2$  of thicknesses between 80 and 120 nm) if an implied photocurrent higher than  $19.0 \text{ mA/cm}^2$  is desired. Moreover, the ITO thicknesses can be further increased to 100 nm (if combined with a  $\text{MgF}_2$  of thicknesses between 90 and 110 nm) if the desired value of the implied photocurrent of the tandem cell is set to be higher than  $18.8 \text{ mA/cm}^2$ .

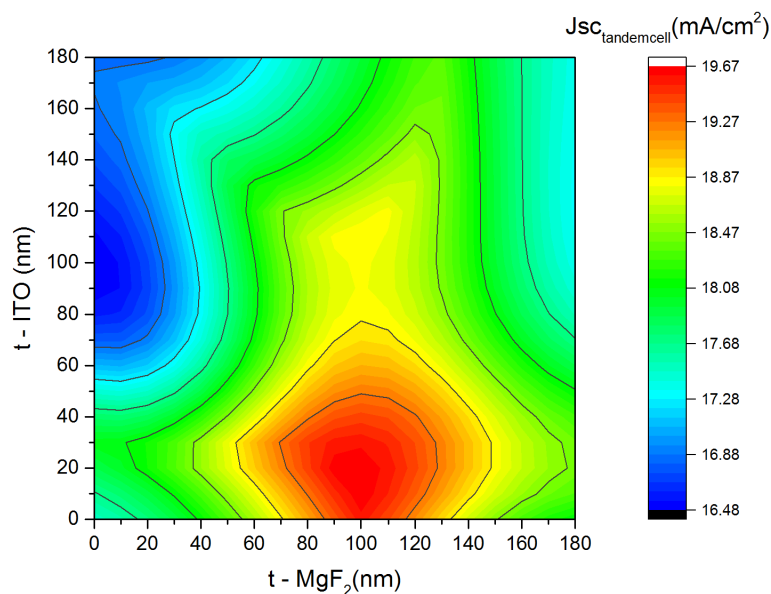


Figure 5.3: GenPro4 [128] simulations of the matched tandem cell implied photocurrent for ITO and  $\text{MgF}_2$  thicknesses varying from 0 to 180 nm.

To summarize, the first optimization aimed at overcoming the limitations of a high front reflection and high parasitic absorption of ITO. In order to do that the thicknesses of the front anti-reflection layers (ITO and  $\text{MgF}_2$ ) have been optimized. The optimal value of tandem implied photocurrent is  $19.7 \text{ mA/cm}^2$  and is achieved with a 20 nm ITO and 100 nm  $\text{MgF}_2$ . The optical simulation of the tandem cell with 20 nm ITO and 100 nm  $\text{MgF}_2$  is shown in Fig. 5.4. However, a 20 nm ITO could be too thin to meet the electrical requirements. Nevertheless, the combination of an ITO up to 60 nm thick and a  $\text{MgF}_2$  with thicknesses comprised between 80 and 120 nm is able to deliver a cell implied photocurrent higher than  $19.0 \text{ mA/cm}^2$ .

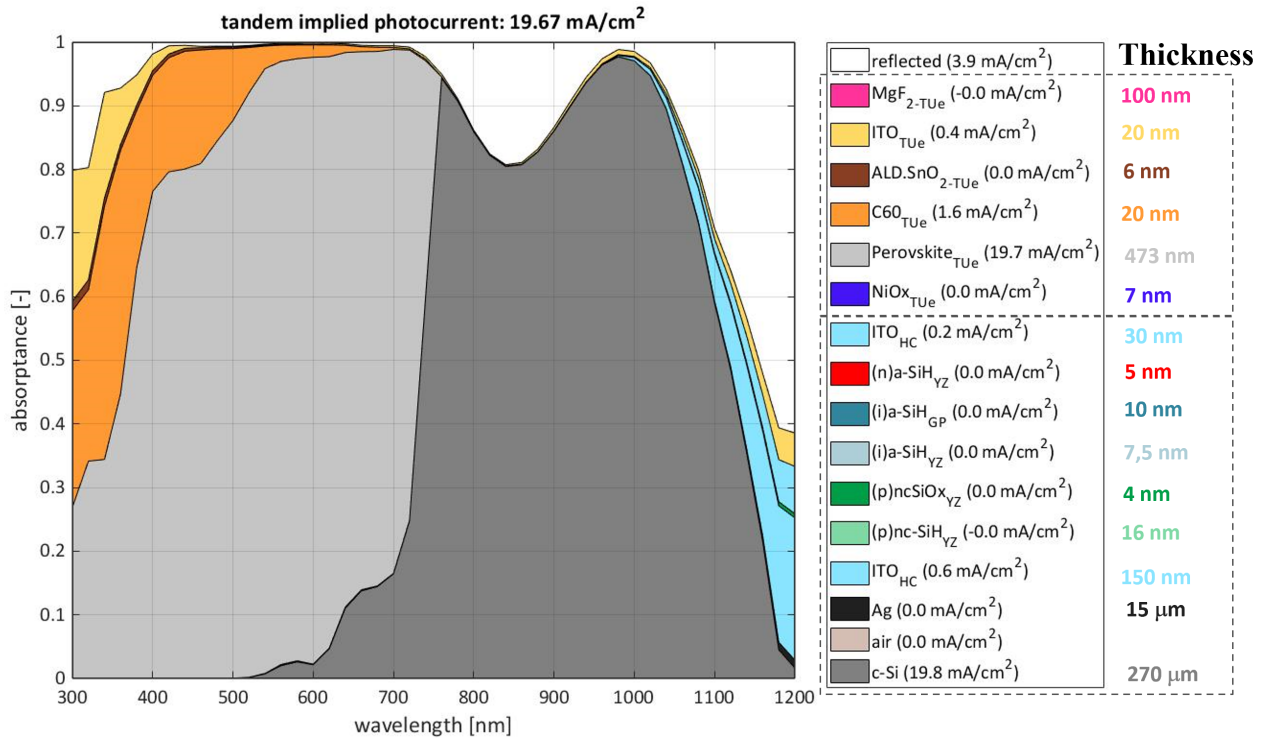


Figure 5.4: GenPro4 [128] simulations of the tandem cell with optimized  $\text{MgF}_2$  (100 nm) and ITO (20 nm).

### 5.3.2. Optimization of the $\text{C}_{60}$ thickness

After having optimized the thicknesses of the front anti-reflective layers various simulations with varying the thickness of  $\text{C}_{60}$  have been conducted. The thicknesses of ITO and  $\text{MgF}_2$  have been set to the optimized values (20 nm, 100 nm) and the thicknesses of the other layers are kept the same as the 22.2% efficiency cell. Instead, the thickness of  $\text{C}_{60}$  has been varied between 10 and 20 nm. The aim of this simulation is to determine the optimal  $\text{C}_{60}$  thickness to minimize its parasitic absorption.

The absorbance-wavelength graph of the cell with 10 nm  $\text{C}_{60}$  is shown in Fig. 5.5. As seen in Fig. 5.5, it has been found that reducing the  $\text{C}_{60}$  thickness to 10 nm is beneficial for reducing the parasitic absorption of  $\text{C}_{60}$ . The parasitic absorption with a 10 nm  $\text{C}_{60}$  is about half of the initial value (from  $1.6 \text{ mA/cm}^2$  (see Fig. 5.4) to  $0.8 \text{ mA/cm}^2$  (see Fig. 5.5)). Moreover, the implied photocurrent of the perovskite top cell increases of about  $0.7 \text{ mA/cm}^2$ , reaching a value of  $20.4 \text{ mA/cm}^2$ . However, there is no improvement in terms of the implied photocurrent of the tandem cell. The implied photocurrent  $\text{Jimp}_{\text{tandem cell}}$  remains  $19.7 \text{ mA/cm}^2$ . as the c-Si bottom cell limits the device current.

In conclusion, this optimization is aimed at reducing the parasitic absorption of  $\text{C}_{60}$ . The reduction of the thickness of  $\text{C}_{60}$  to 10 nm halves the parasitic absorption. As a related advantage the  $\text{Jimp}_{\text{perovskite top cell}}$  increases to  $20.4 \text{ mA/cm}^2$ . However, the tandem cell current is limited by the c-Si bottom cell to  $19.7 \text{ mA/cm}^2$ . In conclusion, the suggestion is to decrease the  $\text{C}_{60}$  thickness to 10 nm. Indeed this could enhance the tandem current if efficient strategies for improving the c-Si current, which is the limiting subcell, are implemented. Note that it should be checked experimentally if a 10 nm  $\text{C}_{60}$  can satisfy the cell electrical requirements. Nevertheless, according to the scientific literature, a 10 nm thick  $\text{C}_{60}$  should be able to satisfy those requirements.

The research of Liu et al. [130], which is also theoretically supported by Golubev et al. [131], has proven that even an ultrathin vapor-deposited 1 nm  $C_{60}$  layer is sufficient to achieve efficient devices, while devices without  $C_{60}$  exhibit poor performance. These works clarify the role of  $C_{60}$  in perovskite solar cells, which is mainly to extract electrons from the perovskite film while suppressing the photocurrent hysteresis. And at the same time prove that thin  $C_{60}$  is sufficient to produce efficient perovskite solar cells, simplify the cell's design and reduce manufacturing costs.

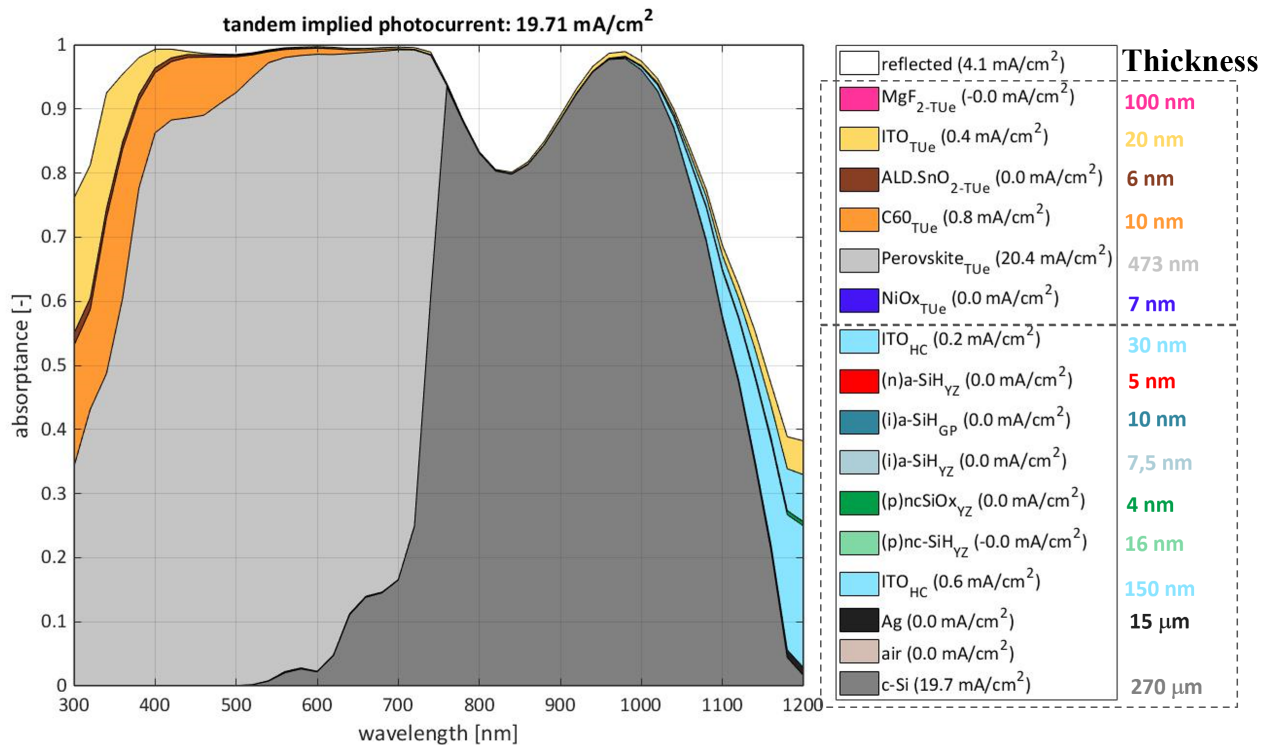


Figure 5.5: GenPro4 [128] simulations of the tandem cell with optimized MgF<sub>2</sub> (100 nm), ITO (20 nm) and C<sub>60</sub> (10 nm)

### 5.3.3. Optimization of the n-type layer of the SHJ bottom cell

Further simulations were performed in order to reduce the reflection on the front side of the SHJ bottom cell. To do that different n-type layers have been simulated and the thickness has been optimized for each material. In particular, the following materials have been simulated:

- (*n*)a-Si:H with thickness varying from 5 to 20 nm.
- (*n*)nc-Si:H with thickness varying from 5 to 20 nm.
- (*n*)nc-SiOx:H with thickness varying from 20 to 110 nm.

The thicknesses of ITO, MgF<sub>2</sub> and C<sub>60</sub> have been set to the optimized values (20 nm, 100 nm, 10 nm) and the thicknesses of the other layers are kept the same as the 22.2% efficiency cell. The result of each simulation for each n-type layer is discussed below.

#### (*n*)a-Si:H

The first type of n-type layers that has been simulated is the standard (*n*)a-Si:H, which is the (*n*)-type contact in the SHJ bottom cell used to fabricate the 22.2% efficiency tandem cell. The simulation consisted of varying the thickness of the (*n*)a-Si:H layer between 5 and 20 nm in order to find an optimal thickness' value.

As a result of this simulation, it was found that increasing the thickness of (*n*)a-Si:H from 5 nm to 20 nm does not lead to much change in the tandem cell performance, as shown in Fig. 5.6. In conclusion, it is suggested to keep (*n*)a-Si:H to about 5 nm for processing advantages.

However, with (*n*)a-Si:H the reflection losses are still quite high. Light reflections occur at an interface between two media of differing refractive indices, and the reflectivity is reduced by minimizing the difference between the refractive indexes of two consecutive layers (see the fundamental optical principles related to an electromagnetic wave traversing an interface between a medium 1 and medium 2, explained in details in ref. [3]). The (*n*)a-Si:H used for the simulation has a refractive index  $n=3.8$  (@ 800 nm) that causes increased reflection when placed in stack with the front ITO layer with  $n=1.7$  (@ 800 nm). It is therefore necessary to find alternative (*n*)-type materials with optimized refractive indexes in order to reduce the reflection at the interface of top and bottom cells. This is why different types of n-layers were simulated, as discussed in the following sections.

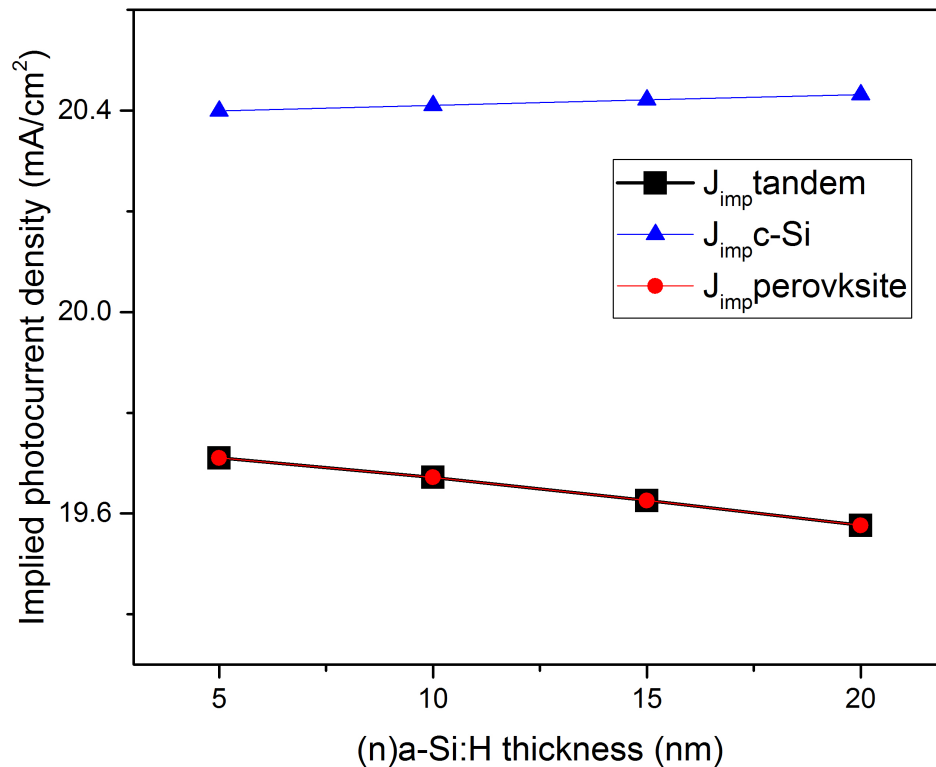


Figure 5.6: GenPro4 [128] simulated implied photocurrent of the tandem cell, c-Si and perovskite subcells as a function of the (*n*)a-Si:H thickness

### (*n*)nc-Si:H

The second type of n-type layer implemented in the simulation is (*n*)nc-Si:H. A (*n*)nc-Si:H layer with a refractive index  $n=3.0$  (@ 800 nm) was implemented in the simulation. The thickness of the (*n*)nc-Si:H was varied between 5 and 20 nm.

It was found that the best performing layer is a 20 nm thick (*n*)nc-Si:H, but also in this case the thickness doesn't have much influence on the tandem cell implied photocurrent density from the optical point of view, as shown in Fig. 5.7. However, also in this case there is no improvement in the cell performance, which results to be comparable to the cell with a 5 nm (*n*)a-Si:H.

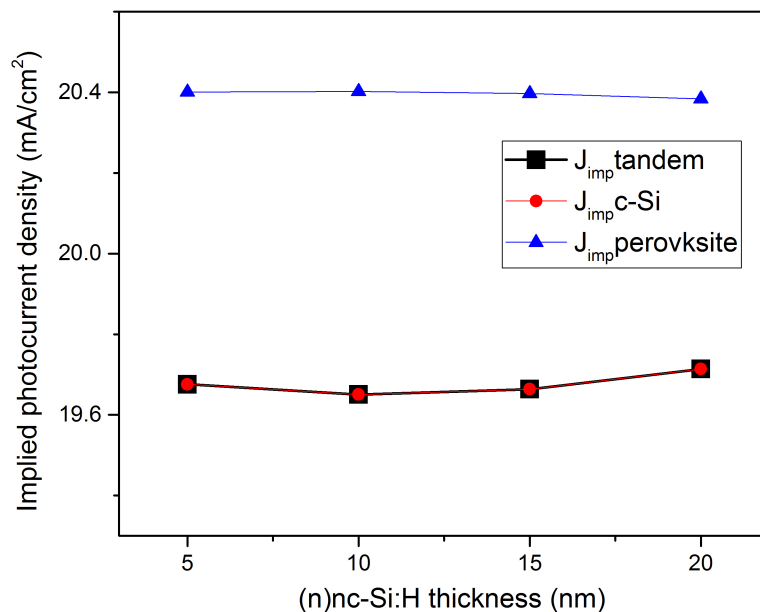


Figure 5.7: GenPro4 [128] simulated implied photocurrent of the tandem cell, c-Si and perovskite subcells as a function of the  $(n)nc-Si:H$  thickness

### $(n)nc-SiOx:H$

As a third type of n-typed layer  $(n)nc-SiOx:H$  has been simulated. The  $(n)nc-SiOx:H$  used for the simulation has a refractive index  $n=2.5$  (@ 800 nm). This refractive index value is comparable to the ones reported in the literature. Mazzarella et al. have reported that the  $(n)nc-SiOx:H$  layer optimization requires adjustment of both refractive index and layer thickness with the optimum at around 2.6 (@ 800 nm) and 110 nm, respectively. The implementation of such a layer in c-Si/perovskite tandem cells resulted in a current gain driven by better light in-coupling into the bottom cell (thereby reducing reflection out of the cell) [24].

As a result of this simulation, it was found that implementing  $(n)nc-SiOx:H$  is beneficial for reducing the reflection at the interface of top and bottom cells. In particular the 110 nm thick  $(n)nc-SiOx:H$  leads to the best performing cell with a  $J_{imp\ tandem\ cell}$  of 20.3 mA/cm<sup>2</sup>. For higher thicknesses the cell performance starts to gradually drop since the  $J_{imp\ c-Si\ subcell}$  starts to decrease till it becomes the limiting cell for the series connection (see Fig. 5.9 for more insight).

The absorptance-wavelength graph of the cell with 110 nm  $(n)nc-SiOx:H$  is shown in Fig. 5.8. As can be seen from Fig. 5.8 the reflection dip in the wavelength range of 700-900 nm is drastically reduced. In particular, the reflection is reduced of about 1.7 mA/cm<sup>2</sup> if compared to the cell with  $(n)a-Si:H$ . This is mainly attributed to use of a  $(n)nc-SiOx:H$  layer with optimized refractive index of about 2.6 (@ 800 nm) that causes decreased reflection when placed in stack of the front ITO layer with  $n=1.7$  (@ 800 nm). Note that the  $(n)a-Si:H$  has a way higher refractive index of about  $n=3.8$  (@ 800 nm).

Driven by better light in-coupling into the bottom cell (thereby reducing reflection out of the cell) the implied photocurrent of the c-Si bottom cell increases of 1.6 mA/cm<sup>2</sup>, reaching a value of 21.3 mA/cm<sup>2</sup>. This is in agreement with what was found by Mazzarella et al. [24]. However, in terms of the implied photocurrent of the tandem cell the  $J_{imp\ tandem\ cell}$  is of 20.3 mA/cm<sup>2</sup> since in this case the perovskite top cell limits the device current.

It is also interesting to plot the tandem cell current as a function of the thickness of the  $(n)nc-SiOx:H$  as shown in Fig. 5.9 It is clear from the figure that, from the optical point of view, the cell performance is comparable for  $(n)nc-SiOx:H$  with a thickness higher than 50 nm. Therefore, for production advantages, it is recommended to deposit a  $(n)nc-SiOx:H$  layer of about 50 nm.

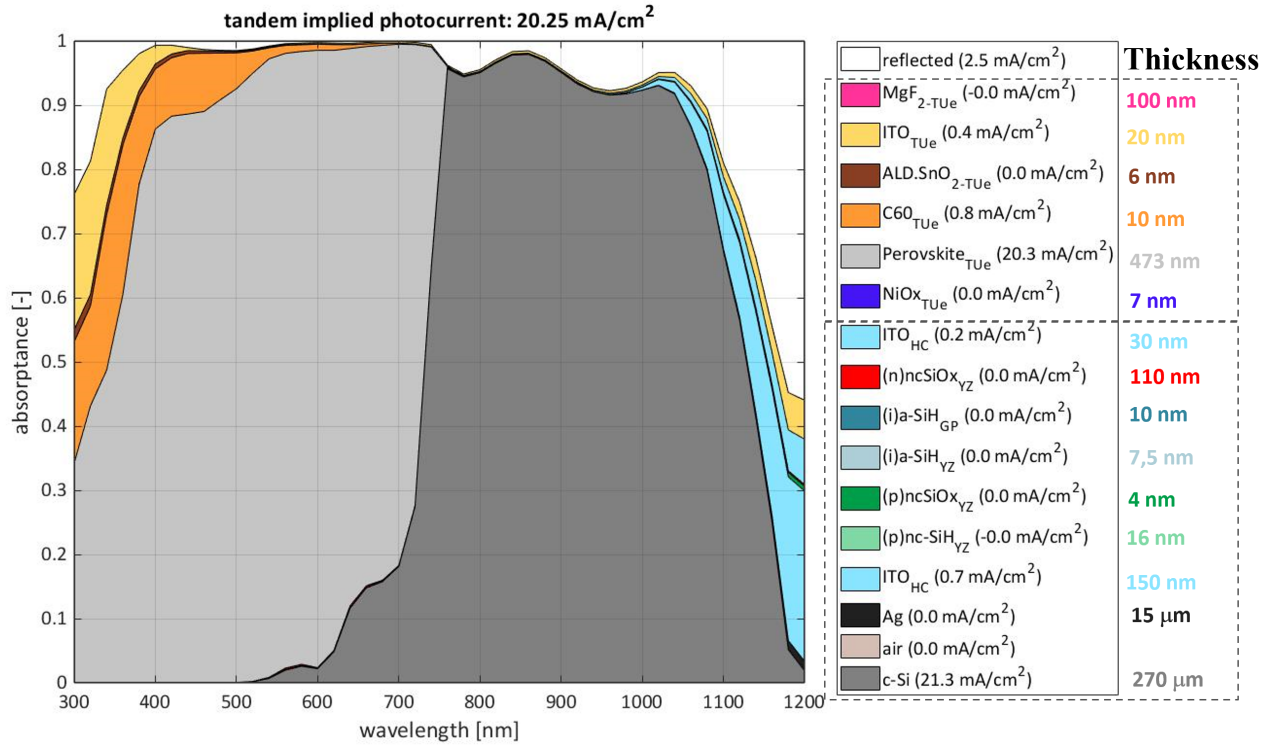


Figure 5.8: GenPro4 [128] simulations of the tandem cell with optimized MgF<sub>2</sub> (100 nm), ITO (20 nm), C<sub>60</sub> (10 nm) and (n)nc-SiOx:H (110 nm)

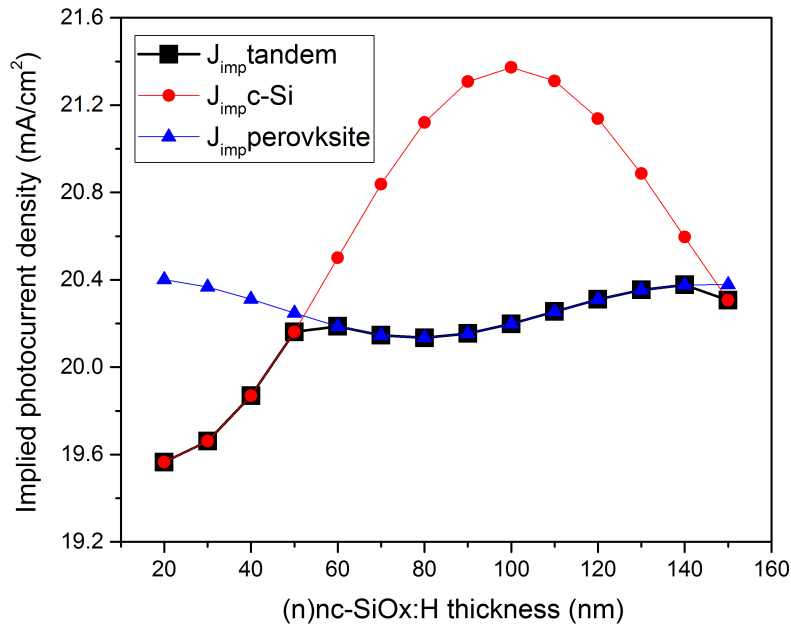


Figure 5.9: GenPro4 [128] simulated implied photocurrent of the tandem cell, c-Si and perovskite subcells as a function of the (n)nc-SiOx:H thickness

In conclusion, this optimization aimed at reducing the reflection on the front side of the SHJ bottom cell. The implementation of a (*n*)nc-SiO<sub>x</sub>:H (*n*=2.5 at 800 nm) thicker than 50 nm is effective in reducing the reflection at the interface of top and bottom cells. As a consequence, the  $J_{\text{imp-c-Si bottom cell}}$  increases to 21.1 mA<sup>2</sup>. However, the cell current is limited by the perovskite top cell to 20.3 mA/cm<sup>2</sup>. The tandem current can be even further improved if the perovskite thickness, which is the limiting subcell, is optimized. The perovskite thickness optimization is discussed in the next section.

### 5.3.4. Optimization of the perovskite thickness

As a result of the previous simulations it was clear that, for the cell with (*n*)nc-SiO<sub>x</sub>:H, the perovskite subcell limits the device current. Therefore in this simulation, the perovskite thickness was varied with the aim of increasing the perovskite current and thus improving the tandem current, due to a better current matching. The perovskite thickness has been varied between 470 and 530 nm. The upper limit of 530 nm was chosen for experimental reasons, as communicated by researchers at TU Eindhoven. The thicknesses of ITO, MgF<sub>2</sub>, C<sub>60</sub> and (*n*)nc-SiO<sub>x</sub>:H have been set to the optimized values (20 nm, 100 nm, 10 nm, 110 nm) and the thicknesses of the other layers are kept the same as the 22.2% efficiency cell.

The result of the simulation is shown in Fig. 5.10. As a result of the simulation it has been found that increasing the perovskite thickness, ideally up to 530 nm, is beneficial for the implied photocurrent density of the tandem cell. The  $J_{\text{imp tandem cell}}$  increases of about 0.3 mA/cm<sup>2</sup> reaching a value of 20.6 mA/cm<sup>2</sup>. It is also worth noticing that the  $J_{\text{imp perovskite top cell}}$  and  $J_{\text{imp c-Si bottom cell}}$  are well-matched, with values of 20.6 mA/cm<sup>2</sup> and 20.7 mA/cm<sup>2</sup> respectively.

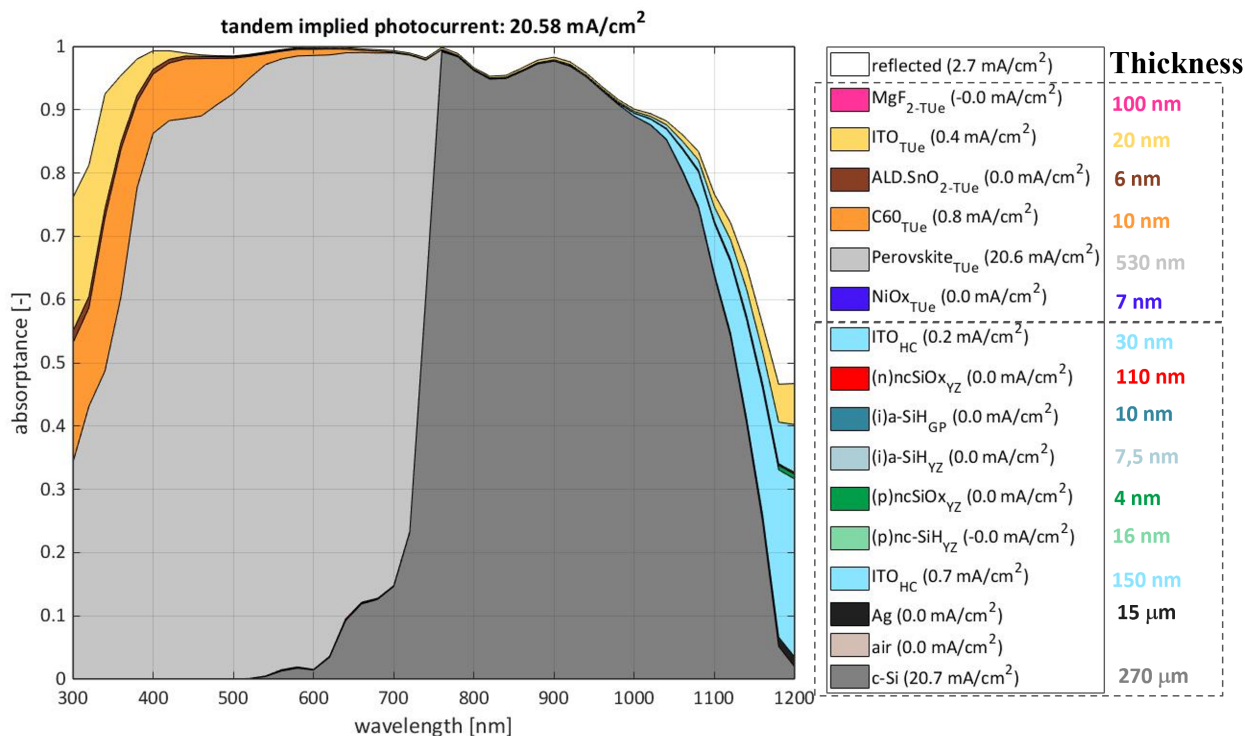


Figure 5.10: GenPro4 [128] simulations of the tandem cell with optimized MgF<sub>2</sub> (100 nm), ITO (20 nm), C<sub>60</sub> (10 nm), (*n*)nc-SiO<sub>x</sub>:H (110 nm) and perovskite (530 nm).

To conclude, this optimization aimed at finding the optimal value of the perovskite thickness in order to improve the tandem current by improving current matching. By increasing the perovskite thickness to 530 nm the  $J_{\text{imp tandem cell}}$  increases to 20.6 mA/cm<sup>2</sup> and the current matching is improved. Therefore, the suggestion would be to increase the perovskite thickness to 530 nm. It is interesting to observe that the upper limit of the perovskite thickness was limited to 530 nm for experimental reasons. However, by simulating perovskite with even higher thicknesses, it was found that depositing a perovskite layer thicker than 530 nm is not beneficial. This is due to the fact that a higher perovskite thickness lowers the  $J_{\text{imp c-Si bottom cell}}$ , which limits the tandem cell current, as shown in Fig. 5.11.

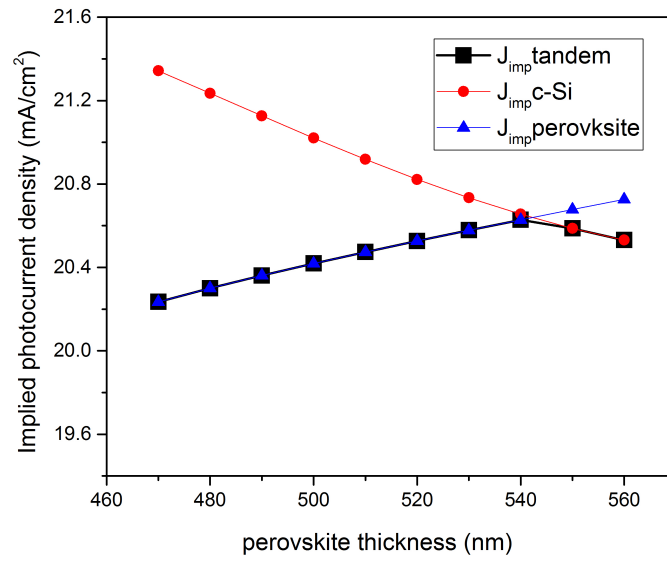


Figure 5.11: .

[GenPro4 [128] simulated implied photocurrent of the tandem cell, c-Si and perovksite subcells as a function of the perovskite thickness [for the cell with 110 nm ( $n$ )nc-SiOx:H].

As an additional note, it is also interesting to report that similar simulations were performed in the case of the cell with a 5 nm ( $n$ )a-Si:H. In this case, increasing the perovskite layer thicknesses doesn't lead to enhancement of the tandem cell performance, as can be seen in Fig. 5.12. This is due to the fact that the tandem current is limited by the c-Si bottom cell that can't reach much higher values of implied photocurrent density due to the high reflection caused by the non-optimal refractive index of the ( $n$ )a-Si:H.

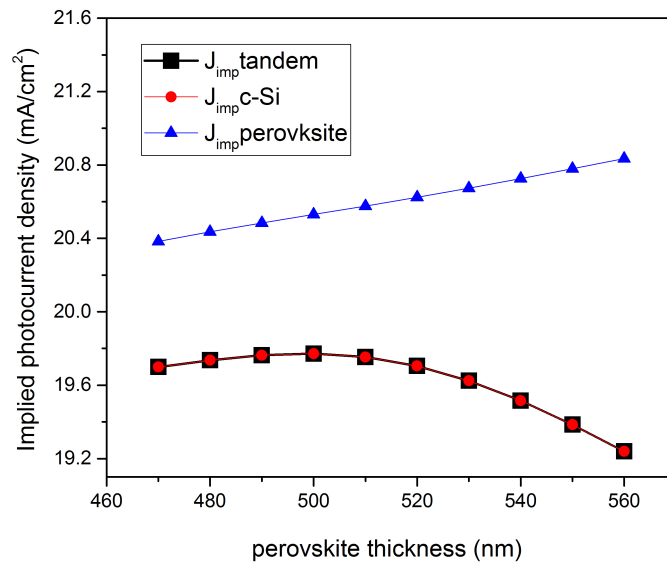


Figure 5.12: .

[GenPro4 [128] simulated implied photocurrent of the tandem cell, c-Si and perovksite subcells as a function of the perovskite thickness [for the cell with 5 nm ( $n$ )a-Si:H].

## 5.4. Summary of the guidelines to improve the tandem cell performance

In summary, starting from the optical simulation of the first fabricated 22.2% efficiency tandem cell, five main optically weak points have been identified. To overcome these limitations, numerous simulations have been conducted. As a result of the simulations, five main changes can be implemented.

The first three changes consist in fabricating a cell with optimized front anti-reflection layers and  $C_{60}$  thickness. This allows reducing the front reflection, the parasitic absorption of the front ITO and  $C_{60}$ . The suggested changes are to:

- $MgF_2$ : reduce the thickness to 100 nm
- ITO: reduce the thickness to 20 nm. In this case, it is also necessary to check whether the layer is too thin to meet the electrical requirements. If the electrical requirements are not satisfied, a proper ITO thickness should be chosen according to the contour plot obtained through the simulations as shown in Fig. 5.3.
- $C_{60}$ : reduce the thickness to 10 nm or even thinner if it's not detrimental to the device performance.

By implementing these three optimizations an improvement of  $1.8 \text{ mA/cm}^2$  with respect to the initial 22.2% tandem cell can be achieved, reaching an implied tandem photocurrent density of  $19.7 \text{ mA/cm}^2$ .

Additionally, if the 5 nm ( $n$ )a-Si:H layer is substituted with a ( $n$ )nc-SiOx:H of thickness higher than 50 nm, the reflection between the top and bottom cell is also reduced. By implementing this additional change, a total improvement of  $2.4 \text{ mA/cm}^2$  with respect to the initial 22.2% tandem cell can be achieved, reaching an implied tandem photocurrent density of  $20.3 \text{ mA/cm}^2$ .

Finally, if also a thicker perovskite layer (530 nm) is implemented, in addition to all the previous improvements also the tandem current can be enhanced by guaranteeing a better current matching. A total improvement of  $2.7 \text{ mA/cm}^2$  with respect to the initial 22.2% tandem cell can be achieved, reaching an implied tandem photocurrent density of  $20.6 \text{ mA/cm}^2$ . This value is promising since the record perovskite/c-Si tandem cell is characterized by photogenerated current densities of 19.41 and  $20.18 \text{ mA/cm}^2$  in the perovskite and silicon subcells respectively, with a measured  $J_{SC}$  of  $19.23 \text{ mA/cm}^2$  [23].



# 6

## Single-side-textured SHJ solar cells

In this chapter, the fabrication and performance of single-side-textured SHJ solar cells are discussed. In SHJ solar cells the dangling bonds of the c-Si wafer surface are passivated with (i)a-Si:H. Heterojunctions are then formed by depositing (*n*)-type and (*p*)-type Si-based thin films on both sides of (i)a-Si:H coated wafers. The doped contacts are manipulated by adding a certain amount of impurity atoms to change their electrical conductivities. This allows a successful extraction of photo-generated carriers while minimizing the carrier recombination losses by field-effect passivation. Accordingly, it is referred to as a "passivated contact" solar cell [132]. Due to a high silicon wafer quality and excellent surface passivation, SHJ solar cells reach very high conversion efficiencies with a record value of 26.7% [4] and  $V_{OC}$  values up to 750 mV [37, 40]. To produce a high-performance device both the passivating (i)a-Si:H layer and the passivating doped contacts have to be optimized to achieve efficient carrier selective collection in SHJ solar cells.

The single-side-textured SHJ solar cells can be designed with a rear emitter (RE) or a front emitter (FE) architecture. In a RJ SHJ solar cell, a stack made of an intrinsic hydrogenated amorphous silicon ((i)a-Si:H) and a (*n*)-type surface field layer is deposited on the flat front side (sunny side) of the cell, and a stack of (i)a-Si:H and (*p*)-type emitter layer is deposited on the textured rear side. In a FJ SHJ solar cell instead, the architecture is flipped: the (*p*)-type emitter is deposited on the front flat sunny side and the (*n*)-type surface field layer on the textured rear side. The architecture of both RJ and FJ single-side-textured SHJ solar cells is shown in Fig. 6.1. In general, for two-terminal (2T) tandem solar cells, RJ SHJ bottom cells with (*n*)-contact on top are preferred due to the optical advantage of the perovskite top cells with the p-i-n configuration [29]. Furthermore the cells with the highest efficiency have been produced by using p-i-n perovskite/ RJ SHJ architectures [19, 20, 23–25]. For the aforementioned reasons, this research will mainly focus on the optimization of single-side-textured RJ SHJ as bottom cells for perovskite/c-Si tandem cells. Besides a FJ SHJ solar cell has also been fabricated so that n-i-p perovskite/FE SHJ tandem cells [14, 30] can be potentially be fabricated and investigated in future researches.

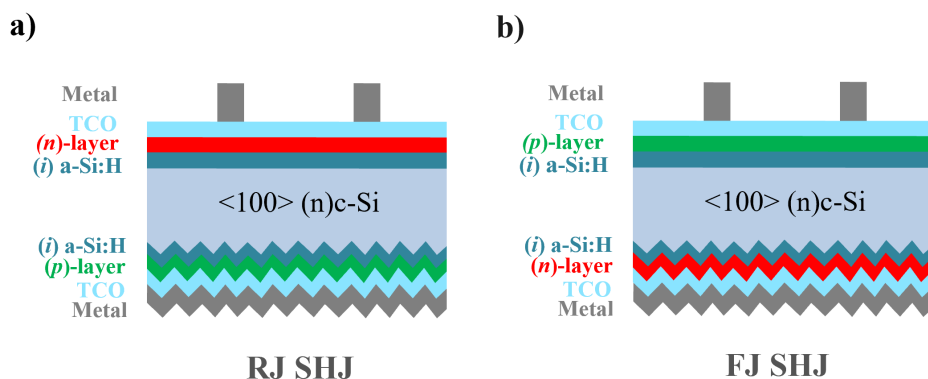


Figure 6.1: The schematic architecture of single side-textured silicon heterojunction (SHJ) solar cell: a) rear emitter (RE) SHJ; b) front emitter (FE) SHJ.

In this work, an overview of the manufacturing process of SHJ is firstly introduced. Afterward, the per-

performances of manufactured single-junctions solar cells are measured and analyzed. Both RJ and FJ SHJ solar cells have been produced and the focus is set on the optimization of (*n*)-type (for RJ SHJ) and *p*-type (for FJ SHJ) doped silicon layers on the front flat <100> SHJ side. For the textured side, previous optimizations investigated by Zhao et al. are adopted [102]. For the RJ SHJ configuration, solar cells with different (*n*)-type layers ((*n*)nc-SiO<sub>x</sub>:H; (*n*)nc-Si:H; (*n*)a-Si:H) have been fabricated. The thickness of each type of doped layer has been chosen according to the one identified as optimal in the optical simulations of the tandem cells, as discussed in chapter 5. In the case of (*n*)nc-SiO<sub>x</sub>:H a full optimization of different combinations of (i)a-Si:H/(*n*)nc-SiO<sub>x</sub>:H has been performed before SHJ cell fabrication, by symmetrically depositing different *i*/*n*-type layer stack combinations on double side flat <100> c-Si wafer. For the FJ SHJ configuration, different (i)a-Si:H/(*p*)-type layers combinations have been analyzed before the SHJ cell fabrication, with an analogous symmetrical deposition approach. After that, a FJ SHJ solar cell has been produced, measured and analyzed. Lastly also a tunnel recombination junction (TRJ) for electron collections has been investigated.

## 6.1. Fabrication process

In this section, the fabrication process of single-side-textured FBC-SHJ solar cells is explained. The pre-deposition treatments, deposition, and the main analysis and characterizations tools are discussed.

### 6.1.1. Pre-deposition treatments

The silicon wafers used for the passivation optimization are Topsil *n*-type double-side polished FZ <100> c-Si with a range of resistivity ( $3\pm 2 \Omega\text{cm}$ ) and thickness ( $280\pm 20 \mu\text{m}$ ). To fabricate single-side-textured wafers a texturing process is done on one side of the c-Si wafer. In order to do that, a 200nm-thick SiN<sub>x</sub> layer is deposited on one side of the substrate to protect one flat side from the texturing process in the TMAH solution. As a result, the non-masked side is textured by immersing the wafer in a TMAH solution, and a pyramidal textured side is obtained. Moreover, as discussed before, contamination-free and low-defect-density c-Si substrates are required for an optimal passivation performance. Thus, after texturing, a wet-chemical wafer cleaning procedure is performed as a pre-deposition treatment. The cleaning cycle for a single-side-textured wafer is repeated three times. The detailed texturing and cleaning processes are explained in chapter 3.

### 6.1.2. Depositions

The deposition process happens in the RF-PECVD just after the pre-deposition treatments are concluded and the wafer is immediately loaded into the RF-PECVD machine. The working principle of RF-PECVD is discussed in detail in chapter 3. The RF-PECVD used in this research is the so-called AMIGO PECVD (Elettorava, S.p.A.) in Else Kooi Lab (EKL) at Delft University of Technology. The deposition process is automated. The input parameters are given in the form of an excel file, where all the single process steps are inputted. For the fabrication of RJ SHJ solar cells, first *i*/*n* contact stack are deposited on the flat side and after that *i*/*p* stack are deposited on the textured side, and viceversa for FJ SHJ solar cells.

Subsequently, transparent conductive oxide (TCO) layers are deposited on both the front and rear sides of the cell precursor via a sputtering method. The working principle of sputtering is discussed in detail in chapter 3. The sputtering tool used in this research is the so-called ZORRO sputtering PECVD (Polyteknik) in Else Kooi Lab (EKL) at Delft University of Technology. Also in this case, the deposition process is automated.

When the TCO layers have been deposited, the metal contacts are added by screen printing on both front and rear sides. The working principle of sputtering is discussed in detail in chapter 3. A picture of the front side of the fabricated cell is shown in Fig. 6.2.

### 6.1.3. Analysis and characterizations

After the SHJ solar cell has been fabricated, it is analyzed with different characterization techniques. A detailed explanation of the working principle of each technique mentioned below is explained in chapter 3.

- **J-V measurement:** it is used to extract the J-V curve of the fabricated solar cell. From this curve, the most important parameters for solar-cell characterization are extracted, such as  $V_{OC}$ ,  $J_{SC}$ , FF, and  $\eta$ . Note that in this chapter, single-junction SHJ solar cells are fabricated. However, it must be taken into account that the cells are optimized to be implemented in a tandem structure, as discussed in chapter 5. Thus, the J-V measurement of single-junction SHJ solar cells mainly aims at checking the FF and  $V_{OC}$  since gain or losses in  $J_{SC}$  and efficiency should be mainly discussed with respect to tandem cells applications.

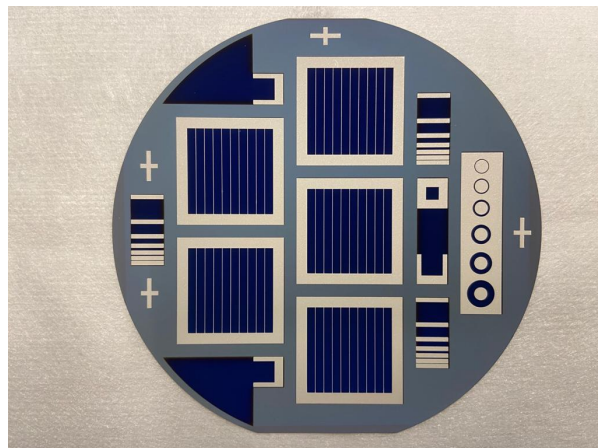


Figure 6.2: The front side of the fabricated SHJ solar cell.

- **SunsVoc measurement:** it is used to obtain a pseudo I-V curve that has no influence from the series resistance ( $R_s$ ). Two main values are extracted from this analysis:  $SunsVoc$  and  $pFF$  which give a hint on the upper limit of  $V_{OC}$  and  $FF$  and on the  $R_{s,SunsVoc}$  induced  $FF$  losses.
- **EQE measurement:** it is carried out to obtain an EQE curve. From EQE an idea of the amount of photogenerated carrier in the absorber layer (and successfully collected at the contacts) can be gained. Moreover, from the EQE measurements, a short circuit current density  $J_{sc,EQE}$  can be determined. The  $J_{sc,EQE}$  usually differs from the  $J_{sc}$  determined via a J-V measurement. Indeed,  $J_{sc,EQE}$  is independent of the spectral shape of the light source used and of the contact area of solar cells, in contrast to determining the  $J_{sc}$  via a J-V measurement. Besides, during the EQE measurement, the  $J_{sc,EQE}$  without the influence of front metal grids can be obtained.
- **UV-Vis-NIR measurement:** it is carried out to estimate the reflectance ( $R$ ) in the SHJ solar cell. After that,  $1-R$  can be plotted along with the EQE curve, and an idea of the main optical and electrical losses such as parasitic absorption and recombination losses can be gained. An example of this curve (taken from experimental results) is shown in Fig. 6.3. The black area (EQE) indicates the amount of charge carriers photogenerated in the absorber layer and successfully collected at the contacts. The grey area ( $1-R$ ) indicates the optical and electrical losses in the cell and the white area instead indicates light reflections.

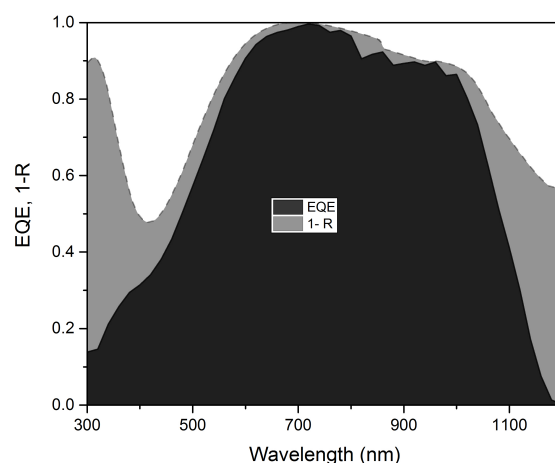


Figure 6.3: An example of EQE and 1-R plot. The black area (EQE) indicates the amount of charge carriers photogenerated in the absorber layer and successfully collected at the contacts; the grey area ( $1-R$ ) indicates the optical and electrical losses in the cell; the white area instead indicates light reflections.

## 6.2. RJ SHJ solar cells

Apart from good surface passivation, there are other key requirements that are necessary to achieve a high-efficiency SHJ solar cell. One of these is the minimization of optical losses. Reflection losses, occurring on the front sunny side of the device, are among the most relevant current losses and reduce the amount of light reaching the silicon absorber layer [133]. Parasitic absorption in the layers also causes current losses.

For RJ SHJ solar cells, the layer on the front sunny side is a ( $n$ )-type silicon-based material. In general different ( $n$ )-type layers can be used. One of the most widely used materials for front contact doped layers in SHJ solar cells is hydrogenated amorphous silicon (a-Si:H). Doped a-Si:H in SHJs are usually quite thin (usually <10 nm [43]), so parasitic absorption can be reduced. However, the photogenerated carriers have a high probability to recombine. This leads to an average photocurrent loss of about 2mA/cm<sup>2</sup> [134]. Moreover, the refractive index of a-Si:H ( $n$  @ 633 nm) is usually above 4.0 and this enhances light reflections when a front TCO of  $n$  around 2 is used. Therefore in general, the optimization of doped a-Si:H is quite challenging since it is difficult to satisfy simultaneously the optical and electrical constraints [133] due to its limited doping efficiency [135].

Alternative materials can be used to overcome the above-mentioned optical and electrical limitations of doped a-Si:H. One of the most promising materials is doped hydrogenated nanocrystalline silicon (nc-Si:H) [77, 78]. It consists of small nanocrystals embedded in an amorphous matrix. The nanocrystals act as an efficient carrier transport path [133] giving anisotropy properties in the growth direction [136]. Because of the mixed crystalline phase, the nc-Si:H film has higher doping efficiency than a-Si:H [137].

Furthermore, nc-Si:H can be alloyed with oxygen to form hydrogenated nanocrystalline silicon oxide (nc-SiO<sub>x</sub>:H), which has the advantage of having tunable optoelectronic properties due to its composite structure [133, 138, 139]. Furthermore, by introducing oxygen in the amorphous network, parasitic absorption can be further reduced [140]. The tunability of their refractive index is particularly interesting because it allows creating a stack of layers with refractive indexes that consecutively decrease from silicon to the ambient air, which reduces reflection losses [133]. Moreover, implementing a ( $n$ )nc-SiO<sub>x</sub>:H in SHJ bottom cells for 2T c-Si/perovskite tandem cells is beneficial for reducing the reflection at the interface between top and bottom cells, as demonstrated by the simulations performed in chapter 5 and by literature findings [24].

Numerous researchers have adopted ( $n$ )-doped nc-SiO<sub>x</sub>:H for RJ SHJ solar cells [133, 141], and have reported that it can lead to short-circuit current ( $J_{SC}$ ) enhancement. However, the cell performance with this oxygen alloy is still limited. Specifically, in the literature has been reported that it was difficult to obtain both high  $V_{OC}$  and FF. A high FF is indeed obtained for a prompt nucleation of nanocrystals, which reduces series resistances ( $R_S$ ) but this requires the implementation of slightly epitaxial intrinsic passivating layers which can reduce  $V_{OC}$ . In order to solve this problem, i.e guaranteeing a high FF (prompt nucleation) without using epitaxial intrinsic layers, CO<sub>2</sub> plasma treatments have been proposed [87].

In this research, multiple RJ SHJ with different ( $n$ )-type layers (( $n$ )nc-SiO<sub>x</sub>:H/( $n$ )nc-Si:H/( $n$ )a-Si:H) have been fabricated, with thicknesses chosen from the one identified as optimal according to the c-Si/perovskite tandem optical simulations (see chapter 5). The performance of each type of cell is reported and analyzed in the sections below. In particular, for ( $n$ )nc-SiO<sub>x</sub>:H a full optimization of different combinations of (i)a-Si:H/( $n$ )nc-SiO<sub>x</sub>:H layers has been performed before the SHJ cell fabrication, by symmetrically depositing different layers combinations on double side flat <100> c-Si wafer.

### 6.2.1. RJ SHJ solar cells with ( $n$ )nc-SiO<sub>x</sub>:H

In this section, the fabricated single-side-textured RJ SHJ solar cells with ( $n$ )nc-SiO<sub>x</sub>:H are measured and discussed. Before the fabrication of the devices, optimizations of the (i)a-Si:H/( $n$ )nc-SiO<sub>x</sub>:H layer stack are performed with symmetrical depositions on flat <100> c-Si surfaces. After that, the single-side-textured solar cells were fabricated with the optimized  $i/n$  combination.

#### Optimization of (i)a-Si:H/( $n$ )nc-SiO<sub>x</sub>:H combination

As it has been found in literature, it is common that the (i)a-Si:H film has to be optimized according to the film which is grown subsequently, apart from being optimized to guarantee a high  $iV_{OC}$  at the a-Si:H/c-Si interface and no epitaxial growth [87]. This is especially true when nanocrystalline doped layers are deposited on top of (i)a-Si:H as high hydrogen flow rates are used to entail the so-called hydrogen-induced crystallization [83]. It is therefore necessary to take into account the effect of this high flow of hydrogen on the underlying (i)a-Si:H layer, as too much hydrogen in the structure can induce defect creation (either at the c-Si surface, or in the remaining film) [142]. For these reasons an optimal (i)a-Si:H layer selection has to be conducted if a subsequent ( $n$ )nc-SiO<sub>x</sub>:H layer deposition is taken into account.

In this section, different (i)a-Si:H/(n)nc-SiO<sub>x</sub>:H layers' combinations have been investigated, as schematically summarized in Fig. 6.4.

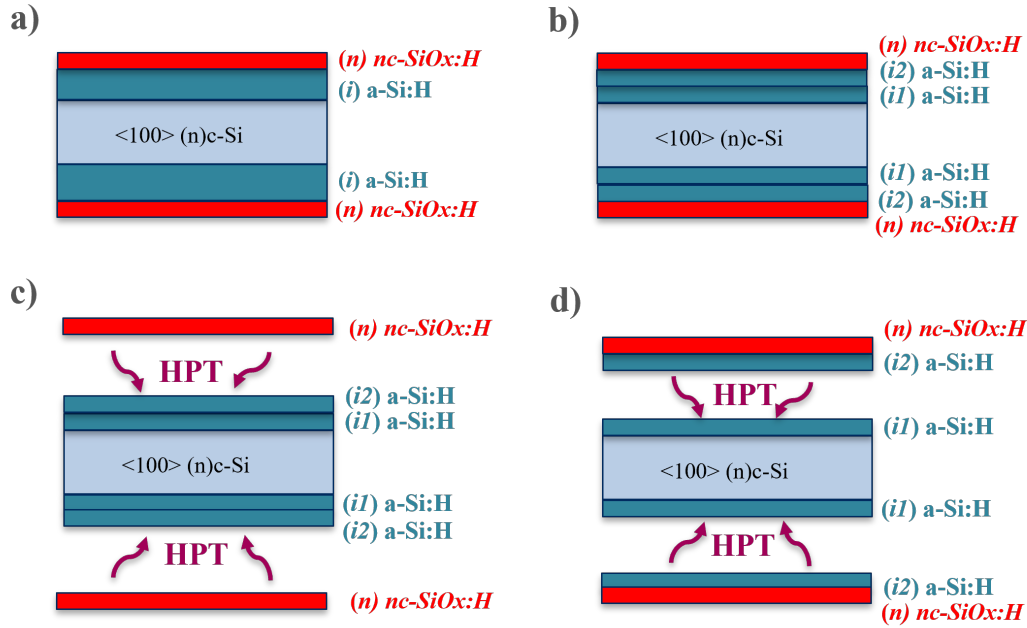


Figure 6.4: Schematic representation of symmetric deposition of (n)nc-SiO<sub>x</sub>:H layer stack on various (i)a-Si:H layer coated flat <100> c-Si surfaces. a) monolayer (i)a-Si:H; b) bilayer (i)a-Si:H; c) bilayer (i)a-Si:H with post HPT treatment; d) bilayer (i)a-Si:H with intermediate HPT treatment.

The optimization approach was to symmetrically deposit (i)a-Si:H/(n)nc-SiO<sub>x</sub>:H layers stack on double-side flat <100> c-Si wafers. Before the deposition, the double-side flat wafer is cleaned one time with the wet-chemical wafer cleaning procedure explained in chapter 3. After the symmetric deposition, the  $\tau_{\text{eff}}$ ,  $i$ -V<sub>OC</sub> of the cell precursor is measured with the photoconductance lifetime tester (see chapter 3). The deposition conditions of the (n)nc-SiO<sub>x</sub>:H layer are kept constant for all the different series (Tab. 6.1) while different (i)a-Si:H layers have been implemented: a) monolayer (i)a-Si:H; b) bilayer (i)a-Si:H; c) bilayer (i)a-Si:H with 50 seconds post HPT treatment; d) bilayer (i)a-Si:H with 20 seconds intermediate HPT treatment. They mainly differ from passivation strategy and hydrogen content and their deposition conditions are the ones previously optimized in this research, as discussed in chapter 4.

Table 6.1: Deposition parameters the (n)nc-SiO<sub>x</sub>:H deposited on top of different (i)a-Si:H layers

Layer	T substrate [°C]	Pressure [mbar]	Power density [mW/cm <sup>2</sup> ]	SiH <sub>4</sub> [sccm]	PH <sub>3</sub> [sccm]	H <sub>2</sub> [sccm]	CO <sub>2</sub> [sccm]
(n)nc-SiO <sub>x</sub> :H	180	2.1	76.4	1	1.2	100	1.6

The measured  $\tau_{\text{eff}}$ ,  $i$ -V<sub>OC</sub> for each combination is reported in Fig. 6.5.

As can be observed from Fig. 6.5 a drop of  $i$ -V<sub>OC</sub> to 689 mV was observed after depositing (n)nc-SiO<sub>x</sub>:H on (i)a-Si:H obtained via bilayer + intermediate HPT approach. This can be ascribed to the deterioration of the passivation qualities to possible excessive H incorporation during the (n)nc-SiO<sub>x</sub>:H deposition. A similar result is observed for the deposition of (n)nc-SiO<sub>x</sub>:H on (i)a-Si:H obtained via bilayer + post HPT approach, and also in this case it is assumed to be due to too high hydrogen content. Indeed a subsequent deposition of nanocrystalline material, with a high H flow, can be comparable to an additional HPT. Instead after the deposition of (n)nc-SiO<sub>x</sub>:H on both monolayer (i)a-Si:H and bilayer (i<sub>1</sub> + i<sub>2</sub>)a-Si:H  $\tau_{\text{eff}}$  is increased to 5.5 ms and 5.9 ms respectively. This may be because that they have lower H-content as compared to the combined (i)a-Si:H + HPT approach. The deposition of (n)nc-SiO<sub>x</sub>:H can also improve passivation similarly to a HPT, since the diffusion of H to the a-Si:H/c-Si interface can be beneficial for the passivation of dangling bonds.

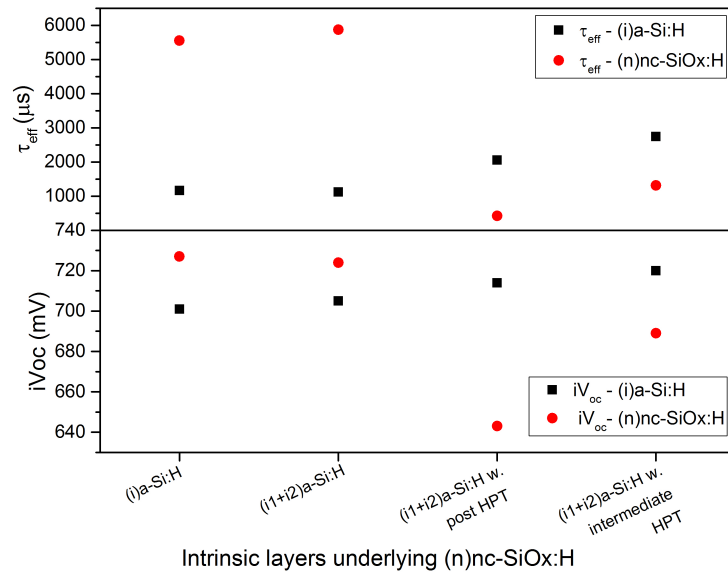


Figure 6.5:  $\tau_{\text{eff}}$  and  $iV_{\text{OC}}$  for each set of combination of (i)a-Si:H/(n)nc-SiOx:H stack on flat <100> coated c-Si surfaces. Set 1) monolayer (i)a-Si:H; Set 2) bilayer (i)a-Si:H; Set 3) bilayer (i)a-Si:H with post HPT treatment; Set 4) bilayer (i)a-Si:H with intermediate HPT treatment.

To summarize, the best combination is found to be (i<sub>1</sub> + i<sub>2</sub>)a-Si:H/(n)nc-SiOx:H and it results in improved  $\tau_{\text{eff}}$  (5.8 ms) and  $iV_{\text{OC}}$  (724 mV) in combination with doped layers. Thus in case of (n)nc-SiOx:H emitter the optimal (i)a-Si:H is different than the best layer found for (i)a-Si:H layer optimization only. This is because the effect of the deposition conditions of the (n)-type layer has to be taken into account, especially the high hydrogen content.

### RJ SHJ solar cells with (n)nc-SiOx:H - results

After having identified the optimal the (i)a-Si:H/(n)nc-SiOx:H combination, it has been implemented on the flat side of a single-side-textured SHJ solar cell. For the i/p layers deposited on the textured side, the deposition conditions optimized previously by Y. Zhao have been adopted[102]. The schematic of single-side-textured RJ SHJ cell fabricated with (n)nc-SiOx:H is shown in Fig. 6.6.

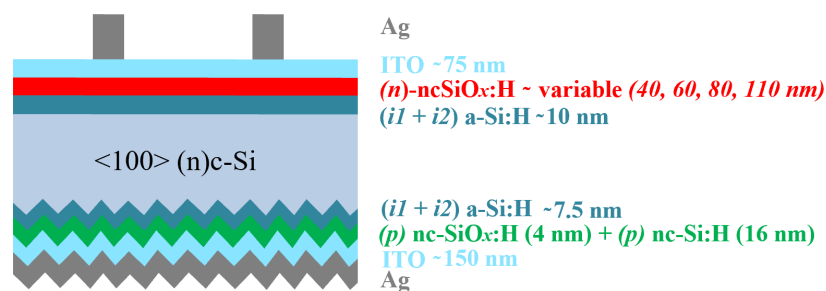


Figure 6.6: Schematic representation the fabricated single-side-textured RJ SHJ solar cell with (n)nc-SiOx:H.

In the optical simulations chapter (chapter 5), the tandem cell current as a function of the thickness of the (n)nc-SiOx:H layer in the SHJ solar cell was analyzed (Fig. 5.9). It was found that, from the optical point of view, the tandem cell performance is comparable for (n)nc-SiOx:H layers with a thickness higher than 50 nm. Therefore, for production advantages of tandem cells, it was recommended to deposit a (n)nc-SiOx:H layer of about 50 nm. In this research, cells with different (n)nc-SiOx:H thicknesses (40, 60, 80, 110 nm) have been produced to test if they lead to high-quality single-side-textured SHJ solar cells mainly in terms of  $V_{\text{OC}}$  and FF.

The resulting J-V parameters of each solar cell are reported in Fig. 6.7.

It can be observed from Fig. 6.7 that the RJ SHJ solar cells with different (*n*)nc-SiOx:H thicknesses have different performances.

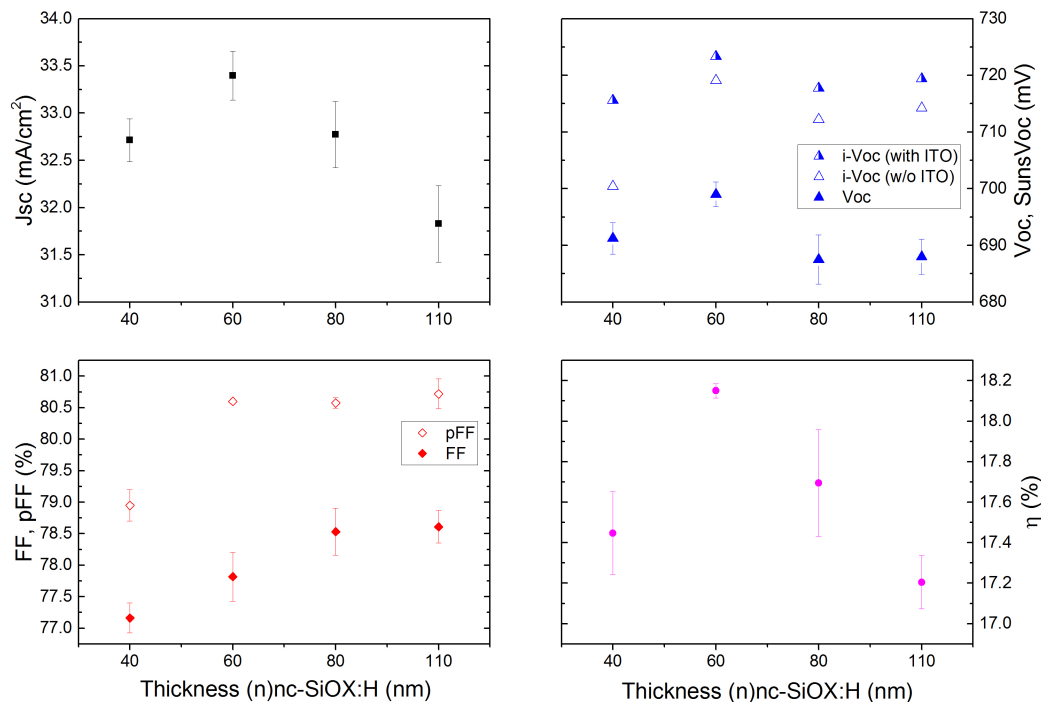


Figure 6.7: The J-V parameters of single-side-textured RJ SHJ cell with different (*n*)nc-SiOx:H thicknesses.

First, a discussion of the FF and  $V_{OC}$  is done, as this research focuses mainly on the evaluation of these values. The highest  $V_{OC}$  is obtained for the cell with 60 nm (*n*)nc-SiOx:H (699 mV) and the lowest for the cell with 80 and 110 nm (*n*)nc-SiOx:H (around 688 mV). Considering the rather slow deposition rate of (*n*)nc-SiOx:H, the lower  $V_{OC}$  can be ascribed to the effect of prolonged deposition of (*n*)-type layer which can have an analogous effect to a thermal treatment that might induce defect generations at the c-Si/(i)a-Si:H interface [143]. The rather low  $V_{OC}$  ( $< 700$  mV) for the whole thickness series can also be partially ascribed to the screen printing process, which substantially deteriorates the  $V_{OC}$  as can be seen from the comparison of the  $i-V_{OC}$  (with ITO) of the cell precursors and the final  $V_{OC}$  of the screen printed solar cells which is about 25 to 30 mV.

The different FFs can be explained with the  $iFF$  and  $R_{S_{SunsVoc}}$  values obtained for each sample are reported in Tab 6.2. Note that the  $R_{S_{SunsVoc}}$  is computed according to the formula reported in section 3.2.5. The cell with 40 nm (*n*)nc-SiOx:H has the lowest FF (77.1 %) which can be mainly ascribed to low  $iFF$  (79.4 %) since  $R_{S_{SunsVoc}}$  are around  $0.45 \Omega\text{cm}^2$ , and are considered to be low [144]. Instead, for the cell with 60, 80 and 110 nm (*n*)nc-SiOx:H the FFs are respectively 77.8 %, 78.5 %, and 78.6 %. From Tab. 6.2 it can be noticed that their  $iFF$ s are comparable, but  $R_{S_{SunsVoc}}$  is slightly higher for the cell with 60 nm which explains the lower FF. The series resistances and low  $iFF$  could be ascribed to the not fully nanocrystalline nature of the first nanometers of the (*n*)nc-SiOx:H layer and to the poor contact to the front TCO [88, 90]. A strategy to overcome this could be to improve a prompt nanocrystals nucleation for example through a  $\text{CO}_2$  plasma treatment [87].

Table 6.2:  $iFF$ , FF, pFF and  $R_{S_{SunsVoc}}$  of single-side-textured RJ SHJ cell with different (*n*)nc-SiOx:H thicknesses.

( <i>n</i> )-type contact	$iFF$ (w/o TCO) [%]	$iFF$ (with TCO) [%]	FF [%]	pFF [%]	$R_{S_{SunsVoc}}$ [ $\Omega\text{cm}^2$ ]
( <i>n</i> )nc-SiOx:H (40 nm)	79.7	79.4	77.1	78.9	$0.45 \pm 0.06$
( <i>n</i> )nc-SiOx:H (60 nm)	81.2	81.6	77.8	80.6	$0.60 \pm 0.09$
( <i>n</i> )nc-SiOx:H (80 nm)	81.3	81.5	78.5	80.6	$0.49 \pm 0.07$
( <i>n</i> )nc-SiOx:H (110 nm)	81.6	81.8	78.6	80.7	$0.54 \pm 0.05$

The highest average  $J_{SC}$  is obtained for the cell with 60 nm ( $n$ )nc-SiOx:H (33.4 mA/cm<sup>2</sup>). The lowest average  $J_{SC}$  value (31.8 mA/cm<sup>2</sup>) is obtained using a 110 nm ( $n$ )nc-SiOx:H layer. For the other cells with a 40 nm and 60 nm thick ( $n$ )nc-SiOx:H layer is around 32.7 mA/cm<sup>2</sup>.

The cell with 60 nm ( $n$ )nc-SiOx:H is the most efficient ( $\eta = 18.2\%$ ), which can be mainly ascribed to a higher  $J_{SC}$  and  $V_{OC}$ . The lowest efficiency is obtained for the cell with the 110 nm ( $n$ )nc-SiOx:H layer ( $\eta = 17.2\%$ ), again probably due to a lower  $J_{SC}$  and  $V_{OC}$ . Instead, the efficiency is around 17.4% and 17.7% for the cells with a 40 and 80 nm ( $n$ )nc-SiOx:H layer respectively.

In order to explain the differences in  $J_{SC}$ , various EQE and reflectance (R) measurements of each cell have been performed and are shown in Fig. 6.9. Moreover, optical simulations of the single-junction SHJ solar cells have been performed with the GenPro4 software [128]. Note that the shape of the simulated absorptance-wavelength graphs (shown in Fig. 6.10) are in agreement with the experimentally measured EQE curves.

The simulated implied photocurrent density of the SHJ solar cell, the reflection losses and parasitic absorption are plotted as a function of the ( $n$ )nc-SiOx:H thickness as shown in Fig. 6.8. It can be observed that from the optical point of view the cell with 60 nm ( $n$ )nc-SiOx:H has minimum reflection losses and higher implied photocurrent density if compared to cells with thicker ( $n$ )nc-SiOx:H layers. Moreover, for ( $n$ )nc-SiOx:H thicker than 60 nm, both higher reflection loss and further increased parasitic absorption of ( $n$ )nc-SiOx:H limit the SHJ cell performance. The optical advantages of a 60 nm ( $n$ )nc-SiOx:H contribute to a higher  $J_{SC}$  in single-junction RJ SHJ solar cells. However, it is good to remark that gain and losses in  $J_{SC}$  should be mainly discussed with respect to tandem cells applications, and the optimized ( $n$ )nc-SiOx:H thickness for the tandem cell from the optical point of view was identified and discussed in chapter 5.

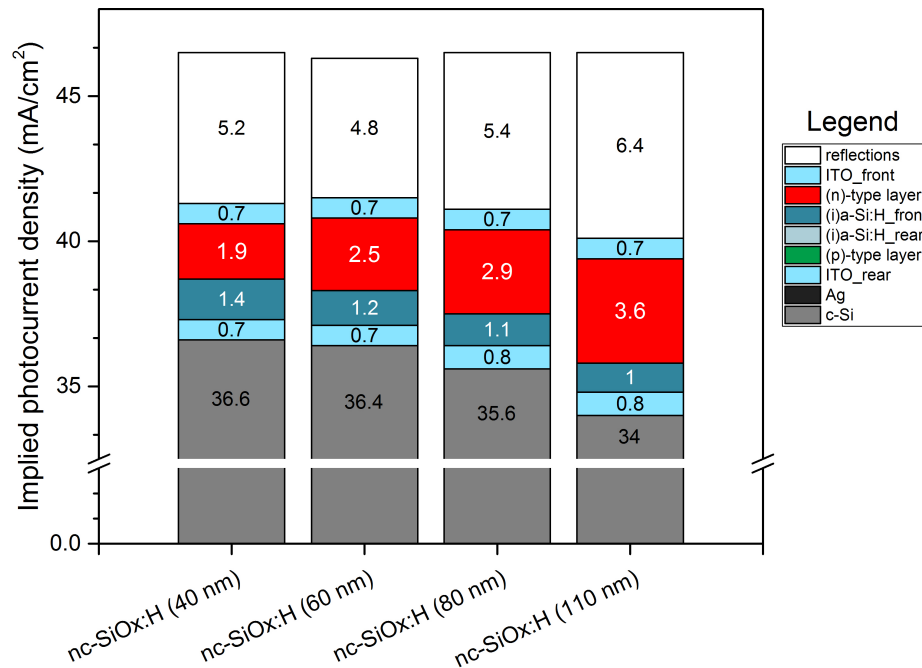


Figure 6.8: The simulated implied photocurrent density, reflection losses and parasitic absorptions of RJ SHJ with different ( $n$ )nc-SiOx:H thicknesses. GenPro4 [128].

In conclusion, 60 nm seems to be the optimal thickness of the ( $n$ )nc-SiOx:H layer in a RJ SHJ, since it results in the highest  $V_{OC}$  and quite good FF. However, it is good to note that the performances of SHJ RJ with varying ( $n$ )nc-SiOx:H thicknesses are quite comparable and all the cells with a ( $n$ )nc-SiOx:H thicker than 50 nm could be used as efficient bottom cells for tandem devices, with average  $V_{OC}$ s ranging from 688 to 699 mV and average FFs from 77.8% to 78.6%. Taking into account production advantages, optical advantages and cell performance, it is recommended to deposit a cell with a ( $n$ )nc-SiOx:H layer with a thickness of 60 nm.

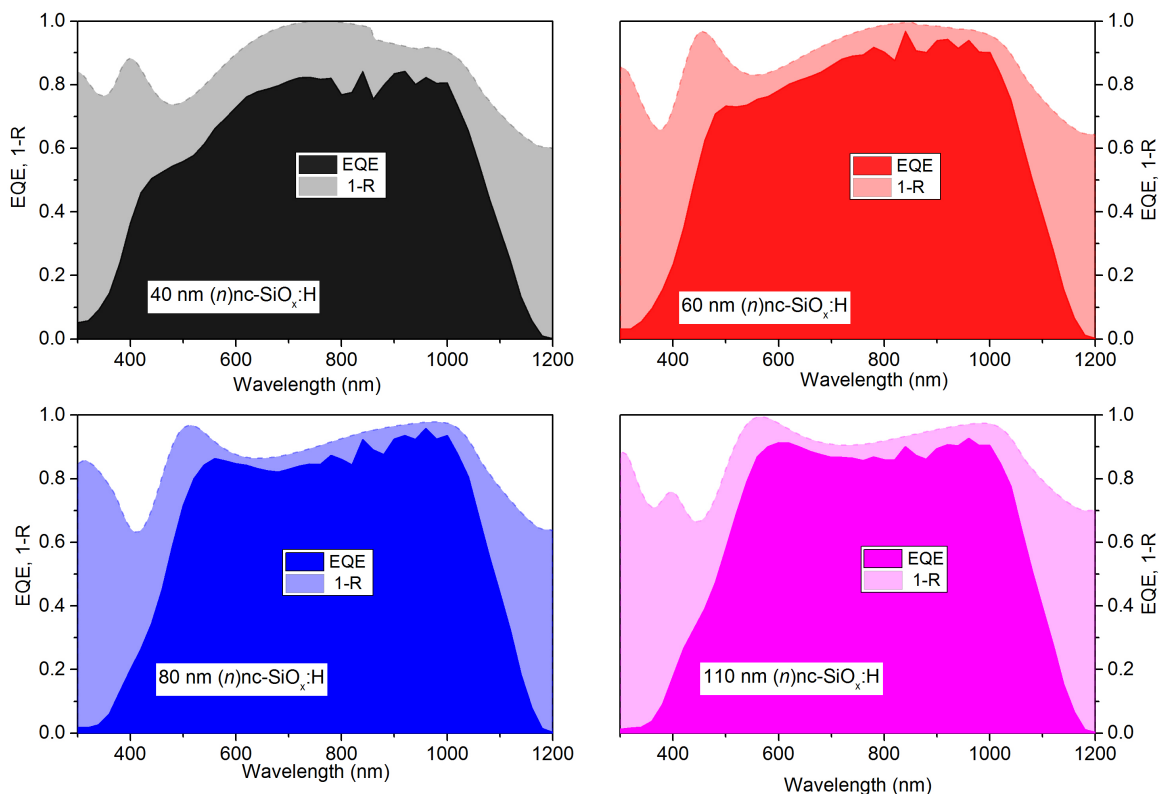


Figure 6.9: The experimentally measured EQE and 1-R curves of single-side-textured RJ SHJ cells with different  $(n)nc-SiO_x:H$  thicknesses.

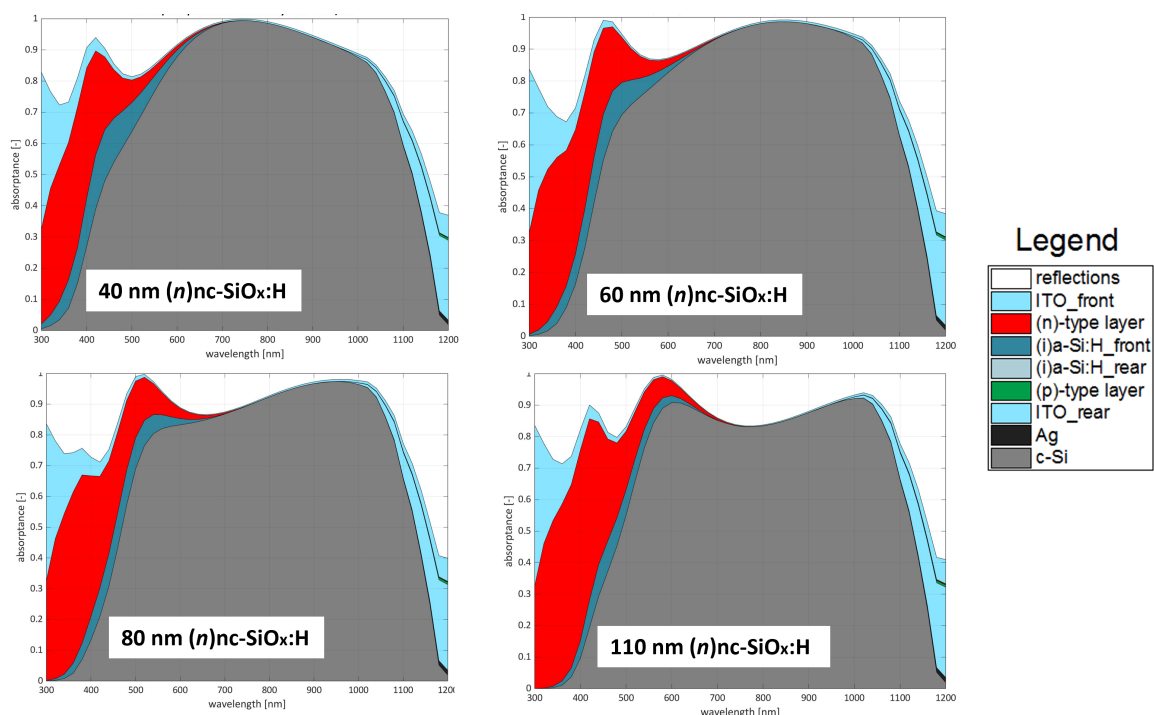


Figure 6.10: The simulated implied photocurrent density, reflection losses and parasitic absorption of RJ SHJ with different  $(n)nc-SiO_x:H$  thicknesses. GenPro4 [128].

### 6.2.2. RJ SHJ solar cells with different types of (*n*)-type layers

After having found the optimal (i)a-Si:H/(*n*)nc-SiO<sub>x</sub>:H combination and having tested the effect of (*n*)nc-SiO<sub>x</sub>:H thickness on the single-side-textured SHJ solar cell performance, different types of (*n*)-layers have been investigated and compared. In this section, RJ SHJ solar cells with the following (*n*)-type layers deposited on the flat side are fabricated. The chosen thickness for each layer is the one identified as optimal in the tandem cell simulations chapter (chapter 5):

- (*n*)a-Si:H - 5 nm
- (*n*)nc-Si:H - 20 nm
- (*n*)nc-SiO<sub>x</sub>:H - 60 nm (this thickness has been chosen as it resulted to be the best performing both optically and electrically, as discussed in the previous section)

A schematic of the three cells is shown in Fig. 6.11 with changing (*n*)-type layers a),b) and c). Note that for each cell, the same layers are used except for the (*n*)-type layer.

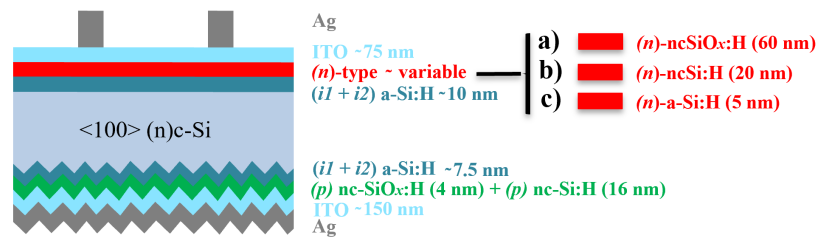


Figure 6.11: Schematic representation the fabricated single-side-textured RJ SHJ solar cell with a) 60 nm (*n*)nc-SiO<sub>x</sub>:H; b) 20 nm (*n*)nc-Si:H; c) 5 nm (*n*)a-Si:H

The resulting J-V parameters of each solar cell are reported in Fig. 6.12.

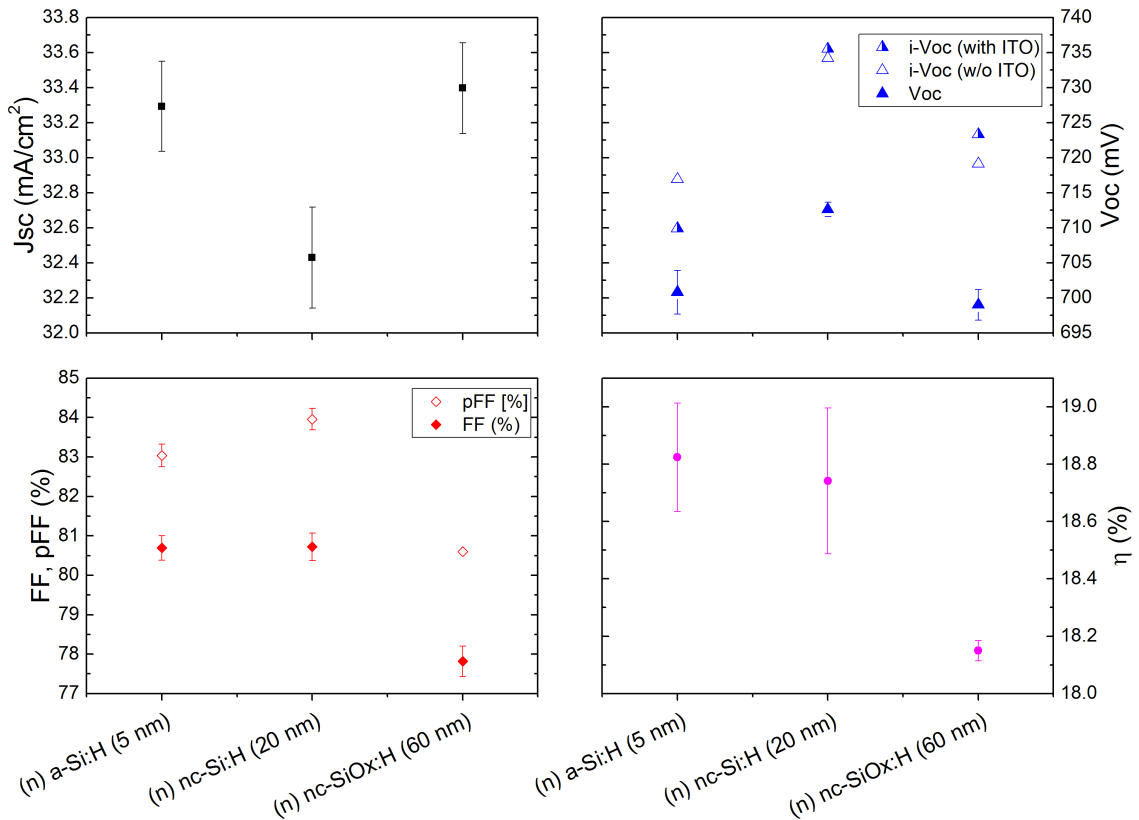


Figure 6.12: The J-V parameters of single-side-textured RJ SHJ cell with different (*n*)-type layers.

Again the main focus is set on investigating  $V_{OC}$  and FF of the cell. The average  $V_{OC}$  is above 700 mV for the cells with ( $n$ )a-Si:H and ( $n$ )nc-Si:H and is 699 for the cell with ( $n$ )nc-SiOx:H. The highest  $V_{OC}$  is obtained for the cell with ( $n$ )nc-Si:H, reaching about 712 mV. This can be ascribed to the higher  $iV_{OC}$  ( $iV_{OC}$  with ITO) of the cell precursor with ( $n$ )nc-Si:H than the  $iV_{OC}$  of the cell precursor with ( $n$ )a-Si:H. This can be due to a beneficial H incorporation during the high-H-flow ( $n$ )nc-Si:H deposition, which can act as an additional hydrogen plasma treatment on the intrinsic layer, increasing its passivation quality due to higher hydrogen incorporation [145, 146]. For nc-SiOx:H instead, a lower  $iV_{OC}$  can be explained by the fact that it has a slow deposition (due to low deposition rate) which, as explained before in section 6.2.1, can generate defects at the c-Si/(i)a-Si:H interface due to the prolong thermal treatment [143]. It is also interesting to note that the  $iV_{OC}$  of the sample with ( $n$ )a-Si:H. This may be due to the very low thickness of the ( $n$ )a-Si:H layer which makes the damage of the hydrogenated amorphous/crystalline silicon interface passivation during TCO deposition [96] easier.

The FF of the cell fabricated with ( $n$ )a-Si:H and ( $n$ )nc-Si:H that both have an average value of 80.6 %, while the FF of the cell with 60 nm ( $n$ )nc-SiOx:H has a lower FF of about 77.8%. The iFFs and  $R_{S_{SunsVoc}}$  of each sample are reported in Tab. 6.3. The sample with ( $n$ )nc-Si:H has the highest value of iFF (85.2 %) but also the highest value of  $R_{S_{SunsVoc}}$  ( $0.82 \Omega cm^2$ ) which have been proven to reduce the FF [144]. The sample with ( $n$ )a-Si:H instead has a lower iFF but also a lower  $R_{S_{SunsVoc}}$  if compared to ( $n$ )nc-Si:H. For this balance between iFF and  $R_s$ , the final FF of the two samples with ( $n$ )a-Si:H and ( $n$ )nc-Si:H is comparable. Instead the low FF of the sample with ( $n$ )nc-SiOx:H is mainly due to a low iFF as already explained before in section 6.2.1

The higher FF of the cell with ( $n$ )nc-Si:H if compared to the cell with ( $n$ )nc-SiOx:H can be related to the presumed higher c-Si/(i)a-Si:H surface damage induced by the prolonged deposition of the oxidic layer, as explained before (as the main reason for different  $V_{OC}$ ). In return, this defective interface and deteriorated passivation quality might also negatively affect the FF, as found by Zhao et al. [127]. It is also interesting to note that the  $R_s$  of the cell with ( $n$ )nc-Si:H are slightly higher than the  $R_{S_{SunsVoc}}$  of the ( $n$ )nc-SiOx:H. This can be ascribed to a more prompt nucleation of the oxidic layer due to the presence of  $CO_2$  in the plasma gas mixture, which can act similarly to a  $CO_2$  treatment, positively affecting the initial stage of the crystalline formation [87].

Table 6.3: iFF, FF, pFF and  $R_{S_{SunsVoc}}$  of single-side-textured RJ SHJ cell with different ( $n$ )-type contacts.

<b>(<math>n</math>)-type contact</b>	<b>iFF (w/o TCO)</b>	<b>iFF (with TCO)</b>	<b>FF</b>	<b>pFF</b>	<b><math>R_{S_{SunsVoc}}</math></b>
	<b>[%]</b>	<b>[%]</b>	<b>[%]</b>	<b>[%]</b>	<b><math>[\Omega cm^2]</math></b>
( $n$ )a-Si:H (5 nm)	83.9	82.8	80.7	83.0	$0.55 \pm 0.02$
( $n$ )nc-Si:H (20 nm)	84.9	85.2	80.7	83.9	$0.78 \pm 0.05$
( $n$ )nc-SiOx:H (60 nm)	81.2	81.6	77.8	80.6	$0.60 \pm 0.09$

The highest  $J_{SC}$  is obtained for the cells made with ( $n$ )nc-SiOx:H and ( $n$ )a-Si:H (around  $33.3 mA/cm^2$ ) and instead is lower for the cells made with ( $n$ )nc-Si:H ( $32.4 mA/cm^2$ ).

The efficiency is quite comparable for all the cells. The average  $\eta$  is 18.2 % for the cell with ( $n$ )nc-SiOx:H and about 18.8 % for the two other cells. The lower efficiency for the ( $n$ )nc-SiOx:H cell is probably mainly attributed due to a lower FF.

In order to explain the differences in  $J_{SC}$ , various EQE and reflectance (R) measurements of each cell have been performed (shown in Fig. 6.13). Moreover, optical simulations of the single-junction SHJ solar cells have been performed with the GenPro4 software [128]. It is interesting to note that the shape of the simulated absorptance-wavelength graphs (shown in Fig. 6.14) are in agreement with the experimentally measured EQE.

The simulated implied photocurrent density, parasitic absorptions, and reflections for the three cells with different ( $n$ )-layers are reported in Fig. 6.15. According to the optical simulations, the cell with ( $n$ )nc-SiOx:H has the highest implied photocurrent density, due to a reduced reflection in the wavelength range of 700-900 nm, which is in agreement with the experimental results. Instead, for the cell with ( $n$ )a-Si:H and ( $n$ )nc-Si:H the simulated implied photocurrent density is comparable, due to a similar balance between reflections and parasitic absorption:

- SHJ cell with ( $n$ )a-Si:H: it has a high reflection ( $8 mA/cm^2$ ) and low parasitic absorption related to the ( $n$ )a-Si:H ( $0.9 mA/cm^2$ ).
- SHJ cell with ( $n$ )nc-Si:H: it has a lower reflection ( $6.6 mA/cm^2$ ) but a higher parasitic absorption related to the ( $n$ )nc-Si:H ( $2.2 mA/cm^2$ ).

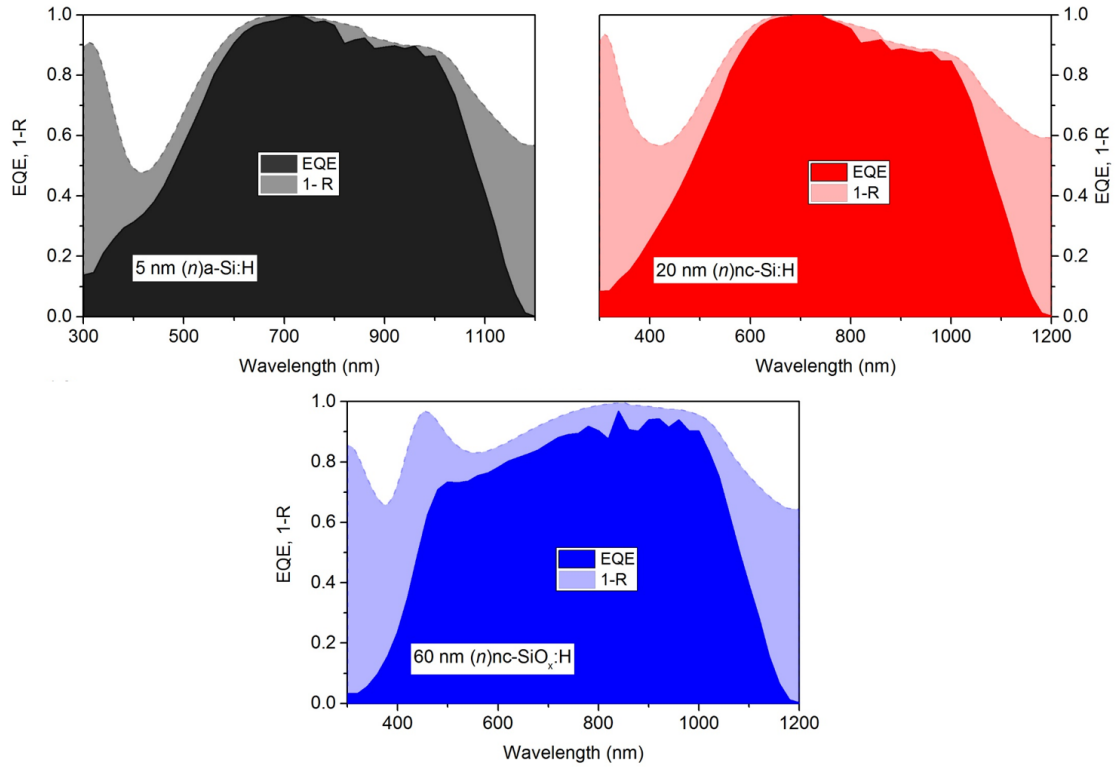


Figure 6.13: The experimentally measured EQE and 1-R curves of single-side-textured RJ SHJ cells with different (n)-type layers.

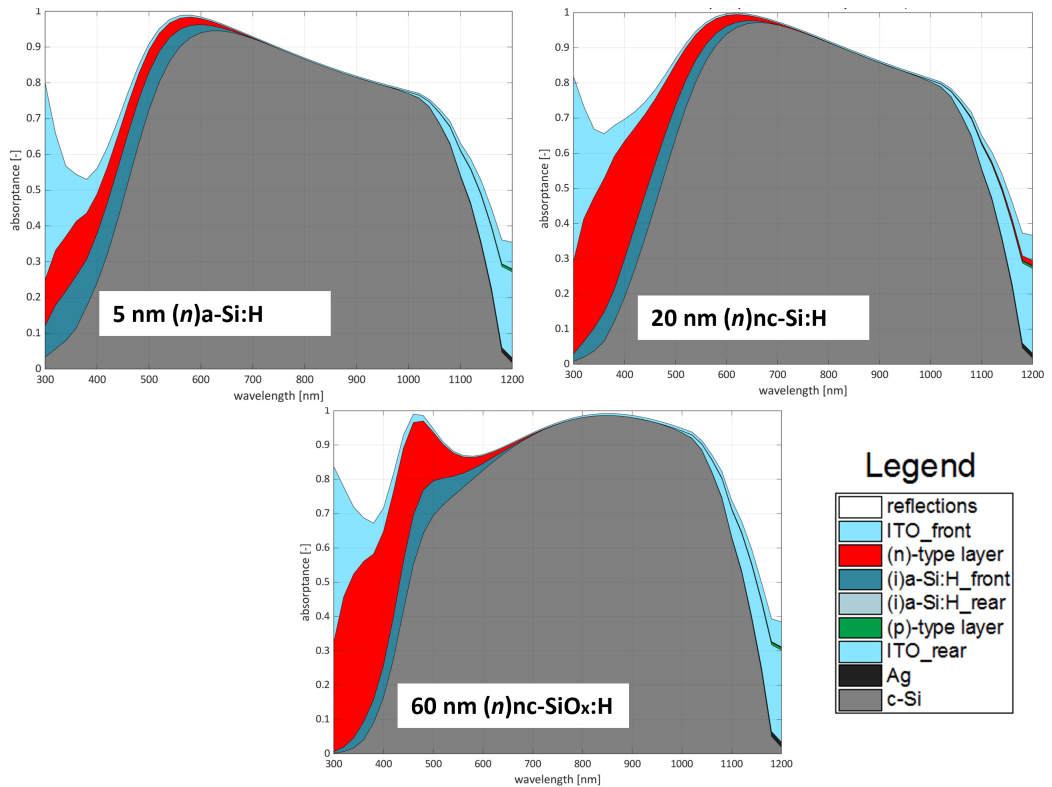


Figure 6.14: The simulated single-side-textured RJ SHJ cells with different (n)-type layers with GenPro4 software [128].

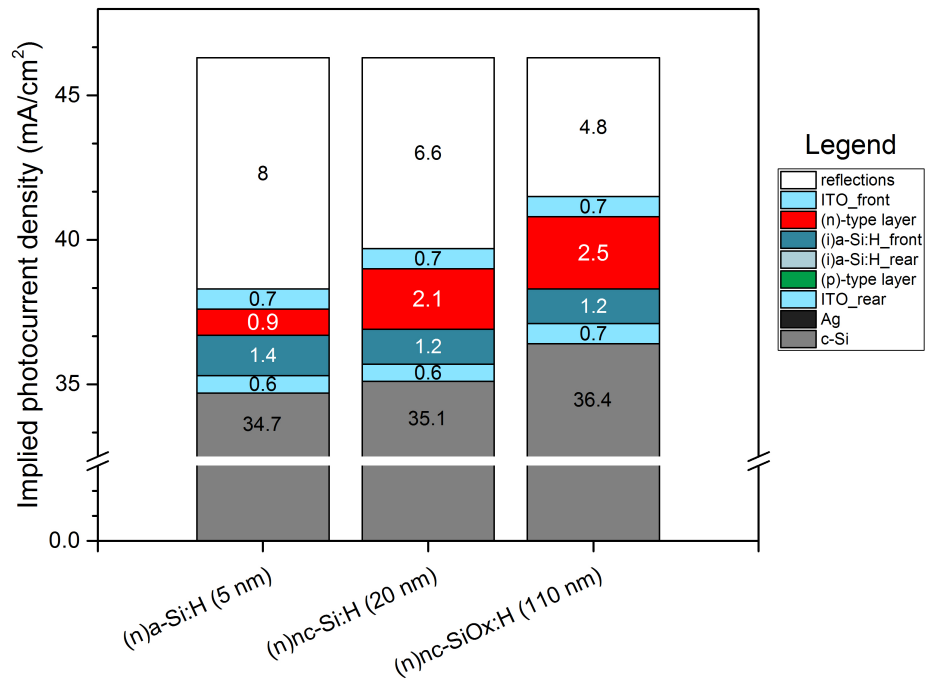


Figure 6.15: The simulated implied photocurrent density, reflection losses and parasitic absorptions of RJ SHJ with different ( $n$ )-type layers. GenPro4 [128].

In conclusion, all the RJ SHJ cells fabricated with different ( $n$ )-type layers have a quite good performance and can be efficiently used as bottom cell for tandem structures.

### 6.3. FJ SHJ solar cells

In general, for two-terminal (2T) tandem solar cells, RJ SHJ bottom cells with (*n*)-contact on top are preferred due to the optical advantage of the perovskite top cells with the p-i-n configuration [29]. However, it should be noted that also few n-i-p perovskite/FE SHJ tandem cells with quite modest efficiencies have been fabricated and reported in the literature [14, 30]. In this research also single-side-textured FJ SHJ are investigated, their performance is tested to check their applicability as bottom cells for tandem devices.

For FJ SHJ solar cell, a (*p*)-type silicon-based semiconductor material is deposited on the top flat sunny c-Si SHJ side. In general, the application of (*p*)a-Si:H for hole collection is challenging because of its high parasitic absorption [134] and moderate doping efficiency [135, 147]. This leads to limitation of the FF and  $V_{OC}$  of the device, due to constraints on the energy alignment for charge carrier transport from c-Si bulk to the ITO [148]. In particular, it is reported in the literature that efficient (*p*)-type contacts are characterized by low activation energy ( $E_a$ ) (higher doping efficiency), which should narrow the space charge region and enhance the selectivity of holes [149]. Hydrogenated nanocrystalline silicon oxide ((*p*)nc-SiOx:H) layers have been proposed as a beneficial carrier transport layer due to their tunable optoelectronic properties (e.g  $E_a$  and bandgap) that can allow obtaining efficient carriers' transport [127, 150]. To further improve the hole-selective transport, a layer stack of (*p*)nc-SiOx:H and (*p*)nc-Si:H can be implemented [149]. The (*p*)-bilayer stack, apart from having optical advantages over the standard doped a-Si:H layer [90], minimizes the transport losses. This happens because it combines a (*p*)nc-SiOx:H layer with a wide  $E_g$  which preserves the passivation quality and improves the hole accumulation at the c-Si/(i)a-Si:H interface and a (*p*)nc-Si:H with a low  $E_a$  that enhances the charge transport from (*p*)-type layer to ITO. It is important to note that for the (*p*)nc-SiOx:H prompt nucleation of nanocrystals is required for its implementation into SHJ solar cells featuring an (i)a-Si:H passivation layer, thus achieving a low  $E_a$  (*p*)-contact close to the c-Si/(i)a-Si:H interface [127].

In this research, a FJ SHJ with a (*p*)-bilayer stack [4 nm (*p*)nc-SiOx:H + 16 nm (*p*)nc-Si:H] deposited on the front flat side has been fabricated. The performance of this cell is reported and analyzed in the sections below. Initially different (*p*)-bilayer/(i)a-Si:H layers stacks have been analyzed before the SHJ cell fabrication, by symmetrically depositing different layers combinations on double side flat <100> c-Si wafer. Specifically, the (*p*)-bilayer is kept constant, and different underlying (i)a-Si:H layers are tested. After having identified the optimal (i)a-Si:H/(*p*)-bilayer combination, it is used to fabricate a FJ SHJ solar cell which has been measured and analyzed.

#### Optimization of (i)a-Si:H/(*p*)-bilayer combination

For the deposition of the (*p*)-bilayer contact, a quite high hydrogen flow rate is used to entail the so-called hydrogen-induced crystallization [83], and its effect on the underlying (i)a-Si:H layer has to be taken into account. Therefore also in this case an optimal (i)a-Si:H layer selection has to be conducted. Similar to what was done previously, also for (*p*)-bilayer structure different underlying (i)a-Si:H passivating layers have been tested, as schematically shown in Fig. 6.16.

The i/p combination optimization approach was to symmetrically deposit (i)a-Si:H/(*p*)-bilayer stacks on double-side flat <100> c-Si wafers. Before deposition, the double-side flat wafer is cleaned one time with the wet-chemical wafer cleaning procedure explained in chapter 3. After the symmetric deposition, the  $\tau_{eff}$ ,  $i-V_{OC}$  of the cell precursor is measured with the photoconductance lifetime tester (see chapter 3). The deposition conditions of the (*p*)-bilayer [4 nm (*p*)nc-SiOx:H + 16 nm (*p*)nc-Si:H] are kept constant for all the different series (Tab. 6.4) while different (i)a-Si:H layers have been implemented: monolayer (i)a-Si:H; bilayer (i)a-Si:H; bilayer (i)a-Si:H with 50 sec post HPT treatment; bilayer (i)a-Si:H with 20 sec pre HPT treatment. They mainly differ from passivation strategy and hydrogen content and their deposition conditions are the ones previously optimized in this research, as discussed in chapter 4.

Table 6.4: Deposition parameters the (*p*)-bilayer [4 nm (*p*)nc-SiOx:H + 16 nm (*p*)nc-Si:H] deposited on top of different (i)a-Si:H layers

Layer	T substrate [°C]	Pressure [mbar]	Power density [mW/cm <sup>2</sup> ]	SiH <sub>4</sub> [sccm]	B <sub>2</sub> H <sub>6</sub> [sccm]	H <sub>2</sub> [sccm]	CO <sub>2</sub> [sccm]
( <i>p</i> )nc-SiOx:H	180	2.1	76.4	0.8	10	170	1.4
( <i>p</i> )nc-Si:H	180	2.1	90.3	0.8	10	170	0

The measured  $\tau_{eff}$ ,  $i-V_{OC}$  for each combination is reported in Fig. 6.17.

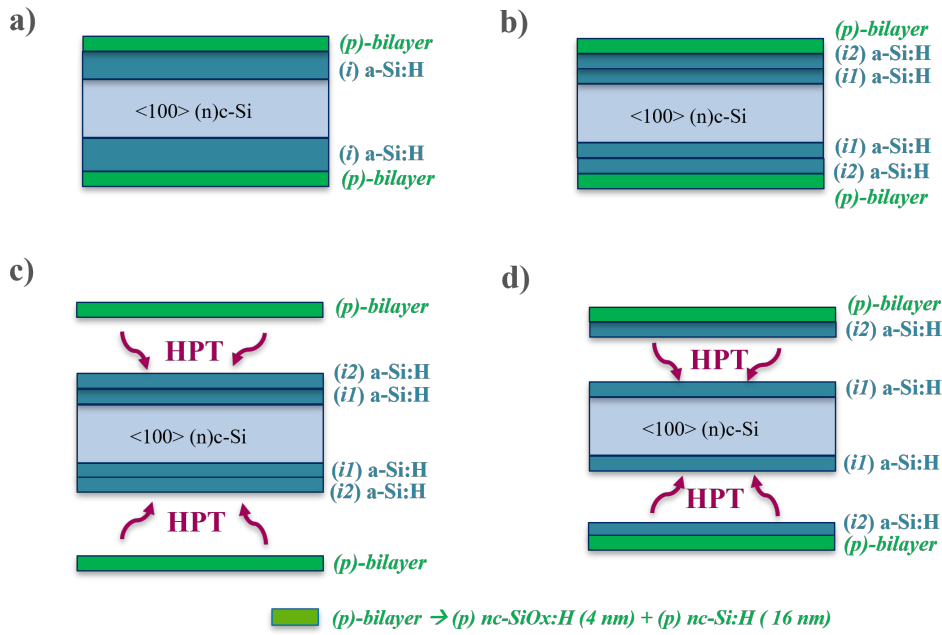


Figure 6.16: Schematic representation of symmetric deposition of (p)-type layer stack on various (i)a-Si:H layer coated flat <100> c-Si surfaces. a) monolayer (i)a-Si:H ; b) bilayer (i)a-Si:H ; c) bilayer (i)a-Si:H with post HPT treatment ; d) bilayer (i)a-Si:H with intermediate HPT treatment.

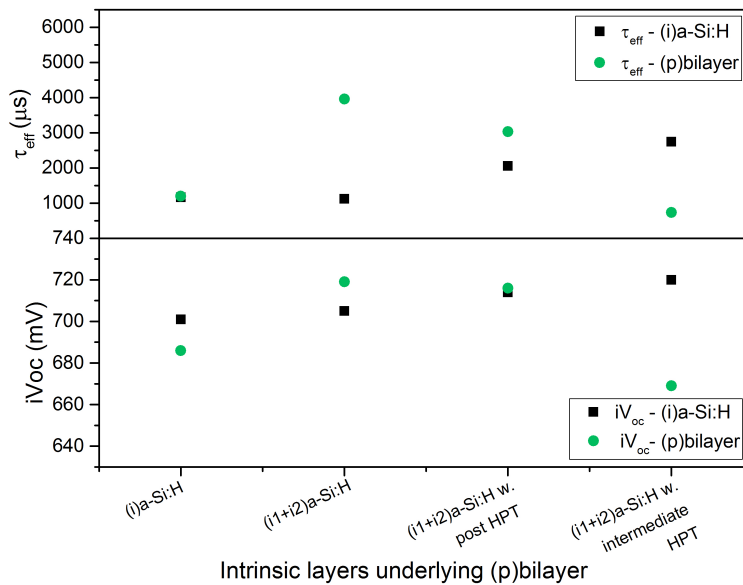


Figure 6.17:  $\tau_{eff}$  and  $iV_{OC}$  for each set of combination of (i)a-Si:H/(p)-bilayer stack on flat <100> coated c-Si surfaces. Set 1) monolayer (i)a-Si:H ; Set 2) bilayer (i)a-Si:H ; Set 3) bilayer (i)a-Si:H with post HPT treatment ; Set 4) bilayer (i)a-Si:H with intermediate HPT treatment

As can be observed from Fig. 6.17 the deposition of (p)-bilayer on a monolayer (i)a-Si:H (Set 1) results in a drop of passivation qualities. This indicates that for (p)-layer passivation, a too low H incorporation in the (i)a-Si:H is not good for the passivation qualities. Indeed the p-type nc-SiOx:H has a lower crystalline fraction (Fc below 20 %) and lower doping efficiency if compared to n-type nc-SiOx:H (Fc above 60 %) [151]. Thus, in the case of p-type nc-SiOx:H it is even more crucial to guarantee a prompt nucleation of crystal to ensure a sufficient Fc and thus enough conductivity. The (i)a-Si:H delays the nucleation and reduces crystalline

fraction in the bulk of (thin) films, which is most likely due to the permeability of the amorphous silicon layer to atomic H [84]. This indicates that a (i)a-Si:H with already a sufficient H content is needed in order to guarantee minimum crystalline nucleation for the (*p*)nc-SiOx:H layer.

Instead, after the deposition of (*p*)-bilayer on both bilayer (Set 2) and bilayer with post HPT (Set 3)  $\tau_{\text{eff}}$  is increased from 1.1 and 2.0 ms to 3.9 ms and 3.0 ms respectively. Instead, a drop of  $i\text{-}V_{\text{OC}}$  to 669 mV was observed also after depositing (*p*)-bilayers on top of (i)a-Si:H obtained via bilayer + intermediate HPT approach. This can be ascribed to the deterioration of the passivation qualities to possible excessive H incorporation during the (*p*)-bilayer deposition, which can induce defect formations and deteriorate passivation quality [142]. As compared to Set 4), the improvements seen in Set 2) and Set 3) could be because they have slightly lower H-content, as proven by the FTIR analysis conducted on those intrinsic layers (see chapter 4).

In comparison to the (*n*)nc-SiOx:H it can be concluded that (*p*)-bilayer layers work better with (i)a-Si:H with quite some hydrogen content. For this reason, the bilayer passivating structure works better than the monolayer if combined with the described (*p*)-bilayer layer stacks (note that the bilayer has a higher hydrogen content than the monolayer, as found and explained in chapter 4).

To summarize, the best combination of (*p*)-bilayer and (i)a-Si:H is obtained for Set 2 (bilayer) and it results in improved  $\tau_{\text{eff}}$  (3.9 ms) and  $i\text{-}V_{\text{OC}}$  (719 mV) in combination with doped layers. Thus in the case of (*p*)-type emitter the optimal (i)a-Si:H is different than the best layer found for (i)a-Si:H layer only. This is because the effect of the deposition conditions of the (*p*)-type layer stack has to be taken into account.

### FJ SHJ solar cells - results

After having identified the optimized (i)a-Si:H/(*p*)bilayer combination, it has been implemented on the flat side of a single-side-textured FJ SHJ solar cell. The schematic of the fabricated single-side-textured FJ SHJ cell is shown in Fig. 6.18.

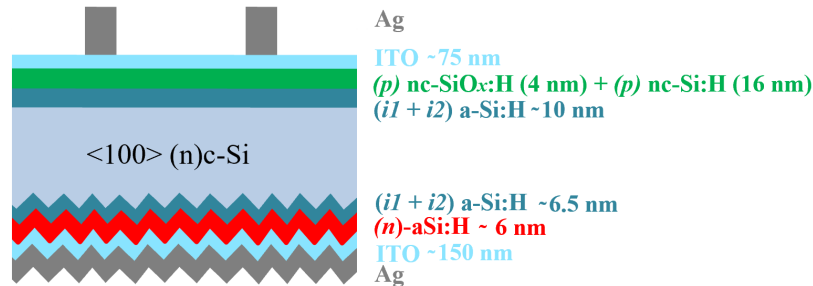


Figure 6.18: Schematic representation of the fabricated single-side-textured FJ SHJ solar cell.

The resulting JV curve and cell parameters are reported in Fig. 6.19. The average  $J_{\text{SC}}$  is around 33.4 mA/cm<sup>2</sup>,  $V_{\text{OC}}$  705 mV, FF 80.5 % and  $\eta$  18.9 %.

The  $V_{\text{OC}}$  of the cell is quite good (705 mV). This indicates that the i/p layer optimization is efficient and the passivation quality of the (i)a-Si:H bilayer is well preserved even after the deposition of the (*p*)-bilayer. However, some losses in  $V_{\text{OC}}$  happen probably during the screen printing process, as can be seen in the  $V_{\text{OC}}$  evolution reported in Fig. 6.19, where a drop in  $V_{\text{OC}}$  of about 30 mV after metallization is observed.

The FF (80.5 %) is also good. However, it can be observed that iFF is pretty high and that the FF is mainly limited by quite high  $R_{\text{Suns}V_{\text{OC}}}$  (0.84  $\Omega\text{cm}^2$ ). The high series resistance can be due to a lower crystalline volume fraction [90], which is usually observed for (*p*)-nc-SiOx:H [151] or due to contact resistances at the different layers interfaces.

The average  $J_{\text{SC}}$  is around 33.4 mA/cm<sup>2</sup> % and  $\eta$  18.9 %. EQE measurements, reflectance (R) measurements and optical simulations with GenPro4 software [128] have been performed in order to understand the reasons behind this  $J_{\text{SC}}$ . The measured EQE and 1-R are shown in Fig. 6.20 a) while the simulated wavelength-absorbance graph is plotted in Fig. 6.20 b) and they are quite in accordance. As can be observed, the cell is characterized by a quite low reflection (simulated value 6.4 mA/cm<sup>2</sup>) and a relatively low parasitic absorption of the (*p*)bilayer.

In conclusion, a performant FJ SHJ solar cell has been fabricated and can be implemented and tested in tandem devices. However, as stated before it's mandatory to fabricate an efficient top n-i-p perovskite cell to produce a high-performance tandem cell, which may be quite challenging according to the literature [29].

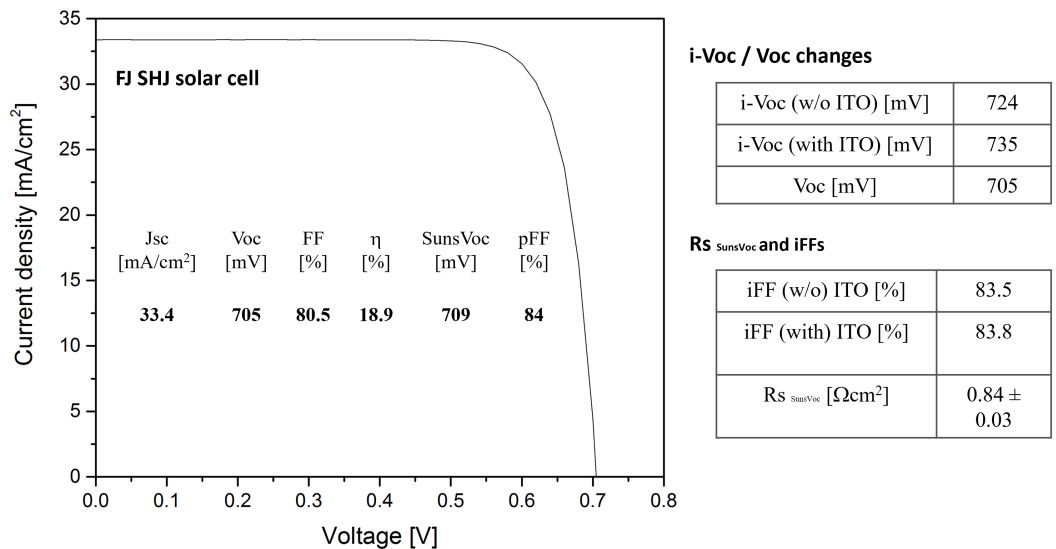


Figure 6.19: The J-V curve of single-side-textured FJ SHJ cell, with details about the values of main measured parameters of the cell.

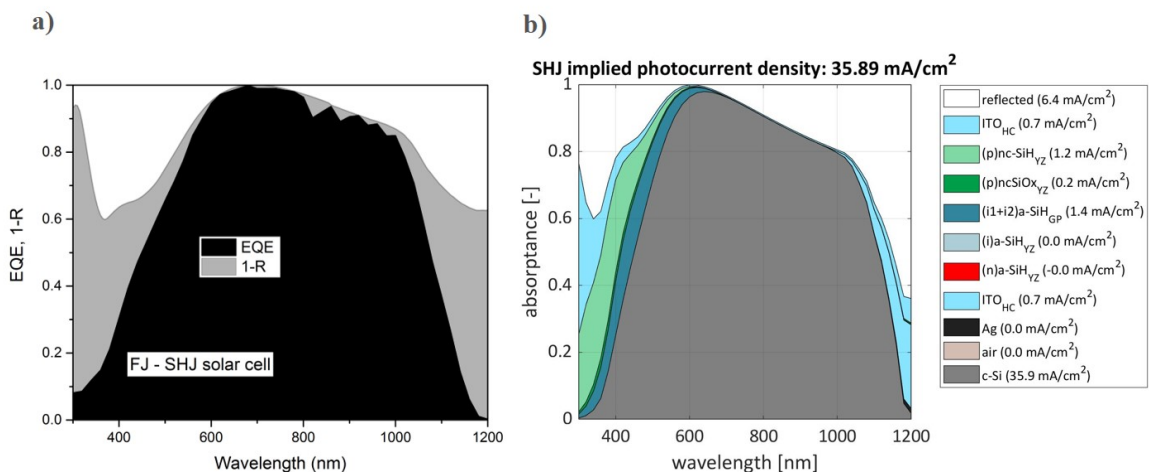


Figure 6.20: Single-side-textured FJ SHJ cell: a) the measured EQE and reflectance b) the simulated absorbance with GenPro4 software [128].

## 6.4. TRJ SHJ solar cells

In 2T tandem cells, it is crucial to have an interconnection layer that physically and electrically connects the two subcells. The interconnection layer enables the recombination of charge carriers (i.e. electrons/holes) collected from the rear of the (n-i-p/p-i-n) perovskite top cell with the charge carriers (holes/electrons) collected from the front of the SHJ bottom cell [152]. An efficient interconnection layer should entail low contact resistance, parasitic absorption, and reflection in the cell. In other words, it should introduce as little optical and electrical losses as possible. In general, different interconnection layers have been developed in the literature. Among those, a TCO layer and a tunneling junction are among the most studied and implemented, and their layer stack is schematically shown in Fig. 6.21 a) and b) respectively, with a representative example of fabricated tandem cell from the literature [153].

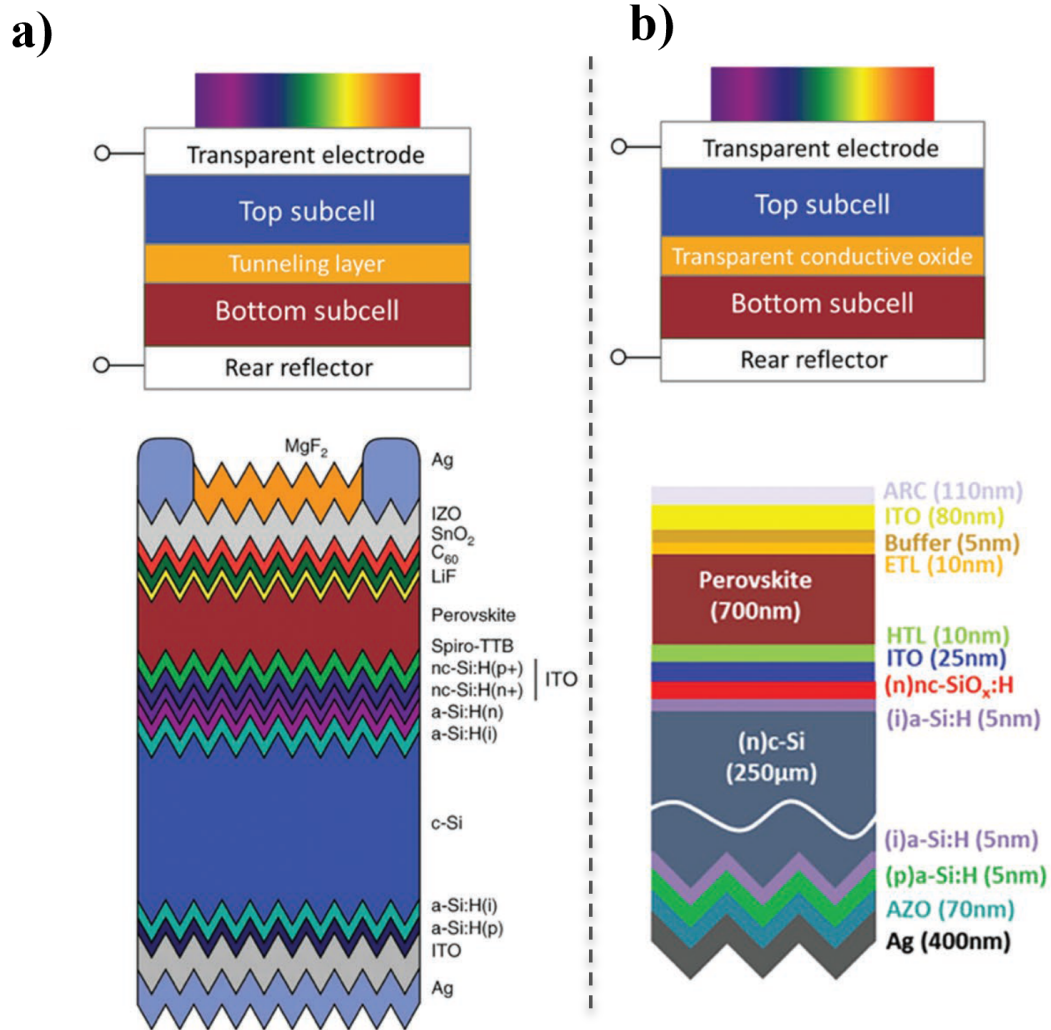


Figure 6.21: Schematics of monolithic tandem structures with a) an interlayer of tunneling junction; b) TCO. Also some representative cells are reported from the literature. Cell a) uses an tunneling interlayer made of a stack of (n+)nc-Si:H/(p+)nc-Si to connect a fully textured Si bottom subcell and a p-i-n perovskite top subcell, resulting in a tandem efficiency of 25.2% [19]. Cell b) uses a ITO recombination layer, to connect a single-side-textured c-Si bottom cell and a p-i-n perovskite top cell, leading to a tandem efficiency of 25.4% [24]. Figure adapted from [153].

A tunnel interlayer is a particularly interesting interlayer. Sahli et al. have reported a 2T tandem cell with a tunneling interlayer made of a stack of (n+)nc-Si:H/(p+)nc-Si that connects a fully textured SHJ bottom cell with a p-i-n top perovskite cell, with a resulting efficiency of 25.2 % [19].

In this work, a SHJ featuring a tunneling recombination junction (TRJ) consisting of a layer stack of (n)nc-Si:H/(p)nc-SiO<sub>x</sub>:H/(p)nc-Si:H has been investigated. The layer stack of the TRJ is shown in Fig. 6.22

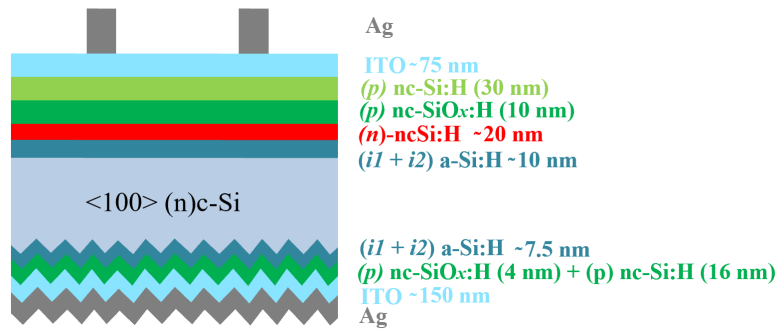


Figure 6.22: Schematic representation the fabricated single-side-textured SHJ solar cell with a TRJ made of a layer stack of  $(n)nc\text{-Si:H}/(p)nc\text{-SiOx:H}/(p)nc\text{-Si:H}$ .

The resulting JV curve and parameters are reported in Fig. 6.23. The average  $J_{SC}$  is around  $33.2 \text{ mA/cm}^2$ ,  $V_{OC}$  is  $709 \text{ mV}$ , FF is  $80.9\%$  and  $\eta$  is  $19.1\%$ .

The  $V_{OC}$  is quite good ( $709 \text{ mV}$ ), once again indicating that the  $(i) a\text{-Si:H}$  bilayer is effective in passivating the  $c\text{-Si}$  surface after the other layers deposition. However, also in this case some  $V_{OC}$  losses are expected due to the screen printing process. This some losses in  $V_{OC}$  happen probably during the screen printing process, as can be seen in the  $V_{OC}$  evolution reported in Fig. 6.23, where a drop in  $V_{OC}$  of about  $25 \text{ mV}$  is observed after metallization.

The FF instead seems to be good (around  $80.9\%$ ). However, the  $iFF$  ( $85.2\%$ ) is way higher than this value. Some possible limitations of FF can be attributed to i) high series resistances due to a too low crystalline volume fraction or a too thick (amorphous) incubation layer and thus poor  $(i) a\text{-Si:H}/\text{nanocrystalline}$  contact ii) a poor tunnel-recombination contact to the ITO front contact [90] iii) resistances at the numerous layer interfaces in this TRJ SHJ cell iv) poor tunneling efficiency of the TRJ.

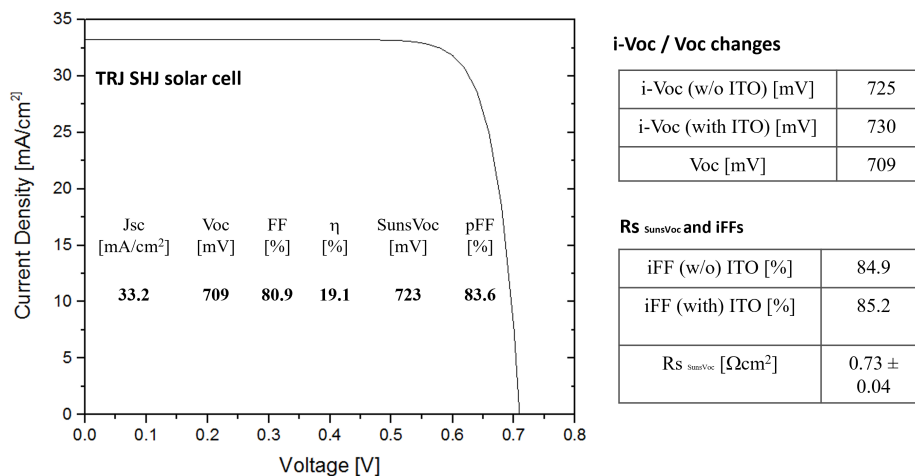


Figure 6.23: The J-V curve of single-side-textured TRJ SHJ cell

In order to boost tunnel efficiency and produce efficient interband tunnel-junction, some key strategies are [154]:

- Guarantee a good selectivity on  $c\text{-Si}$  surface by field-effect passivation. In this case, the  $n$ -type layer should provide sufficient field-effect passivation to achieve selectively collection of electrons, and meanwhile, strong enough to screen the field-effect from  $p$ -type layer above.
- Lossless carrier collection at tunneling junction. This requires highly doped adjacent  $n$ -type and  $p$ -type layers, which narrow the space charge region, thus enhances the probability for tunneling recombination; Thus the doping efficiency of the layers should be checked. Moreover, the crystalline growth of the  $(p)nc\text{-SiOx:H}$  on top of the  $(n)nc\text{-Si:H}$  should be facilitated since it grows on top of an already crystalline layer [87]. This can eventually enhance the tunneling probability.

The average  $J_{SC}$  is around  $33.2 \text{ mA/cm}^2$ . EQE measurements, reflectance (R) measurements and optical simulations with GenPro4 software [128] have been performed in order to understand the reasons behind this  $J_{SC}$ . The measured EQE and 1-R are shown in Fig.6.24 a) while the simulated wavelength-absorbance graph is plotted in Fig.6.24 b) and they are quite in accordance. As can be observed, the reflection is quite low (simulated value  $5.9 \text{ mA/cm}^2$ ) which indicates that the stacking of the layer is good in terms of refractive index. However, the stacking of the TRJ layers increases the parasitic absorption which limits the implied photocurrent density.

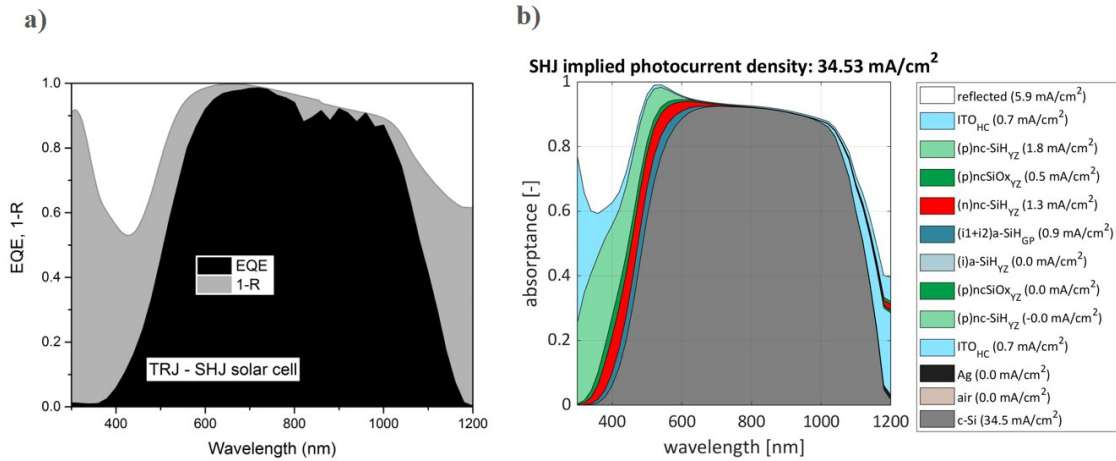


Figure 6.24: Single-side-textured TRJ SHJ cell: a) the measured EQE and reflectance b) the simulated absorbance with GenPro4 software [128].

## 6.5. Summary

In this chapter different types of single-side-textured SHJ solar cells have been fabricated and measured. Both RJ and FJ have been manufactured, even if it is known from the literature that RJ SHJ cells are preferred to be used as bottom cells in tandem devices due to the optical advantage of the perovskite top cells with the p-i-n configuration. In particular, for the RJ SHJ configuration, solar cells with three different (*n*)-type layers [(*n*)nc-SiOx:H;(*n*)nc-Si:H;(*n*)a-Si:H] have been investigated. The thicknesses of each (*n*)-type layer have been chosen according to the optimal thicknesses individuated from the tandem optical simulations (chapter 5). Furthermore, FJ SHJ and TRJ SHJ have been also analyzed.

The results of the five types of single-side-textured SHJ solar cells are presented in Tab. 6.5. From the results, it can be concluded that the doped contacts were successfully implemented into SHJ solar cells, which delivered  $V_{OC}$  in the range from 700 to 714 mV and FFs range from 77.8% to 80.9%. Therefore, different well-functioning SHJ solar cells have been developed and are ready to be tested and implemented a bottom cells for tandem devices.

Table 6.5: The results of the manufactured single-side-textured SHJ solar cells with the best performance.

Sample	Jsc [mA/cm <sup>2</sup> ]	Voc [mV]	FF [%]	$\eta$ [%]	pFF [%]
RJ SHJ w. ( <i>n</i> )a-Si:H	33.6	704	80.7	19.1	80.7
RJ SHJ w. ( <i>n</i> )nc-Si:H	33.2	714	80.7	19.1	84.3
RJ SHJ w. ( <i>n</i> )nc-SiOx:H	33.4	700	77.8	18.2	80.6
FJ SHJ	33.4	705	80.5	18.9	84
TRJ SHJ	33.2	709	80.9	19.1	83.6

# 7

## Conclusions

With the final goal of optimizing single-side-textured silicon heterojunction solar cells for tandem silicon / perovskite applications a comprehensive study 'from layer to device' is conducted during this Master thesis research. Two main research objectives have been investigated: i) the optimization of (i)a-Si:H in terms of good passivation quality, uniformity, and reproducibility; ii) the optimization of single-side-textured SHJ solar cells for tandem applications through optical simulations and cell's manufacturing. In this chapter, the main results are summarized and conclusions are drawn.

### 7.1. Optimization of hydrogenated intrinsic amorphous silicon passivating layer

The implementation of an intrinsic hydrogenated amorphous layer ((i)-a-Si:H) between the c-Si substrate and the doped layers is crucial to achieving SHJ with a high  $V_{OC}$  and high efficiencies. The intrinsic layer has to provide excellent chemical passivation of the c-Si surface and have superior bulk qualities to minimize current losses. The initial approach was to optimize RF-PECVD deposition conditions of a (i)a-Si:H monolayer for symmetric <100> flat c-Si surfaces. The optimized (i)a-Si:H monolayer (10-nm-thick) was obtained using pure  $\text{SiH}_4$ , which results in rather moderate passivation performances ( $\tau_{\text{eff}} = 1.2$  ms,  $i\text{-}V_{OC} = 701$  mV).

After the monolayer optimization, further deposition methods were investigated with the aim of improving passivation qualities by incorporating more H in the (i)a-Si:H layer without promoting detrimental epitaxial growth on the <100> flat c-Si surface. Specifically, hydrogen plasma treatment (HPT), bilayer deposition, and the combination of bilayer deposition with different HPT treatments have been tested. With a bilayer approach, which features firstly a less H-containing (i)a-Si:H to prevent epitaxial growth and then a second H-rich (i)a-Si:H layer, the passivation properties were slightly enhanced to  $\tau_{\text{eff}}=1.4$  ms and a  $i\text{-}V_{OC}=704$  mV. Subsequently, by combining the bilayer approach with a post HPT,  $\tau_{\text{eff}}$  of 2.0 ms and an  $i\text{-}V_{OC}$  of 714 mV were achieved. Lastly, by combining the bilayer approach with an intermediate HPT, the optimal passivation sample was deposited, with  $\tau_{\text{eff}}$  of 2.4 ms and an  $i\text{-}V_{OC}$  of 720 mV on the flat <100> surface.

Moreover, an extensive characterization has been conducted to find the correlation between the optimal deposition conditions and the layer properties. The deposited (i)a-Si:H layers have been characterized mainly via Fourier-transform infrared spectroscopy (FTIR) and led to the conclusion that the passivation layer containing sufficient H and a higher fraction of monohydrides, and thus fewer defects, is beneficial for achieving better passivation qualities.

### 7.2. Optimization of single-side-textured SHJ solar cells for tandem applications

SHJ bottom cells with (*n*)-contact on top are the preferred cells for 2T tandem devices due to the optical advantage of the perovskite top cells with the p-i-n configuration. During this master thesis research, a first tandem cell has been fabricated in collaboration with TU Eindhoven resulting in 22.2% efficiency. After that, multiple optical simulations have been performed using the GenPro4 simulation software. Through the simulations, the main optical limitations of the first fabricated tandem cell have been identified as well as some possible strategies to overcome them. In particular, it was found that by optimizing the front anti-reflection

layers ( $\text{MgF}_2$  and ITO) thicknesses (at 100 nm and 20 nm, respectively), and reducing  $C_{60}$  thickness from 20 to 10 nm, front reflections, and parasitic absorption can be minimized, with a gain of implied photocurrent density of  $1.8 \text{ mA/cm}^2$  for the tandem cell. Moreover, by implementing  $(n)\text{nc-SiOx:H}$  doped layer in the SHJ bottom cell, instead of standard  $(n)\text{a-Si:H}$  layer, the reflection between the top and bottom cell is also reduced. By adopting all the above-mentioned optimizations and adjusting the perovskite layer from 473 nm to 530 nm as well, a total improvement of  $2.7 \text{ mA/cm}^2$  in implied photocurrent density with respect to the initial 22.2% tandem cell can be achieved.

Following the identification of the most promising layer stack for SHJ bottom cells for tandem applications, both single-side-textured RJ and FJ were fabricated. Initially, the passivation quality of  $(i)\text{a-Si:H}/(n)$ -layer and  $(i)\text{a-Si:H}/(p)$ -layer on different  $(i)\text{a-Si:H}$  were investigated. Then, RJ solar cells with three different  $(n)$ -type layers [ $(n)\text{nc-SiOx:H};(n)\text{nc-Si:H};(n)\text{a-Si:H}$ ] (with optimal thicknesses individuated from the tandem optical simulations have been manufactured and measured). Besides, a TRJ SHJ solar cell with a layer stack of  $(n)\text{nc-Si:H}/(p)\text{nc-SiOx:H}/(p)\text{nc-Si:H}$  has been fabricated and measured as well.

In conclusion, various doped contacts (both  $n$ - and  $p$ -type) were successfully implemented into SHJ solar cells, which delivered  $V_{\text{OCs}}$  in the range from 700 to 714 mV and FFs range from 77.8% to 80.9%. Hence multiple well-functioning SHJ solar cells have been manufactured and optimized as bottom cells for high-efficiency perovskite/ $c$ -Si tandem devices.

# 8

## Outlooks

Based on the understanding of the whole process and acquired practical experience, outlooks are given in this section in order to improve the achievable efficiency perovskite/c-Si tandem cells, mainly focusing on the optimization of the bottom SHJ solar cell.

### 8.1. Layer optimization for the single-side-textured SHJ bottom cell

#### Optimization of (i)a-Si:H passivating layer

Multiple strategies have been tested in this research in order to optimize the passivation quality of the (i)a-Si:H layer, and a quite good passivation has been obtained. However, different deposition strategies still need to be further optimized and investigated. For example, the optimization on monolayer (i)a-Si:H with a subsequent post HPT treatment still needs further tests and optimizations, as discussed in section ?? of the Appendix. Moreover, further annealing treatments can be investigated [113, 155]. The effect of thickness of the (i)a-Si:H layer on the SHJ solar cells properties can also be tested. In particular, thinner layer can be investigated as they may lead to an improvement in terms of FF [156].

#### Optimization of (i)a-Si:H/(n)a-Si:H layer stack

In this research, the (i)a-Si:H/(n)-type layer stack has been optimized mainly for (i)a-Si:H/(n)nc-SiO<sub>x</sub>:H. For the other (n)-type layers [(n)a-Si:H, (n)nc-Si:H], the same optimized bilayer (i)a-Si:H layer has been assumed when single-junction RJ SHJ solar cells are produced. Note that this can be a good assumption for the (n)nc-Si:H layer since it has similar deposition conditions with respect to (n)nc-SiO<sub>x</sub>:H. However, especially for (n)a-Si:H it is recommended to re-perform the i/n optimization, testing different (i)a-Si:H/(n)a-Si:H layers stacks, since the amorphous doped contact is deposited with a lower hydrogen flow than the nanocrystalline doped contacts (n)nc-SiO<sub>x</sub>:H and (n)nc-Si:H]. Moreover, the thickness of the (i)a-Si:H can also be varied in all the cases in order to try further optimizations.

### 8.2. Optimization of the perovskite/c-Si tandem cell layer stack

Different strategies to tackle the major optical limitations of the first fabricated solar cell were proposed and discussed in details in this thesis (see chapter 5). However, even by implementing the suggested strategies, there are still some significant current losses in the wavelength range of 900 nm to 1200 nm. In order to improve light absorption in this wavelength range, some additional strategies can be tested and investigated.

For example, different TCOs materials can be tried, such as tungsten-doped indium oxide (IWO) and hydrogenated fluorine-doped indium oxide (IFO:W). Indeed IWO, if compared to the conventional ITO, has been proven to have the optical advantage of a much lower parasitic absorption in the NIR region [157]. A similar enhancement of light management in the NIR region can be achieved with IFO:W which, if compared to ITO, has higher electron mobility and a higher refractive index (especially in the NIR range) which contributes to enhanced ARC properties [158].

However, the implementation of IWO, even if it reduces parasitic absorption, can still entail quite high rear-side internal reflections, indicating that a large amount of NIR light escapes after passing through the cell. This could also be solved with appropriate manipulation strategies. For example to increase the internal

reflectance, a dielectric back reflector can be implemented. [159] or nanoparticles can be inserted in between the absorber and the rear side metal reflector as back reflectors [160].

Moreover, to further enhance the implied photocurrent of the tandem cell, an inverted pyramidally-textured PDMS front reflective layer can be implemented to reduce reflections while at the same time increasing the path length of light due to the scattering at the textured surface [30]. This could further enhance the light incorporation for tandem cells and lead to an efficiency improvement.

Amongst the most challenging layers to design and fabricate in two-terminal tandems are the recombination layers between the top and bottom cell. Currently, TCOs have been successfully implemented in silicon/perovskite tandems. In this research, the TCO recombination junction layer needs to be further optimized in order to achieve high efficiency tandem cells. In particular, it has to be optimized to provide at the same time low electrical resistance, excellent transparency, negligible parasitic absorption and reflection losses. Similarly, also the TCO-free tunnel junctions need further investigation. Moreover, through energy-level engineering on both sides of the recombination junction, possibly through doping strategies, it may be possible to enhance carrier transport [152]. Besides, a new class of materials for the recombination layer can be developed. A promising concept was introduced by Al-Ashouri et al. and consists of self-assembled monolayers (SAM) with HTL properties in tandem solar cells, which is also serving as the recombination junction together with the ITO electrodes [23]. This concept introduces the challenge of simultaneously optimizing the ITO according to the adjacent layers of both top and bottom cells. In summary, an optimized recombination junction design between top and bottom cell is of high importance and more effort is needed to research on this aspect.

### **Experimental optimization of the metallization process**

As found in this research, the screen printing is a major limitation of the maximum  $V_{OC}$  of the fabricated single-junction SHJ solar cell. Note that this is not a big problem in the perspective of tandem applications, since in that case screen printing is not done on the front side of the SHJ solar cell. However, different metallization methods can be tested, such as metal evaporation and electroplating.

# 9

## Acknowledgments

I wanted to express my sincere and deep appreciation towards the whole PVMD group, which gave me the opportunity to experience working in a research group that is a leader in the solar energy research sector. It was a truly enriching experience, firstly because I was in contact with experts and experienced researchers daily. Their way of conducting scientific researches taught me how to plan a consistent scientific research and it was absolutely helpful and inspirational having discussions with them, always motivating me to keep learning and be curious to understand and exploring new scientific challenges. Moreover, I experienced the unique and fascinating work environment of a world-class cleanroom. I am convinced that my thesis experience is a successful example of a scientific collaboration between different research groups with various expertise, connecting different universities (TU Delft and TU Eindhoven) and also different Departments of TU Delft (Materials Science at the 3mE faculty, where I pursued my Master Degree, and the PVMD group in the Department of Electrical Sustainable Energy, where I conducted my Master thesis research).

I want to express my most sincere gratitude to my supervisors Prof. dr. Olindo Isabella and Dr. Amarante Bottger for the crucial role they had for me in this Master Thesis, giving me precious suggestions, guidance and inspirational ideas.

A special thanks goes to my daily supervisor, Ir. Yifeng Zhao, for having always assisted in the lab work, having shared his knowledge and expertise with me and having helped me along the way. He has really proved to be a valuable supervisor, both in the academic field but most importantly a truly inspiring person in life and he has always supported me in the most joyful but also in the most difficult situations. I will always be thankful to him for this.

Sincere thanks also to Dr. Luana Mazzarella for precious scientific discussions and kind help, to Dr. Rudi Santbergen for having shared his knowledge in the use of GenPro4 software, and to Dr. Peyman Taheri for having helped me with FTIR data elaboration. To all the inspiring professors and researchers I met at TU Delft, a sincere thanks for being an example and point of reference for me.

I would also like to thank Martijn Tijssen, Stefaan Heirman and Daragh O'Connor for their kind support in the laboratory, for having shared and helped with their expertise in the equipment and tools in the laboratory.

The memory I will have of this experience will always be a treasure for me. I will never forget the unconditional help and support that I received during this pretty tough historical period of COVID-19, that sometimes made this Master Thesis experience challenging, but unforgettable due to the emotional and supporting network that was surrounding me all the time.

My thanks also goes to my friends and colleagues, especially to Jasmine Nespoli, Leon Crousen, Manas Tripathi, Myrto Despotopoulou and Tom Hautvast for accompanying me in this adventure. A big thanks also to my roommates, especially to Dilge Gul, Elsie Loukiantchenko, Ericka Matsuda Martin, Maria Seoane, Megan Segeren, Natalia Elias Ortgega and Zoe Kirschfink for their unconditional love and support.

Lastly but most importantly, I would like to thank my parents, my brother, my family and my best friends in general for their selfless dedication, support and love. Even though they are far apart, they have been and will always be my most solid foundation.



# A

## Appendix

### A.1. Thesis Approach

Given the research objective and research questions, a constructive methodology of the thesis is proposed in this section. Each result obtained during the experimental activity must meet the requirements listed in section A.1.1.

The first research question, which concerns the optimization of the deposition conditions of (i)a-Si:H, has been addressed in the first place (chapter 4). In order to do so, different deposition parameters have been varied and the effects of each parameter were studied while keeping the other parameters constants. After depositing the layer with different processing parameters, the passivation quality of the (i)a-Si:H layer is measured and the layer is characterized. The main characterization methods of the deposited (i)a-Si:H layer are presented in chapter 3. Once the deposition parameters have been optimized, different deposition approaches and post-deposition treatments have been tested as well, and also these layers have been characterized. Each result has been properly analyzed, such that the optimal processing conditions of (i)a-Si:H in terms of passivation quality, uniformity and reproducibility have been identified.

Subsequently, the second research question has been addressed, which concerns the optimization of the single-side-textured SHJ solar cells for tandem applications. A first single-side-textured SHJ solar cell has been used to fabricate a first tandem cell in collaboration between TU Delft (c-Si bottom cell) and TU Eindhoven (perovskite top cell). Starting from this cell, some advanced optical simulations have been performed in order to identify the main optical limitations of the first fabricated tandem cell. From the identified optical drawbacks, new optimized configurations of both the top perovskite and bottom SHJ cells have been identified. Thus, in chapter 6, the single-side-textured SHJ bottom cells identified as optimal boosting the efficiency of the first fabricated tandem cell are successfully fabricated, measured, and analyzed. SHJ bottom cells with different doped layers have been tested, and the doped/intrinsic layer combination has been optimized.

During the whole research project, a collaboration with perovskite and simulation partners has been held. The collaboration was essential to fabricate and test monolithic 2T perovskite/SHJ solar cells, to identify the main improvements points, and to perform optical simulations of the tandem cell.

#### A.1.1. Methodology for experimental results collection and elaboration

To answer the research questions 1) the experimental result must satisfy the following points:

- High reproducibility, especially in terms of passivation qualities. Reproducibility is evaluated by repeating the same experiment and check if the same, or at least very similar, results are obtained.
- Variation of one parameter at a time, while keeping the other parameters constant in order to identify and select the optimal deposition conditions for an optimal passivation quality
- Comparable layers should be deposited, especially in terms of thickness. Indeed passivation qualities are highly dependent on thickness (a detailed explanation can be found in section 2.1.4). If not comparable, a correction should be made in order to avoid false judgment.

The results have been elaborated frequently such that the best optimization strategy was constantly updated and modified throughout the research progress.

Instead, to answer the research questions 2) the experimental result must satisfy the following points:

- Performing optical simulations with the experimentally obtained input files (nk files), thicknesses, and layer properties.
- High reproducibility of the sample's electrical and optical qualities. Reproducibility is evaluated by repeating the same experiment and check if the same, or at least very similar, results are obtained.
- Comparable back-end processing for the SHJ solar cells (ITO and metallization deposition), in order to make the cell's performance within one batch comparable.

### A.1.2. Work Package Definition

The following tables summarize the work packages that will be used throughout the research.

<b>Work Package 1</b>	
Title	Optimization deposition parameters of (i)a-Si:H in terms of good passivation quality, uniformity, and reproducibility
Duration	Nov 2020 - March 2021
Description	<ul style="list-style-type: none"> <li>- Familiarize with the main state-of-art of the identified subject</li> <li>- Select the parameters that will be firstly tested</li> <li>- Collect characterization data and experimental results</li> <li>- Elaborate the collected results</li> <li>- Evaluate a re-acquisition of data if not accurate or not comparable</li> <li>- Change in the optimization strategy if not efficient</li> <li>- Individuate the best deposition conditions for each tested parameter in order to continue the optimization research</li> </ul>
<b>Work Package 2</b>	
Title	Optimization the single-side-textured silicon heterojunction solar cell for tandem application
Duration	March 2020 - July/August 2021
Description	<ul style="list-style-type: none"> <li>- Familiarise with the main state-of-art of the identified subject</li> <li>- Fabricate and measure a first tandem cell in collaboration with TU Eindhoven</li> <li>- Perform optical simulation of the cell in order to identify the most promising bottom SHJ cell improvements</li> <li>- Select the doped layers that will be tested</li> <li>- Optimize doped/intrinsic layer combination</li> <li>- Collect characterization data and experimental results</li> <li>- Elaborate the collected results</li> <li>- Evaluate a re-acquisition of data if not accurate</li> <li>- Fabricate single-junction SHJ solar cells</li> <li>- Measure the cells performance in order to test their applicability in tandem cells</li> <li>- Fabricate more SHJ bottom cells and send them to TU Eindhoven to fabricate new optimized tandem cells.</li> </ul>
<b>Work Package 3</b>	
Title	Writing of the Master Thesis
Duration	March 2020 - July/August 2021
Description	The writing of the thesis has been performed in parallel with the experimental work. In particular, moments during which experimental facilities were not available (because booked by other users or because in maintenance) have been used to write the Master Thesis report.

## A.2. Monolayer with post HPT

As stated in chapter 4, hydrogen plasma treatments after the monolayer intrinsic layer deposition has also been tested in research. Indeed, this approach was proposed in the scientific literature as beneficial for the passivation quality due to enhanced chemical passivation due to the diffusion of hydrogen in the layer and at the c-Si/(i)a-Si:H interface [95].

Thus, after having optimized the monolayer (i)a-Si:H deposition, the application of a post HPT treatment was investigated. However, the optimization of the conditions of the HPT treatment on the monolayer resulted to be difficult and not replicable. The passivation quality of the samples deteriorated in all the tests of HPT post treatments, as shown in Fig. A.1. These results are probably due to non-optimized HPT conditions, and it was found to be difficult to optimize the treatment in the AMIGO PECVD deposition tool. Therefore, other approaches were investigated.

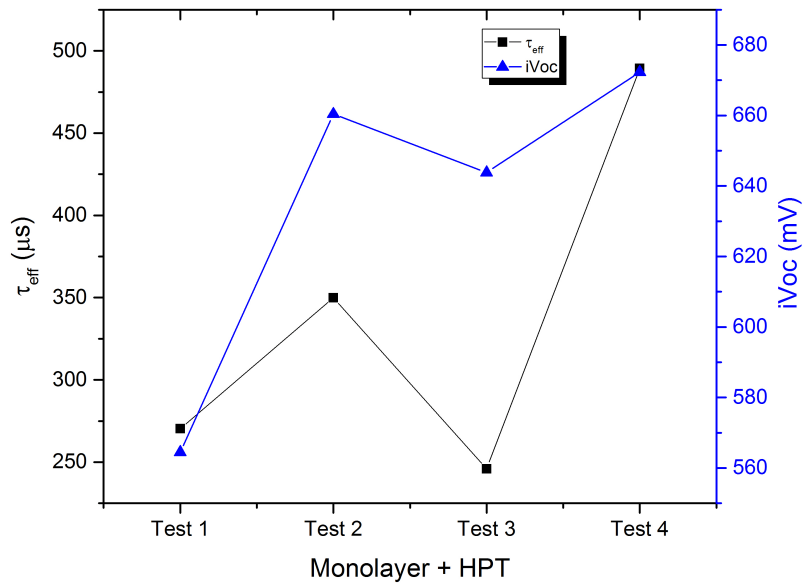


Figure A.1:  $\tau_{\text{eff}}$ ,  $i_{\text{Voc}}$  of symmetric passivation samples deposited with monolayer (i)a-Si:H + post HPT treatment (various tests were performed for the HPT).



# Bibliography

- [1] Q. "Schiermeier, J. Tollefson, T. Scully, A. Witze, and O. Morton. "energy alternatives: Electricity without carbon". *"Nature News"*, "454"("7206"):"816–823", "2008".
- [2] N. Kannan and D. Vakeesan. Solar energy for future world:-a review. *Renewable and Sustainable Energy Reviews*, 62:1092–1105, 2016.
- [3] A. H. Smets, K. Jäger, O. Isabella, R. Van Swaaij, and M. Zeman. *Solar Energy: The Physics and Engineering of Photovoltaic Conversion, Technologies and Systems*. Uit Cambridge Ltd, 2016.
- [4] M. A. Green. Commercial progress and challenges for photovoltaics. *Nature Energy*, 1(1):1–4, 2016.
- [5] C. Battaglia, A. Cuevas, and S. De Wolf. High-efficiency crystalline silicon solar cells: status and perspectives. *Energy & Environmental Science*, 9(5):1552–1576, 2016.
- [6] ISE Fraunhofer. Photovoltaics Report. Technical Report September, 2020. URL <https://www.ise.fraunhofer.de/content/dam/ise/de/documents/publications/studies/Photovoltaics-Report.pdf>.
- [7] A. Richter, M. Hermle, and S. W. Glunz. Reassessment of the limiting efficiency for crystalline silicon solar cells. *IEEE journal of photovoltaics*, 3(4):1184–1191, 2013.
- [8] K. Yoshikawa, H. Kawasaki, W. Yoshida, T. Irie, K. Konishi, K. Nakano, T. Uto, D. Adachi, M. Kanematsu, H. Uzu, et al. Silicon heterojunction solar cell with interdigitated back contacts for a photoconversion efficiency over 26%. *Nature energy*, 2(5):17032, 2017.
- [9] B. Chen, X. Zheng, Y. Bai, N. P. Padture, and J. Huang. Progress in tandem solar cells based on hybrid organic–inorganic perovskites. *Advanced Energy Materials*, 7(14):1602400, 2017.
- [10] S. S. Hegedus and A. Luque. Status, trends, challenges and the bright future of solar electricity from photovoltaics. *Handbook of photovoltaic science and engineering*, pages 1–43, 2003.
- [11] H. Uzu, M. Ichikawa, M. Hino, K. Nakano, T. Meguro, J. L. Hernández, H.-S. Kim, N.-G. Park, and K. Yamamoto. High efficiency solar cells combining a perovskite and a silicon heterojunction solar cells via an optical splitting system. *Applied Physics Letters*, 106(1):013506, 2015.
- [12] Y. Li, H. Hu, B. Chen, T. Salim, J. Zhang, J. Ding, N. Yuan, and Y. M. Lam. Reflective perovskite solar cells for efficient tandem applications. *Journal of Materials Chemistry C*, 5(1):134–139, 2017.
- [13] M. Jaysankar, W. Qiu, M. van Eerden, T. Aernouts, R. Gehlhaar, M. Debucquoy, U. W. Paetzold, and J. Poortmans. Four-terminal perovskite/silicon multijunction solar modules. *Advanced Energy Materials*, 7(15):1602807, 2017.
- [14] L. Yan, C. Han, B. Shi, Y. Zhao, and X. Zhang. A review on the crystalline silicon bottom cell for monolithic perovskite/silicon tandem solar cells. *Materials Today Nano*, 7:100045, 2019.
- [15] J. Werner, B. Niesen, and C. Ballif. Perovskite/silicon tandem solar cells: Marriage of convenience or true love story?—an overview. *Advanced Materials Interfaces*, 5(1):1700731, 2018.
- [16] I. Almansouri, A. Ho-Baillie, S. P. Bremner, and M. A. Green. Supercharging silicon solar cell performance by means of multijunction concept. *IEEE Journal of Photovoltaics*, 5(3):968–976, 2015.
- [17] K. Jäger, L. Korte, B. Rech, and S. Albrecht. Numerical optical optimization of monolithic planar perovskite-silicon tandem solar cells with regular and inverted device architectures. *Optics Express*, 25(12):A473–A482, 2017.

- [18] M. Taguchi, A. Yano, S. Tohoda, K. Matsuyama, Y. Nakamura, T. Nishiwaki, K. Fujita, and E. Maruyama. 24.7% record efficiency hit solar cell on thin silicon wafer. *IEEE Journal of photovoltaics*, 4(1):96–99, 2013.
- [19] F. Sahli, J. Werner, B. A. Kamino, M. Bräuninger, R. Monnard, B. Paviet-Salomon, L. Barraud, L. Ding, J. J. D. Leon, D. Sacchetto, et al. Fully textured monolithic perovskite/silicon tandem solar cells with 25.2% power conversion efficiency. *Nature materials*, 17(9):820–826, 2018.
- [20] K. Bush, A. Palmstrom, Z. Yu, M. Boccard, R. Cheacharoen, J. Mailoa, D. McMeekin, R. Hoyer, C. Bailie, T. Leijtens, et al. a, d. harwood, w. ma, f. moghadam, hj snaith, t. buonassisi, zc holman, sf bent and md mcgehee. *Nat. Energy*, 2:17009, 2017.
- [21] E. Köhnen, M. Jošt, A. B. Morales-Vilches, P. Tockhorn, A. Al-Ashouri, B. Maccò, L. Kegelmann, L. Korte, B. Rech, R. Schlattmann, et al. Highly efficient monolithic perovskite silicon tandem solar cells: analyzing the influence of current mismatch on device performance. *Sustainable Energy & Fuels*, 3(8):1995–2005, 2019.
- [22] S. De Wolf, J. Holovsky, S.-J. Moon, P. Loper, B. Niesen, M. Ledinsky, F.-J. Haug, J.-H. Yum, and C. Ballif. Organometallic halide perovskites: sharp optical absorption edge and its relation to photovoltaic performance. *The journal of physical chemistry letters*, 5(6):1035–1039, 2014.
- [23] A. Al-Ashouri, E. Köhnen, B. Li, A. Magomedov, H. Hempel, P. Caprioglio, J. A. Márquez, A. B. M. Vilches, E. Kasparavicius, J. A. Smith, et al. Monolithic perovskite/silicon tandem solar cell with > 29% efficiency by enhanced hole extraction. *Science*, 370(6522):1300–1309, 2020.
- [24] L. Mazzarella, Y.-H. Lin, S. Kirner, A. B. Morales-Vilches, L. Korte, S. Albrecht, E. Crossland, B. Stanowski, C. Case, H. J. Snaith, et al. Infrared light management using a nanocrystalline silicon oxide interlayer in monolithic perovskite/silicon heterojunction tandem solar cells with efficiency above 25%. *Advanced Energy Materials*, 9(14):1803241, 2019.
- [25] B. Chen, Z. Yu, K. Liu, X. Zheng, Y. Liu, J. Shi, D. Spronk, P. N. Rudd, Z. Holman, and J. Huang. Grain engineering for perovskite/silicon monolithic tandem solar cells with efficiency of 25.4%. *Joule*, 3(1):177–190, 2019.
- [26] M. H. Futscher and B. Ehrler. Efficiency limit of perovskite/si tandem solar cells. *ACS Energy Letters*, 1(4):863–868, 2016.
- [27] Oxford PV hits new world record for solar cell. URL <https://www.oxfordpv.com/news/oxford-pv-hits-new-world-record-solar-cell>. Visited on 2021-01-20.
- [28] QD solar technology. URL <https://qdsolarinc.com/technology>. Visited on 2021-01-20.
- [29] S. Altazin, L. Stepanova, J. Werner, B. Niesen, C. Ballif, and B. Ruhstaller. Design of perovskite/crystalline-silicon monolithic tandem solar cells. *Optics express*, 26(10):A579–A590, 2018.
- [30] F. Hou, C. Han, O. Isabella, L. Yan, B. Shi, J. Chen, S. An, Z. Zhou, W. Huang, H. Ren, et al. Inverted pyramidally-textured pdms antireflective foils for perovskite/silicon tandem solar cells with flat top cell. *Nano Energy*, 56:234–240, 2019.
- [31] J. Shi, M. Boccard, and Z. Holman. Plasma-initiated rehydrogenation of amorphous silicon to increase the temperature processing window of silicon heterojunction solar cells. *Applied Physics Letters*, 109(3):031601, 2016.
- [32] W. van Sark, L. Korte, and F. Roca. *Physics and technology of amorphous-crystalline heterostructure silicon solar cells*. Springer, 2012.
- [33] B. Shi, B. Liu, J. Luo, Y. Li, C. Zheng, X. Yao, L. Fan, J. Liang, Y. Ding, C. Wei, et al. Enhanced light absorption of thin perovskite solar cells using textured substrates. *Solar Energy Materials and Solar Cells*, 168:214–220, 2017.
- [34] S. Albrecht, M. Saliba, J. P. C. Baena, F. Lang, L. Kegelmann, M. Mews, L. Steier, A. Abate, J. Rappich, L. Korte, et al. Monolithic perovskite/silicon-heterojunction tandem solar cells processed at low temperature. *Energy & Environmental Science*, 9(1):81–88, 2016.

- [35] S. Albrecht, M. Saliba, J.-P. Correa-Baena, K. Jäger, L. Korte, A. Hagfeldt, M. Grätzel, and B. Rech. Towards optical optimization of planar monolithic perovskite/silicon-heterojunction tandem solar cells. *Journal of Optics*, 18(6):064012, 2016.
- [36] J. Jeong, M. Kim, J. Seo, H. Lu, P. Ahlawat, A. Mishra, Y. Yang, M. A. Hope, F. T. Eickemeyer, M. Kim, et al. Pseudo-halide anion engineering for  $\alpha$ -fapbi 3 perovskite solar cells. *Nature*, 592(7854):381–385, 2021.
- [37] D. Deligiannis, J. van Vliet, R. Vasudevan, R. A. van Swaaij, and M. Zeman. Passivation mechanism in silicon heterojunction solar cells with intrinsic hydrogenated amorphous silicon oxide layers. *Journal of Applied Physics*, 121(8):085306, 2017.
- [38] J. Ge, Z. Ling, J. Wong, T. Mueller, and A. Aberle. Optimisation of intrinsic a-si: H passivation layers in crystalline-amorphous silicon heterojunction solar cells. *Energy Procedia*, 15:107–117, 2012.
- [39] M. Bivour, C. Reichel, M. Hermle, and S. W. Glunz. Improving the a-si: H (p) rear emitter contact of n-type silicon solar cells. *Solar Energy Materials and solar cells*, 106:11–16, 2012.
- [40] M. Taguchi, A. Terakawa, E. Maruyama, and M. Tanaka. Obtaining a higher voc in hit cells. *Progress in photovoltaics: research and applications*, 13(6):481–488, 2005.
- [41] H. Fujiwara and M. Kondo. Real-time monitoring and process control in amorphous/ crystalline silicon heterojunction solar cells by spectroscopic ellipsometry and infrared spectroscopy. *Applied Physics Letters*, 86(3):032112, 2005.
- [42] R. Rizzoli, E. Centurioni, J. Plá, C. Summonte, A. Migliori, A. Desalvo, and F. Zignani. Open circuit voltage in homojunction and heterojunction silicon solar cells grown by vhf-pecvd. *Journal of non-crystalline solids*, 299:1203–1207, 2002.
- [43] D. Pysch, C. Meinhard, N.-P. Harder, M. Hermle, and S. W. Glunz. Analysis and optimization approach for the doped amorphous layers of silicon heterojunction solar cells. *Journal of Applied Physics*, 110(9):094516, 2011.
- [44] T. M. Razykov, C. S. Ferekides, D. Morel, E. Stefanakos, H. S. Ullal, and H. M. Upadhyaya. Solar photovoltaic electricity: Current status and future prospects. *Solar energy*, 85(8):1580–1608, 2011.
- [45] J. Ramanujam and A. Verma. Photovoltaic properties of a-si: H films grown by plasma enhanced chemical vapor deposition: a review. *Materials Express*, 2(3):177–196, 2012.
- [46] A. Smets and M. Van De Sanden. Relation of the si h stretching frequency to the nanostructural si h bulk environment. *Physical Review B*, 76(7):073202, 2007.
- [47] H. Meddeb, T. Bearda, Y. Abdelraheem, H. Ezzaouia, I. Gordon, J. Szlufcik, and J. Poortmans. Structural, hydrogen bonding and in situ studies of the effect of hydrogen dilution on the passivation by amorphous silicon of n-type crystalline (1 0 0) silicon surfaces. *Journal of Physics D: Applied Physics*, 48(41):415301, 2015.
- [48] G. Lucovsky, R. Nemanich, and J. Knights. Structural interpretation of the vibrational spectra of a-si: H alloys. *Physical Review B*, 19(4):2064, 1979.
- [49] M. A. Wank. Manipulating the hydrogenated amorphous silicon growing surface. 2011.
- [50] W. Liu, L. Zhang, R. Chen, F. Meng, W. Guo, J. Bao, and Z. Liu. Underdense a-si: H film capped by a dense film as the passivation layer of a silicon heterojunction solar cell. *Journal of Applied Physics*, 120(17):175301, 2016.
- [51] A. Matsuda and K. Tanaka. Investigation of the growth kinetics of glow-discharge hydrogenated amorphous silicon using a radical separation technique. *Journal of applied physics*, 60(7):2351–2356, 1986.
- [52] J. Perrin, Y. Takeda, N. Hirano, Y. Takeuchi, and A. Matsuda. Sticking and recombination of the sih<sub>3</sub> radical on hydrogenated amorphous silicon: The catalytic effect of diborane. *Surface Science*, 210(1-2):114–128, 1989.

- [53] W. Kessels, A. Smets, D. Marra, E. Aydil, D. Schram, van de Sanden, and MCM. On the growth mechanism of a-si: H. *Thin Solid Films*, 383(1-2):154–160, 2001.
- [54] J. Knights, R. Lujan, M. Rosenblum, R. Street, D. Bieglesen, and J. Reimer. Effects of inert gas dilution of silane on plasma-deposited a-si: H films. *Applied Physics Letters*, 38(5):331–333, 1981.
- [55] A. von Keudell and J. R. Abelson. Direct insertion of sih 3 radicals into strained si-si surface bonds during plasma deposition of hydrogenated amorphous silicon films. *Physical Review B*, 59(8):5791, 1999.
- [56] J. Perrin, J. Schmitt, C. Hollenstein, A. Howling, and L. Sansonnens. The physics of plasma-enhanced chemical vapour deposition for large-area coating: industrial application to flat panel displays and solar cells. *Plasma Physics and Controlled Fusion*, 42(12B):B353, 2000.
- [57] J. Ballutaud. Study of radio-frequency plasma deposition of amorphous silicon for the improvement of solar cell production, 10.5075/epfl-thesis-2900. 2004.
- [58] A. Gallagher. Neutral radical deposition from silane discharges. *Journal of applied physics*, 63(7):2406–2413, 1988.
- [59] C. Tsai, J. Knights, G. Chang, and B. Wacker. Film formation mechanisms in the plasma deposition of hydrogenated amorphous silicon. *Journal of Applied Physics*, 59(8):2998–3001, 1986.
- [60] Y.-S. Cho, C.-H. Hsu, S.-Y. Lien, D.-S. Wu, and I.-C. Hsieh. Effect of hydrogen content in intrinsic a-si: H on performances of heterojunction solar cells. *International Journal of Photoenergy*, 2013, 2013.
- [61] U. Das, M. Burrows, M. Lu, S. Bowden, and R. Birkmire. Surface passivation and heterojunction cells on si (100) and (111) wafers using dc and rf plasma deposited si: H thin films. *Applied Physics Letters*, 92(6):063504, 2008.
- [62] B. Demareux, R. Bartlome, J. P. Seif, J. Geissbühler, D. T. Alexander, Q. Jeangros, C. Ballif, and S. De Wolf. Low-temperature plasma-deposited silicon epitaxial films: Growth and properties. *Journal of Applied Physics*, 116(5):053519, 2014.
- [63] P. R. i Cabarrocas, R. Cariou, and M. Labrune. Low temperature plasma deposition of silicon thin films: From amorphous to crystalline. *Journal of Non-Crystalline Solids*, 358(17):2000–2003, 2012.
- [64] D. Levi, C. Teplin, E. Iwaniczko, Y. Yan, T. Wang, and H. Branz. Real-time spectroscopic ellipsometry studies of the growth of amorphous and epitaxial silicon for photovoltaic applications. *Journal of Vacuum Science & Technology A: Vacuum, Surfaces, and Films*, 24(4):1676–1683, 2006.
- [65] S. De Wolf. Intrinsic and doped a-si: H/c-si interface passivation. In *Physics and technology of amorphous-crystalline heterostructure silicon solar cells*, pages 223–259. Springer, 2012.
- [66] F. Jona. Study of the early stages of the epitaxy of silicon on silicon. *Applied Physics Letters*, 9(6):235–237, 1966.
- [67] R. Hamers, U. Köhler, and J. Demuth. Epitaxial growth of silicon on si (001) by scanning tunneling microscopy. *Journal of Vacuum Science & Technology A: Vacuum, Surfaces, and Films*, 8(1):195–200, 1990.
- [68] A. G. Aberle. *Crystalline silicon solar cells: advanced surface passivation and analysis*. Centre for Photovoltaic Engineering. University of New South Wales, 1999.
- [69] S. Olibet, E. Vallat-Sauvain, and C. Ballif. Model for a-si: H/c-si interface recombination based on the amphoteric nature of silicon dangling bonds. *Physical Review B*, 76(3):035326, 2007.
- [70] J.-W. A. Schüttauf, K. H. van der Werf, I. M. Kielen, W. G. van Sark, J. K. Rath, and R. E. Schropp. Excellent crystalline silicon surface passivation by amorphous silicon irrespective of the technique used for chemical vapor deposition. *Applied physics letters*, 98(15):153514, 2011.
- [71] H. Fujiwara and M. Kondo. Effects of a-si: H layer thicknesses on the performance of a-si: H/ c-si heterojunction solar cells. *Journal of Applied Physics*, 101(5):054516, 2007.

- [72] J.-C. Hsiao, C.-H. Chen, C.-C. Lin, D.-C. Wu, and P. Yu. Effect of hydrogen dilution on the intrinsic a-si: H film of the heterojunction silicon-based solar cell. *Journal of the Electrochemical Society*, 158(9): H876, 2011.
- [73] D. Deligiannis, R. Vasudevan, A. H. Smets, R. A. van Swaaij, and M. Zeman. Surface passivation of c-si for silicon heterojunction solar cells using high-pressure hydrogen diluted plasmas. *AIP Advances*, 5(9):097165, 2015.
- [74] W. Guo, L. Zhang, J. Bao, F. Meng, Y. Chen, E. Lee, Z. Feng, P. J. Verlinden, and Z. Liu. Microstructure of hydrogenated amorphous silicon layers studied by spectroscopic ellipsometry for the surface passivation in heterojunction solar cells. In *2015 IEEE 42nd Photovoltaic Specialist Conference (PVSC)*, pages 1–4. IEEE, 2015.
- [75] D. Deligiannis, V. Marioleas, R. Vasudevan, C. C. Visser, R. A. van Swaaij, and M. Zeman. Understanding the thickness-dependent effective lifetime of crystalline silicon passivated with a thin layer of intrinsic hydrogenated amorphous silicon using a nanometer-accurate wet-etching method. *Journal of Applied Physics*, 119(23):235307, 2016.
- [76] X. Ru, M. Qu, J. Wang, T. Ruan, M. Yang, F. Peng, W. Long, K. Zheng, H. Yan, and X. Xu. 25.11% efficiency silicon heterojunction solar cell with low deposition rate intrinsic amorphous silicon buffer layers. *Solar Energy Materials and Solar Cells*, 215:110643, 2020.
- [77] J. P. Seif, A. Descoedres, G. Nogay, S. Hänni, S. M. De Nicolas, N. Holm, J. Geissbühler, A. Hessler-Wyser, M. Duchamp, R. E. Dunin-Borkowski, et al. Strategies for doped nanocrystalline silicon integration in silicon heterojunction solar cells. *IEEE Journal of Photovoltaics*, 6(5):1132–1140, 2016.
- [78] G. Nogay, J. P. Seif, Y. Riesen, A. Tomasi, Q. Jeangros, N. Wyrsh, F.-J. Haug, S. De Wolf, and C. Ballif. Nanocrystalline silicon carrier collectors for silicon heterojunction solar cells and impact on low-temperature device characteristics. *IEEE Journal of Photovoltaics*, 6(6):1654–1662, 2016.
- [79] T. Itoh, K. Yamamoto, K. Ushikoshi, S. Nonomura, and S. Nitta. Characterization and role of hydrogen in nc-si: H. *Journal of non-crystalline solids*, 266:201–205, 2000.
- [80] E. Vallat-Sauvain, U. Kroll, J. Meier, A. Shah, and J. Pohl. Evolution of the microstructure in microcrystalline silicon prepared by very high frequency glow-discharge using hydrogen dilution. *Journal of Applied Physics*, 87(6):3137–3142, 2000.
- [81] L. Houben, M. Luysberg, P. Hapke, R. Carius, F. Finger, and H. Wagner. Structural properties of microcrystalline silicon in the transition from highly crystalline to amorphous growth. *Philosophical Magazine A*, 77(6):1447–1460, 1998.
- [82] V. Smirnov, A. Lambertz, S. Moll, M. Bär, D. E. Starr, R. G. Wilks, M. Gorgoi, A. Heidt, M. Luysberg, B. Holländer, et al. Doped microcrystalline silicon oxide alloys for silicon-based photovoltaics: Optoelectronic properties, chemical composition, and structure studied by advanced characterization techniques. *physica status solidi (a)*, 213(7):1814–1820, 2016.
- [83] S. Sriraman, S. Agarwal, E. S. Aydil, and D. Maroudas. Mechanism of hydrogen-induced crystallization of amorphous silicon. *Nature*, 418(6893):62–65, 2002.
- [84] P. Roca i Cabarrocas, N. Layadi, T. Heitz, B. Drévilion, and I. Solomon. Substrate selectivity in the formation of microcrystalline silicon: Mechanisms and technological consequences. *Applied Physics Letters*, 66(26):3609–3611, 1995.
- [85] J. Koh, H. Fujiwara, R. Koval, C. Wronski, and R. Collins. Real time spectroscopic ellipsometry studies of the nucleation and growth of p-type microcrystalline silicon films on amorphous silicon using b 2 h 6, b (ch 3) 3 and bf 3 dopant source gases. *Journal of applied physics*, 85(8):4141–4153, 1999.
- [86] H. A. Gatz, J. K. Rath, M. A. Verheijen, W. M. Kessels, and R. E. Schropp. Silicon heterojunction solar cell passivation in combination with nanocrystalline silicon oxide emitters. *physica status solidi (a)*, 213(7): 1932–1936, 2016.

- [87] L. Mazzarella, S. Kirner, O. Gabriel, S. S. Schmidt, L. Korte, B. Stannowski, B. Rech, and R. Schlatmann. Nanocrystalline silicon emitter optimization for si-hj solar cells: substrate selectivity and co2 plasma treatment effect. *physica status solidi (a)*, 214(2):1532958, 2017.
- [88] S. Kirner, L. Mazzarella, L. Korte, B. Stannowski, B. Rech, and R. Schlatmann. Silicon heterojunction solar cells with nanocrystalline silicon oxide emitter: insights into charge carrier transport. *IEEE Journal of Photovoltaics*, 5(6):1601–1605, 2015.
- [89] A. Richter, V. Smirnov, A. Lambertz, K. Nomoto, K. Welter, and K. Ding. Versatility of doped nanocrystalline silicon oxide for applications in silicon thin-film and heterojunction solar cells. *Solar Energy Materials and Solar Cells*, 174:196–201, 2018.
- [90] L. Mazzarella, S. Kirner, B. Stannowski, L. Korte, B. Rech, and R. Schlatmann. p-type microcrystalline silicon oxide emitter for silicon heterojunction solar cells allowing current densities above 40 ma/cm<sup>2</sup>. *Applied Physics Letters*, 106(2):023902, 2015.
- [91] N. H. Nickel and W. Jackson. Hydrogen-mediated creation and annihilation of strain in amorphous silicon. *Physical Review B*, 51(8):4872, 1995.
- [92] H. Ge. Development of high efficiency shj/poly-si passivating contact hybrid solar cells. 2017.
- [93] D. Zhang. Surface passivation and optical design of silicon heterojunction solar cells. Master's thesis, TU Delft, 2015.
- [94] P. Babál. Doped nanocrystalline silicon oxide for use as (intermediate) reflecting layers in thin-film silicon solar cells. 2014.
- [95] M. Mews, T. F. Schulze, N. Mingirulli, and L. Korte. Hydrogen plasma treatments for passivation of amorphous-crystalline silicon-heterojunctions on surfaces promoting epitaxy. *Applied Physics Letters*, 102(12):122106, 2013.
- [96] B. Demaurex, S. De Wolf, A. Descoeur, Z. Charles Holman, and C. Ballif. Damage at hydrogenated amorphous/crystalline silicon interfaces by indium tin oxide overlayer sputtering. *Applied Physics Letters*, 101(17):171604, 2012.
- [97] G. Papakonstantinou. Investigation and optimization of the front metal contact of silicon heterojunction solar cells. 2014.
- [98] H. Fujiwara. *Spectroscopic ellipsometry: principles and applications*. John Wiley & Sons, 2007.
- [99] A. Ferlauto, G. Ferreira, J. M. Pearce, C. Wronski, R. Collins, X. Deng, and G. Ganguly. Analytical model for the optical functions of amorphous semiconductors from the near-infrared to ultraviolet: Applications in thin film photovoltaics. *Journal of Applied Physics*, 92(5):2424–2436, 2002.
- [100] R. A. Sinton and A. Cuevas. Contactless determination of current–voltage characteristics and minority-carrier lifetimes in semiconductors from quasi-steady-state photoconductance data. *Applied Physics Letters*, 69(17):2510–2512, 1996.
- [101] A. Cuevas and D. Macdonald. Measuring and interpreting the lifetime of silicon wafers. *Solar Energy*, 76(1-3):255–262, 2004.
- [102] Y. Zhao. Contact Stack Evaluation for SHJ Solar Cells and Process Development of IBC-SHJ Solar Cells. Master's thesis, TU Delft, 2018.
- [103] FTIR Interferometer. URL [https://commons.wikimedia.org/wiki/File:FTIR\\_Interferometer.png](https://commons.wikimedia.org/wiki/File:FTIR_Interferometer.png). Visited on 2021-01-20.
- [104] W. Beyer and M. A. Ghazala. Absorption strengths of si-h vibrational modes in hydrogenated silicon. *MRS Online Proceedings Library*, 507(1):601–606, 1998.
- [105] A. Smets, W. Kessels, and M. Van de Sanden. Vacancies and voids in hydrogenated amorphous silicon. *Applied physics letters*, 82(10):1547–1549, 2003.

- [106] M. Brodsky, M. Cardona, and J. Cuomo. Infrared and raman spectra of the silicon-hydrogen bonds in amorphous silicon prepared by glow discharge and sputtering. *Physical Review B*, 16(8):3556, 1977.
- [107] A. Langford, M. Fleet, B. Nelson, W. Lanford, and N. Maley. Infrared absorption strength and hydrogen content of hydrogenated amorphous silicon. *Physical Review B*, 45(23):13367, 1992.
- [108] D. Pysch, A. Mette, and S. W. Glunz. A review and comparison of different methods to determine the series resistance of solar cells. *Solar Energy Materials and Solar Cells*, 91(18):1698–1706, 2007.
- [109] F. S. Rocha, A. J. Gomes, C. N. Lunardi, S. Kaliaguine, and G. S. Patience. Experimental methods in chemical engineering: Ultraviolet visible spectroscopy—uv-vis. *The Canadian Journal of Chemical Engineering*, 96(12):2512–2517, 2018.
- [110] Applications and Use of Integrating Spheres with the LAMBDA 650 and 850 UV/Vis and LAMBDA 950 UV/Vis/NIR Spectrophotometers. URL [https://www.perkinelmer.com/CMSResources/Images/44-74191APP\\_LAMBDA650IntegratingSpheres.pdf](https://www.perkinelmer.com/CMSResources/Images/44-74191APP_LAMBDA650IntegratingSpheres.pdf). Visited on 2021-01-20.
- [111] A. Neumüller, O. Sergeev, S. J. Heise, S. Bereznev, O. Volobujeva, J. F. L. Salas, M. Vehse, and C. Agert. Improved amorphous silicon passivation layer for heterojunction solar cells with post-deposition plasma treatment. *Nano energy*, 43:228–235, 2018.
- [112] H. Sai, P.-W. Chen, H.-J. Hsu, T. Matsui, S. Nunomura, and K. Matsubara. Impact of intrinsic amorphous silicon bilayers in silicon heterojunction solar cells. *Journal of Applied Physics*, 124(10):103102, 2018.
- [113] F. Wang, X. Zhang, L. Wang, Y. Jiang, C. Wei, S. Xu, and Y. Zhao. Improved amorphous/crystalline silicon interface passivation for heterojunction solar cells by low-temperature chemical vapor deposition and post-annealing treatment. *Physical Chemistry Chemical Physics*, 16(37):20202–20208, 2014.
- [114] M. Jeon, S. Yoshida, and K. Kamisako. Hydrogenated amorphous silicon film as intrinsic passivation layer deposited at various temperatures using rf remote-pecvd technique. *Current Applied Physics*, 10(2):S237–S240, 2010.
- [115] H. Fujiwara and M. Kondo. Impact of epitaxial growth at the heterointerface of a-si: H/ c-si solar cells. *Applied Physics Letters*, 90(1):013503, 2007.
- [116] J. Gope, S. Kumar, A. Parashar, P. Dixit, C. Rauthan, O. Panwar, D. Patel, and S. Agarwal. Amorphous and nanocrystalline silicon made by varying deposition pressure in pecvd process. *Journal of non-crystalline solids*, 355(45-47):2228–2232, 2009.
- [117] S. Kim, V. A. Dao, Y. Lee, C. Shin, J. Park, J. Cho, and J. Yi. Processed optimization for excellent interface passivation quality of amorphous/crystalline silicon solar cells. *Solar energy materials and solar cells*, 117:174–177, 2013.
- [118] S.-K. Kim, J. C. Lee, S.-J. Park, Y.-J. Kim, and K. H. Yoon. Effect of hydrogen dilution on intrinsic a-si: H layer between emitter and si wafer in silicon heterojunction solar cell. *Solar energy materials and solar cells*, 92(3):298–301, 2008.
- [119] H. Hao, X. Liao, X. Zeng, H. Diao, Y. Xu, and G. Kong. Structure, stability and photoelectronic properties of transition films from amorphous to microcrystalline silicon. *Journal of crystal growth*, 281(2-4):344–348, 2005.
- [120] U. Kroll, J. Meier, P. Torres, J. Pohl, and A. Shah. From amorphous to microcrystalline silicon films prepared by hydrogen dilution using the vhf (70 mhz) gd technique. *Journal of Non-Crystalline Solids*, 227:68–72, 1998.
- [121] J. Temmler, L. Bodlak, A. Moldovan, M. Bivour, A. Wolf, and J. Rentsch. Passivation and microstructure of dual intrinsic a-si: H layers for shj solar cells. 2019. presented at the 36th European PV Solar Energy Conference and Exhibition.
- [122] M. Zeman, O. Isabella, J. Zhou, and G. Yang. Mask-less patterning of amorphous silicon layers for low-cost silicon hetero-junction interdigitated back-contact solar cells. 2018.

- [123] Y.-L. Hsieh, C.-L. Tseng, C.-C. Lee, Y.-K. Fuh, J.-Y. Chang, J.-Y. Lee, and T. T. Li. Improved process stability on an extremely thin amorphous/crystalline silicon interface passivation layer by using predeposition on the chamber wall. *ECS Journal of Solid State Science and Technology*, 7(8):P355, 2018.
- [124] T. Schulze, H. Beushausen, C. Leendertz, A. Dobrich, B. Rech, and L. Korte. Interplay of amorphous silicon disorder and hydrogen content with interface defects in amorphous/crystalline silicon heterojunctions. *Applied Physics Letters*, 96(25):252102, 2010.
- [125] A. Descoeurdes, L. Barraud, S. De Wolf, B. Strahm, D. Lachenal, C. Gu erin, Z. Holman, F. Zicarelli, B. Demaurex, J. Seif, et al. Improved amorphous/crystalline silicon interface passivation by hydrogen plasma treatment. *Applied Physics Letters*, 99(12):123506, 2011.
- [126] Y. Zhang, C. Yu, M. Yang, L.-R. Zhang, Y.-C. He, J.-Y. Zhang, X.-X. Xu, Y.-Z. Zhang, X.-M. Song, and H. Yan. Significant improvement of passivation performance by two-step preparation of amorphous silicon passivation layers in silicon heterojunction solar cells. *Chinese Physics Letters*, 34(3):038101, 2017.
- [127] Y. Zhao, P. Procel, C. Han, L. Mazzarella, G. Yang, A. Weeber, M. Zeman, and O. Isabella. Design and optimization of hole collectors based on nc-siox: H for high-efficiency silicon heterojunction solar cells. *Solar Energy Materials and Solar Cells*, 219:110779, 2021.
- [128] R. Santbergen, T. Meguro, T. Suezaki, G. Koizumi, K. Yamamoto, and M. Zeman. Genpro4 optical model for solar cell simulation and its application to multijunction solar cells. *IEEE journal of photovoltaics*, 7(3):919–926, 2017.
- [129] M. Mazur, R. Pastuszek, D. Wojcieszak, D. Kaczmarek, J. Domaradzki, A. Obstarczyk, and A. Lubanska. Effect of thickness on optoelectronic properties of ito thin films. *Circuit World*, 2020.
- [130] D. Liu, Q. Wang, C. J. Traverse, C. Yang, M. Young, P. S. Kuttipillai, S. Y. Lunt, T. W. Hamann, and R. R. Lunt. Impact of ultrathin c60 on perovskite photovoltaic devices. *ACS nano*, 12(1):876–883, 2018.
- [131] T. Golubev, D. Liu, R. Lunt, and P. Duxbury. Understanding the impact of c60 at the interface of perovskite solar cells via drift-diffusion modeling. *AIP Advances*, 9(3):035026, 2019.
- [132] T. G. Allen, J. Bullock, X. Yang, A. Javey, and S. De Wolf. Passivating contacts for crystalline silicon solar cells. *Nature Energy*, 4(11):914–928, 2019.
- [133] L. Mazzarella. Nanocrystalline silicon and silicon oxide contact layers for silicon heterojunction solar cells. 2017.
- [134] Z. C. Holman, A. Descoeurdes, L. Barraud, F. Z. Fernandez, J. P. Seif, S. De Wolf, and C. Ballif. Current losses at the front of silicon heterojunction solar cells. *IEEE Journal of Photovoltaics*, 2(1):7–15, 2012.
- [135] W. Rehm, R. Fischer, J. Stuke, and H. Wagner. Photo and dark conductivity of doped amorphous silicon. *physica status solidi (b)*, 79(2):539–547, 1977.
- [136] O. Vetterl, F. Finger, R. Carius, P. Hapke, L. Houben, O. Kluth, A. Lambertz, A. M uck, B. Rech, and H. Wagner. Intrinsic microcrystalline silicon: A new material for photovoltaics. *Solar energy materials and solar cells*, 62(1-2):97–108, 2000.
- [137] M. Sharma, J. Panigrahi, and V. K. Komarala. Nanocrystalline silicon thin film growth and application for silicon heterojunction solar cells: a short review. *Nanoscale Advances*, 2021.
- [138] A. Shah, J. Meier, E. Vallat-Sauvain, N. Wyrsh, U. Kroll, C. Droz, and U. Graf. Material and solar cell research in microcrystalline silicon. *Solar energy materials and solar cells*, 78(1-4):469–491, 2003.
- [139] P. Cuony, D. T. Alexander, I. Perez-Wurfl, M. Despeisse, G. Bugnon, M. Boccard, T. S oderstr om, A. Hessler-Wyser, C. H ebert, and C. Ballif. Silicon filaments in silicon oxide for next-generation photovoltaics. *Advanced Materials*, 24(9):1182–1186, 2012.
- [140] A. Sarker, C. Banerjee, and A. Barua. Preparation and characterization of n-type microcrystalline hydrogenated silicon oxide films. *Journal of Physics D: Applied Physics*, 35(11):1205, 2002.

- [141] Y. Zhao, L. Mazzarella, P. Procel, C. Han, G. Yang, A. Weeber, M. Zeman, and O. Isabella. Doped hydrogenated nanocrystalline silicon oxide layers for high-efficiency c-si heterojunction solar cells. *Progress in Photovoltaics: research and applications*, 28(5):425–435, 2020.
- [142] J. Geissbühler, S. De Wolf, B. Demareux, J. P. Seif, D. T. Alexander, L. Barraud, and C. Ballif. Amorphous/crystalline silicon interface defects induced by hydrogen plasma treatments. *Applied Physics Letters*, 102(23):231604, 2013.
- [143] S. De Wolf and M. Kondo. Boron-doped a-si: H/ c-si interface passivation: Degradation mechanism. *Applied Physics Letters*, 91(11):112109, 2007.
- [144] F. Feldmann, M. Bivour, C. Reichel, M. Hermle, and S. W. Glunz. Passivated rear contacts for high-efficiency n-type si solar cells providing high interface passivation quality and excellent transport characteristics. *Solar energy materials and solar cells*, 120:270–274, 2014.
- [145] L. V. Mercaldo, E. Bobeico, I. Usatii, M. Della Noce, L. Lancellotti, L. Serenelli, M. Izzi, M. Tucci, and P. D. Veneri. Potentials of mixed-phase doped layers in p-type si heterojunction solar cells with zno: Al. *Solar Energy Materials and Solar Cells*, 169:113–121, 2017.
- [146] H. Umishio, H. Sai, T. Koida, and T. Matsui. Nanocrystalline-silicon hole contact layers enabling efficiency improvement of silicon heterojunction solar cells: Impact of nanostructure evolution on solar cell performance. *Progress in Photovoltaics: Research and Applications*, 29(3):344–356, 2021.
- [147] W. Spear and P. Le Comber. Substitutional doping of amorphous silicon. *Solid state communications*, 17(9):1193–1196, 1975.
- [148] S. M. De Nicolás, D. Muñoz, A. Ozanne, N. Nguyen, and P. Ribeyron. Optimisation of doped amorphous silicon layers applied to heterojunction solar cells. *Energy Procedia*, 8:226–231, 2011.
- [149] P. Procel, G. Yang, O. Isabella, and M. Zeman. Theoretical evaluation of contact stack for high efficiency ibc-shj solar cells. *Solar Energy Materials and Solar Cells*, 186:66–77, 2018.
- [150] J. Sritharathikhun, F. Jiang, S. Miyajima, A. Yamada, and M. Konagai. Optimization of p-type hydrogenated microcrystalline silicon oxide window layer for high-efficiency crystalline silicon heterojunction solar cells. *Japanese Journal of Applied Physics*, 48(10R):101603, 2009.
- [151] K. Ding, U. Aeberhard, A. Lambertz, V. Smirnov, B. Holländer, F. Finger, and U. Rau. Impact of doped microcrystalline silicon oxide layers on crystalline silicon surface passivation. *Canadian journal of physics*, 92(7/8):758–762, 2014.
- [152] M. De Bastiani, A. S. Subbiah, E. Aydin, F. H. Isikgor, T. G. Allen, and S. De Wolf. Recombination junctions for efficient monolithic perovskite-based tandem solar cells: physical principles, properties, processing and prospects. *Materials Horizons*, 7(11):2791–2809, 2020.
- [153] H. Shen, D. Walter, Y. Wu, K. C. Fong, D. A. Jacobs, T. Duong, J. Peng, K. Weber, T. P. White, and K. R. Catchpole. Monolithic perovskite/si tandem solar cells: pathways to over 30% efficiency. *Advanced Energy Materials*, 10(13):1902840, 2020.
- [154] A. Tomasi, B. Paviet-Salomon, Q. Jeangros, J. Haschke, G. Christmann, L. Barraud, A. Descoeur, J. P. Seif, S. Nicolay, M. Despeisse, et al. Simple processing of back-contacted silicon heterojunction solar cells using selective-area crystalline growth. *Nature Energy*, 2(5):1–8, 2017.
- [155] B. Macco, J. Melskens, N. J. Podraza, K. Arts, C. Pugh, O. Thomas, and W. M. Kessels. Correlating the silicon surface passivation to the nanostructure of low-temperature a-si: H after rapid thermal annealing. *Journal of Applied Physics*, 122(3):035302, 2017.
- [156] H. Liu. Optimization of Hydrogenated a-Si layer for Si Heterojunction Solar Cells. Master's thesis, TU Delft, 2020.
- [157] C. Han, Y. Zhao, L. Mazzarella, R. Santbergen, A. Montes, P. Procel, G. Yang, X. Zhang, M. Zeman, and O. Isabella. Room-temperature sputtered tungsten-doped indium oxide for improved current in silicon heterojunction solar cells. *Solar Energy Materials and Solar Cells*, 227:111082, 2021.

- 
- [158] C. Han, L. Mazzarella, Y. Zhao, G. Yang, P. Procel, M. Tijssen, A. Montes, L. Spitaleri, A. Gulino, X. Zhang, et al. High-mobility hydrogenated fluorine-doped indium oxide film for passivating contacts c-si solar cells. *ACS applied materials & interfaces*, 11(49):45586–45595, 2019.
- [159] O. Isabella, S. Dobrovolskiy, G. Kroon, and M. Zeman. Design and application of dielectric distributed bragg back reflector in thin-film silicon solar cells. *Journal of non-crystalline solids*, 358(17):2295–2298, 2012.
- [160] B. G. Lee, P. Stradins, D. L. Young, K. Alberi, T.-K. Chuang, J. G. Couillard, and H. M. Branz. Light trapping by a dielectric nanoparticle back reflector in film silicon solar cells. *Applied Physics Letters*, 99(6):064101, 2011.